INFORMATION TO USERS

This manuscript has been reproduced from the microfilm master. UMI films the text directly from the original or copy submitted. Thus, some thesis and dissertation copies are in typewriter face, while others may be from any type of computer printer.

The quality of this reproduction is dependent upon the quality of the copy submitted. Broken or indistinct print, colored or poor quality illustrations and photographs, print bleedthrough, substandard margins, and improper alignment can adversely affect reproduction.

In the unlikely event that the author did not send UMI a complete manuscript and there are missing pages, these will be noted. Also, if unauthorized copyright material had to be removed, a note will indicate the deletion.

Oversize materials (e.g., maps, drawings, charts) are reproduced by sectioning the original, beginning at the upper left-hand corner and continuing from left to right in equal sections with small overlaps. Each original is also photographed in one exposure and is included in reduced form at the back of the book.

Photographs included in the original manuscript have been reproduced xerographically in this copy. Higher quality 6" x 9" black and white photographic prints are available for any photographs or illustrations appearing in this copy for an additional charge. Contact UMI directly to order.

UMI

A Bell & Howell Information Company
300 North Zeeb Road, Ann Arbor MI 48106-1346 USA
313/761-4700 800/521-0600

Downloaded from SHAREOK. Persistent Handle URL: https://hdl.handle.net/11244/5519

UNIVERSITY OF OKLAHOMA

GRADUATE COLLEGE

GREEN THUNDERSTORMS

A Dissertation

SUBMITTED TO THE GRADUATE FACULTY

in partial fulfillment of the requirements for the

degree of

Doctor of Philosophy

By

FRANK WOOLSEY GALLAGHER III
Norman, Oklahoma
1997

UMI Number: 9806312

Copyright 1997 by
Gallagher, Frank Woolsey, III

All rights reserved.

UMI Microform 9806312
Copyright 1997, by UMI Company. All rights reserved.

This microform edition is protected against unauthorized
copying under Title 17, United States Code.

UMI
300 North Zeeb Road
Ann Arbor, MI 48103

GREEN THUNDERSTORMS

A Dissertation APPROVED FOR THE
SCHOOL OF METEOROLOGY

BY

William H. Beasley

Ray F. Bohren

Howard B. Bluestein

Fred Brock

[illegible]

Susan Postawko

© Copyright by FRANK WOOLSEY GALLAGHER III 1997
All Rights Reserved.

Dedication

It is rare to meet someone who gives you the freedom to follow your dreams. I have been fortunate enough to have been married to such a person for the past seven years. In my endeavor to follow my childhood dreams of obtaining a Ph.D. I sold our house, moved us to a basement, and brought her half-way across the country to a termite infested home in the land of the Red Earth. All the while she encouraged me when I was down, celebrated with me when I was up, and was always vigilant in making sure I did what I had to do.

For all this, and much more, I dedicate this volume to my lovely bride, Elizabeth Ann.

I love you, HB!

Acknowledgments

Not to offend my committee, but I must first thank my parents, Frank and Martha Anne. Throughout my life they have given me a strong, stable family structure that has allowed me to pursue my sometimes crazy adventures. Their teachings and wisdom have allowed my to get where I am today. I love them both. I also thank Beth's parents, Bob and Weetie. Although I never met Beth's mom, her influence is felt daily. Bob supplied us with a cozy basement and, without his generosity, support, and guidance, I could not have even thought of going back to school. I love you, Bob. Thank you for helping bring Jesus back into my life.

I would like to thank my primary advisor, Dr. William H. Beasley for allowing me to pursue this research in my own way. He was always there, except for the off-chance when he had to deal with some departmental crisis, to offer guidance when needed. This project would not have existed had it not been for the creative mind of Dr. Craig F. Bohren. His leadership, exemplified by his life-long achievements, inspired me in the early 1980's and again in the middle 1990's. His suggestions were always razor sharp, cutting away much of the rubbish I tend to accumulate and getting to the core of the problem. I wish I could have spent much more time under his direct tutelage. Thanks are also due to the rest of my committee, Drs. Fred V. Brock, Howard B. Bluestein, Susan

Postawko, and Mark Keil. Their careful reviews of the manuscript and insightful questions forced me to significantly improve the manuscript. Special consideration goes to Fred Brock. He supported me soon after I arrived in Oklahoma and taught me to be a more thoughtful and careful worker. He kept me involved with instrumentation and gave me additional support through a teaching assistantship.

Many others were involved in my professional development. Dr. Jerry Straka allowed my to design and build the second generation of TURTLE sensors. Dr. Erik Rasmussen allowed me to participate in VORTEX in 1994 and 1995 to not only sharpen my storm intercept skills, but also to collect much of the green thunderstorm data presented in this volume. I appreciate the opportunity to assist him in constructing the mobile mesonet instruments. Dr. Roger Wakimoto allowed me to fly in the NCAR Electra aircraft, a mission that provided some of the best green thunderstorm data. Dr. Josh Wurman for giving me the opportunity to participate in the construction and operation of the Doppler-on-Wheels radar equipment.

I wish to thank the School of Meteorology office staff: Nancy, Celia, Marcia, and Alyssa for keeping all the paperwork in order and donuts on the table. Celia, do you really want to see a blue baboon? Finally, I want to thank the many friends who kept me insane all these years: Todd Crawford, David Dowell, Tom Renkevens, Andy Wood, Steve Gaddy, Brent Gordon — my VORTEX companion who did not stop in the path of a tornado when asked to do so, Ken Eack, Mark Askelson — for beating off dumb farmers in Otis, CO, Tom Condo, Gary McManus, Carl Levison, Dan Weber, and the list goes on. Thanks to you all and many who I failed to mention by name.

This research was supported under NSF grant ATM-9400208 from the Physical Meteorology Program. Craig Bohren is supported under NSF grant ATM-9400211. Much of the vehicle support for VORTEX was provided by the Center for Analysis and Prediction of Storms under NSF grand ATM-9120009. Additional vehicle support and guidance were provided by the National Severe Storms Laboratory in Norman, Oklahoma. I also wish to thank Robert Maddox (NSSL), and Kelvin Drogeimier (CAPS) for their support.

Special thanks to George, Critter, and particularly Hobie.

Table of Contents

Dedication iv
Acknowledgments v
List of Figures xi
List of Plates xviii
Abstract xix
Chapter 1: Introduction 1
Chapter 2: PR®-650 Spectrophotometer 8
2.1 Spectrophotometers 8
2.2 PR®-650 Instrument 9
2.2.1 Measurement Technique 10
2.2.2 Light Path Through the Instrument 11
2.2.3 Data Storage and Display 13
2.2.4 Calibration 13
2.2.5 Measurement Error 14
2.2.5.1 Measurement Drift 14
2.2.5.2 Bias or Offset 14
2.2.5.3 Effects of Spectral and Colorimetric Error 15
2.2.5.4 Difference Between 2° and 10° Field of View 17
Chapter 3: Human Color Vision and Colorimetry 20
Introduction 20
3.1 Concept of Color 20
3.2 Elementary Colorimetry 22
3.3 A Warning 27
3.4 Chromaticity Examples 28
3.5 Color Discrimination Thresholds 34
Chapter 4: Spectral Measurements and Observations 36
Introduction 36
4.1 Analysis by Dominant Wavelength 37
4.1.1 Blue-Green Storm Spectra 39
4.1.2 Yellow-Green Storm Spectra 39
4.2 Analysis by Time of Day 40
4.3 Individual Storm Analysis 44
4.3.1 Example #1 — Blue Thunderstorm in Southwest Oklahoma 44
4.3.2 Example #2 — Yellow-Green Thunderstorm in the Texas Panhandle 47
4.3.3 Example #3 — Green Thunderstorm in Southwest Oklahoma 49
4.3.4 Example #4 — Aircraft Observations Over Texas 54
Chapter 5: An Introduction to Prevailing Hypotheses 59
Introduction 59

5.1 Fankhauser *et al.* 59
5.2 Fraser Hypothesis 63
5.3 Ground Reflection 63
5.4 Bohren Theory 64
5.5 Hail as the Cause of the Green Light — Part 1 65
Chapter 6: Fraser Theory 67
Introduction 67
6.1 The Solar Spectrum 67
6.1.1 Solar Radiation Outside the Earth's Atmosphere 68
6.1.2 Surface Spectrum 69
6.2 Theoretical Development 71
6.3 Results of the Fraser Hypothesis 80
6.4 Using a Non-Black Cloud 88
6.5 Another Perspective on the Fraser Theory 100
6.6 Summary 103
Chapter 7: Ground Reflection Hypothesis and the IR Spike Phenomenon 105
Introduction 105
7.1 Theoretical Development 106
7.2 Simple Radiation Model 109
7.3 Observational Data 116
7.4 Ground Reflection Summary 119
7.5 Near Infrared Spikes 120
7.6 Observations of Infrared Spikes 120
7.7 Source of IR Spikes 123
7.7.1 Instrumentation Effects 123
7.7.2 The Bay and the Plains Experiment 124
7.8 Effect of Skylight and Solar Zenith Angle 126
7.8.1 Analytical Computations 126
7.8.2 Setting Sun Experiment 126
7.8.3 Ground Reflection Indicator 129
7.8.4 Ground Reflection Examples 131
7.8.5 Visual Effects of IR Spikes 133
Chapter 8: The Bohren Theory and Why Thunderstorms are Green 137
Introduction 137
8.1 Theoretical Development 137
8.1.1 Water is Blue 139
8.1.2 Numerical Simulations 141
8.2 Bohren Theory of Green Thunderstorms 150
8.2.1 Introduction 150
8.2.2 Theoretical Analysis 151
8.2.2.1 Optical Thickness 151
8.2.2.2 Scattering in a Cloud 152
8.2.2.3 Absorption and Cross Sections 155

8.2.3 Bohren's Derivation 157
8.2.4 Eddington's Approximation 160
8.3 Description of a Simple Numerical Model 161
8.4 Model Parameters 163
8.4.1 Cloud Thickness 163
8.4.2 Drop Size Distributions 164
8.4.3 Liquid Water Content 165
8.5 Model Calculations 166
8.5.1 Small Drops 166
8.5.2 Realistic Drop Sizes 168
8.6 Comparisons With Measurements 170
8.6.1 15 km Thickness 171
8.6.2 5 km Thickness 175
8.7 Hail as the Cause of the Green Light — Part 2 176
8.8 The Slab Model — Reprise 178
8.9 Conclusion 179
Chapter 9: A Mechanism for the Green Light - 7 May 1995 181
Chapter 10: Summary and Conclusions 192
References 196
Appendix A: Derivation of the Spherical Earth Approximation 202
Appendix B: Derivation of the Eddington Approximation 207

List of Figures

Fig. 2-1 A schematic of the light path in the PR®-650 spectrophotometer. 10
Fig. 2-2 Schematic of the Pritchard® mirror. 11
Fig. 2-3 Plot of the color accuracy of the PR®-650 spectrophotometer on a CIE 1976 UCS diagram. 16
Fig. 2-4 The difference in chromaticity of a computed spectrum using the Fraser theory with a distance to the storm of 20 km and a solar zenith angle of 20° between the CIE 1931 2° and CIE 1964 10° color matching functions. 18
Fig. 2-5 The difference in chromaticity of a measurement between the CIE 1931 2° and CIE 1964 10° color matching functions. 19
Fig. 3-1 Color matching functions defined by Wright. 23
Fig. 3-2 CIE 1964 10° color matching functions. 24
Fig. 3-3 CIE 1976 UCS chromaticity diagram. 26
Fig. 3-4 Spectrum of the blue sky shown in Plate 3-1. 29
Fig. 3-5 Spectrum of the blue sky shown in Plate 3-1 plotted on a CIE 1976 UCS chromaticity diagram 30
Fig. 3-6 Spectrum of the snow capped mountaintops shown in Plate 3-2. 32
Fig. 3-7 Spectrum of the snow capped mountains shown in Plate 3-2 plotted on a CIE 1976 UCS chromaticity diagram. 33
Fig. 4-1 Histogram of the dominant wavelengths for all spectra recorded during the 1995-1996 observation period. 37
Fig. 4-2 Histogram of the dominant wavelengths of all of the spectra recorded during the 1995-1996 observation period. 38
Fig. 4-3 Histogram of the dominant wavelengths of green only spectra recorded during the 1995-1996 observation period. 40
Fig. 4-4 Scatter plot of the relationship between the dominant wavelengths of spectra of thunderstorms that were subjectively observed as being green in color and the time of day. 40
Fig. 4-5 A plot of the "average" green storm spectra for thirteen green thunderstorm events. 41
Fig. 4-6 The relationship between the percentage of storms that were subjectively observed to be gray/blue (solid) and green (dashed) for one-hour intervals throughout the day. 42

Fig. 4-7 Scatter plot of the dominant wavelength verses time of day for all of the spectra recorded of thunderstorms that subjectively appeared green to the observer. 43
Fig. 4-8 WSR-88D radar composite of the 16 April 1995 storm in southwestern Oklahoma. 45
Fig. 4-9 Spectrum of a blue thunderstorm recorded on 16 April 1995 at 2310 UTC in Grandfield, Oklahoma looking to the north northeast of a storm located over Geronimo, Oklahoma. 46
Fig. 4-10 Spectrum of a yellow-green thunderstorm recorded on 24 May 1996 at 0001 UTC 16 km east of Miami, Texas. 48
Fig. 4-11 Spectra of a severe thunderstorm observed near Mountain Park, Oklahoma on 7 May 1995 51
Fig. 4-12 Spectra of a thunderstorm observed to be dark blue and blue-green in color recorded from the NCAR Electra aircraft on 31 May 1995 near Sweetwater, Texas. 55
Fig. 6-1 Curves of solar irradiance measured outside the earth's atmosphere and at the earth's surface. 69
Fig. 6-2 Direct normal solar spectral irradiance measured on 4 June 1987 at Cape Canaveral, Florida. 70
Fig. 6-3 Geometry for the derivation of the Schwarzschild equation of radiative transfer. 72
Fig. 6-4 Three curves representing the sunlight component (dashed) for a zenith angle of 85°. 80
Fig. 6-5 Computed spectrum of light using the Fraser theory with a solar zenith angle of 85° and a distance to the storm of 35 km. 81
Fig. 6-6 CIE 1976 UCS chromaticity diagram of the spectrum in Fig. Fig. 6.3-2. 82
Fig. 6-7 A graph showing the variation in the dominant wavelength (solid) and excitation purity (dashed) with solar zenith angle for a distance to the storm of 35 km using the Fraser theory. 83
Fig. 6-8 CIE 1976 UCS chromaticity diagram showing the variation of chromaticity with solar zenith angle for a distance to the storm of 35 km using the Fraser theory. 85
Fig. 6-9 CIE 1976 UCS chromaticity diagram showing the variation of chromaticity with distance to the storm for a solar zenith angle of 80° using the Fraser theory. 86
Fig. 6-10 A graph showing the variation in the dominant wavelength (solid) and excitation purity (dashed) with distance to the storm for a solar zenith angle of 80° using the Fraser theory. 87
Fig. 6-11 Geometry of the reflected light from a distant cloud. 88

Fig. 6-12 The variation in dominant wavelength with changes in cloud reflectivity using the Fraser theory. The distance to the storm was fixed at 10 km and the solar zenith angle was 70°. 90
Fig. 6-13 CIE 1976 UCS diagram showing the variation in chromaticity with changes in cloud reflectivity using the Fraser theory. The distance to the storm was 35 km and the solar zenith angle was 70°. 91
Fig. 6-14 CIE 1976 UCS chromaticity diagram showing an observation (×) compared to three Fraser theory calculations: black cloud (▲), 3 % reflecting cloud (●), and a 10 % reflecting cloud (■). 93
Fig. 6-15 Spectra of an observation and two different Fraser theory calculations. The observation (solid) was recorded on 17 April 1995 at 0046 UTC, 8 km west of Walters, Oklahoma looking east. The black cloud calculation is dashed and the dotted line represents a cloud reflectivity of 3 %. 94
Fig. 6-16 CIE 1976 UCS chromaticity diagram indicating five spectra, one an observation and four of Fraser calculations. 95
Fig. 6-17 A closeup view of the data shown in Fig. 6-16. 96
Fig. 6-18 Spectra of the Ocala observation (solid) and the 2% Fraser theory computed spectrum (dashed). 97
Fig. 6-19 Spectra of the mean Ocala observation (solid) and the 2% Fraser theory computed spectrum (dashed). 98
Fig. 6-20 Spectrum of a greenish-blue patch of sky looking to the east on 21 June 1995 at 2354 UTC 1 km north of Otis, Colorado. 101
Fig. 6-21 Comparison of an observation (solid) with a calculated spectrum (dotted) using the Fraser theory and a fourth-order approximation to represent the blue skylight. 102
Fig. 7-1 Schematic of the optical path of a beam of light that passes through a cloud, reflects of the ground, then reflects off the cloud to the observer. 106
Fig. 7-2 Spectral reflectance curve of green grass. 108
Fig. 7-3 Geometry of the nonabsorbing ground reflection problem. 110
Fig. 7-4 Spectrum of young wheat growing in a field in Mountain Park, Oklahoma. 111
Fig. 7-5 Computed total radiance (solid), transmitted radiance (dashed), and reflected radiance (dotted) with no solid angle dependence, calculated using a cloud reflectance of 1.0 and a cloud transmission of 10^{-6}. 112
Fig. 7-6 Computed total radiance (solid), transmitted radiance (dashed), and reflected radiance (dotted) with no solid

angle dependence, calculated using a cloud reflectance of 1.0 and a cloud transmission of 10^{-6}. The solar zenith angle was 85°. 114
Fig. 7-7 CIE 1976 UCS chromaticity diagram showing the three computed spectra: (○) total light observed, (×) transmitted light, and (□) reflected light. 115
Fig. 7-8 Spectrum of a green thunderstorm recorded on 7 May 1995 at 2231 UTC 16 km east-southeast of Mountain Park, Oklahoma. 116
Fig. 7-9 A comparison of the spectrum of foliage underneath a green thunderstorm (solid) to a difference spectrum derived from subtracting a green storm spectrum from a blue thunderstorm spectrum (dotted). 117
Fig. 7-10 Spectrum of a green thunderstorm. Recorded on 7 May 1995 at 2212 UTC in Mountain Park, Oklahoma. 121
Fig. 7-11 Spectrum of a green thunderstorm. Recorded on 25 May 1996 at 0002 UTC 18 km east of Miami, Texas. 122
Fig. 7-12 Spectrum of the light from a hot stove element. 123
Fig. 7-13 A comparison of the ratio of 748 nm to 412 nm wavelengths at various observation angles over water and over a field of growing wheat. 125
Fig. 7-14 Computed attenuation ratio of blue (470 nm) light to red (700 nm) light in a molecular atmosphere. 127
Fig. 7-15 The spectra of solar radiation reflected off the MacBeth "white" square on the MacBeth Color Checker Chart at various solar zenith angles. 128
Fig. 7-16 Difference spectrum between spectra recorded at solar zenith angles of 61.9° and 86.8°. 129
Fig. 7-17 Spectrum of a "brownish" looking cloud. Spectrum recorded on 7 May 1995 at 2232 UTC 16 km east southeast of Mountain Park, Oklahoma. 131
Fig. 7-18 Spectrum of a "brownish" looking cloud. Spectrum recorded on 18 May 1995 at 0011 UTC in Rose, Oklahoma. 132
Fig. 7-19 Actual and "corrected" spectra of a green thunderstorm. Spectrum recorded on 7 May 1995 at 2212 UTC in Mountain Park, Oklahoma. 134
Fig. 7-20 Actual and "corrected" spectra of a green thunderstorm. Spectrum recorded on 25 May 1996 at 002 UTC 18 km east of Miami, Texas. 135
Fig. 7-21 Actual and "corrected" spectra of green foliage beneath a green thunderstorm. 136
Fig. 8-1 Schematic of the path of light simulated by the slab model. 137
Fig. 8-2 Absorption of radiation by pure liquid water. 139

Fig. 8-3 Relationship between the solar zenith angle of the incident radiation and the dominant wavelength of the resultant illumination. The slab depth is 5 m. 141
Fig. 8-4 Relationship between the solar zenith angle of the incident radiation and the dominant wavelength of the resultant illumination. The slab depth is 10 m. 142
Fig. 8-5 CIE 1976 UCS chromaticity diagram showing the variation in chromaticity with a change in solar zenith angle. 143
Fig. 8-6 The variation in dominant wavelength of the simulated light from the bottom of a slab of water of various thickness. 144
Fig. 8-7 CIE 1976 UCS chromaticity diagram indicating the variation in chromaticity of the light passing through the slab with a change in the thickness of the slab. 145
Fig. 8-8 Spectra of light from the slab model for a solar zenith angle of 75° and various slab depths. 147
Fig. 8-9 Slab thickness for green light for different solar zenith angles. A wavelength of 510 nm was chosen to represent "green" light. 148
Fig. 8-10 Comparison of a computed spectrum (solid) to an observation (dashed). The computed spectrum is for a slab of 10.5 m thick and a solar zenith angle of 75°. 149
Fig. 8-11 Basic scattering geometry. 153
Fig. 8-12 The dashed curve shows the third order approximation used in the Green Thunderstorm Optical Model. 162
Fig. 8-13 CIE 1976 UCS chromaticity diagram showing the variation in chromaticity of a simulated cumulonimbus cloud with changes in cloud liquid water content. The cloud thickness is 15 km, the mean drop diameter is 5 μm, and the solar zenith angle is 85°. 167
Fig. 8-14 CIE 1976 UCS chromaticity diagram showing the variation in chromaticity of a simulated cumulonimbus cloud with changes in cloud liquid water content. Liquid water content (g m^{-3}) is shown next to the chromaticity points. The cloud thickness is 15 km, the mean drop diameter is 22 μm, and the solar zenith angle is 85°. 168
Fig. 8-15 The path of solar radiation through the atmosphere for a 5 km and 15 km thick cloud. 171
Fig. 8-16 CIE 1976 UCS chromaticity diagram showing the variation in chromaticity of a simulated cumulonimbus cloud with changes in cloud liquid water content. 172
Fig. 8-17 Calculated spectrum using a 15 km thick cloud, 5 μm drop size, and a liquid water content of 1 g m^{-3} compared to an observation. 173

Fig. 8-18 CIE 1976 UCS chromaticity diagram showing the variation in chromaticity of a simulated cumulonimbus cloud with changes in cloud liquid water content. Liquid water content (g m^{-3}) is shown next to the chromaticity points. The cloud thickness is 5 km, the mean drop diameter is 5 μm, and the solar zenith angle is 55°. 174
Fig. 8-19 Calculated spectrum using a 5 km thick cloud, 22 μm drop size, and a liquid water content of 2.9 g m^{-3} compared to an observation. 176
Fig. 8-20 CIE 1976 UCS chromaticity diagram showing the variation in chromaticity of a simulated cumulonimbus cloud with changes in cloud liquid water content. Liquid water content (g m^{-3}) is shown next to the chromaticity points. The cloud thickness is 5 km, the mean drop diameter is 3000 μm, and the solar zenith angle is 55°. 177
Fig. 9-1 Sounding from Altus, Oklahoma on 7 May 1995. Launch time is 1918 UTC. 181
Fig. 9-2 Composite radar summary for 7 May 1995 between 1800 UTC and 2100 UTC in Oklahoma and north Texas. 182
Fig. 9-3 A map of significant hail fall reports in southwestern Oklahoma on 7 May 1995. 183
Fig. 9-4 Composite radar summary between 2200 UTC on 7 May 1995 and 0100 UTC on 8 May 1995 in Oklahoma and north Texas. 184
Fig. 9-5 Spectra of a severe thunderstorm observed near Mountain Park, Oklahoma on 7 May 1995. 185
Fig. 9-6 WSR 88D reflectivity from the Twin Lakes (TLX) radar at 2206 UTC 186
Fig. 9-7 Schematic of the path of light through the thunderstorm and the relative position of the observer when the first spectrum was recorded at 2206 UTC in Mountain Park, Oklahoma on 7 May 1995. 187
Fig. 9-8 WSR 88D reflectivity from the Twin Lakes (TLX) radar at 2232 UTC. 188
Fig. 9-9 Schematic of the path of light through the thunderstorm and the relative position of the observer when the last spectrum was recorded at 2232 UTC 16 km to the east southeast of Mountain Park, Oklahoma on 7 May 1995. 190
Fig. A-1 Geometry used for the spherical earth approximation derivation. 202
Fig. A-2 Sunset geometry. 205
Fig. B-1 Plane parallel geometry. 208
Fig. B-2 Spherical coordinates. 208
Fig. B-3 Scattering geometry of incident solar radiation. 210

Fig. B-4 Scattering angle geometry. 215
Fig. B-5 Geometry for irradiance boundary conditions. 228
Fig. B-6 Layered, plane-parallel atmosphere geometry. 230
Fig. B-7 Geometry for the downwelling irradiance below a thunderstorm. 242

List of Plates

Plate 1-1 John Steuart Curry, *Tornado Over Kansas*, 1929. Oil on canvas, 118 cm x 153 cm. Collection of the Muskegon Museum of Art, Hackley Art Gallery, Muskegon, Michigan. 5

Plate 2-1 The Photo Research PR®-650 Spectrophotometer. 9

Plate 3-1 Photograph of the blue sky that coincides with the spectrum shown in Figure 3-4. 28

Plate 3-2 Photograph of the snow capped mountains coincides with the spectrum shown in Figure 3-6. 31

Plate 4-1 Photograph of the thunderstorm that coincides with the spectrum shown in Figure 4-8. 47

Plate 4-2 Photograph of the thunderstorm that coincides with the spectrum shown in Figure 4-10. 49

Plate 4-3 Photograph of the thunderstorm that coincides with the spectrum shown in Figure 4-11a. 52

Plate 4-4 Photograph of the thunderstorm that coincides with the spectrum shown in Figure 4-11d. 53

Plate 4-5 Photograph of the thunderstorm of Figure 4-12 56

Plate 4-6 Photograph of the thunderstorm near Sweetwater, Texas. 57

Plate 5-1 The cover of the May 1983 issue of the *Bulletin of the American Meteorological Society*. 61

Abstract

Many people around the world have observed green light apparently emanating from severe thunderstorms, but until recently there has been no scientific study of the phenomenon. Green thunderstorms have been observed from time to time in association with deep convection or severe weather events. Some skeptics who have not personally observed a green thunderstorm suggest that they are some kind of illusion.

The existence of green thunderstorms has been objectively demonstrated by recording spectra of light from thunderstorms using a handheld spectrophotometer. During the spring and summer of 1995 and the spring of 1996 numerous storms were observed and spectra of the light emanating from these storms were recorded. Observations were made both at the ground and aboard research aircraft. Furthermore, time series of spectra were recorded as the observed color of some storms changed from dark blue to a bluish-green.

Several hypotheses have been advanced to explain the occurrence of green light in connection with severe storms. Fankhauser gave some observational support to the belief that green light from thunderstorms is possible and believed that the source of the light is from the blue sky penetrating thin regions in the clouds. Fraser believes that light from the setting sun, in combination with the process of scattering by atmospheric molecules, creates the green light associated with severe weather and the thunderstorm acts only as a

black backdrop. Unfortunately, no cloud illuminated by the sun is black and the green airlight produced by the Fraser theory is in reality overwhelmed by light reflected by the cloud.

Often the unusual coloration has been attributed to hail or to reflection of light from foliage on the ground. The quantitative measurements made during the observation period fail to support these assumptions. We have observed thunderstorms to be green over ground that was not green and we have observed blue thunderstorms over ground that was green.

Finally, Bohren believes that reddened sunlight in combination with filtering done by naturally blue-colored water creates green light. Given our observations, this is the most likely explanation for the green light. Our observations and calculations indicate that, depending on the microphysical parameters of the cloud, sunlight transmitted by the cloud may appear green.

Chapter 1: Introduction

Through the ages man has explored his surroundings. Often the result of such exploration is an extension of human knowledge. Simple observations of a natural phenomenon often have initiated a series of studies that eventually resulted in an entirely new idea. James Burke (1978) traces the development of several present day inventions, such as television sets, that began with seemingly unrelated events. Research on interesting phenomena often leads to surprising results. On the surface, the study of the colors of thunderstorms may seem unimportant, even trivial, but the possibility of using spectrophotometry to learn something potentially useful about thunderstorms, to me, makes the endeavor worthwhile.

We ask the seemingly simple question: What exactly is a green thunderstorm? The obvious answer is that a green thunderstorm is a thunderstorm that appears green in color. Human beings are not very good at identifying specific colors but are rather good at matching colors. So when one looks at the sky and sees a green storm, that color observed may be various shades of green. In fact, different people may see slightly different colors, so that there is no single green color associated with thunderstorms. The mechanisms of human vision and perception are extremely complicated and shall be discussed here briefly only to give a quantitative framework to the recorded and

computed spectra. The next logical question to ask is, "What is so special about the color green?"

The green color from a thunderstorm is remarkable for two reasons. First, green is usually associated with the ground below and not the sky above. As the daytime progresses from dawn to dusk, the sky changes color depending on atmospheric conditions or cloud cover. If one first considers a cloudless day, the sky overhead changes from a purple or reddish glow in the early morning to a deep blue near noon. During the day, the sky takes on different shades of blue, with the deepest blue approximately 95° from the sun, when the sun is low in the sky, to 65° from the sun when the sun is high (Minnaert 1954). Toward the horizon, the sky color becomes less and less saturated and may even appear white. When clouds are added into the sky scene, the early morning (or late evening) red is projected onto the clouds for an often spectacular display of atmospheric optics. During the better part of the day, clouds usually appear either a bright white or a dull gray to the casual observer. Green grass grows on the ground and is quite familiar to any observer. The green in trees is skyward to most people, but the color is easily rooted to the ground through the trunk and branches. Trees grow from the ground and do not belong to the sky.

Second, green color is commonly associated with specific types of severe weather. Much folklore has developed as a result of the association between the green color in the clouds and nasty weather including hail or tornadoes. Throughout recent history, the association between the green sky and certain types of weather has been noted by mariners sailing the oceans of the earth. One of the earlier modern references is by

Admiral Fitzroy where he states that "When the sky is of a sickly-looking greenish hue, wind or rain may be expected (QJRMS 1930)." Along similar lines, Lt. Cmdr. H. E. Turner writes that "among experienced seamen in the China Seas a green sky is regarded as the forerunner of a typhoon (QJRMS 1930)." Colonel E. Gold, while he was the First Mate on the *Euripides* noted, when asked about the color of the sky, that "a green sky [is] for wind" (Pick 1930). Events of green skies also have been reported in the literature by people on land. Smythe, in his book *Climbs and Ski Runs*, mentions three examples of green sky observed in the Alps at sunrise. His reports include details of bad weather following the observance of the green sky. He concludes that

> "If that dawn is green he may, without any other reason or data, confidently forecast bad weather within twenty-four hours (QJRMS 1930)

Pick (1930) delved into some of the historical records of the British Meteorological Offices and found references to green sky conditions in "some part or another" of the sky on nearly 40 days between 1 October 1929 and 31 March 1930. He found that, for the sixteen observed events (at Cranwell and London), in every case the green color was associated with a strong trough located to the north or west of the United Kingdom. As a result, he concluded that

> "the green color in the sky, at least in the British Isles, is definitely to be ranked as a concomitant or as a herald of bad weather."

His second result of the study was that very strong winds aloft were associated with the green color. These examples demonstrate the assumed connection between green sky and bad weather although no other reason other than an association is given for the cause of the green sky. Even some twentieth century paintings show this association.

John Steuart Curry, a member of the Midwestern Triumvirate of American Regionalism, painted a scene of a Kansan family running for cover to protect itself from an oncoming tornado. The painting, *Tornado Over Kansas* (Plate 1-1), shows a brightly illuminated green sky behind a barn. Whether Curry actually observed this phenomenon is unknown to the author but the green sky color is an interesting coincidence and, for those who see the painting in the Muskegon Museum of Art, it may tend to perpetuate the association between green skies and bad weather.

With the increase in interest in storm chasing over the past decade or so, a flurry of reports in various media continue to perpetuate the link between green thunderstorms and violent weather. John Fuller (1987), in his novel *Tornado Watch #211*, writes

> "Then, suddenly, the breeze died and a rather ominous still calm fell over the landscape. There also was that strange yellow sky."

Plate 1-1 - John Steuart Curry (1897-1946), *Tornado Over Kansas*, 1929. Oil on canvas, 118 cm x 153 cm. Collection of the Muskegon Museum of Art, Muskegon, Michigan.

This is one of many variants on the reported color of the sky associated with severe weather. While investigating some "distinctive cloud forms beneath a large cumulonimbus," Fankhauser *et al.* (1983) report "the luminous azure color emitted" by the walls of a "vault" structure. They refer to an earlier report by Donaldson *et al.* (1965) when describing the observed color as "exud(ing) a continuous soft white light of blue-green hue, much like a fluorescent lamp." A true green color has also been reported. For example, the *Ozaukee Press* [Wisconsin] noted in 1991 (Bohren and Fraser 1993) that

"the sky turned an ominous shade of green." Edwards, in a 1995 article about VORTEX (Rasmussen *et al.* 1994), writes that "all around, the gray sky is turning a glowing emerald green." The Weather Channel writes in their 1994 desk calendar that "During severe thunderstorms, a definite green tint in the dark clouds is often a sign of nearby hail and perhaps tornadoes." As final example, the University Corporation for Atmospheric Research brochure for their 1997 Visiting Scientist Program shows a photograph of a tornado that is clearly green in color. Although the photograph may have been changed in color in the printing process, the unmistakably green color of the tornado and surrounding clouds in the image continues to perpetuate the association between green thunderstorms and bad weather. There are many more examples of this type of observation scattered about in the media. Itemizing them further could lead to a cure for insomnia. The examples provided are enough to demonstrate that green sky color and bad weather are anecdotally linked, with little scientific explanation given for the phenomenon.

This study was done to answer two main questions. The first question is "Are green thunderstorms real?" The anecdotal evidence cited might seem to answer this question in the affirmative but a few skeptics may claim that the green color is a figment of the imagination of the observer. Given the uncertain nature of the color memory of humans, definitive spectroscopic measurements are the means by which this question can be answered. The procedure is outlined by Bohren and Fraser (1993):

> "What is the next step in unraveling the puzzle of green thunderstorms? We need observations--informed observations--and our most fervent wish

is that someone, somewhere, will point a spectrophotometer skyward during the few fleeting minutes during which the sky turns an awe-inspiring green."

The second task is to explain the cause of green light from thunderstorms. None of the anecdotal stories can be counted as scientific evidence but they do provide a starting point for careful analysis of hypotheses.

A spectrophotometer was taken into the field during the spring and summer of 1995 and 1996 to record spectra of storms that appeared subjectively green and non-green to the observer. Once the data were obtained, they had to be put into a form in which one can extract the color information. A brief venture into human color vision and colorimetry is given in Chapter 3. Chapter 4 presents the data collected and the final four chapters are devoted to analyzing the data in light of prevailing theories. The last chapter offers an explanation of the color observed during a particular green thunderstorm event.

Chapter 2: PR®-650 Spectrophotometer

2.1 Spectrophotometers

A spectrophotometer is a device designed to measure the spectral transmittance and spectral reflectance of objects (Wyszecki and Stiles 1982). Typically the spectrophotometers have been used in studies of the spectral reflectance or transmittance of objects such as fabrics or painted surfaces. There are two basic types of spectrophotometers: conventional scanning and fast scanning. Regardless of the type of instrument used, a diffraction grating is used to break the incident light into its spectral constituents.

The PR®-650, the instrument used in this study, is a fast scanning spectrophotometer that uses a holographic diffraction grating and a linear diode detector. The instrument rapidly takes spectral measurements of whatever is in its 1° field of view and stores the spectral measurement on a memory card. The calibration and operation of the PR®-650 reduce some error involved in making a measurement but do not eliminate all of the error. It will be shown that the instrument error does not significantly affect the outcome of the colorimetric measurements of green thunderstorms.

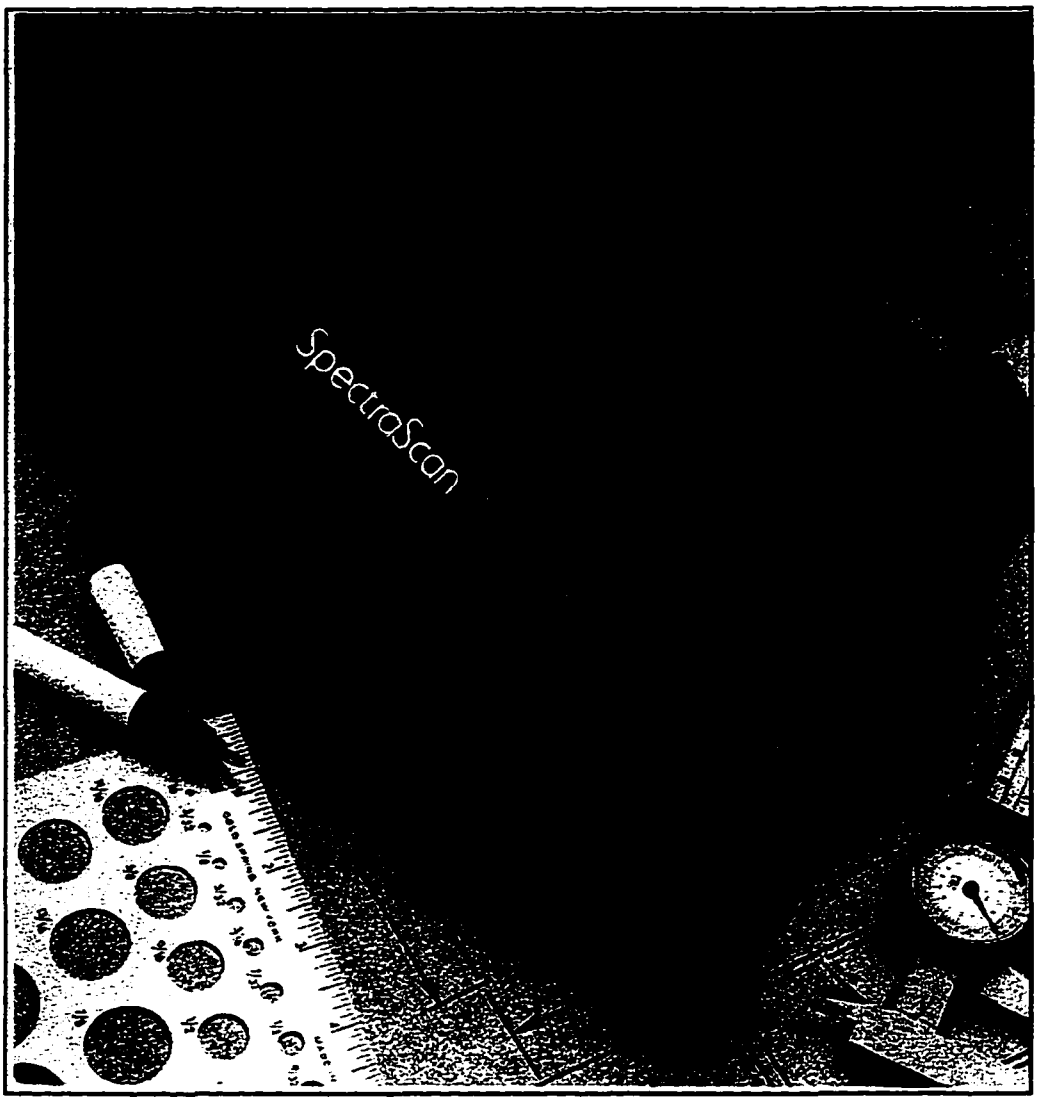

Plate 2-1 - The Photo Research PR®-650 Spectrophotometer.

2.2 PR®-650 Instrument

The PR®-650 (Plate 2-1) is a fast scanning spectrophotometer that acquires the spectrum of optical radiation from 380 nm to 780 nm simultaneously in parallel under microcomputer control.

2.2.1 Measurement Technique

The instrument is designed to acquire spectra of both steady-state light sources and repetitively pulsed light sources. For our purposes, we consider only steady-state sources. The steady state measurement cycle consists of two parts. The first part is the measurement of the optical radiation. The second part is a "dark" measurement; the instrument takes a reading while no light is permitted to strike the detector. This "dark" measurement is subtracted from the "light" measurement to eliminate any spurious noise or offset (see Section 2.2.5) that may be inherent in the electronics of the instrument.

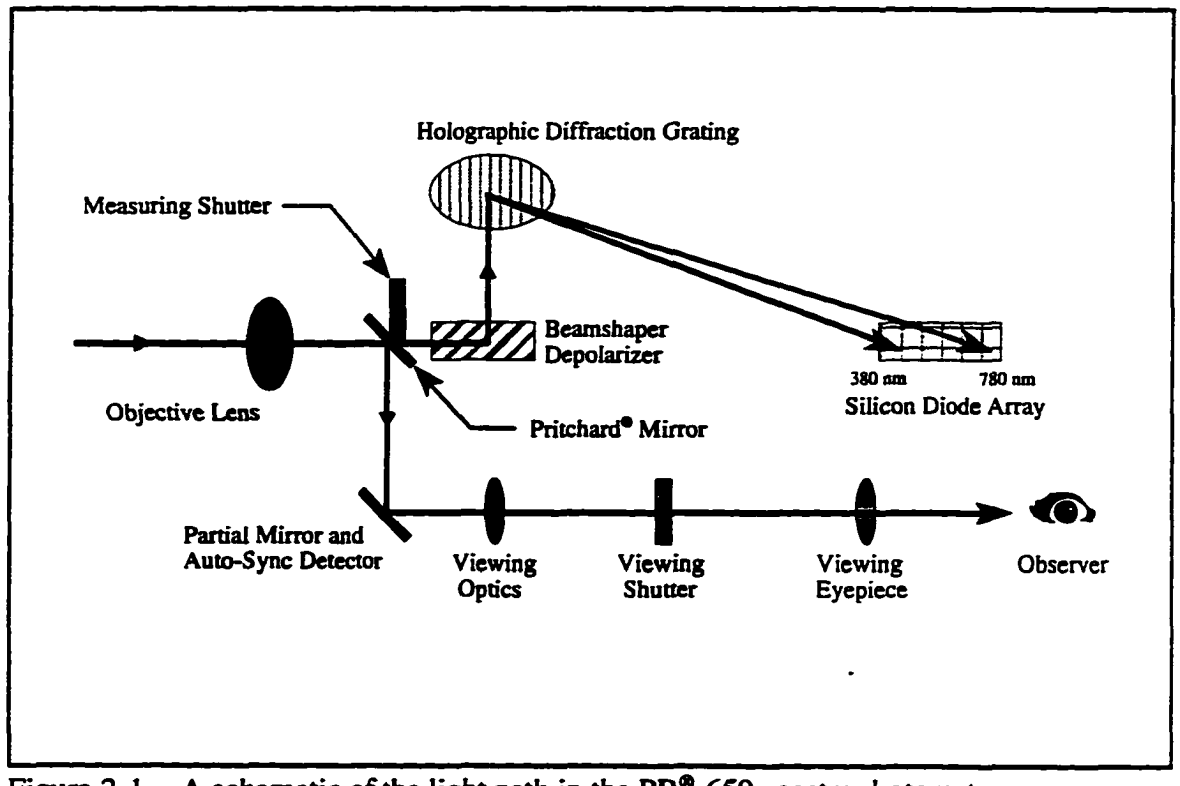

Figure 2-1 - A schematic of the light path in the PR®-650 spectrophotometer.

2.2.2 Light Path Through the Instrument

The measurement (Fig. 2-1) is made when light passes through the objective lens of the PR®-650 and enters the instrument. The objective lens forms an image at the Pritchard® mirror (Fig. 2-2). Part of the incident light is reflected by the mirror and is sent onto the viewing system. The remainder passes through a 1° aperture and is sent on to a shutter. During a measurement, when the shutter is open, light is passed so it can reach the holographic diffraction grating and then the detector. The shutter automatically closes to take the "dark" measurement immediately following the "light" measurement. Once the light passes through the measuring shutter, the light is shaped to a slit function and depolarized. A grating monochromator, transmits polarized light selectively; therefore, the light must be depolarized before entering the grating. The light is then directed to a concave holographic diffraction grating polychromator (Fig. 2-1). The grating diffracts the light into its constituents from 380 nm to 780 nm and, being concave, focuses the diffracted spectrum onto a photodiode array, such that each end of the spectrum is permanently aligned with the detector array. The silicon detector has photosensitive elements with rectangular shapes that match the shape of the entrance slit of the polychromator. The individual elements of the photodetector resolve all of the intermediate spectral bands.

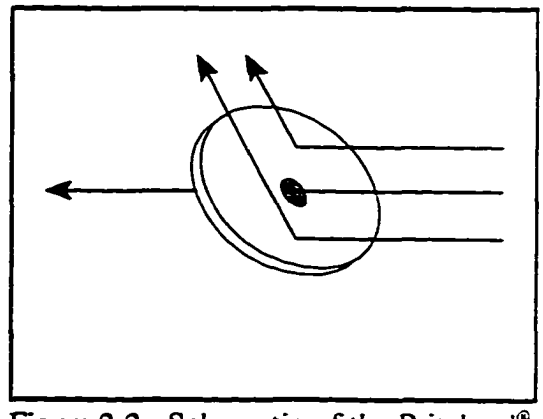

Figure 2-2 - Schematic of the Pritchard® mirror.

The light reflected by the Pritchard® mirror is sent to a second, partially silvered, mirror. Forty percent of the light is sent to a synchronization detector. The remaining 60 percent is sent to the viewing eyepiece so the user can precisely and unambiguously align the measuring aperture on the target. The operator sees a bright, erect, magnified image with a black dot in the center of the image. The dot is created by the hole in the mirror, and since only light passing through the hole is being measured, the dot accurately defines the 1° measuring field within the 7° viewing field. In other words, the measuring and viewing fields are self-aligning.

The PR®-650 automatically adapts to a wide range of incident signal levels. The instrument can operate in bright and dim light although there are threshold limits to both. The PR®-650 accomplishes this Automatic Adaptive Sensitivity® by selecting the integration time based on the available signal level. For example, the stronger the signal, the shorter the integration time required to obtain a spectrum. In the timed integration mode, the adaptive sensitivity cycle begins by performing a "light" measurement using the minimum allowable integration of 10 ms. The analog-to-digital (A/D) converter obtains spectral intensity values for each of the 128 detector elements. If the dynamic range for the peak element is less than optimal, the integration time is increased by a calculated amount and another measurement is made. This process continues until the optimal level or maximum allowable integration time is achieved. If the maximum allowable integration time is used there is insufficient light to acquire the target. A warning signal is sent to the display and the eyepiece and the measurement is aborted.

2.2.3 Data Storage and Display

The spectral data are stored on a removable integrated circuit memory (ICM) card. The 256K card includes the PR®-650 operating program, correction factors, and memory storage for at least 150 measurements. Data may also be displayed on a backlit super-twist liquid crystal display located on the rear of the spectrophotometer. Once stored on the ICM card, the data may be downloaded to a computer for processing and analysis.

2.2.4 Calibration

Spectroradiometers have to be calibrated accurately for wavelength, spectral response, and absolute response. To calibrate for wavelength accuracy, a source with sharp spectral peaks is measured with the spectrophotometer. For the PR®-650, Photo Research® uses a Helium source for calibration (Daniel 1996). The spectrum of helium is well known and has several well-defined emission lines throughout the visible wavelengths. The wavelengths are well defined and have been found to vary only in the sub-nanometer range. Therefore, the Helium calibration lamps are considered intrinsic standards and do not require additional calibration or verification.

A spectral radiance standard with a known response is required to calibrate the system for spectral and absolute accuracy. This is usually an incandescent lamp operating at a constant color temperature. The measured spectrum is compared with the known response of the standard illuminant and spectral correction factors are established. A linearity check is also done usually using the spectral radiance standard.

2.2.5 Measurement Error

2.2.5.1 Measurement Drift

Drift is the error that occurs when measurement results change although the input is constant. Drift is typically caused by small changes, such as thermal variations, pressure variations, age of the component, etc., in the imperfect electronic components. Drift often occurs over a long period and requires that the instrument be periodically recalibrated. The PR®-650 compensates for drift by taking two readings (light and dark) during a single measurement cycle. The same drift should be present in both measurements and is subtracted out. To maintain truly long-term accuracy, annual recalibration is recommended by the manufacturer.

2.2.5.2 Bias or Offset

In this context, bias of a measurement is referred to as a constant error in the measurement. The reading may be either consistently too high or too low. As stated previously, the spectrophotometer makes two measurements in succession. The first is the light measurement where light is allowed to reach the detector. If there is a high bias or offset, the spectral measurement will also be high. The second measurement does not allow the light to reach the detector. The detector should have an output of zero for all wavelengths. This is typically not the case. If there is a high, or positive, bias, then the dark reading will be positive and nonzero. To remove the bias, the dark measurement is subtracted from the light measurement. The PR®-650 does this automatically.

2.2.5.3 Effects of Spectral and Colorimetric Error

Spectrophotometers all have limitations on their ability to discern one wavelength of radiation from the next. The PR®-650 has a defined spectral accuracy of ±2 nm. The spectrophotometer reports radiances every 4 nm throughout the spectral range of 380-780 nm. The spectral accuracy indicates that some of the energy that belongs at, say, 541 nm would be placed in the 540 nm bin. The half-power bandwidth of 8 nm also indicates that some energy is not precisely assigned to the correct wavelength bin. This error would affect the magnitude of the radiances assigned to each spectral bin. Since we are trying to measure the color of the light from clouds, the exact shape of the spectrum is not important. Minor shifts in the spectrum curve from one example to the next may give the same dominant wavelength and purity (see Chapter 3) and the same perceived color. The colorimetric accuracy of the instrument is more relevant to this study.

The colorimetric, or color, accuracy of the instrument specifies the limits of variability in the determination of the chromaticity coordinates (see Chapter 3) upon repeated measurements of a particular source of illumination. The PR®-650 has a specified color accuracy of ±0.002u′ and ±0.003v′ with a given resolution of 0.001 units where u′ and v′ are the chromaticity coordinates of the Commission International de l'Eclairage (CIE) 1976 UCS chromaticity diagram. The spectrum locus on the CIE 1976 UCS chromaticity chart has with maximum values of approximately 0.62 on the abscissa

(u′) and 0.58 on the ordinate (v′); therefore, the color accuracy is better than 0.32%u′ and 0.52%v′. This accuracy is specified for CIE Illuminant A but we assume that color differences are approximately equal throughout the entire chromaticity diagram. Fig 2-3

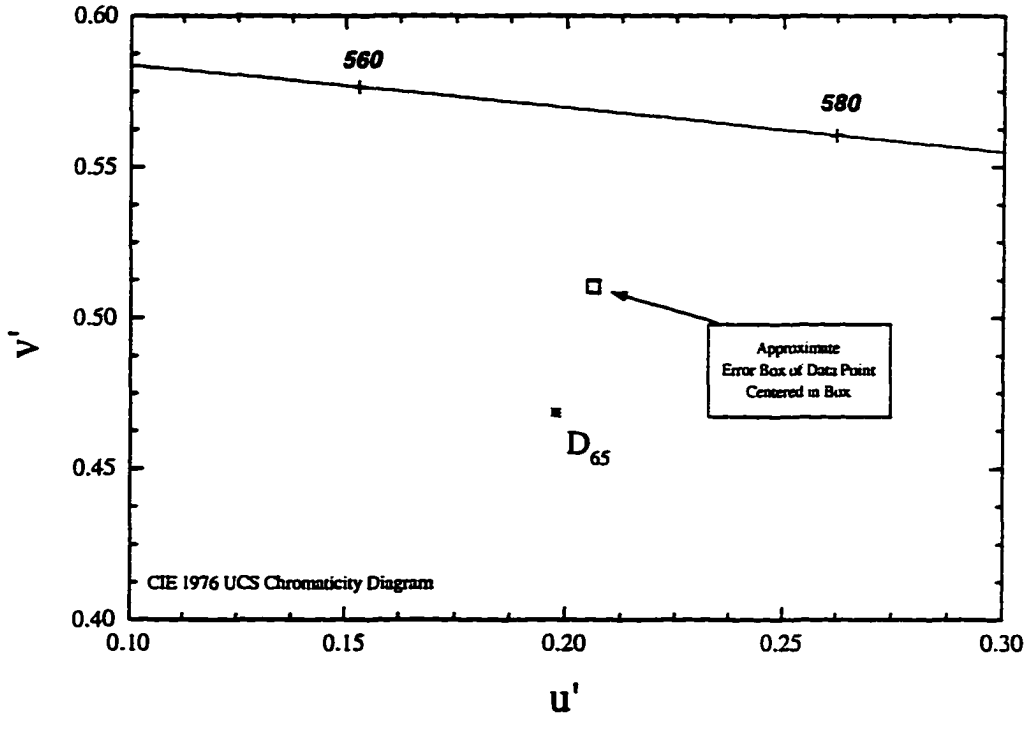

Figure 2-3 - Plot of the color accuracy of the PR®-650 spectrophotometer on a CIE 1976 UCS diagram. The error bars in the u′ and v′ directions are represented by the small error box. The color accuracy is specified for CIE Illuminant A.

shows the color accuracy of a particular spectrum. The chromaticity point of the example chosen is not too far from the CIE Illuminant A in order to be close to the point for the specified instrument color accuracy. The actual chromaticity point is not plotted on the figure; however, a square, representing the approximate error bars in the u′ and v′ directions, is placed on the diagram surrounding the chromaticity point. Regardless of

where the error box is placed, the effects on the computation of the dominant wavelength and purity are small, typically less than one or two nm. The only placement for a chromaticity point that could cause problems with the computation of dominant wavelength due to the color error is extremely close to the achromatic point. Of course, with the chromaticity point being so near the achromatic point, the observer would not perceive a difference between the illuminant under test and the achromatic standard illuminant so the question of dominant wavelength becomes moot. See Chapter 3 for a thorough discussion of the CIE colorimetric system.

2.2.5.4 Difference Between 2° and 10° Field of View

In 1964 the CIE introduced a set of color matching functions that are intended to be used for less stringent viewing conditions than the original 2° matching functions (Wyszecki and Stiles 1982). The new functions are used when the colors viewed subtended a large angle. They are based on data from observers who viewed matching fields that subtended an angle of 10°. Since the color of the light of thunderstorms comes from a relatively large area subtending a relatively large angle from the observer's point of view, all of the following colorimetric quantities are computed assuming a 10° standard observer.

To check the effects of using the 10° standard observer rather than the 1931 2° standard observer, two sets of colorimetric data are analyzed. Fig. 2-4 shows the chromaticity of a computed spectrum using the Fraser theory (see Chapter 6) with a distance to the storm of 20 km and a solar zenith angle of 20°. The 2° analysis resulted in

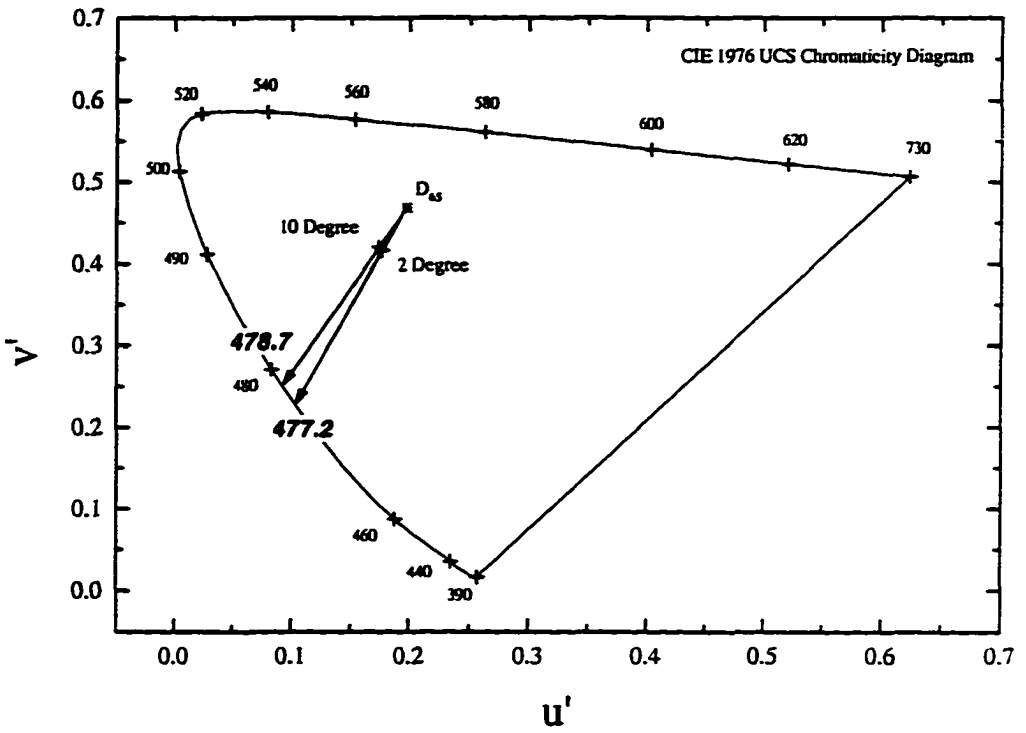

Figure 2-4 - The difference in chromaticity of a computed spectrum using the Fraser theory with a distance to the storm of 20 km and a solar zenith angle of 20° between the CIE 1931 2° and CIE 1964 10° color matching functions. The computed dominant wavelengths are shown in bold typeface.

a dominant wavelength of 477.2 nm whereas the 10° analysis yielded a dominant wavelength of 478.7 nm, an increase of 1.5 nm. This represents a blue color in both examples. The second example (Fig. 2-5) is a plot of the data from a green thunderstorm recorded on 7 May 1995 at 2230 UTC 16 km ESE of Mountain Park, Oklahoma (see Chapter 4 for more on this example). The difference between the dominant wavelengths of the 2° and 10° observers is 12.6 nm, with the 10° observer seeing the slightly more red. Although the difference in the chromaticity points is small (note the closeness of the '+'

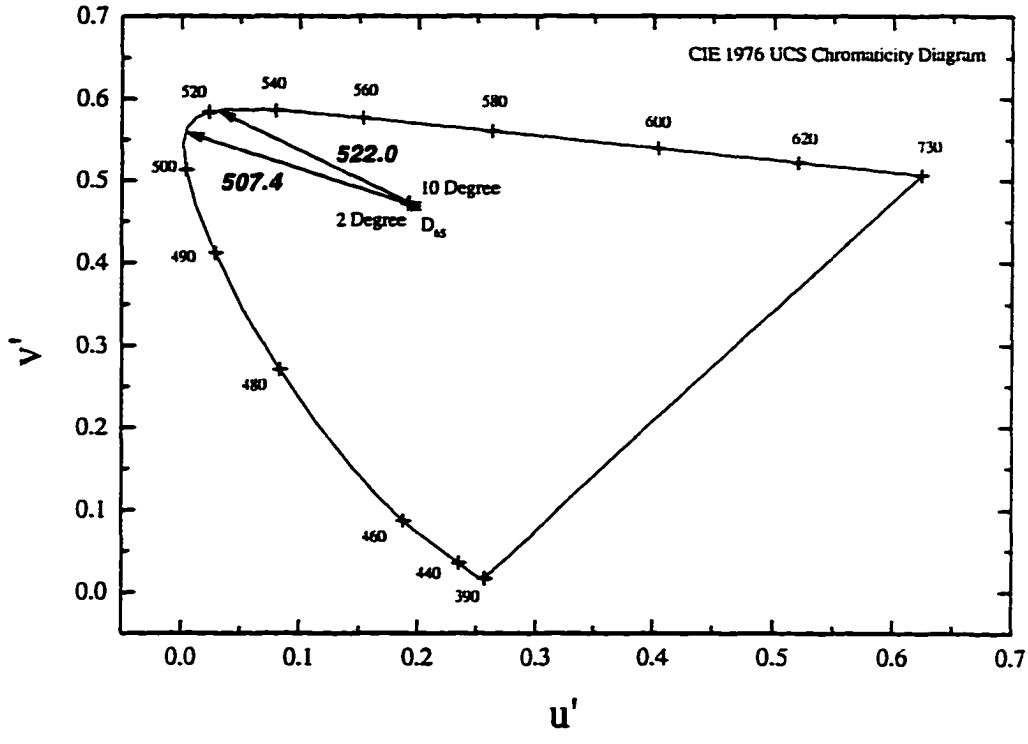

Figure 2-5 - The difference in chromaticity of a measurement between the CIE 1931 2° and CIE 1964 10° color matching functions. The computed dominant wavelengths are shown in bold typeface. The measurement was recorded on 7 May 1995 at 2230 UTC in Mountain Park, Oklahoma.

marks on the chart), the dominant wavelength difference could be significant depending on circumstances. Since the purity is so low (less than 2%), the likelihood that an observer would see a difference in color is low; both are rather near the achromatic white point. In both examples, the 2° matching functions resulted in a "bluer" dominant wavelength but, in each example, the observer would likely not perceive a difference.

Chapter 3: Human Color Vision and Colorimetry

Introduction

We take for granted the fact that a ripe beefsteak tomato appears red, grass appears green, and the cloudless sky at noon appears blue. We know that the eyes contain cells to detect various wavelength bands of radiation and, somehow, the brain is able not only to assemble an image, but also to create the image in color and in three dimensions. We do not understand fully how the brain accomplishes this but some aspects of the perception of color are relatively well known.

3.1 Concept of Color

Different colors are seen when the same object is viewed in different kinds of light. Light alone, without any tangible object reflecting the light, is responsible for the blue color of the sky we see. The concept of color is not a characteristic of an object, but rather a characteristic of the light. Light and color are visual aspects of the observer's environment. For example, if one looks at the light of the setting sun very low on the horizon, the color of the sun appears reddish or orange. We know that the sun itself did not significantly change from earlier in the day (if it did our life would be quite different) so what must have changed is the color of the light that reaches our eyes. The color of an object that we see is usually not attributed to the light that reaches the retina. The light

itself is not ordinarily recognized as carrying any kind of information about the object. We simply assign the object a particular color. We cannot measure the wavelength of light as an instrument can, but we can interpret the sensations evoked by such an illumination, though that sensation is vastly different from what our simple measurement techniques can tell us. As Parsons writes (OSA 1953):

> The common attribution of colors to objects themselves, thus implying that the colors are properties of the objects themselves, is largely a matter of memory. We say that snow is white, soot is black, blood red, because under the ordinary conditions of life the objects appear to be these hues. In this sense the colors may well be termed "memory colors."

From this, the CIE has provided us with several definitions of color. The first is "perceived color." This is defined as that aspect of a visual perceptual phenomenon, distinct from form, shape, size, position, gloss, or texture, that enables a person to distinguish between elements of the visual field and to characterize the elements by color names such as white, black, yellow, red, blue, etc. Another definition is psychophysical color. This is defined as a characteristic of visible radiation by which an observer may distinguish such differences between fields of view of the same shape, size, position, and structure as may be caused by differences in the spectral composition of the radiation (Robertson 1992). Psychophysical color can be defined mathematically by values known as tristimulus values and is what we shall discuss in the following chapters.

3.2 Elementary Colorimetry

Colorimetry, for our purposes, is the branch of science that is concerned with specifying numerically the color of a physically defined visual stimulus (Wyszecki and Stiles 1982). The three different cone types indicate that human vision is trichromatic and, by means of such, we are able to distinguish between small differences in color. It is now time to show how a spectrum gets represented in numerically defined color coordinates.

Any color can be represented as a sum of three primary colors. Equation 3-1 shows a simple color mixture formula where **C** is the color to be matched, **R**, **G**, and **B**

$$C = \bar{r}R + \bar{g}G + \bar{b}B \qquad 3\text{-}1$$

are the primary colors, and $\bar{r}$, $\bar{g}$, and $\bar{b}$ are the amounts of the primary colors needed to match the observed color **C**. During the late 1920's Wright conducted some color-matching experiments where he had ten subjects match various colors by adjusting three primary sources (Wyszecki and Stiles 1982). Wright's primary colors were centered on 460 nm, 530 nm, and 650 nm. Figure 3-1 shows curves, called color matching functions, that were the results of these experiments. One interesting aspect of these functions is that they have some wavelength bands in which the relative light intensity is negative. Consider, for example, an observed color that has a central wavelength of 510 nm. In order to match this color, the ten observers, on average, required 0.25 units of **B**, 0.95

units of **G**, and -0.2 units of **R**. What this means is that the observers had to add 0.2 units of **R** to the original color, **C**, in order to match the other two. This can be written as

$$C + \bar{r}R = \bar{g}G + \bar{b}B \qquad 3\text{-}2$$

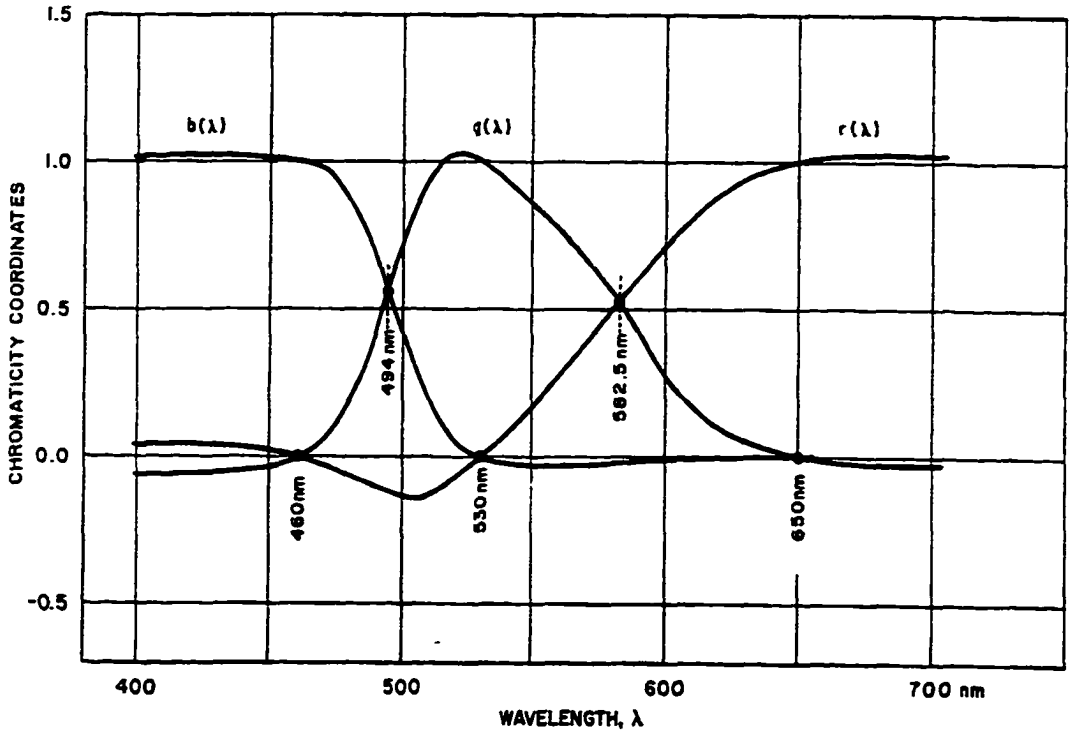

Figure 3-1 - Color matching functions defined by Wright (Wyszecki and Stiles 1982).

Because of these negative numbers, the CIE decided to change the color matching functions to all positive values. The functions do not coincide with human vision but instead are representative of a "standard observer." The standard is fine as long as all parties agree to its use.

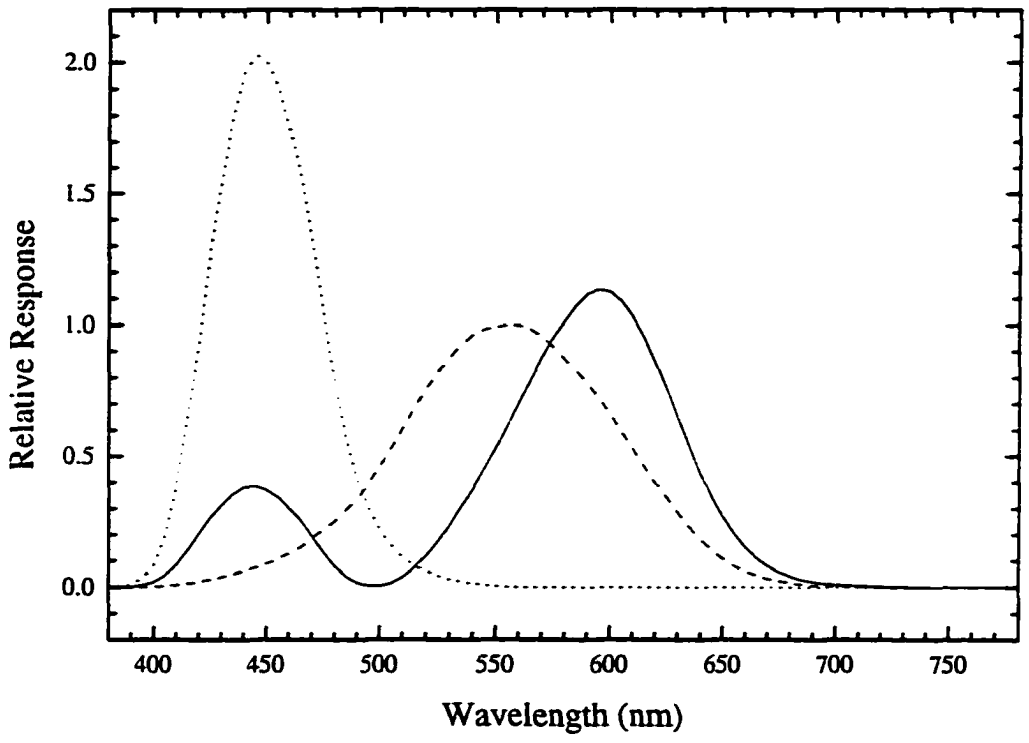

Figure 3-2 - CIE 1964 10° color matching functions. The solid line is the $\bar{x}_{10}$ color matching function, the dashed line is the y_{10} color matching function, and the dotted line is the z_{10} color matching function.

When color matching experiments are done in a laboratory environment, the field of view of the observer is limited. Originally the CIE chose to use a 2° field of view for the standard observer and the color matching functions were called $\bar{x}$, $\bar{y}$, and $\bar{z}$. Certain applications, including the observation of green thunderstorms, require a wider field of view. Responding to this need, the CIE created a set of 10° color matching functions, called $\bar{x}_{10}$, $\bar{y}_{10}$, and $\bar{z}_{10}$. These are shown in Figure 3-2.

The next step in the process is to form tristimulus values. These are numbers that represent the spectrum in a three dimensional color space. They are formed by

integrating the product of the observed spectrum [L(λ)] and each color matching function over the visible wavelengths then multiplying the result by a normalizing constant k:

$$X = k \int L(\lambda)\, \bar{x}(\lambda)\, d\lambda,$$
$$Y = k \int L(\lambda)\, \bar{y}(\lambda)\, d\lambda, \qquad 3\text{-}3$$
$$Z = k \int L(\lambda)\, \bar{z}(\lambda)\, d\lambda.$$

In order to plot this point on a two-dimensional graph, the tristimulus values are transformed into chromaticity coordinates x and y:

$$x = \frac{X}{X + Y + Z},$$
$$y = \frac{Y}{X + Y + Z}. \qquad 3\text{-}4$$

These chromaticity coordinates are defined for the 1931 CIE chromaticity diagram. In 1976 the CIE attempted to correct the 1931 diagram by changing the shape of the figure such that linear differences in chromaticity would approximately represent equal changes in color. The result is the CIE 1976 uniform chromaticity scale (UCS) diagram (Fig. 3.3). The transformation equations between 1931 CIE chromaticity (x, y) and CIE 1976 UCS chromaticity (u′, v′) are

$$u' = \frac{4x}{-2x + 12y + 3},$$

$$v' = \frac{9y}{-2x + 12y + 3}. \qquad 3\text{-}5$$

The color specification of a spectrum may be described by either chromaticity coordinates or by the dominant wavelength and excitation purity. The dominant

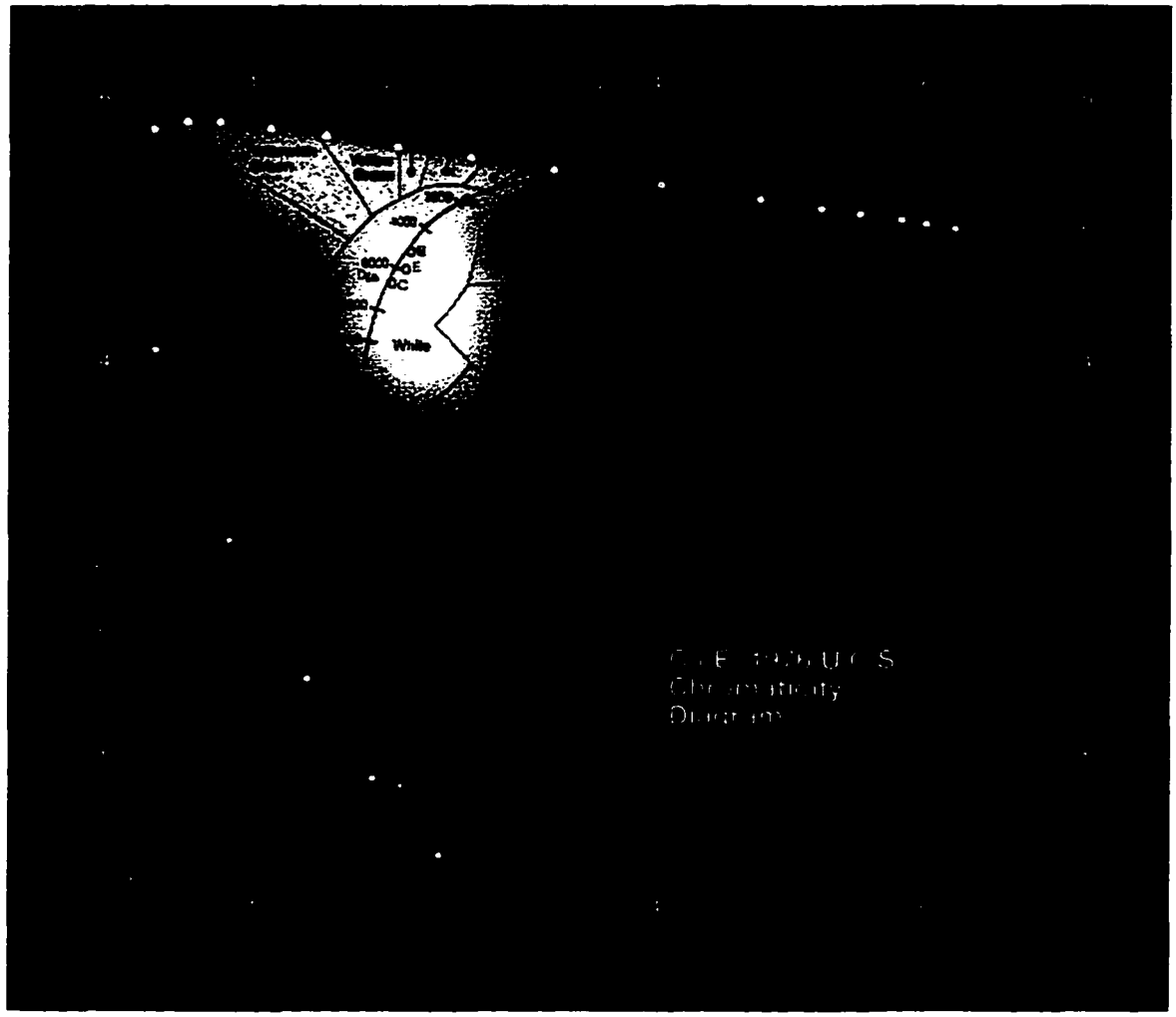

Figure 3-3 - CIE 1976 UCS chromaticity diagram. The colors on the chart approximately represent the colors seen by a typical observer.

wavelength is defined as the wavelength of a monochromatic (single color) light source, which, when mixed with an appropriate amount of achromatic (white) light yields a color that will exactly match the observed color. The excitation purity is strictly defined for the 1931 CIE chromaticity diagram as the ratio of the distance between the chromaticity point and the achromatic point to the distance between the spectrum locus, at the dominant wavelength, and the achromatic point. It is a measure of the saturation of the observed color; the higher the purity, the higher the color saturation. The purity computed using the CIE 1931 chart is fixed for a given spectrum and does not change if the chromaticity is shown on a different chart.

3.3 A Warning

One must be cautioned in the use of dominant wavelength and purity. Both of these quantities are entirely dependent on the selection of the achromatic point. Changing the achromatic point, for a given spectrum, will change the values of the dominant wavelength and purity. The assignment of any color name to a particular dominant wavelength might change if the achromatic point changes. In this study, the achromatic point will always be the CIE D_{65} standard. In this way, any changes in dominant wavelength and purity between spectra can be compared. Any color name given to a specific region of dominant wavelengths will be constrained by this selection of the achromatic point. The placement of the chromaticity point on the CIE diagram gives the best indication of the color of the spectrum. Because of this, the chromaticity of the spectra will be shown often. Changes in the perceived color of a given illumination

source can be easily seen by changes on the chromaticity chart. The best way to understand the CIE diagram fully is by the use of an example or two.

3.4 Chromaticity Examples

The first example is a spectrum recorded of a deep blue sky on 14 May 1995 at 1612 UTC in Moore, Oklahoma (Plate 3-1). The spectrum (Fig. 3-4) shows a maximum in radiance in the wavelength band normally associated with violet color, and a decreasing radiance with either increasing or decreasing wavelength. We perceive a blue

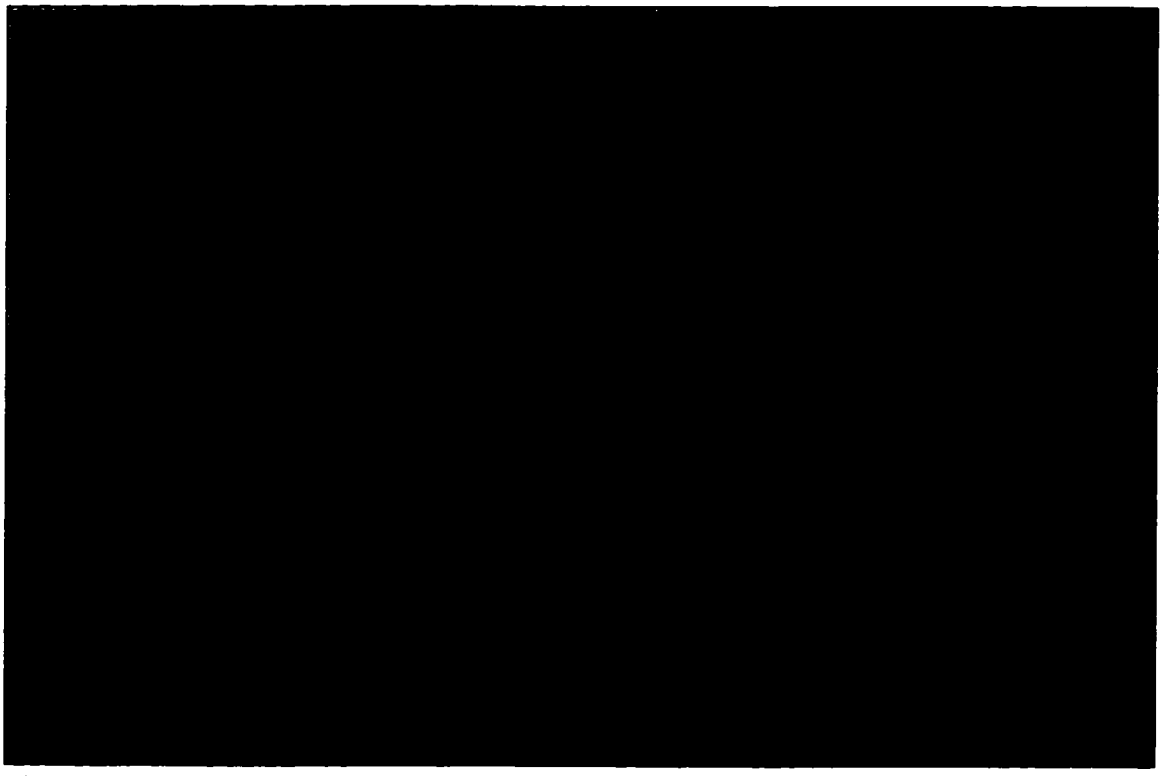

Plate 3-1 - Photograph of the blue sky that coincides with the spectrum shown in Figure 3.4. The photograph was taken on 14 May 1995 at 1612 UTC in Moore, Oklahoma looking to the northwest and at an elevation of approximately 45°.

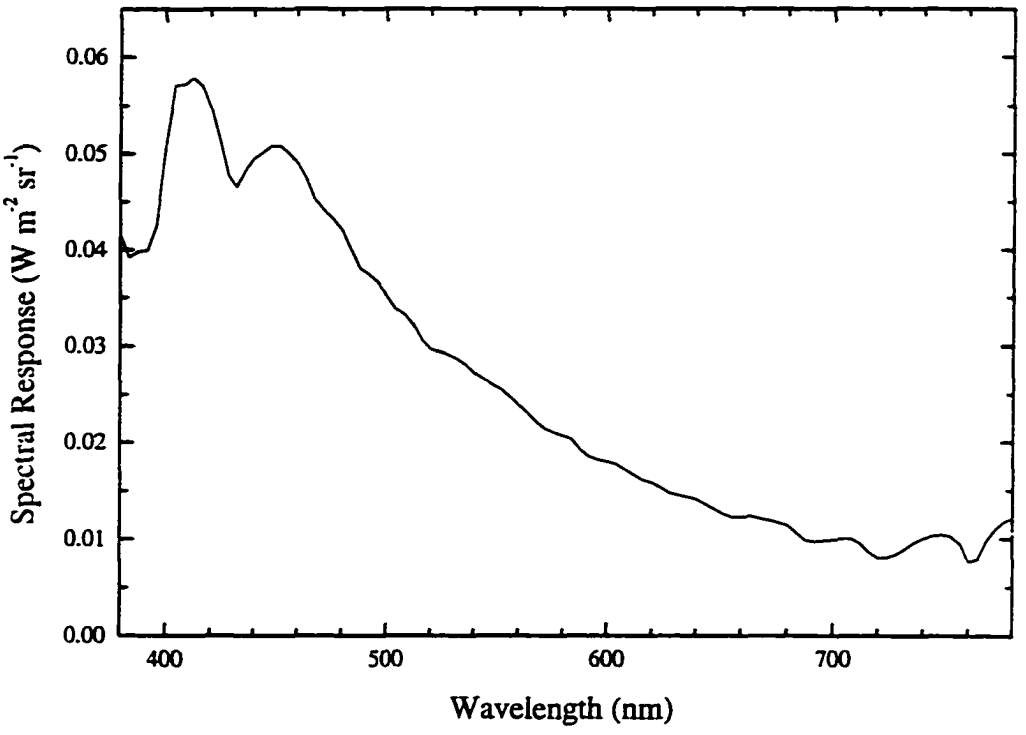

Figure 3-4 - Spectrum of the blue sky shown in Plate 3-1. The spectrum was recorded on 14 May 1995 at 1612 UTC in Moore, Oklahoma looking to the northwest and at an elevation of approximately 45°. The sky was clear.

sky rather than a violet one because the sensitivity of the human eye decreases substantially in the violet part of the spectrum. Although the sky appears a deep blue color, there is still a significant amount of radiance in the "non-blue" wavelengths (λ>480 nm).

The chromaticity of the spectrum is plotted on a CIE 1976 UCS chromaticity diagram as a diamond-plus symbol (Fig. 3-5). The achromatic point, selected as CIE standard illuminant D_{65}, is represented by * and is a good representation of daylight color. The curved line, with wavelength tic marks, is called the spectrum locus and each

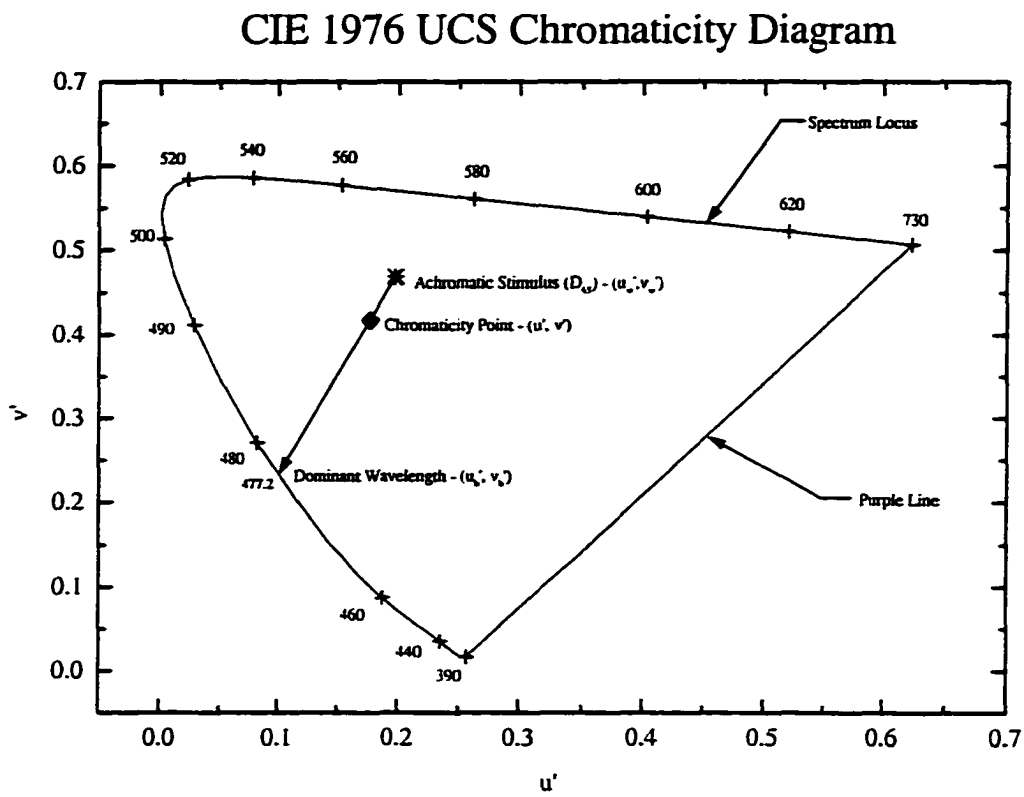

Figure 3-5 - Spectrum of the blue sky shown in Plate 3-1 plotted on a CIE 1976 UCS chromaticity diagram. The chromaticity point is represented by the ◊ symbol. The spectrum was recorded on 14 May 1995 at 1612 UTC in Moore, Oklahoma looking to the northwest and at an elevation of approximately 45°. The achromatic (CIE standard illuminant D_{65}) point is represented by ✳.

point on the curve represents a pure spectral color. The straight line connecting the 390 nm point and the 730 nm point is called the purple line and represents colors created by mixing various amounts of violet and red light; these colors are not pure spectral colors and cannot be assigned a dominant wavelength.

The dominant wavelength for the blue sky spectrum is found by drawing a line from the achromatic (D_{65}) point, through the chromaticity point, to the spectrum locus.

The wavelength value of the intersection of this new line and the spectrum locus is the dominant wavelength. The purity is found by taking a ratio of the distance between the chromaticity point and the achromatic point to the distance between the achromatic point and the spectrum locus at the dominant wavelength *on the CIE 1931 chart*. For the blue sky spectrum, the dominant wavelength was found to be 477 nm, a wavelength normally associated with the color blue. Although the observer witnessed a very deep blue sky, the purity was calculated to be only 30 %. Humans have the ability to see vivid colors even at relatively low purities.

The second example is a spectrum recorded of snow-capped mountains in Rocky Mountain National Park on 25 June 1995 at 2305 UTC (Plate 3-2). A realistic

Plate 3-2 - Photograph of the snow-capped mountains coincides with the spectrum shown in Figure 3-6. The photograph was taken on 25 June 1995 at 2305 UTC in the Rocky Mountain National Park, Colorado.

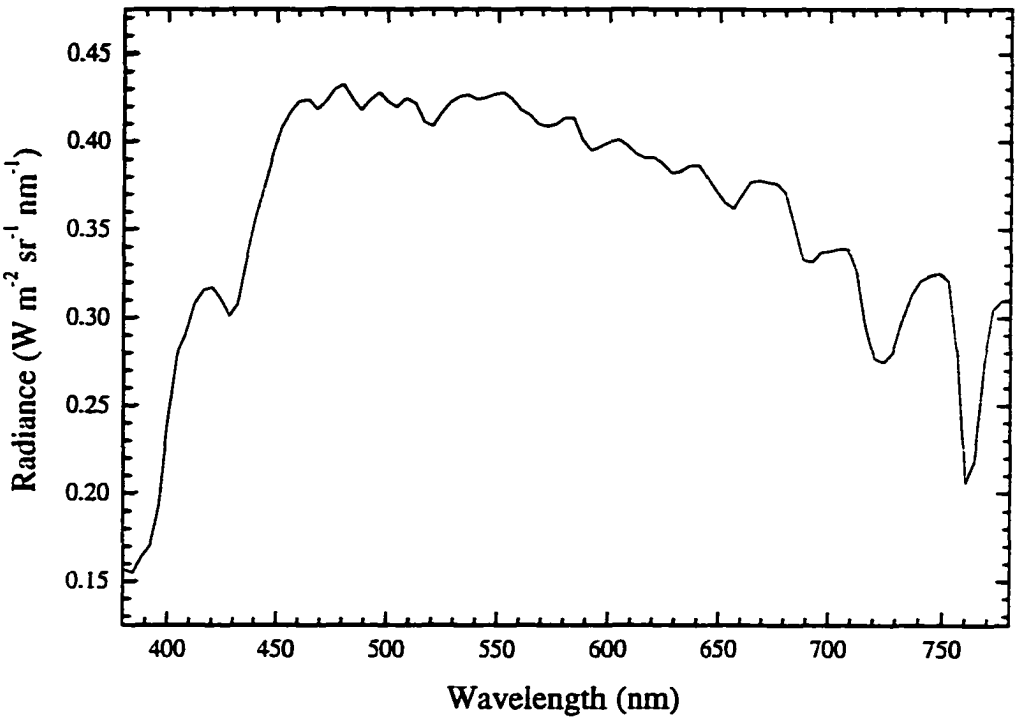

Figure 3-6 - Spectrum of the snow-capped mountaintops shown in Plate 3-2. The spectrum was recorded on 25 June 1995 at 2305 UTC in the Rocky Mountain National Park, Colorado.

approximation is that snow nearly perfectly reflects light incident upon it (Bohren 1991). The measured spectrum of the light reflected by the snow represents predominantly the light from the sun. The spectrum (Fig. 3-6) shows a relatively constant radiance in the wavelength band of 450-650 nm. This is the wavelength band where the color receptors of the eye have the greatest sensitivity. The flat spectrum means that equal amounts of energy reach the observer's eye across the entire wavelength band.

The spectrum is plotted on a CIE 1976 UCS chromaticity diagram as a diamond-plus symbol (Fig. 3-7). As before, the achromatic point is represented by ∗. The

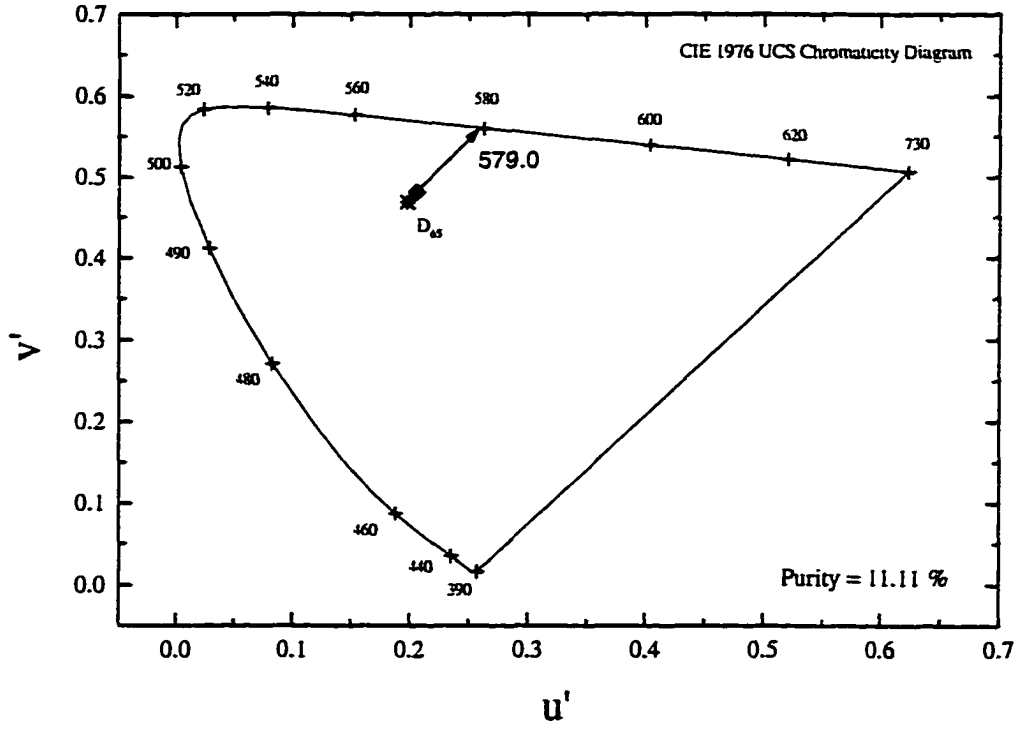

Figure 3-7 - Spectrum of the snow-capped mountains shown in Plate 3-2 plotted on a CIE 1976 UCS chromaticity diagram. The chromaticity point is represented by the ⌖ symbol. The spectrum was recorded on 25 June 1995 at 2305 UTC in Rocky Mountain National Park. The achromatic (CIE standard illuminant D_{65}) point is represented by the ✳ symbol.

recorded spectrum has a dominant wavelength of 579 nm, a wavelength typically associated with the color yellow. The sun is often characterized as being yellow in color and this result tends to confirm that characterization. The purity is 11 % suggesting a perceived pale yellow color. The snow-covered mountaintop appears white as it is the brightest object in the observers field of view. Bright light, with a low purity, is often recognized as "white" by the observer.

3.5 Color Discrimination Thresholds

No discussion about the color of anything would be complete without the inclusion of remarks about human color discrimination thresholds. Discrimination thresholds can be specified in several different ways. Those most important to the study of green thunderstorms are wavelength differences and purity differences. Wyszecki and Stiles (1982) give an excellent overview of this subject.

Discrimination of differences in wavelengths are defined as just noticeable differences in the wavelengths of two similarly colored lights, and have been studied extensively (e.g. Birch and Wright 1961, and Bouman and Walraven 1972). In particular, Wright and Pitt found in laboratory experiments that humans can discriminate 1 nm differences in wavelength in a wavelength band near 500 nm and 600 nm (Wyszecki and Stiles 1982). Everywhere else in the visible spectrum, differences are greater than 2 nm and rise to near 6 nm in the short and long wavelength ends of the visible spectrum. Bedford and Wyszecki (1958) found a similar wavelength dependence but discrimination was rarely better than 2 nm. Purity differences (e.g. Kaiser *et al.* 1976) are tested when additive mixtures of a single color light source and white light are varied in luminance. Others (see Wyszecki and Stiles 1982) have chosen to test the just noticeable difference between a pure white light source and a test light source. Wyszecki and Stiles (1982) show that the locus of just noticeable difference from "white" is significantly worse than the ability to match specific colors using the same "white" color. This indicates that if a cloud slowly changes color in small incremental steps from gray, the observer may not notice the effect until the color difference is beyond a certain threshold. If a spectrum

reveals that the purity is very low, a significant change in the dominant wavelength, still with a low purity, may not be noticed by the observer. This is an important consideration in the effort to understand green thunderstorms. As a final blow to our ability to see color correctly, particularly in a storm environment, Cornsweet (1970) writes,

> The hue of a stimulus strongly depends upon the state of the retina being illuminated. If a stimulus is presented to a part of the retina that has previously been adapted to colored light, the hue of the stimulus will be changed. In general, the hue will tend to move toward the hue of the wavelength that is the complement of the adapting light.

If an observer were to look at an object that was blue, not too dissimilar to the light from the bottom of a typical thunderstorm, and then look at something white (or gray), then the light seen may appear reddish or orange. This is not to say that green thunderstorms are not real (this point shall be examined later) but that any color we see in the sky is affected by what we saw most recently and the color adjacent to the part of the sky being observed. Given this caveat, it is time to proceed with the data analysis.

Chapter 4: Spectral Measurements and Observations

Introduction

During the spring and summer of 1995 and the spring of 1996 hundreds of spectra of thunderstorms were recorded in Oklahoma, Texas, Kansas, Colorado, and Florida on 49 observation days. Most of the storms encountered were subjectively observed to be the typical blue-gray color most often associated with thunderstorms. On several occasions spectra were recorded from thunderstorms that subjectively appeared green to the observer. Different observers see the green color differently, but with these occurrences, the observers all noticed an unusual greenish color. To summarize all of the spectral data, histograms were created to show the most common dominant wavelengths observed. The number of spectra shown on the histograms is not equivalent to the number of storms. Usually, when collecting data of an individual storm, multiple spectra were recorded, often varying the observation angle. Multiple spectra recorded of storms that appeared green to the observer will have some spectra that have green dominant wavelengths and some spectra, recorded in a slightly different part of the storm, that have blue dominant wavelengths. Storms that appeared blue to the observer would only have spectra with blue dominant wavelengths. Furthermore, several spectral measurements of the same green storm are each individually represented.

4.1 Analysis by Dominant Wavelength

Fig. 4-1 shows a histogram of dominant wavelengths of all of the storm spectra recorded during the observation period. Many of the storms had multiple spectra recorded so Figure 4-1 must be used with caution. The first observation that is immediately apparent is the bimodal nature of the distribution. The two dominant wavelength peaks occur near 485 nm and 570 nm. The dominant wavelength of 485 nm is typically associated with the perceived color of blue or greenish-blue. The dominant wavelength of 570 nm is typically associated with the perceived color of yellow or greenish-yellow. These two dominant wavelength peaks are representative of the two predominant colors of the sky: blue from the sky, and yellow from the solar disk. The next step is to separate out the green storm spectra from the non-green storm spectra.

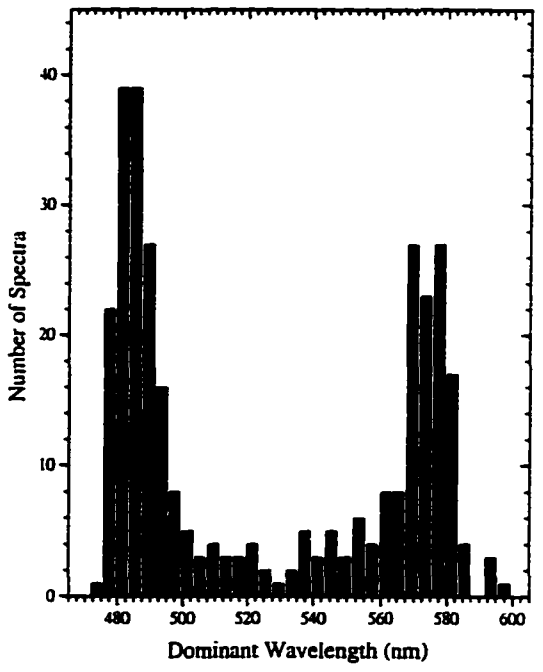

Figure 4-1 - Histogram of the dominant wavelengths for all spectra recorded during the 1995-1996 observation period. Histogram bin size is 4 nm.

Figure 4-2 shows a pair of histograms for which the darker bars represent the number of spectra recorded that were subjectively observed as blue or gray and the lighter bars represent the number of spectra recorded that were subjectively observed as green.

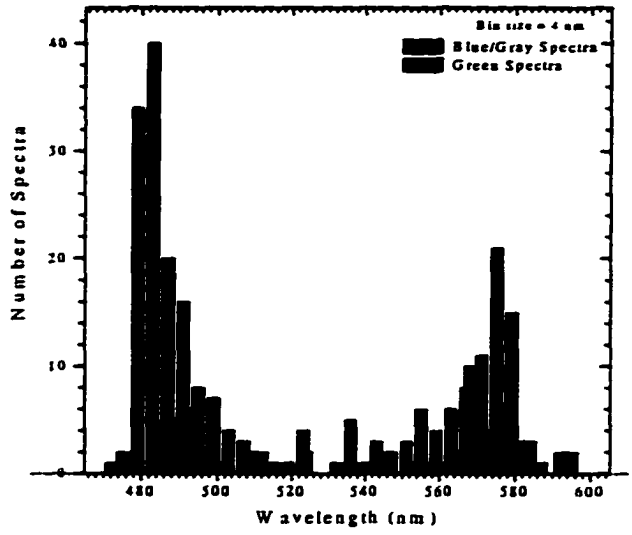

Figure 4-2 - Histogram of the dominant wavelengths of all of the spectra recorded during the 1995-1996 observation period. The darker bars represent blue spectra, the lighter bars represent green spectra. Histogram bin size is 4 nm.

The most striking aspect is the bimodal nature of the data. As before, the peaks in the histograms occur in two wavelength bands, near the dominant wavelengths associated with blue sky and the solar disk. There is a relative minimum in the green and yellowish-green portion of the spectrum.

The histogram of storms that were subjectively observed to be green also shows a bimodal distribution although there are a few more spectra with dominant wavelengths in the center portion of the spectrum. Each of the peaks of the green spectra is slightly shifted toward the middle of the spectrum compared to the blue/gray histogram. The bimodal nature of the histogram leads one to consider the possibility that there may be two different mechanisms working to create the colors seen in the clouds. While

reserving an attempt at explaining the differences for future chapters, green thunderstorms can be classified into two categories, a blue-green type and a yellow-green type.

4.1.1 Blue-Green Storm Spectra

The first green thunderstorm type is the blue-green type. Storms with spectra that had dominant wavelengths less than 520 nm were classified as blue-green. Only 27 spectra of this type were recorded so any statistical discussion must be undertaken with caution. The mean dominant wavelength for blue-green storms was 492.7 nm with a mean purity of 6.4 %. These parameters indicate an observed color of pale blue-green. Although blue-green color was observed at times between 18:48 UTC to 01:08 UTC, the mean time for the occurrence of blue-green storms was 22:09 UTC.

4.1.2 Yellow-Green Storm Spectra

The second category of green thunderstorms is the yellow-green type. These spectra are those with dominant wavelengths greater than 520 nm. There are 43 observations of this type of spectra so the statistics still must be viewed with caution. The mean dominant wavelength for yellow-green storms was 563.2 nm with a mean purity of 8.3 %. These parameters indicate an observed color of pale yellow-green. Although yellow-green color was observed from 20:33 UTC to 01:08 UTC, the mean time for yellow-green storms was 23:33 UTC, nearly an hour and a half later than for the blue-green spectra.

4.2 Analysis by Time of Day

Figure 4-3 shows a histogram of the green thunderstorm spectral data versus time of day. As expected, the majority of the spectra were recorded in the late afternoon although some of the observations are surprisingly early in the day. There is a cutoff of data just beyond 20:00 LT due to the lower limit of light sensitivity of the spectrophotometer. Green storms were observed after that time, but no objective measurement could be made. The number of green thunderstorm observations increased with time of day, and the dominant wavelength increased as well. Figure 4-4 shows a scatter plot of dominant wavelengths versus time of day for storms that subjectively appeared green to the observer. The straight line fit indicates that the dominant wavelength increases from near 490

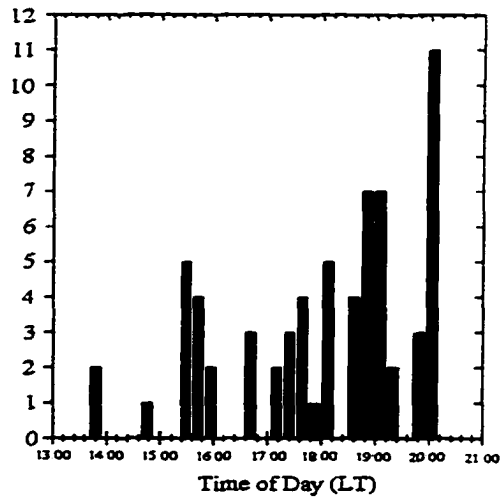

Figure 4-3 - Histogram of the dominant wavelengths of green only spectra recorded during the 1995-1996 observation period. The time of day is in local time.

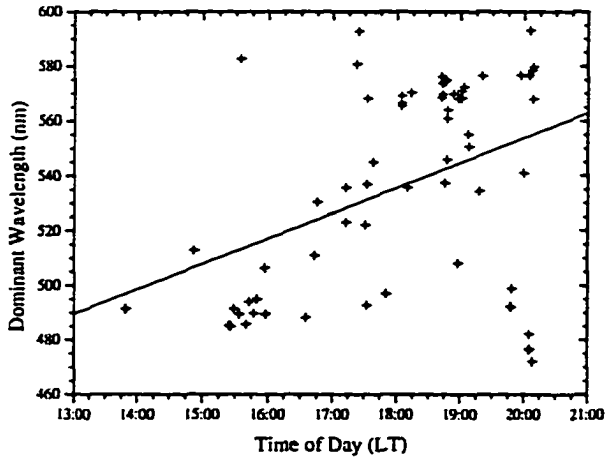

Figure 4-4 - Scatter plot of the relationship between the dominant wavelengths of spectra of thunderstorms that were subjectively observed as being green in color and the time of day. The solid line represents a linear fit. Correlation for the fit is 0.41.

nm just after noon to just over 560 nm towards dark. The correlation is weak (R=0.41) but the trend is clear. One difficulty in analyzing these data is the fact that few of the measurements, for different storms, were recorded at the same storm relative location. In an attempt to overcome this difficulty, a single "representative" or "average" spectrum was created for a given green thunderstorm by averaging the dominant wavelengths and observation times. Only spectra that were recorded from approximately the same storm-relative location were accepted since most of the green light emanated from near the precipitation core. During the observation period there were thirteen green thunderstorm events. Figure 4-5 shows a plot of these averaged data. On a few of the dates, more than one storm occurred. This is indicated by a number next to the letter on the graph (e.g. C1, C2, etc.). The scatter of the spectra is rather large, although, as shown from the linear fit, there is a trend for green storms later in the day to have longer dominant wavelengths. This could be because as the sun sets, the light we see from it becomes more red, thereby creating a "redder" dominant wavelength later in the

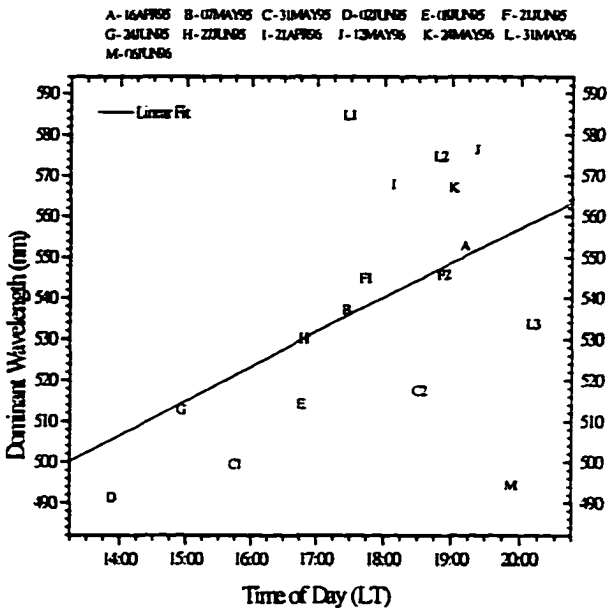

Figure 4-5 - A plot of the "average" green storm spectra for thirteen green thunderstorm events. The solid line is a linear fit to the data.

day. This also shows that green thunderstorms can be created from sunlight at nearly any zenith angle but the dominant wavelength of that green light increases with increasing solar zenith angle.

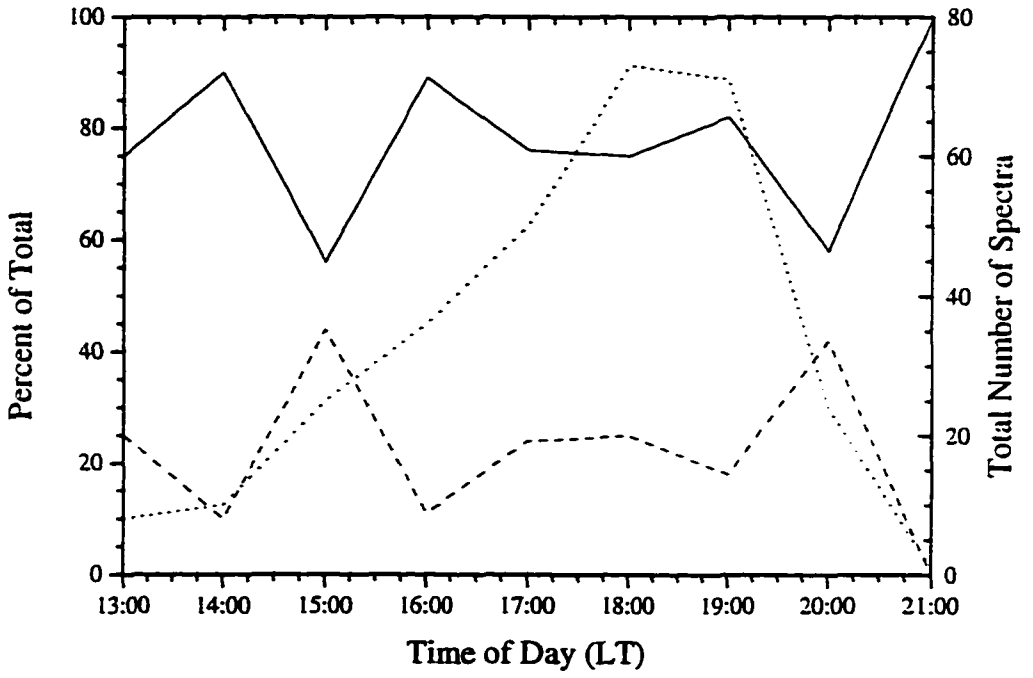

Figure 4-6 - The relationship between the percentage of storms that were subjectively observed to be gray/blue (solid) and green (dashed) for one-hour intervals throughout the day. The number of spectra recorded of all storms (dotted) is shown for comparison.

The number of green storm spectra as a percentage of all spectra is fairly constant (Fig. 4-6) throughout the day. In this analysis, data were grouped in one hour intervals. Then the percentage of green storms and the percentage of the gray/blue storms were calculated. The sum of the two curves is 100 %. The total number of recorded spectra is also shown on the graph. As stated previously, the number of measurements increases

with the time of day until darkness prevented further measurements. Given such a small sample size, any conclusions must be drawn carefully. Given that most of the storms observed were very thick, it appears to be safe to say that green color was observed in approximately 25% of all storms observed.

Before venturing into analysis of individual storms, we consider a plot of the dominant wavelengths for all of the green thunderstorm spectra verses the time of day (Fig. 4-7). Most of the data points for each individual storm are clustered around each

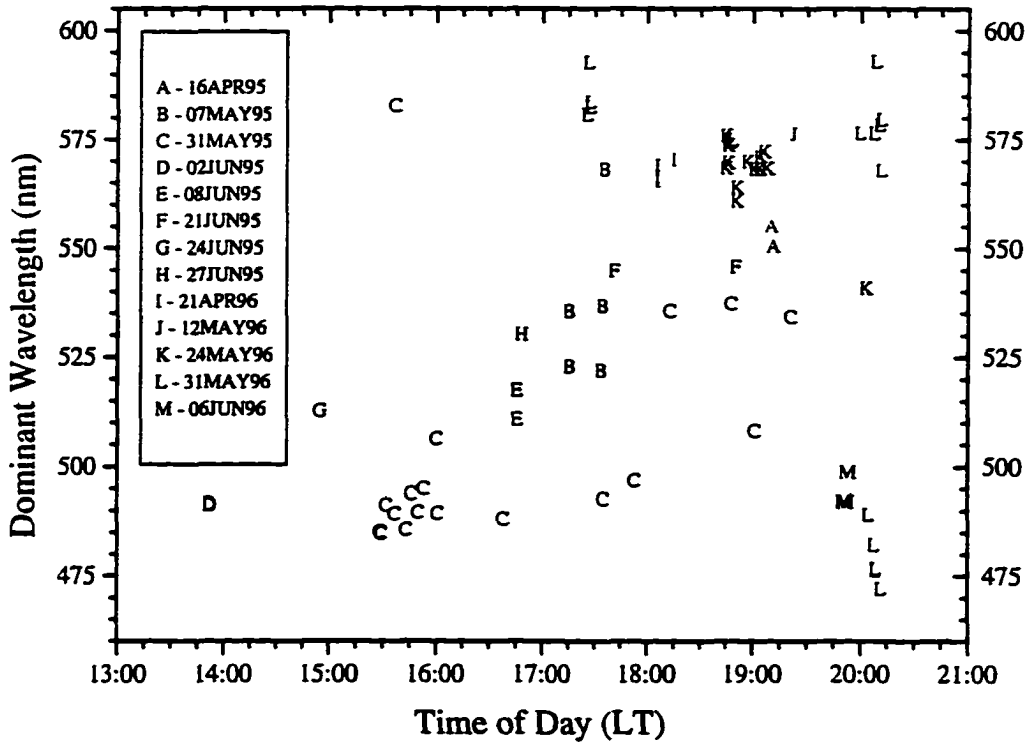

Figure 4-7 - Scatter plot of the dominant wavelength verses time of day for all of the spectra recorded of thunderstorms that subjectively appeared green to the observer. Each letter represents an individual observing day. The date of the storms are shown in the legend.

other. For example, the data for the 24 May 1996 storm (K) are clustered near 19:00 LT and 560 nm. This indicates that most of the measurements were recorded in a brief period in the lifetime of the storm, so that recorded spectra for the same event were very similar. Two storms violated the tendency for all data to be near the same time and dominant wavelength. The first example is the 31 May 1995 Electra flight (C). During this flight, green storms were observed over a long period of time (from around 15:15 LT to 19:15 LT). However, the dominant wavelengths did not vary much until later in the day. This storm will be discussed in more detail in the next sections. The second unclustered data set was from the 31 May 1996 storm (L). The varying dominant wavelengths, for the same time of day, were discussed previously. Figure 4-7 clearly shows the variation in dominant wavelengths at 20:00 LT for this example; some are near 480 nm, and others are near 575 nm.

4.3 Individual Storm Analysis

In the following sections four examples of spectra recorded of green and nongreen thunderstorms are presented. These are not the only examples observed but represent the best examples of the first quantitative measurement made of green thunderstorms. For brevity, only two of these examples will be discussed in detail.

4.3.1 Example #1 — Blue Thunderstorm in Southwest Oklahoma

This first example is from a storm VORTEX (Rasmussen *et al.* 1994) intercepted in southwest Oklahoma during the afternoon of 16 April 1995. A powerful trough over

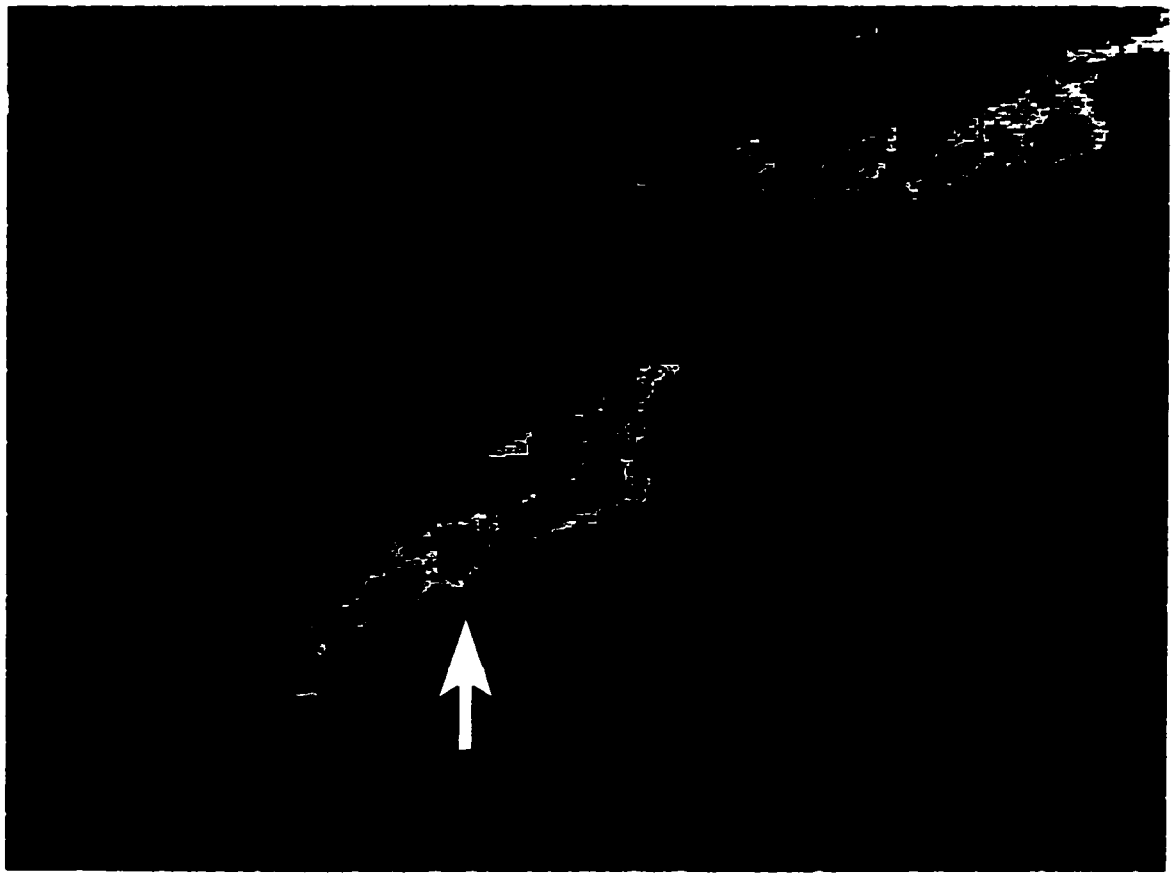

Figure 4-8 - WSR-88D radar composite of the 16 April 1995 storm in southwestern Oklahoma. This radar image was recorded approximately one hour after the spectral measurements were taken. Radar images were unavailable at the time of the observation. The storms have moved to the southeast of the observation point. The arrow points to the studied cell.

the western United States ejected several short waves over the Central Great Plains. A surface low formed in the eastern Oklahoma Panhandle with an associated dry line extending from the low into northwestern Texas. A line of strong to severe thunderstorms (Fig. 4-8) developed over southwestern Oklahoma and was intercepted by VORTEX around 2200 UTC. The observed storm developed a mesocyclone structure and entered Cotton County, Oklahoma at 2300 UTC. A spectrum was recorded of this storm, located in Geronimo, Oklahoma at 2310 UTC, from a position approximately 35

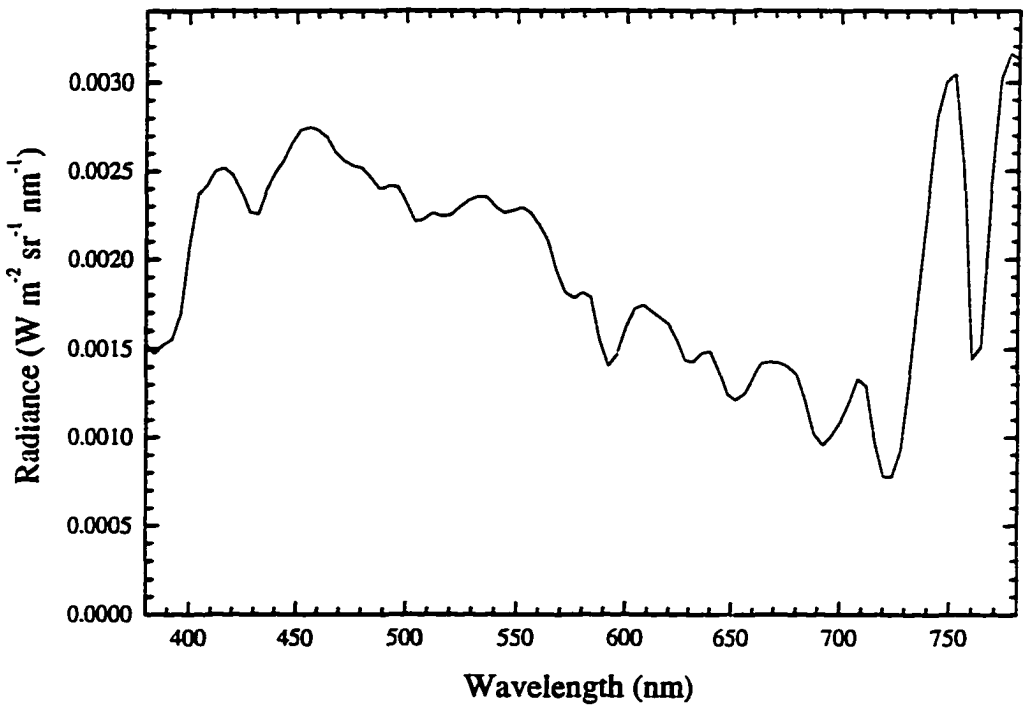

Figure 4-9 - Spectrum of a blue thunderstorm recorded on 16 April 1995 at 2310 UTC in Grandfield, Oklahoma looking to the north northeast of a storm located over Geronimo, Oklahoma.

km to the south southwest in Grandfield, Oklahoma (Fig. 4-9). Plate 4-1 shows a photograph of the storm. The spectrum was recorded in the dark area just above the pole in the center part of the photograph. The spectrum shows relatively large radiance, peaking at 456 nm, in the wavelength band normally associated with the color blue, and a decreasing amount elsewhere. The dominant wavelength was calculated to be 483.9 nm, a wavelength normally associated with the color blue, and the purity was computed to be 8.7%. The observers indicated that the color of the storm looked to be the typical gray/blue color of severe storms.

Plate 4-1 - Photograph of the thunderstorm that coincides with the spectrum shown in Figure 4-9. The photograph was taken on 16 April 1995 at 2310 UTC in Grandfield, Oklahoma looking to the north northeast and at an elevation of approximately 5°. The spectrum was recorded in the dark region just above the pole in the center of the photograph.

4.3.2 Example #2 — Yellow-Green Thunderstorm in the Texas Panhandle

A series of supercell thunderstorms developed in the Texas and Oklahoma Panhandles on 24 May 1996. One of the storms was intercepted 18 km west of Miami, Texas. The storm had a well developed mesocyclone and wall cloud. The color of the clouds was observed to be bright green on each side of the lower clouds shown on the right side of Plate 4-2. Light levels were low but sufficient to record several spectra of the green light. Figure 4-10 shows a spectrum of the green light recorded on 25 May 1995 at 0001 UTC. The spectrum peaks near 550 nm, the region where the human eye is

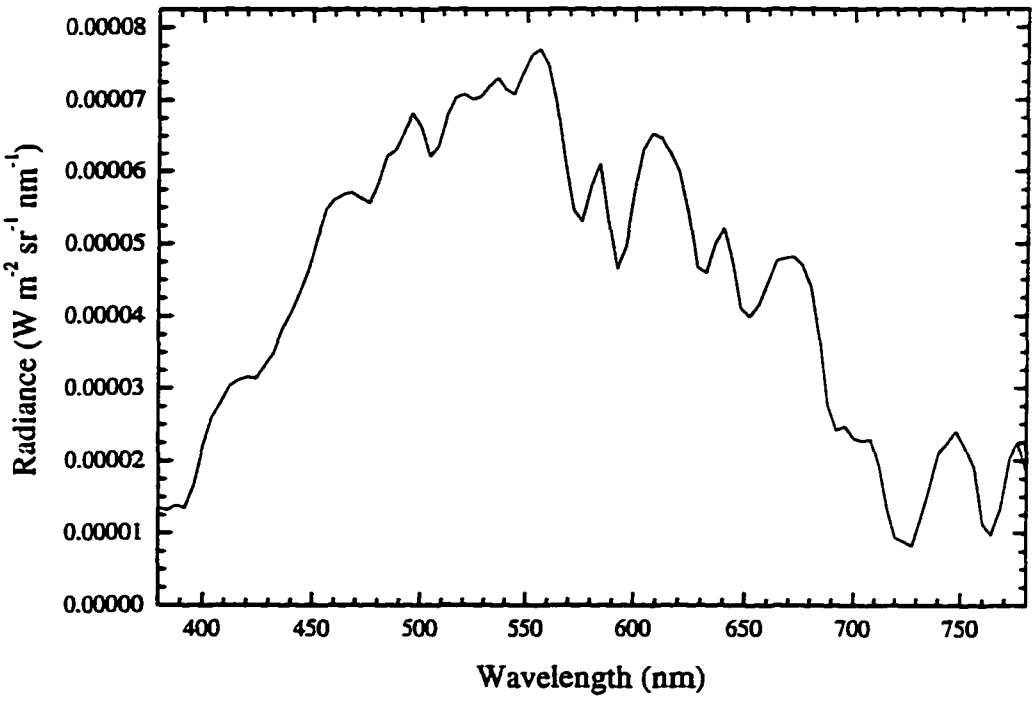

Figure 4-10 - Spectrum of a yellow-green thunderstorm recorded on 25 May 1996 at 0001 UTC 16 km west of Miami, Texas. The view is to the west southwest looking to the north of a wall cloud.

most sensitive to light. This is a very different spectrum from the one shown in Fig. 4-9. This yellow-green spectrum has much less radiance in the blue part of the spectrum and the radiance variations in the near infrared are much smaller. Although the total radiance measured by the spectrophotometer was low, the observers noticed that the green sky appeared "bright" and the coloration was described as "spectacular." The dominant wavelength of the spectrum was calculated to be 568.3 nm with a purity of 21.5 % which a typical observer would perceive as a yellow-green color. To give some idea about what this purity indicates, Gallagher *et al.* (1996) show that a deep blue sky has a purity of approximately 30%.

Plate 4-2 - Photograph of the thunderstorm that coincides with the spectrum shown in Figure 4-10. The photograph was taken on 25 May 1996 at 0001 UTC 16 km west of Miami, Texas. looking to the west southwest and at an elevation of approximately 5°. The spectrum was recorded in brighter area in the center of the photograph.

4.3.3 Example #3 — Green Thunderstorm in Southwest Oklahoma

This example is also from a storm VORTEX intercepted in southwest Oklahoma during the afternoon of 7 May 1995. Widespread severe weather developed over the region as a strong short wave ejected to the northeast from a deep trough centered over Arizona at 1200 UTC. On the surface at 1200 UTC there was a low centered over west-central New Mexico with a cold front that extended from eastern Colorado southward into Mexico. A warm front extended from a second low just west of the Oklahoma Panhandle, across the Oklahoma panhandle then southeastward through Oklahoma City

then eastward again along the Red River. Winds in the warm sector were fairly strong and dew points were in the upper 60s to low 70s. A dryline extended from the low in New Mexico southward through the Big Bend region of Texas into Mexico.

By 1800 UTC the low in New Mexico had drifted to the northeast and was centered north of Amarillo, TX. The cold front had moved east of Abilene, TX, whereas the warm front had drifted southward and now crossed the extreme southwestern corner of Oklahoma. A squall line developed in the far eastern portion of the Texas Panhandle and moved eastward into Oklahoma. VORTEX intercepted a high-precipitation supercell (Doswell and Burgess, 1993), with a strong eastward moving gust front that had formed in this line. A spectrum was recorded (Fig. 4-11a) in Mountain Park, OK, located about halfway between Lawton and Altus, at 2206 UTC looking to the northwest at a point under the approaching outflow boundary in the precipitation core region (Plate 4-3).

The dominant wavelength was 486.1 nm, which is in the wavelength regions typically observed as blue. Visual observations confirmed the blue color of the clouds, which is typical of the color seen in the core of a severe thunderstorm. We observed the approach of the outflow boundary for several minutes and recorded a second spectrum (Fig. 4-11b) three minutes later, looking at the same region of the sky. Although we noticed little change visually in cloud color toward the green, a slow change in spectral characteristics of the storm was beginning to occur. The dominant wavelength increased to 494.7 nm. After another three minutes, we recorded a spectrum (Fig. 4-11c), again looking at the same portion of the sky, under the advancing gust front. A distinct change

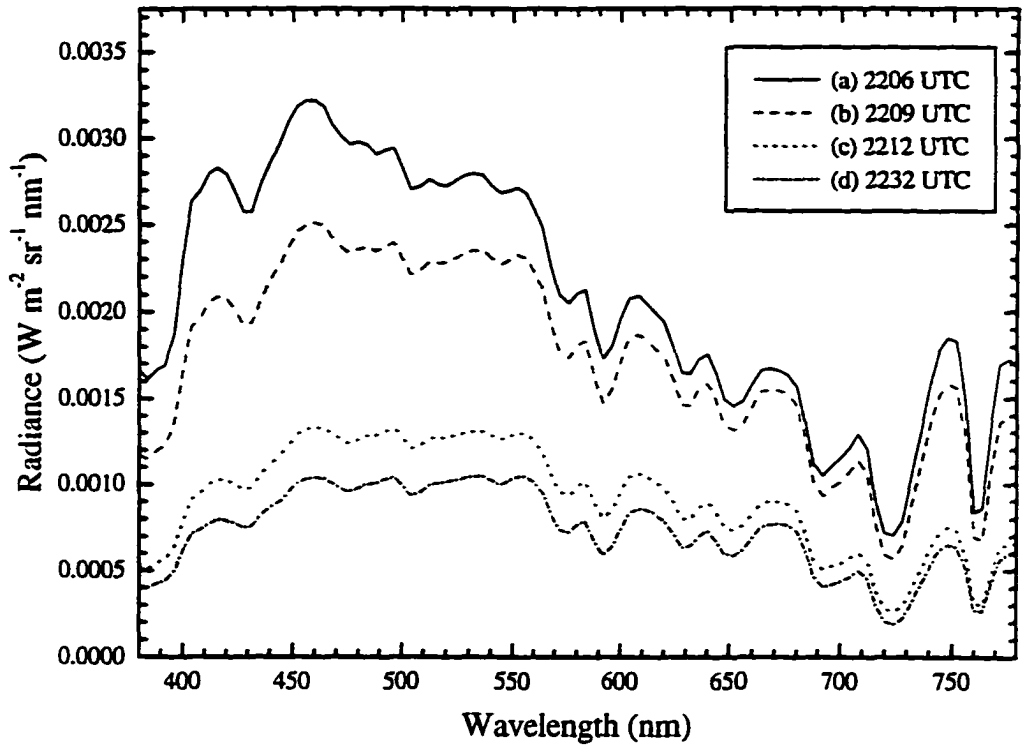

Figure 4-11 - Spectra of a severe thunderstorm observed near Mountain Park, Oklahoma on 7 May 1995 looking to the northwest. (a) 2206 UTC: The storm appeared to be dark blue in color. The peak spectral radiance occurs at 456 nm. The dominant wavelength is 486.1 nm and the excitation purity is calculated to be 8.00%. (b) 2209 UTC: The sky coloration had changed little from that of 2206 UTC. The peak spectral radiance occurs at 460 nm. The dominant wavelength is 494.7 nm and the excitation purity is calculated to be 3.23%. (c) 2212 UTC: Visual observers noted a greenish cast to the clouds. Spectrum was recorded looking to the north. The peak spectral radiance occurs at 460 nm. The dominant wavelength is 522.9 nm and the excitation purity is calculated to be 2.12%. (d) 2232 UTC: Spectrum of a green thunderstorm. Spectrum was recorded 16 km east-southeast of Mountain Park, Oklahoma looking to the north. The peak spectral radiance occurs at 536 nm. The dominant wavelength is 536.8 nm and the excitation purity is calculated to be 2.86%.

can be seen in the spectrum although little had changed visually. The dominant wavelength increased to 535.5 nm. There is a noticeable increase in the radiance of the green portion of the spectrum relative to the entire spectrum, particularly in the region

between 500 and 550 nm. Although the sky appeared to change little between Fig. 4-11a and Fig. 4-11c, the luminance decreased from 193.9 Cd m^{-2} to 90.5 Cd m^{-2}, a reduction of 53.4%. This could indicate that the optical thickness of the cloud had increased in the region where the spectral measurement was taken. If so, the observed shift in the spectrum toward the green should be consistent with Bohren's theory, to be discussed further in a later chapter. It should be noted that we have not eliminated the possibility that this could have been a result of changes in geometrical factors as the storm

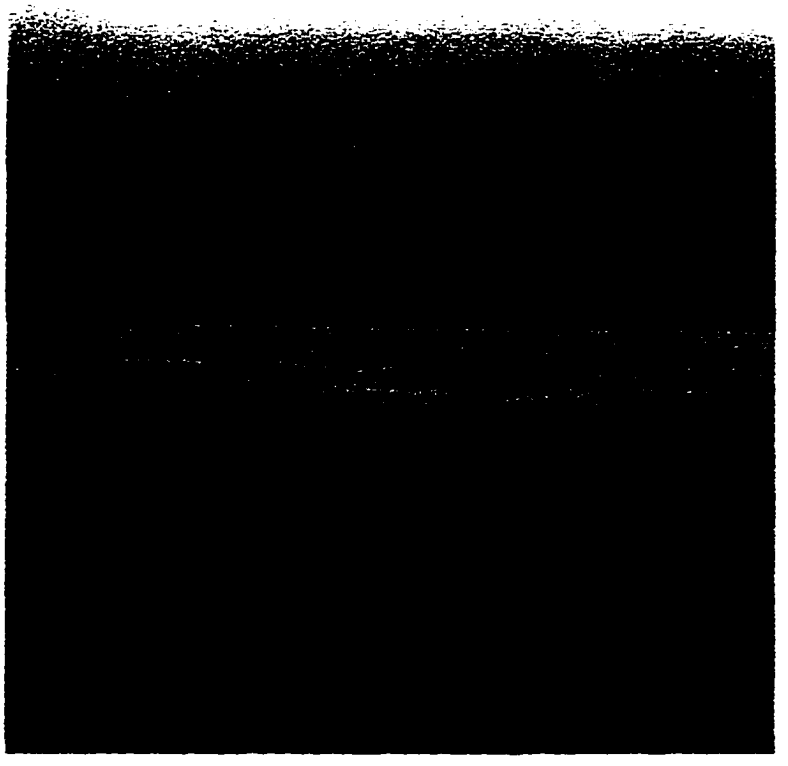

Plate 4-3 - Photograph of the thunderstorm that coincides with the spectrum shown in Figure 4-11a. The photograph was taken on 7 May 1995 at 2207 UTC in Mountain Park, Oklahoma looking to the northwest and at an elevation of approximately 5°. The spectrum was recorded in an area just above the mountain in the center of the photograph. Note that the ground is covered with young, growing wheat.

approached, but, as will be shown in Section 7.8.2, the small change in the solar zenith angle had little effect on the observed color of the storm..

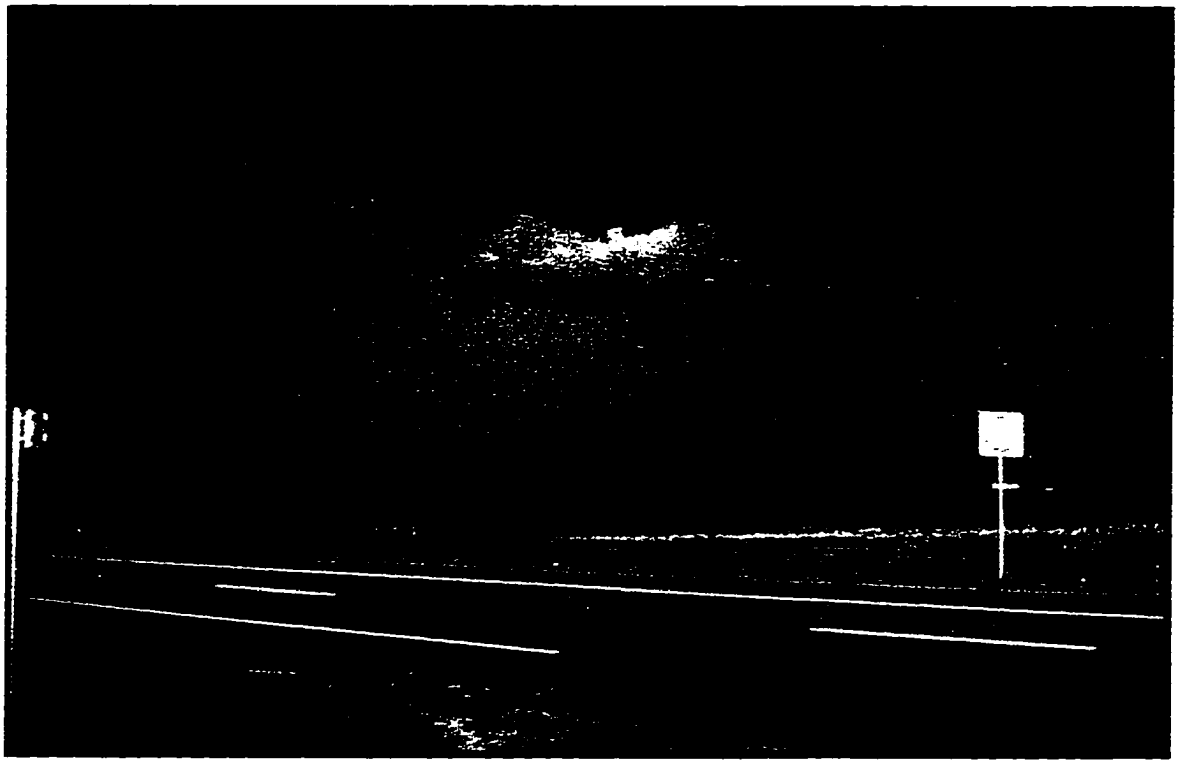

Plate 4-4 - Photograph of the thunderstorm that coincides with the spectrum shown in Figure 4-11d. The photograph was taken on 7 May 1995 at 2230 UTC 16 km east southeast of Mountain Park, Oklahoma looking to the north at an elevation of approximately 5°. The spectrum was recorded in area in the center of the photograph.

We continued to observe the approach of the storm until the outflow boundary was just to our northwest. To avoid being caught in the precipitation core and to allow us to continue to observe the storm, we moved to a position approximately 16 km to the east-southeast of Mountain Park, OK. Observers at this time noticed a dramatic shift in the color of the storm to a bright bluish green (Plate 4-4). The observers believed that the sky was brighter at this time. The data show that actually the luminance, as well as the

radiance at all wavelengths, had decreased throughout the observation period. We recorded a spectrum (Fig. 4-11d) at 2232 UTC looking to the north under the outflow boundary. The dominant wavelength had shifted to 536.8 nm and the peak in the spectrum occurred at 536 nm. There was also a further reduction in the luminance of the clouds as the color continued to shift toward the green. The luminance dropped to 71.5 Cd m^{-2}, approximately one-third the value recorded only 25 minutes earlier. To the best of our knowledge, this was the first spectrum ever recorded of a severe thunderstorm that visually appeared green. Furthermore, the transition in color from blue to green was gradual and the spectra clearly show that there is no distinct maximum in the green portion of the spectrum.

4.3.4 Example #4 -- Aircraft Observations Over Texas

The fourth example is from a severe storm near Sweetwater, TX on 31 May 1995. An upper level trough was positioned over Colorado at 1200 UTC on 30 May 1995. The trough drifted slightly eastward during the next twelve hours while a weak jet streak rotated around the bottom of the trough. A series of surface low pressure centers developed over the western Texas Panhandle and eastern New Mexico during the evening of 30 May 1995. The pressure centers moved little during the day of the 31st, but a dryline did develop from just west of Amarillo southward to the Big Bend region of Texas. The dryline advanced slowly eastward, initiating a few storms in west Texas.

The storms that developed were outside the VORTEX region so the ground crews did not operate. To study the storm, we flew on the NCAR Electra aircraft. The Electra

encountered two cells that appeared to have been initiated along a mesoscale outflow boundary. The photograph shown in Plate 4-5 is of the first cell and was taken between the times the last two spectra, shown in Fig, 4-12, were recorded. The two cells merged around 2100 UTC and a large hook echo and mesocyclone developed near Sweetwater,

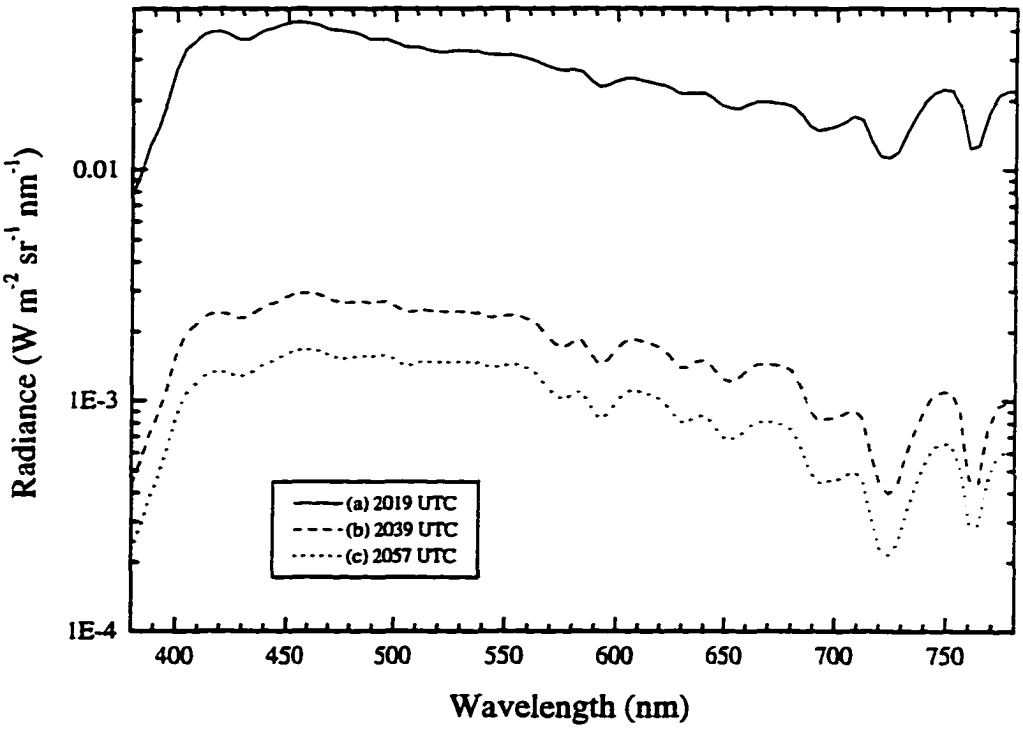

Figure 4-12 - Spectra of a thunderstorm observed to be dark blue and blue-green in color. The ordinate is plotted in logarithmic coordinates in order to show the large differences between the curves. These spectra was recorded from the NCAR Electra aircraft on 31 May 1995 near Sweetwater, Texas looking to the north. (a) 2019 UTC: The storm appeared visually to be blue in color. The peak spectral radiance occurs at 452 nm. The dominant wavelength is 479.0 nm and the excitation purity is calculated to be 12.19%. (b) 2039 UTC: Spectrum of a precipitation core of a severe thunderstorm observed to be light blue-green in color. The peak spectral radiance occurs at 460 nm. The dominant wavelength is 485.8 nm and the excitation purity is calculated to be 9.72%. (c) 2057 UTC: Spectrum of very bright, light blue-green colored clouds associated with a severe thunderstorm near Sweetwater, Texas. The peak spectral radiance occurs at 460 nm. The dominant wavelength is 489.5 nm and the excitation purity is calculated to be 7.98%.

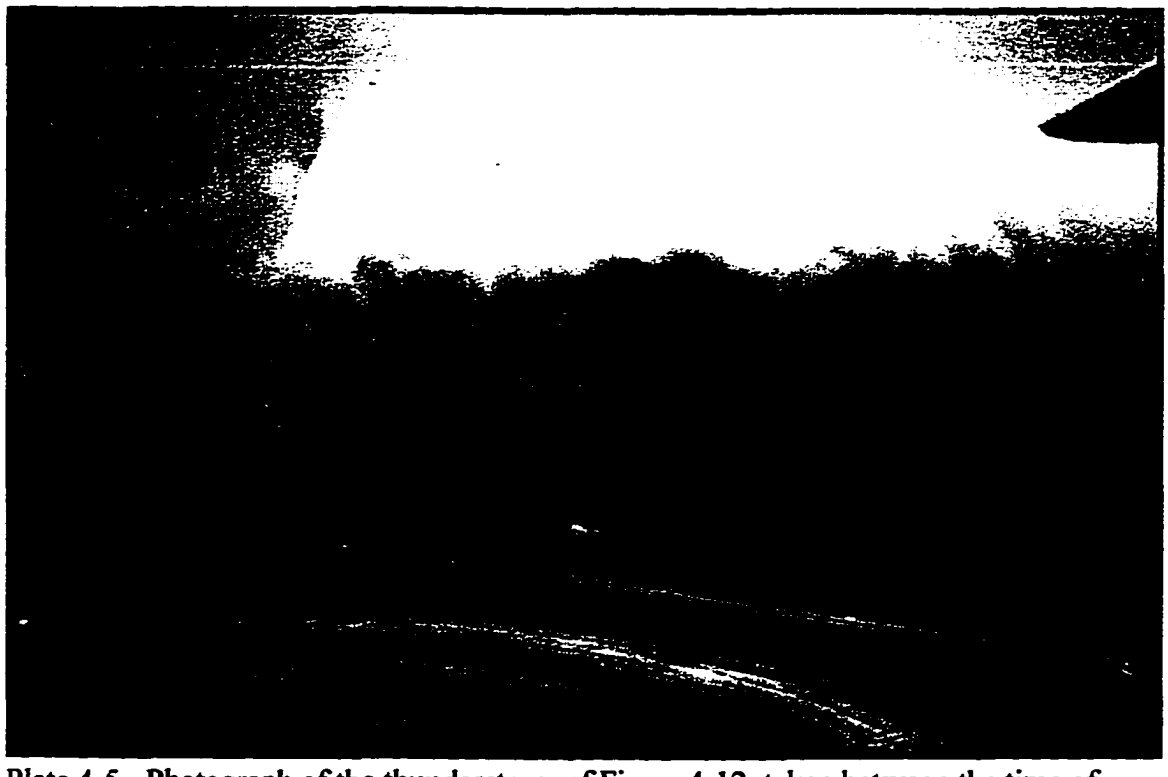

Plate 4-5 - Photograph of the thunderstorm of Figure 4-12, taken between the time of spectrum (b) and spectrum (c). The photograph was taken on 31 May 1995 at 2047 UTC from the NCAR Electra aircraft near Sweetwater, Texas. The view is to the north.

TX. Another cell developed to the south. At 2143 UTC, the Electra flew to the southern cell and began radar studies.. The racetrack patterns flown by the Electra were predominantly oriented east-west, giving us a view of all the storms to the north. The aircraft windows were clean and untinted offering us a clear view of the storms.

We were able to obtain 30 spectra of light emanating from the region of the storms, most of which were of green color. The green light emanated primarily from the core precipitation area and was perceived brightest just under the cloud base. Figure 4-12a shows a spectrum of the storm recorded at 2019 UTC, with the instrument pointed just under the cloud base. The color of the cloud was observed to be dark blue. The spectrum peak is at 452 nm and the dominant wavelength is 479 nm. This is in the

spectral region usually associated with the color blue. At 2039 UTC a spectrum (Fig. 4-12b) of the same storm revealed a slight shift in the spectral characteristics; furthermore, we observed the precipitation core taking on a greenish cast. The spectral peak had shifted 8 nm toward the green and the dominant wavelength also shifted toward the green. The gradual trend toward the green continued, both visually and as measured by the instrument, for as long as we observed this storm. As in the previous example, the luminance decreased as the color of the clouds shifted toward the green. The last spectrum (Fig. 4-12c) of light from this storm was recorded at 2057 UTC. The dominant wavelength had shifted to 489.5 nm. The difference between the first and last spectra

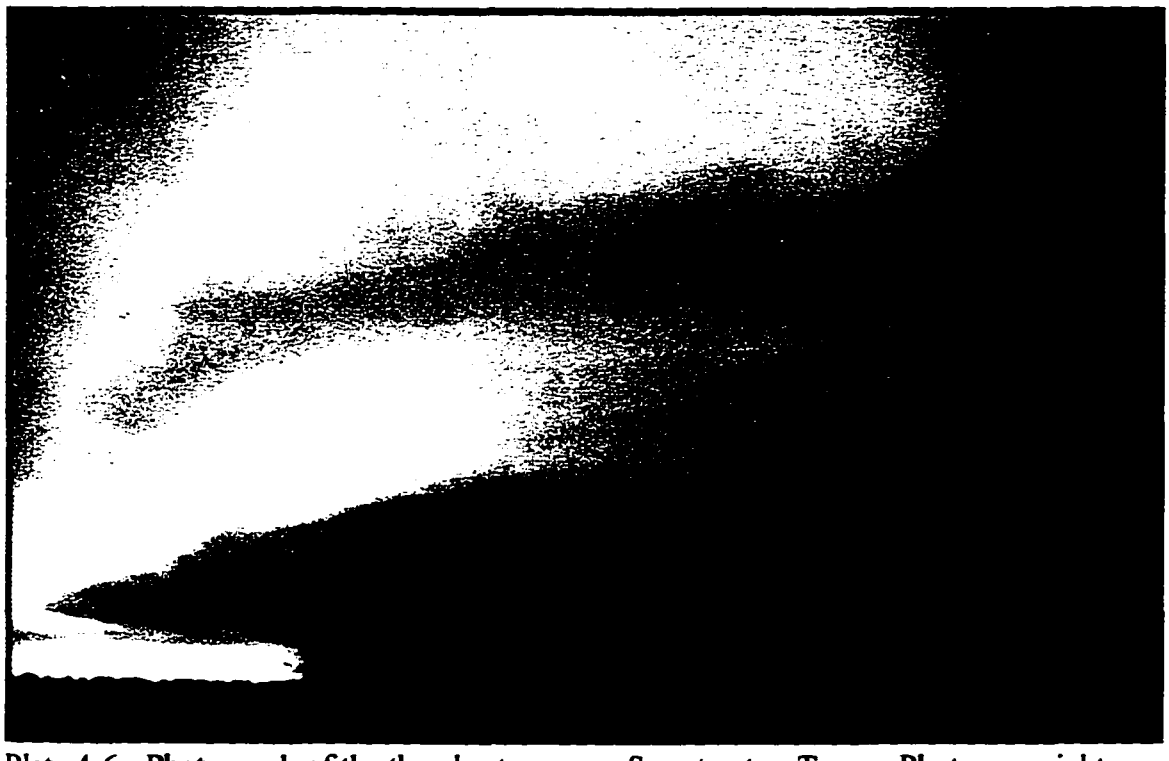

Plate 4-6 - Photograph of the thunderstorm near Sweetwater, Texas. Photo copyright (1995) by Charles A. Doswell III, used by permission.

recorded of this storm appears to be a relative reduction in the short wavelengths and a flattening of the spectrum.

One of the best photographs taken of a green thunderstorm is shown in Plate 4-6. Charles Doswell was chasing the same pair of thunderstorms being observed by the Electra aircraft. No precise time or location information was recorded to correlate the photograph to the spectral data. Unfortunately, this rendition of the photograph does not do justice to the observed green light emanating from the precipitation core region of the storm. The color of the ground and that of the green light from the storm are very different, an important observation relevant to the hypothesis that the green color in the clouds can be caused by reflections from the ground.

Chapter 5: An Introduction to Prevailing Hypotheses

Introduction

Although green thunderstorms have been a topic of occasional interest for years (Donaldson *et al.* 1965, Fankhauser *et al.* 1983, Bohren and Fraser 1993), until now little or no research has been conducted on this problem. Most references to green thunderstorms are offered as notes in discussions of other topics or are offered as anecdotal evidence supporting a connection with a certain type of meteorological phenomenon. Detailed analysis will be presented in the following chapters in order to explore the most prevalent current hypotheses of the cause of green thunderstorms. An optical cloud model will be presented in Chapter 8 and will be used to test some of these prevailing hypotheses. Other green colors are often observed in the atmosphere, such as the corona (Lynch and Livingston 1995, Minnaert 1954) or the green flash (Minnaert 1954) but are not included here as they are phenomena not closely associated with thunderstorms.

5.1 Fankhauser *et al.*

In the late spring and early summer of 1981 Fankhauser and colleagues (Fankhauser *et al.* 1983) were trying to document "some distinctive cloud forms often

observed beneath large cumulonimbus clouds." In particular they were looking at features in the inflow of storms in southeastern Montana as part of the Cooperative Convective Precipitation Experiment (CCOPE). Several research aircraft were involved, including the NCAR Sabreliner, the University of Wyoming's King Air, the South Dakota School of Mines and Technology T-28 penetrating aircraft, and an Aero Commander supporting research for the Desert Research Institute of the University of Nevada (Fankhauser *et al.* 1983).

On 11 July 1981 the study team observed many "intriguing cloud forms" as they flew near an intense thunderstorm that developed approximately 40 km south of Miles City, Montana. Of particular interest to us are their visual sightings of unusual coloration of the walls of the vault region of the storm. They characterized the color of the illumination as a luminous azure color. Azure is defined by Webster's Ninth Collegiate Dictionary (Mish 1989) as "the color of the clear sky, heraldic color blue, the unclouded sky." This is clearly not the color of the clouds that is usually observed beneath a large thunderstorm. Most often we observe a dark gray to dark blue color, certainly not that of clear sky. Observers on the aircraft modified their description of the color away from the dictionary definition to one of a more greenish color. They indicate the color as "exuding a continuous soft white light of blue-green hue, much like a fluorescent lamp" referring to an earlier description by Donaldson *et al.* (1965). The photograph on the cover of the *Bulletin* for May 1983 shows the color observed by the researchers (Plate 5-1). The researchers claim that the color picture is faithful to their observations but they did not

Plate 5-1 - The cover of the May 1983 issue of the *Bulletin of the American Meteorological Society*. The cover shows the blue-green light that Fankhauser *et al.* describe in their article. They claim that the color shown on the cover is representative to the color they observed.

carry instrumentation to make quantitative measurements. They only made rough qualitative judgements about what they saw.

Fankhauser and his colleagues believe the coloration was caused by blue skylight penetrating through thin areas in the cloud deck. Their viewing position is under a weak echo region of a storm with a cloud free "vault" to their west with the sun behind the storm. They argue that the direct rays from the sun were blocked by the severe thunderstorm and the only possible light remaining is that scattered by the atmosphere, the typical blue sky. They dismiss the possibility that the cloud hydrometeors may have

any role in selective absorption by referring to Zuev (1970) and Tricker (1970) who state that the extinction coefficient of visible light is independent of wavelength for particles of cloud droplet size or larger. We will address this issue later as part of the development of the optical model.

Their observations show that the sky to the east of the storm was free of clouds. The cloud structure they describe as a "cloud-free vault" is a clear region, or break, in the cloud base. They believe that this break or thinning of the shelf is sufficient to allow blue light from the clear sky to pass to the observers. They state that the vault region is an area where drier air is rising and this may be enough to reduce the cloud thickness to allow the blue light through. Measurements recorded by the aircraft seem to support this. When the aircraft flew near the cloud-free vault, there was a local maximum of upward vertical velocity, a drop in equivalent potential temperature, a drop in the mixing ratio, and a drop in potential temperature. This may be an explanation for one type of unusual coloration from the clouds but they come near to contradicting themselves when discussing the implications of a thicker cloud:

> "If cloud surrounding the vault had been thicker, then a color closer to gray likely would have prevailed. Indeed, the colors observed within the cloud-free vault on an earlier northbound pass (at ~2012 MDT) were more greenish-gray."

This observation and that by Donaldson *et al.* (1965) indicates that a greenish color to the clouds may be associated with strong thunderstorms.

5.2 Fraser Hypothesis

According to Fraser (Bohren and Fraser 1993), green light does not emanate from the thunderstorm itself. Rather, the storm provides a dark backdrop against which green airlight is seen. During the day, a black object at a distance will not appear black. Light scattered by the intervening air will cause the object to appear brighter than it actually is. If we assume that this airlight is sunlight scattered by molecules and particles that are small compared with the wavelength of the light, the color of the scattered light will be dominated by various shades of blue. If the source of the scattered light is predominantly red, such as light from the setting sun, then the airlight can be perceived as various shades of green. The Fraser Hypothesis will be covered in detail in Chapter 6.

5.3 Ground Reflection

Among those who do not discount observations of green thunderstorms completely, some believe that the green light associated with some severe thunderstorms is directly attributable to reflection from green vegetation. Most people who profess such explanations do not provide any physical reasoning to back up their statements. The best arguments seem to relate an area of ground being illuminated by the sun that directly reflects to the cloud base of a severe thunderstorm. Bohren and Fraser (1993) refute this hypothesis with some elementary arguments. They first put forth an argument against the

ground reflection theory by asking why some thunderstorms are green when they are observed over different kinds of terrain. Conversely, they ask why are not all thunderstorms green when they pass over a large region of green vegetation. Additional discussion of this hypothesis can be found in Chapter 7.

5.4 Bohren Theory

Bohren (Bohren and Fraser 1993) states that green light does emanate from the thunderstorm itself. Since absorption of light by water, either in a solid or liquid state, is at a minimum in the wavelengths of light that correspond to a blue color and rises steadily with increasing wavelength, any sunlight that passes through an appreciable distance in cloud hydrometeors will take on a bluish cast. Late in the day, sunlight is enriched in the longer wavelength (redder) light because a large portion of the shorter wavelength (bluer) light is scattered out. When this reddened light illuminates an object with an absorption minimum in the blue, the result can be perceptually green transmitted light. The primary requirement is that the path through the water (or ice) be long enough to allow sufficient absorption of the light at the long-wavelength (red) end of the spectrum. The Bohren theory seems to operate in the regions of the storms where we have observed and recorded spectra of green thunderstorm light. Bohren (Bohren and Fraser 1993) gives an overview of his theory which shall not be repeated here. We will test his theory using his final equation, which is based on the Eddington approximation (Shettle and Weinman 1970), and will be discussed in detail in Chapter 8.

5.5 Hail as the Cause of the Green Light — Part 1

The common belief that hail is the cause of green thunderstorms is likely one of the most widespread, unsupported claims in meteorology. Repeatedly in discussions with students, scientists, and others the color of the clouds is not only associated with hail, but also somehow caused by it. When asked about the cause of the green light, many people responded only with stories of association between the green light and hail. As an example of the prevalence of this belief a few comments are given below that are somewhat representative of the beliefs of many people.

> "... two years ago my parents remarked on how green the clouds of a late-afternoon thunderstorm were and, sure enough, that thunderstorm dropped up to tennis ball sized hail a few miles to the west;"

> "... I glanced outside and everything was a greenish hue. Sure enough, one minute later we had some decent hail. Sure enough, two minutes after that the NWS warned of a possible funnel . . . "

From someone who lived in Brisbane, Australia:

> "When I lived in Brisbane, Australia, I often noticed the greenish colouration of the clouds with severe thunderstorms. It was always associated with large hail."

Finally I quote a scientist at a national laboratory:

> "Scientifically, no one knows precisely what creates the green tint in some thunderstorms, but anecdotal evidence is vastly greater on the side of the color being *associated* with hail rather than with tornadoes."

Anecdotal stories do not represent evidence in the scientific sense but they do indicate a widespread misconception as to the cause of green thunderstorms. Bohren and Fraser (1993) gave the most detailed analysis to date explaining that hail is not a necessary condition for green color to form. They derive an approximate equation that relates integrated liquid water for clear, spherical hail to the integrated liquid water of cloud drops and the ratio of their diameters:

$$H_{hail} = H_{cloud} \left(\frac{d_{hail}}{d_{cloud}}\right)^{1/2}. \qquad 5\text{-}1$$

To get the same results of a cloud consisting of 1.5 cm of liquid water path (LWP) and 10 μm diameter droplets, one would need a LWP of 47.4 cm of 1 cm diameter hail. This would accumulate to more than 0.5 m of hail in a given location, not a likely occurrence. A more thorough discussion of the effects of large hydrometeors will be given in Chapter 8 and in the example in Chapter 9.

Chapter 6: Fraser Theory

Introduction

According to Fraser (Bohren and Fraser 1993), green light does not emanate from the thunderstorm itself. Rather, the storm provides a dark backdrop against which green airlight is seen. During the day, a black object at a distance will not appear black. Light scattered by the intervening air will cause the object to appear brighter than it actually is. If this airlight is assumed to be sunlight scattered by molecules and particles that are small compared with the wavelength of the light, the color of the scattered light will be dominated by various shades of blue. If the source of light is predominantly red, such as light from the setting sun, the airlight can be perceived as various shades of green.

6.1 The Solar Spectrum

Before getting too deeply involved in the modeling of atmospheric phenomena, it would be wise to take a closer look at the fundamental source of radiation: the sun. The sun is the nearest star to the earth and is the source of energy to keep life going on earth. It is essentially a nuclear fusion reactor that emits electromagnetic radiation across the spectrum, but this study is concerned only with a small wavelength band called visible light.

6.1.1 Solar Radiation Outside the Earth's Atmosphere

Of the electromagnetic energy that is emitted from the sun, approximately 50% lies in wavelengths longer than the visible region, about 40% in the visible region (400-700 nm), and about 10% in wavelengths shorter than the visible (Liou 1980). All except 0.1% of the sun's output occurs in the wavelength band 180 nm $< \lambda <$ 10 000 nm (Foukal 1990). The spectrum of the sun can be represented reasonably well by a blackbody curve of 6000 K. The fit is very good for wavelengths longer than the visible. However, the solar spectrum deviates appreciably from a blackbody curve in the ultraviolet portion of the spectrum. In the interval 210-260 nm, the equivalent blackbody temperature of the sun lies somewhat above 5000 K. It then falls gradually to a minimum level of about 4700 K at 140 nm. From there, toward shorter wavelengths, a large amount of energy flux is observed at the Lyman-α emission line of 121.6 nm associated with the first excited and ground states of hydrogen atoms (Liou 1980). Figure 6-1 shows curves of solar irradiance measured outside the earth's atmosphere and at the earth's surface. As shown in the figure, little of the shortwave radiation reaches the surface. The first reason is that solar radiation falls off rapidly in intensity in the ultraviolet and shorter wavelengths so there is little to reach the earth's atmosphere begin with. Furthermore, the earth's atmosphere absorbs a significant portion of this part of the solar spectrum. The atmospheric absorption bands are indicated in Fig. 6-1 by shading and are discussed in the next section. The physical makeup of the sun causes the solar irradiance curve (outside the atmosphere) to vary from that of a blackbody.

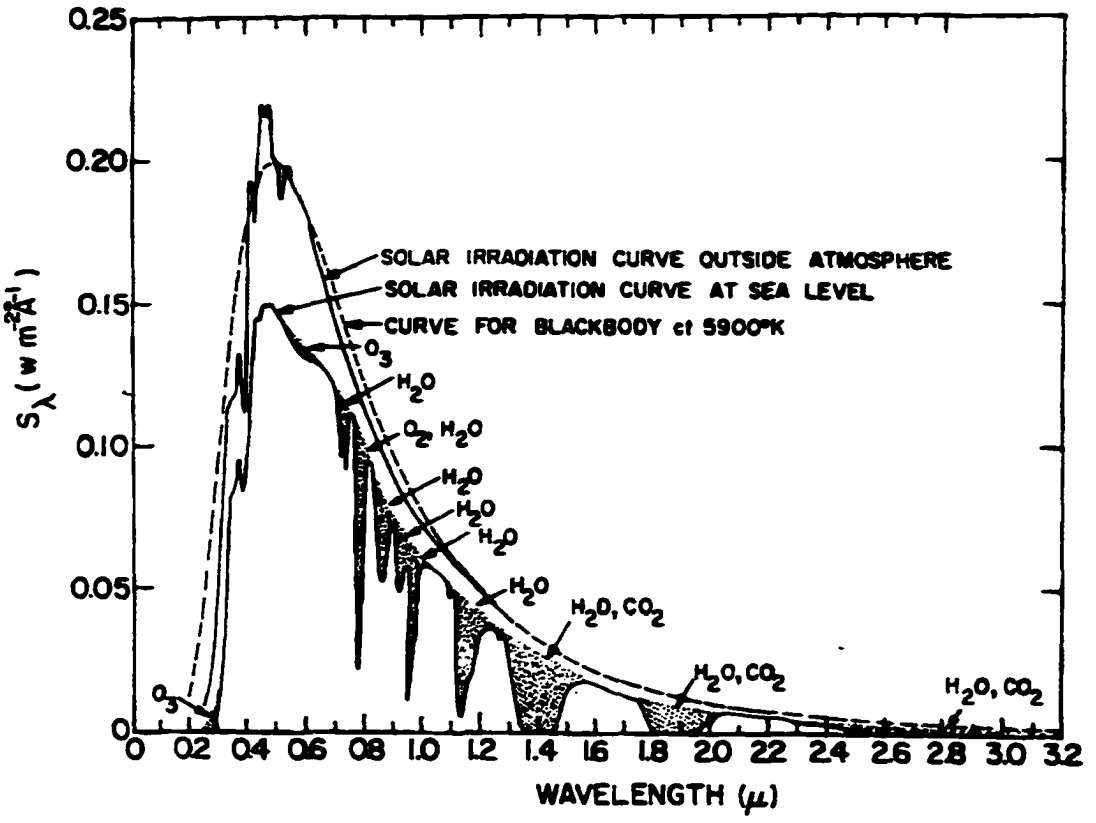

Figure 6-1 - Curves of solar irradiance measured outside the earth's atmosphere and at the earth's surface. The dashed line is a curve for a blackbody at a temperature of 5900 K. The shading represents absorption due to the indicated gasses in the clear atmosphere. The outer envelope of the shaded region denotes the reduction of the solar irradiance due to scattering (Kondratyev 1969).

6.1.2 Surface Spectrum

The radiation at the surface of the earth is influenced by several factors. Absorption of radiation by atmospheric constituents effectively filters out most of the radiation shorter than near ultraviolet wavelengths. The second factor is clouds. Globally averaged, clouds reflect 31% of the insolation (Wallace and Hobbs 1977). Finally, scattering of solar radiation by molecules and particles in the atmosphere reduces the amount of radiation reaching the surface. The solar spectrum (Fig. 6-2) used in all of the

following analysis is one measured at the earth's surface at Cape Canaveral, Florida on 4 June 1987 at 1531 UTC (Riordan *et al.* 1990). The original irradiance measurements

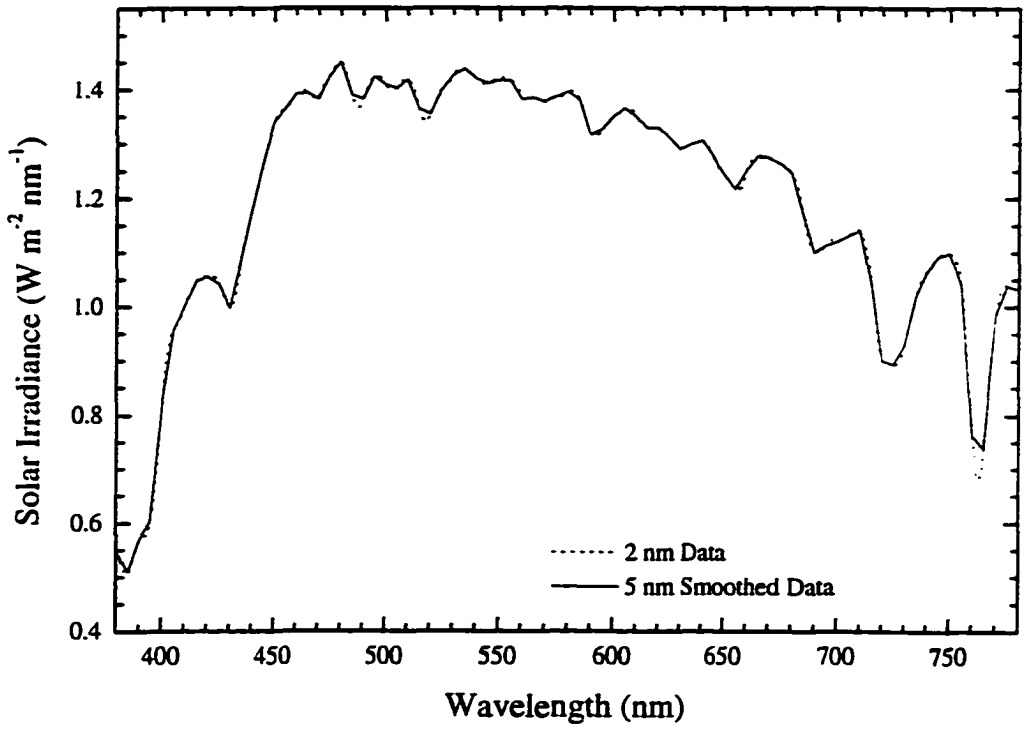

Figure 6-2 - Direct normal surface solar spectral irradiance measured on 4 June 1987 at Cape Canaveral, Florida. The dashed curve is the original 2 nm spectral data. The solid line is the smoothed 5 nm spectral data used for the simulation calculations. Data taken from Riordan (1990).

were made at 2 nm increments but, in the optical models presented here, the calculations are done at 5 nm increments. The 2 nm data was smoothed to 5 nm data for use in the models. The two irradiance curves are shown in Fig. 6-2.

6.2 Theoretical Development

To begin the analysis of Fraser's theory in more detail, a slight detour is taken to derive Schwarzchild's equation of radiative transfer. Following Kondratyev (1969), to simplify the derivation, the variations in the solar radiation are assumed to be sufficiently slow that any changes in the radiation field occur instantaneously in the entire region between the observer and cloud. This allows for the removal any time-dependent terms from the derivation. Furthermore it is assumed that the radiation is unpolarized. This simplifies the analysis tremendously by not having to consider the Stokes parameters. Finally, we consider a nonrefractive medium. Although the atmosphere is somewhat refractive, as suggested by the false apparent position of the sun at sunrise and sunset, we will ignore this effect as it is not likely to have an effect on the apparent color of the storm.

According to the radiative transfer equation for the transmission of light through a medium, the net change in radiance is the sum of the change in radiance due to extinction, and the change in radiance due to emission. In the treatment of radiative transfer in the atmosphere, emission at wavelengths shorter than infrared is usually considered negligible. In the case of a cloud illuminated by solar radiation, the emission of shortwave radiation is very small and can be neglected. Thus the emission term is the contribution by scattering alone. Referring to Fig. 6-3, $I_\lambda(p',\bar{s})$ is defined as the

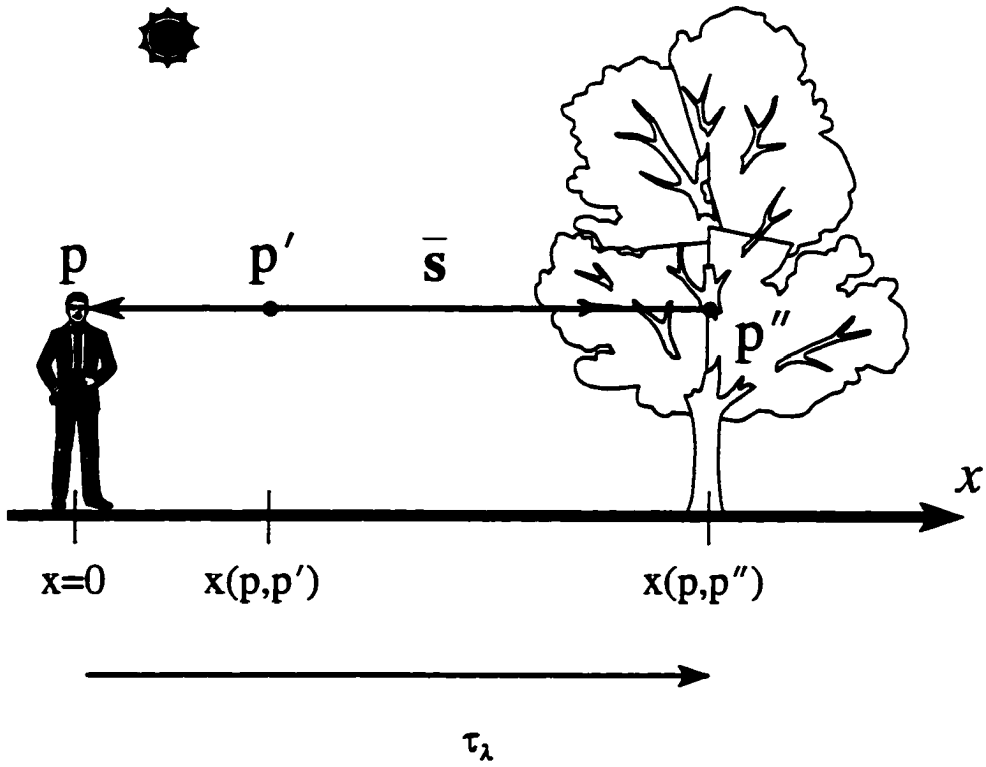

Figure 6-3 - Geometry for the derivation of the Schwarzschild equation of radiative transfer. The path s is defined as the path from the object to the observer. The optical path τ_λ is defined from the observer to the object.

monochromatic radiance at p′ (by an observer at x=0) looking along the path $\bar{s}$. $J_\lambda(p',\bar{s})$ is the monochromatic source function representing the radiance due to emission or scattering of light of light at p′ to the observer along the observer's line of sight ($\bar{s}$). The change in radiance can be written as:

$$dI_\lambda(p',\bar{s}) = -s_\lambda \, ds \, I_\lambda(p',\bar{s}) + s_\lambda \, ds \, J_\lambda(p',\bar{s}) \qquad 6\text{-}1$$

where s_λ is the monochromatic extinction coefficient, and ds is the differential unit of length along $\bar{s}$. An increment of monochromatic optical path ($d\tau_\lambda$) or optical depth is written as:

$$d\tau_\lambda = -s_\lambda \, ds. \qquad 6\text{-}2$$

The optical depth represents the amount of extinction one can expect when passing radiation through a unit depth of the atmosphere. Writing the transfer equation in terms of optical depth,

$$\frac{dI_\lambda(p',\bar{s})}{d\tau_\lambda} = I_\lambda(p',\bar{s}) - J_\lambda(p',\bar{s}) \qquad 6\text{-}3$$

This equation is solved if we multiply by the integrating factor $e^{-\tau_\lambda(p,p')}$:

$$e^{-\tau_\lambda(p,p')} \frac{dI_\lambda(p',\bar{s})}{d\tau_\lambda} = I_\lambda(p',\bar{s}) \, e^{-\tau_\lambda(p,p')} - J_\lambda(p',\bar{s}) \, e^{-\tau_\lambda(p,p')} \qquad 6\text{-}4$$

Then,

$$\frac{d}{d\tau_\lambda}[I_\lambda(p',\bar{s})e^{-\tau_\lambda(p,p')}] = -J_\lambda(p',\bar{s}) \, e^{-\tau_\lambda(p,p')}. \qquad 6\text{-}5$$

Since the derivative is in terms of optical depth, integrating over the total optical depth from the observer, at p, to the target object, at p″, yields:

$$I_\lambda(p,\bar{s}) = I_\lambda(p'',\bar{s})\, e^{-\tau_\lambda'} + \int_0^{\tau_\lambda'} J_\lambda(p',\bar{s})\, e^{-(\tau_\lambda'-\tau_\lambda)}\, d\tau_\lambda \qquad 6\text{-}6$$

where τ_λ' indicates the optical depth from p to p″. This equation states that the radiance at p along $\bar{s}$ is given by the radiance at p″ along $\bar{s}$ attenuated by the optical path (between p and p″) plus the sum of the contributions of each intervening element (between p and p″) attenuated by its optical path. This is the Schwarzchild equation of radiative transfer.

In analyzing any situation in radiative transfer we need to be certain of our definitions and the type of data used in the analysis. Before doing any work on the Fraser problem, we must first consider the radiation from the sun. In any standard reference regarding the sun, spectral irradiances are often presented as solar spectral radiation. For example, the solar constant is an integrated irradiance over all wavelengths. Irradiance, or total flux density of radiant energy, is defined as the normal component of radiance (also called intensity) integrated over a hemispherical solid angle and, in general, may be written as:

$$F_\lambda = \int_\Omega I_\lambda \cos\theta\, d\Omega. \qquad 6\text{-}7$$

In this equation I_λ is the monochromatic radiance defined as the flux of energy in a given direction per second, per unit solid angle, per wavelength interval, per unit area perpendicular to the given direction and θ is the angle between the normal to the receiving surface and the given direction. We shall assume for our analysis that the detector, be it our eyes or the spectrophotometer, is always oriented along the normal to

the receiving surface so that θ is always zero and the cosine term is unity leaving an integral over solid angle. One of the assumptions of irradiance is that it is the flux of radiant energy through a unit area. This means that only radiant energy from a single hemisphere, or 2π steradians, is received. Furthermore, in a nonscattering atmosphere, only radiation in a direction along the line of sight from the observer to the sun, which can be reasonably approximated by the solar disk, is nonzero. So the integral is evaluated:

$$F_\lambda = I_\lambda \, \delta\omega_s \qquad 6\text{-}8$$

where $\delta\omega_s$ is the solid angle subtended by the sun at the earth's surface at the mean earth-sun distance. The monochromatic solar radiance can be written as:

$$I_\lambda = \frac{F_\lambda}{\delta\omega_s}. \qquad 6\text{-}9$$

Fraser (1978) assumed that the backdrop is completely black, thereby eliminating the background illumination term $[I_\lambda(p'',\bar{s})]$ in the Schwarzchild equation. The only source of light that reaches the observer is that of light scattered by the atmosphere between the observer and the black cloud. This light is often referred to as airlight. We shall examine the validity of a perfectly black cloud later. Fraser (1978) continues by assuming that the earth between the storm and the observer is flat, a good assumption in western Oklahoma, and that there are no clouds between the storm and the observer. This second factor allows the airlight source function to be independent of (horizontal) optical

depth as we assume that there are no inhomogeneities in the illumination of the path between the observer and the storm. With $J_\lambda \neq f(\tau_\lambda)$ the integral for the source term is solved:

$$I_\lambda(p,\bar{s}) = J_\lambda(p',\bar{s})\ [1-e^{-\tau_\lambda'}]. \qquad 6\text{-}10$$

We now need to consider in more detail the airlight source term $J_\lambda(p',\bar{s})$. This term represents the light scattered to the observer, along the line of sight, by the intervening atmosphere between the black cloud and the observer. This path is illuminated by attenuated solar radiation:

$$I_{\lambda_{sg}} = I_{\lambda_s} e^{-\tau_{\lambda_s}} \qquad 6\text{-}11$$

where $I_{\lambda_{sg}}$ is the radiance of the solar radiation at the ground and τ_{λ_s} is the optical path between the sun and the earth's surface and I_{λ_s} is the solar radiation at the top of the atmosphere. The airlight source function (J_λ) represents the contribution of light scattered to the observer from everything along the line of sight. This can be written as:

$$J_\lambda(p',\bar{s}) = \frac{1}{4\pi}\int_{4\pi} I_{\lambda_{sg}}\ P\ d\omega. \qquad 6\text{-}12$$

where P is the scattering phase function and the integral is over 4π steradians indicating that light from an entire solid angle may be scattered toward the observer. Assuming that the atmosphere consists only of molecules, the phase function may be approximated by (Liou, 1992):

$$P(\phi) = \frac{3}{4}(1 + \cos^2\phi) \qquad 6\text{-}13$$

where ϕ represents the scattering angle. For our purposes, we shall assume that the scattering angle to be: $\phi = \pi/2 - \theta$, since the observer is looking horizontally at the black cloud. We can rewrite the equation for the source term as:

$$J_\lambda(P',\bar{s}) = \frac{1}{4\pi}(\frac{3}{4})(1+\cos^2\phi)I_{\lambda_s} e^{-\tau'_\lambda}\int_{4\pi} d\omega \qquad 6\text{-}14$$

where, since the scattering angle is fixed for a given time, it may be removed from the integral. Since the source (Eq. 6-11) is sunlight at the ground, the integral over solid angle can be approximated by the solid angle subtended by the solar disk as viewed from the ground, $\delta\omega_s$. Finally, the entire scattering source term can be approximated by:

$$J_\lambda(P',\bar{s}) \approx \frac{\delta\omega_s}{4\pi}(\frac{3}{4})(1 + \cos^2\phi)\, I_{\lambda_s}\, e^{-\tau_{\lambda_s}}. \qquad 6\text{-}15$$

where $\delta\omega_s$ is the solid angle subtended by the sun. We now substitute this equation into the overall radiance equation (Eq. 6-6) to the radiance at p observed along $\bar{s}$

$$I_\lambda(p,\bar{s}) = \frac{3\delta\omega_s}{16\pi}(1+\cos^2\phi)\, I_{\lambda_s}\, e^{-\tau_{\lambda_s}}\,[1-e^{-\tau_\lambda'}]. \qquad 6\text{-}16$$

To evaluate this equation, we must return to the definition of optical depth. An increment of optical depth was defined (Eq. 6-2) as the extinction coefficient multiplied by a unit distance along the line of sight. We have two different optical depths to evaluate. The first is the optical depth of the path between the sun and the earth's surface. Since there is little matter in space to attenuate the radiation, we consider only the atmospheric optical depth. We approximate this as:

$$\tau_{\lambda_s} = \frac{s_\lambda h}{\cos\theta} \qquad 6\text{-}17$$

where s_λ is the extinction coefficient (or the scattering coefficient in a nonabsorbing atmosphere), h is the scale height of the atmosphere (~8 km), and θ is the solar zenith angle. At larger solar zenith angles, the light must traverse more of the atmosphere thereby increasing the optical depth. To allow us to accurately model the setting of the sun, we introduce the relationship for a spherical earth (see Appendix A for derivation):

$$\frac{1}{\cos\theta} = \frac{(r_e+h)\ \cos[\sin^{-1}(\frac{r_e\sin\theta}{r_e+h})]\ -\ r_e\cos\theta}{h} \qquad 6\text{-}18$$

where r_e is the radius of the Earth, h is the scale height of the atmosphere, and θ is the solar zenith angle. This term will be substituted for $1/\cos\theta$ in the following equations wherever $1/\cos\theta$ occurs (e.g. Eqs. 6-17, 6-22, etc.), but, for simplicity will still be written as $1/\cos\theta$. The second optical depth is that from the observer to the storm. It is defined as:

$$\tau_\lambda' = d\, s_\lambda \qquad 6\text{-}19$$

where d is the distance to the storm. Kondratyev (1969) specifies a function for the scattering coefficient in a molecular atmosphere:

$$s_\lambda = \frac{32\pi^3}{3\lambda^4}\frac{(m-1)^2}{N} \qquad 6\text{-}20$$

where m is the bulk index of refraction and N is the number density of the molecules. m-1 varies with wavelength from a value of 3.4817×10^{-4} at 200 nm and 0°C to 2.8757×10^{-4} at 2000 nm and 0°C (Goody and Yung 1989). This departure in the λ^{-4} dependence is small compared to the λ^{-4} dependence itself. Therefore, a compromise value suggested by Kondratyev (1969), m-1 = 2.932×10^{-4}, is used. The number density (N) was calculated for the atmosphere at the Earth's surface. We can write the scattering coefficient as

$$s_\lambda = \frac{1.071\times10^{-3}}{\lambda^4} \qquad 6\text{-}21$$

where λ is expressed in μm. Fraser's value for the constant in Eq. 6-21 of 1.00×10^{-3} seemed reasonable and was accepted to simplify calculations further. Thus the equation used for the calculation of the total radiance at p along $\bar{s}$ is:

$$I_\lambda(p,\bar{s}) = \frac{I_{\lambda_s} 3\delta\omega_s}{16\pi}(1+\cos^2\phi)\, e^{-\frac{0.001h\lambda^{-4}}{\cos\theta}}\,[1-e^{-0.001s\lambda^{-4}}]. \qquad 6\text{-}22$$

6.3 Results of Fraser Hypothesis

Given the simplifications and assumptions made during the previous derivation, the Fraser hypothesis supports the occurrence of a special type of green thunderstorm. As we have seen, there are two optical processes that combine to create the light viewed by the observer. These two processes are the sunlight being attenuated by the molecules in the atmosphere (called the sunlight process) and the scattering of that sunlight to the

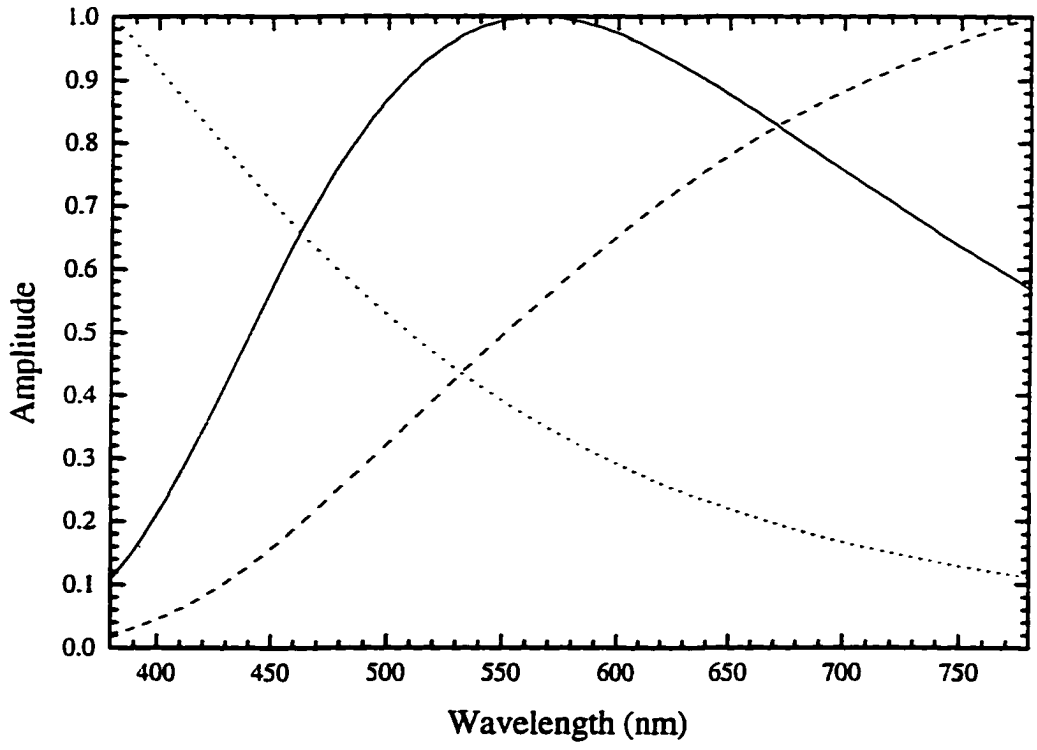

Figure 6-4 - Three curves representing the sunlight process (dashed) for a zenith angle of 85°, the airlight process (dotted) for a distance to the storm of 35 km, and a combination of the two effects (solid). The incident spectrum is assumed to be flat.

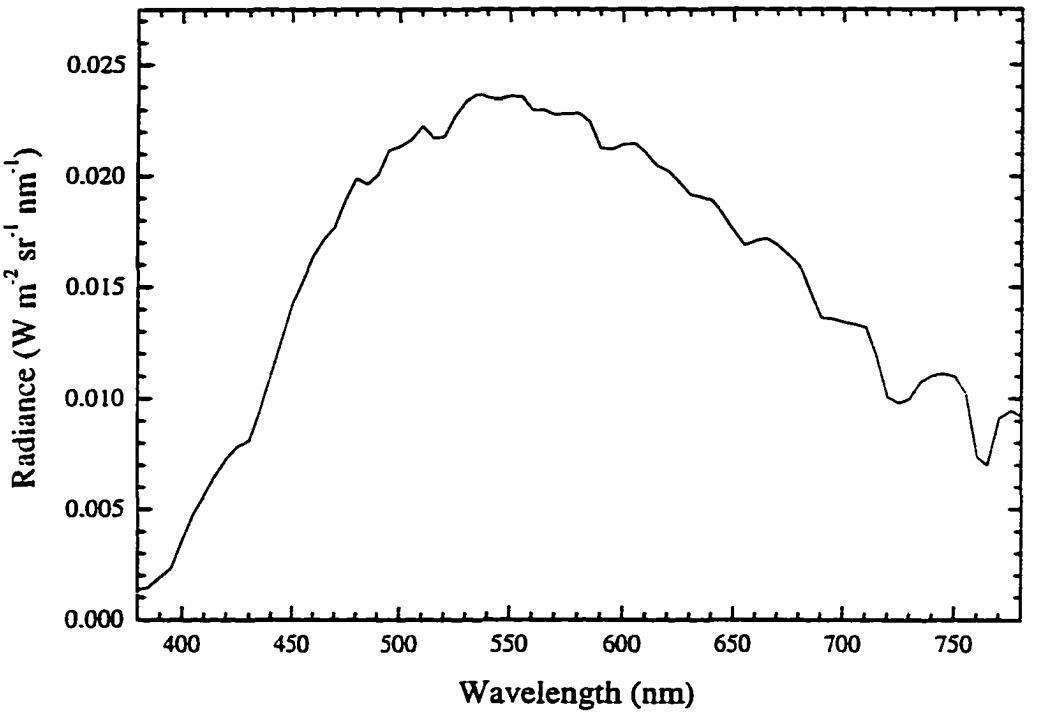

Figure 6-5 - Computed spectrum of light using the Fraser theory with a solar zenith angle of 85° and a distance to the storm of 35 km.

observer (called the airlight process); these are shown in Fig. 6-4. The sunlight function, for a setting sun with a solar zenith angle of 85°, has a maximum in the long wavelength portion of the spectrum. The airlight function, calculated using a horizontal distance to the storm of 35 km, is greatest in the short wavelength portion of the spectrum. The combination of these two functions yields a curve that has a peak in the middle wavelengths. The combined function was created by multiplying the two exponential terms in Eq. 6-22. The fact that the combined function peaks in the central portion of the visible spectrum indicates that the general approach taken thus far is at least reasonable.

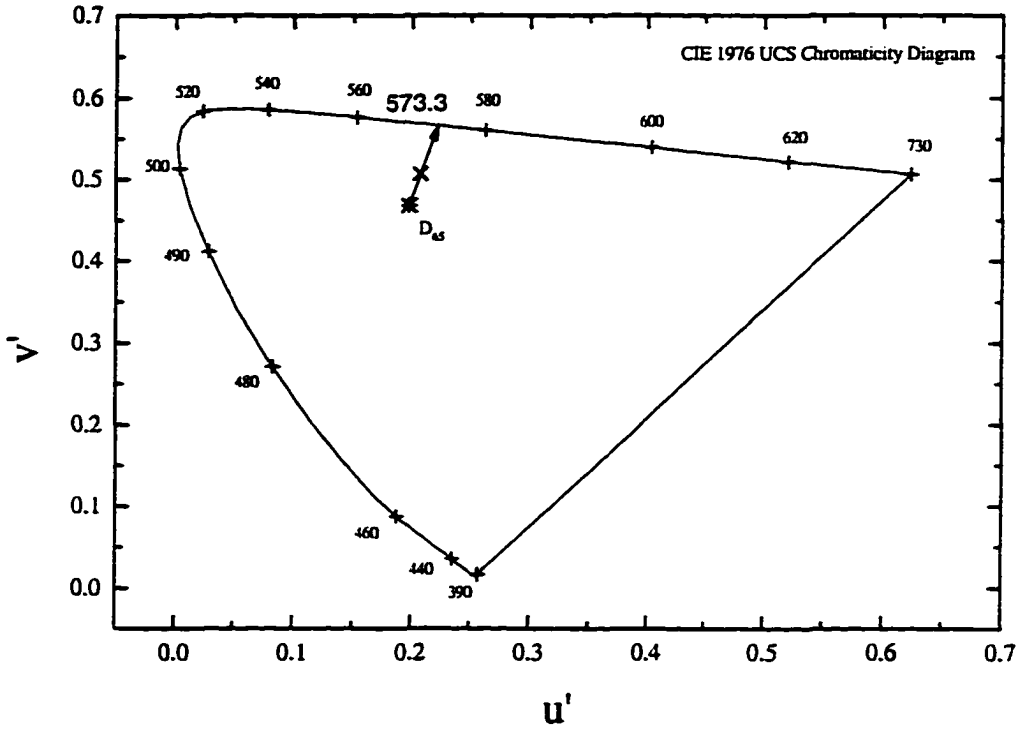

Figure 6-6 - CIE 1976 UCS chromaticity diagram of the spectrum in Fig. Fig. 6.3-2. The dominant wavelength is 573.3 nm and the excitation purity is 32.45 %. The spectrum is represented by the × symbol and the D_{65} achromatic point is represented by the * symbol.

The next step would be to insert a realistic spectrum for the radiance of the sunlight in Eq. 6-22. Figure 6-5 shows a computed spectrum, using Eq. 6-22, of the resulting radiation using sunlight as a source. The curves presented in Fig. 6-4 represent an ideal representation of airlight and sunlight and were calculated using the exponential terms in Eq. 6-22. The computed spectrum, while showing more ripple structure in the curve, maintains the basic shape predicted by the ideal curves. The peak wavelength of the computed spectrum shown in Figure 6-5 is 550 nm, a wavelength typically associated with the color yellowish-green. Figure 6-6 shows the computed spectrum of Fig. 6-5

plotted on a CIE 1976 chromaticity diagram (CIE 1978). As a reminder, the CIE diagram represents a color space where an individual spectrum is represented by a pair of chromaticity coordinates (u', v'). The coordinates are arrived at by integrating over wavelength the spectral power of the sample stimulus multiplied by three previously defined color-matching functions (Wyszecki and Stiles 1982). Any source of visible light is perceived by a human observer to be equivalent to a mixture of white light and light of a single wavelength. This single wavelength is called the dominant wavelength. The

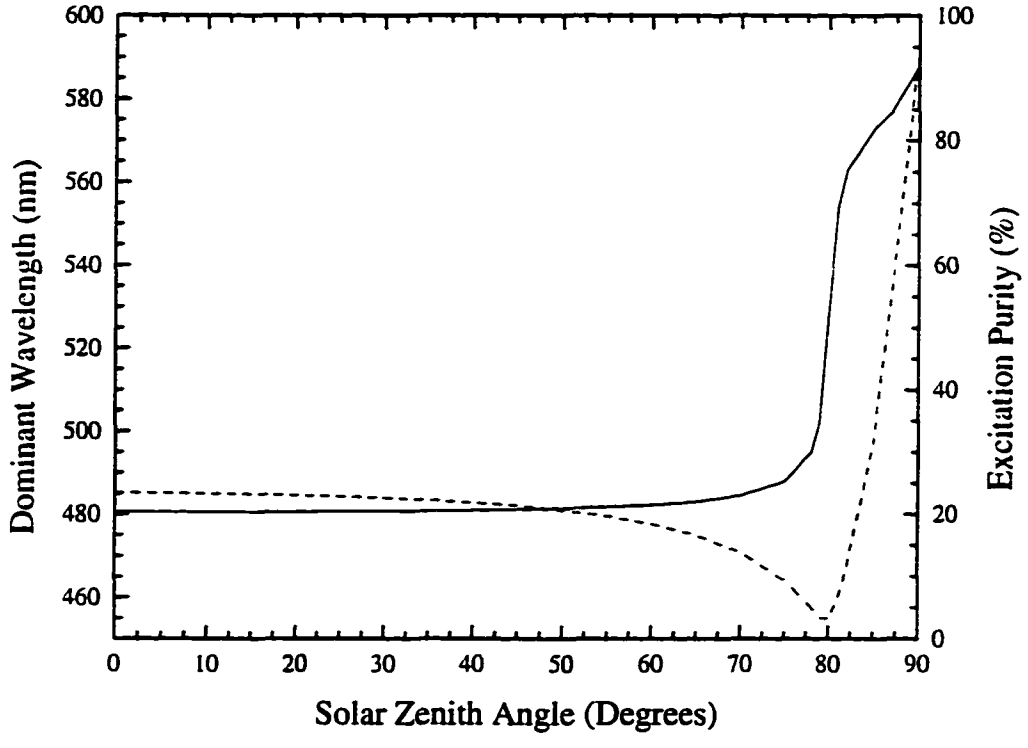

Figure 6-7 - A graph showing the variation in the dominant wavelength (solid) and excitation purity (dashed) with solar zenith angle for a distance to the storm of 35 km using the Fraser theory. A black cloud background is assumed.

relative amount of the single wavelength light in the mixture is called the purity. We have chosen to use the CIE (Commission Internationale de l'Eclairage) standard illuminant D_{65} for the white light (achromatic) source needed to compute the dominant wavelength and purity. D_{65} represents a phase of natural daylight and is the primary standard daylight illuminant and is represented by $*$.

Fraser's calculations were shown only at one solar zenith angle and one distance to a storm. To evaluate his theory further, his study was expanded to include various solar zenith angles and distances to the storm. Figure 6-7, not shown by Fraser, indicates how the purity and dominant wavelength change with solar zenith angle for a constant distance (35 km) to the storm. For a low zenith angle, the light received by the observer is blue indicating that the sunlight has not been sufficiently reddened by the atmosphere to create any color other than blue when the light is scattered by the atmospheric molecules. The purity and dominant wavelength vary slightly for zenith angles less than about 70°. As the zenith angle approaches 80° the purity drops to a minimum and the dominant wavelength increases rapidly toward the red part of the spectrum. If green is assumed to be represented by a wavelength band centered near 515 nm, then this figure shows that greenest spectrum is also associated with very low purity. This means that if a green sky were to occur as a result of the process described by the Fraser theory, the purity might be so low that a person with normal vision might not be able to discern a color. As the solar zenith angle increases beyond 80°, the sunlight is too red for the formation of any color other than red light seen by the observer.

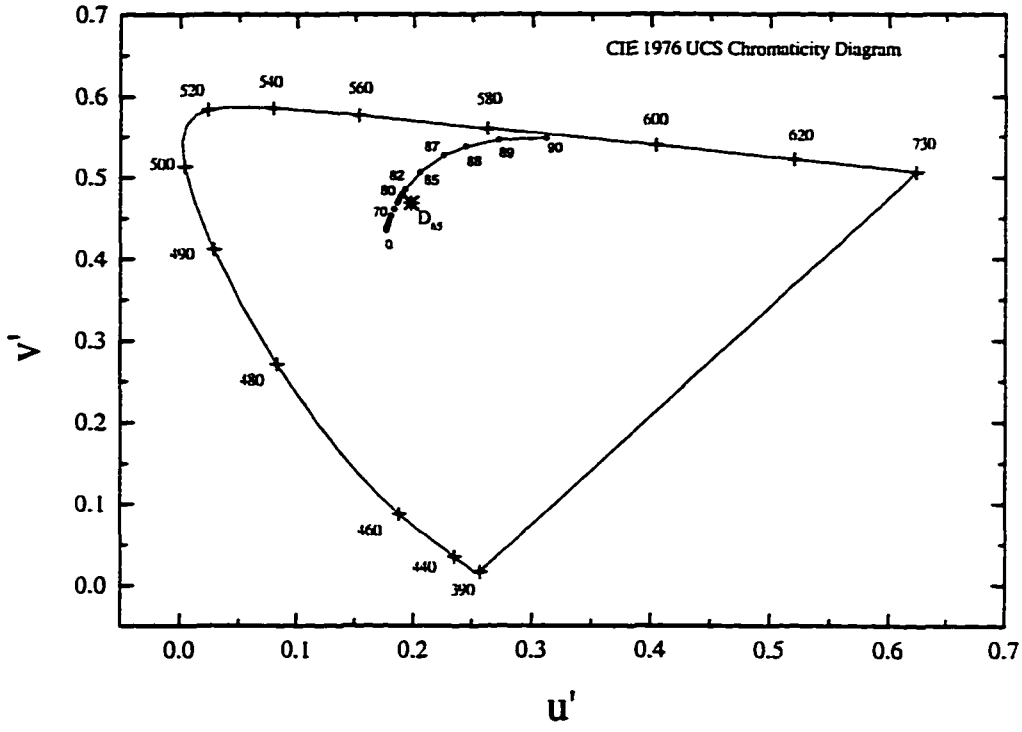

Figure 6-8 - CIE 1976 UCS chromaticity diagram showing the variation of chromaticity with solar zenith angle for a distance to the storm of 35 km using the Fraser theory. A black cloud background is assumed. The numbers indicated next to the plotted points represent solar zenith angle.

This same result can be seen in Fig. 6-8, which shows a series of spectra, plotted as chromaticity points, on a CIE 1976 UCS chromaticity diagram. Again, the distance to the storm was kept constant at 35 km and the solar zenith angle was varied from 0° to 90°. With small solar zenith angles, the dominant wavelength is in the region of the spectrum typically associated with blue colors. At large zenith angles, the dominant wavelength is in the region of the spectrum typically associated with red colors. In a narrow region of zenith angles, from about 80° to 81°, the Fraser theory can produce a

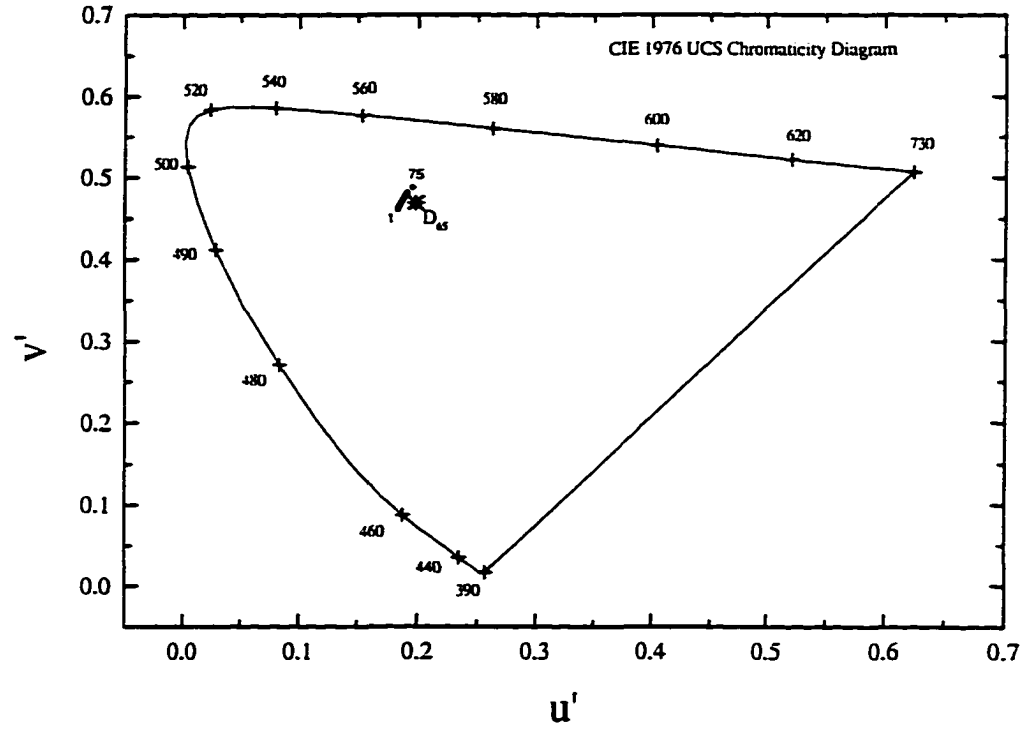

Figure 6-9 - CIE 1976 UCS chromaticity diagram showing the variation of chromaticity with distance to the storm for a solar zenith angle of 80° using the Fraser theory. A black cloud background is assumed. The numbers indicated next to the plotted points represent distance to the storm in km.

green color, but as shown in Fig. 6-7, the purity is low, and the light is very near white. The green color predicted might not be apparent to an observer.

The next step in the analysis is to check to see how the color or chromaticity varies with distance to the storm given a particular solar zenith angle. From the results above, a green solar zenith angle, 80°, was chosen. Figure 6-9 shows a series of spectra plotted as chromaticity points on a CIE 1976 UCS chromaticity diagram. The solar zenith angle was kept constant at 80° and the distance to the storm was varied from 1 km

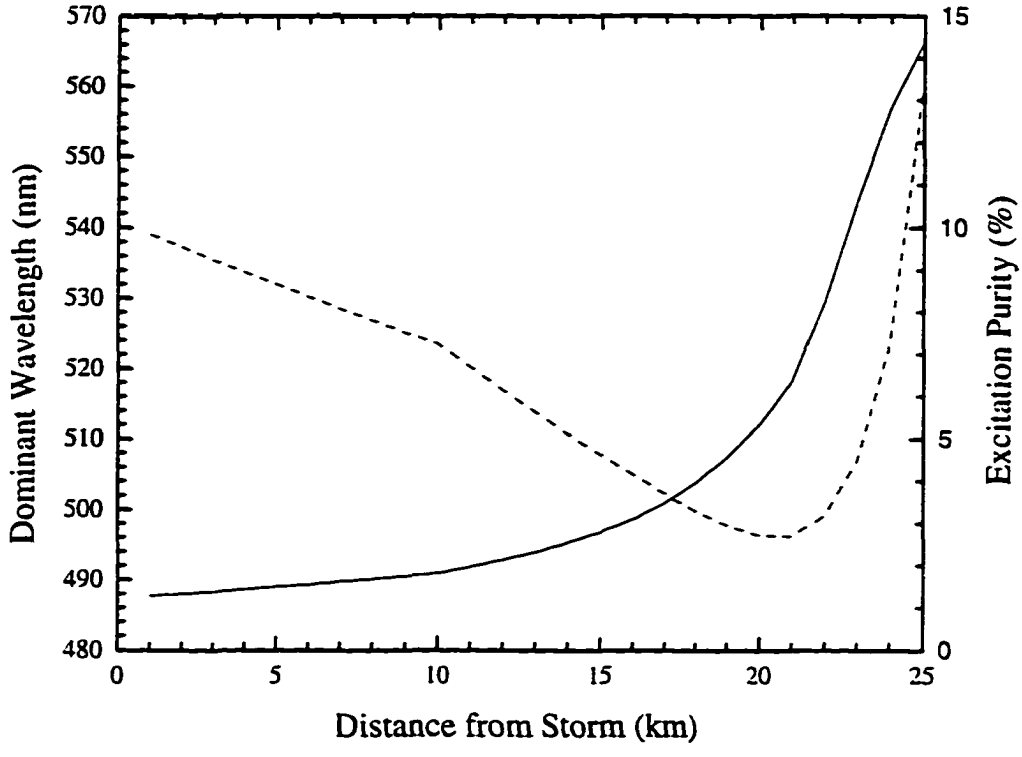

Figure 6-10 - A graph showing the variation in the dominant wavelength (solid) and excitation purity (dashed) with distance to the storm for a solar zenith angle of 80° using the Fraser theory. A black cloud background is assumed.

to 75 km. The dominant wavelengths representing green occur at a distance to the storm between 22 and 32 km. This also occurs at the minimum in the purity (Fig. 6-10) again indicating that if the green color does occur as predicted by Fraser, the purity would be so low that an observer might not be able to distinguish a green coloration in the sky. At large distances from the storm, the dominant wavelength of the observed light is essentially that of the incident attenuated sunlight.

Fraser's theory assumes a perfectly black cloud as a backdrop to the airlight being viewed by the observer. This is an unrealistic assumption. To improve upon Fraser's theory, a non-black cloud of varying reflectance will be added to the calculation of the observed radiance. This will be called the "Gray-Cloud" approximation given the typically perceived color of clouds.

6.4 Using a Non-Black Cloud

In the real world, no cloud is perfectly black so the backdrop will never be completely black and will contribute some radiation received by the observer. As an estimate of a typical thunderstorm cloud, an albedo varying from near zero to approximately 40 % will be used to represent a somewhat dark gray cloud. As a true gray

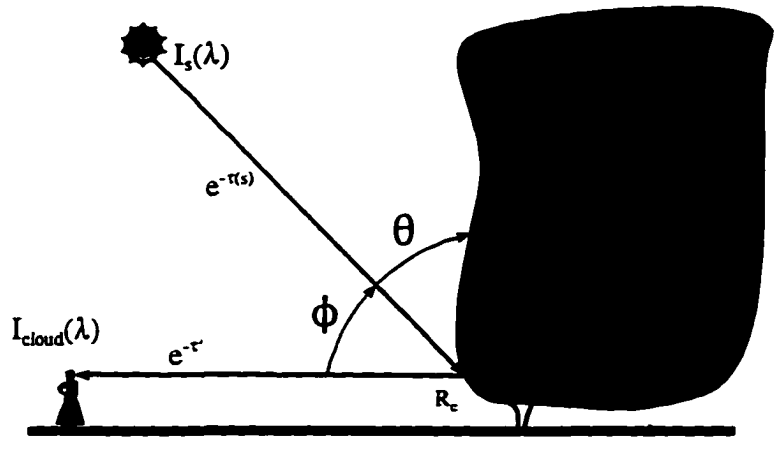

Figure 6-11 - Geometry of the reflected light from a distant cloud. θ is the solar zenith angle and ϕ is the reflection angle.

is a nonchromatic color, the reflectance from the cloud will be nonselective in wavelength. Figure 6-11 shows the path of the illumination for the light reflected by the cloud.

The additional reflected radiation consists of two parts. The incident sunlight illuminating the cloud is represented, as in the previous case by:

$$I_{\lambda_{ig}} = I_{\lambda_s} e^{-\tau_{\lambda_s}}. \qquad 6\text{-}23$$

Assuming a perfectly diffuse cloud, the radiation being reflected by the cloud to the observer through the optical depth of the atmosphere between the cloud and the observer is given by: $(2/\pi)(\cos\theta)(e^{-\tau'})$. Combining these effects, we get a relationship for the light from the non-black cloud:

$$I_{\lambda_c} = \left(\frac{R \cos\phi \; e^{-\tau'}}{\pi}\right) (I_{\lambda_s} \; \delta\omega_s) \; e^{-\tau_s} \qquad 6\text{-}24$$

where R is the nonselective, diffuse reflectance of the cloud, and $\delta\omega_s$ is the solid angle of the solar disk. The $\cos\phi$ term accounts for the reflection angle between the incident radiation and the line of sight of the observer. Since the airlight has already been accounted for, we shall neglect any additional airlight caused by the light reflected by the cloud. This term gets added onto the previously derived equation (Eq.6- 22) for I resulting in the equation for the Gray-Cloud approximation:

$$I_\lambda(p,\bar{s}) = \frac{I_{\lambda_s} 3\delta\omega_s}{16\pi} (1+\cos^2\phi)\, e^{-\frac{0.001h\lambda^{-4}}{\cos\theta}} [1-e^{-0.001s\lambda^{-4}}] + I_{\lambda_s} (\frac{R}{\pi}) (\delta\omega_s \cos\phi)\, e^{-(\frac{0.001h\lambda^{-4}}{\cos\theta})-0.001s\lambda^{-4}} \qquad 6\text{-}25$$

where, as before, $1/\cos\theta$ is replaced by the spherical earth term given in Eq. 6-18.

Although the Fraser theory predicts a special type of green thunderstorm, only a small amount of reflected or transmitted light from a cloud can overwhelm the light scattered by the atmosphere. Using Eq. 6-25 and the geometry shown in Fig. 6-11, the dominant wavelength of the observed radiation was computed for various values of R

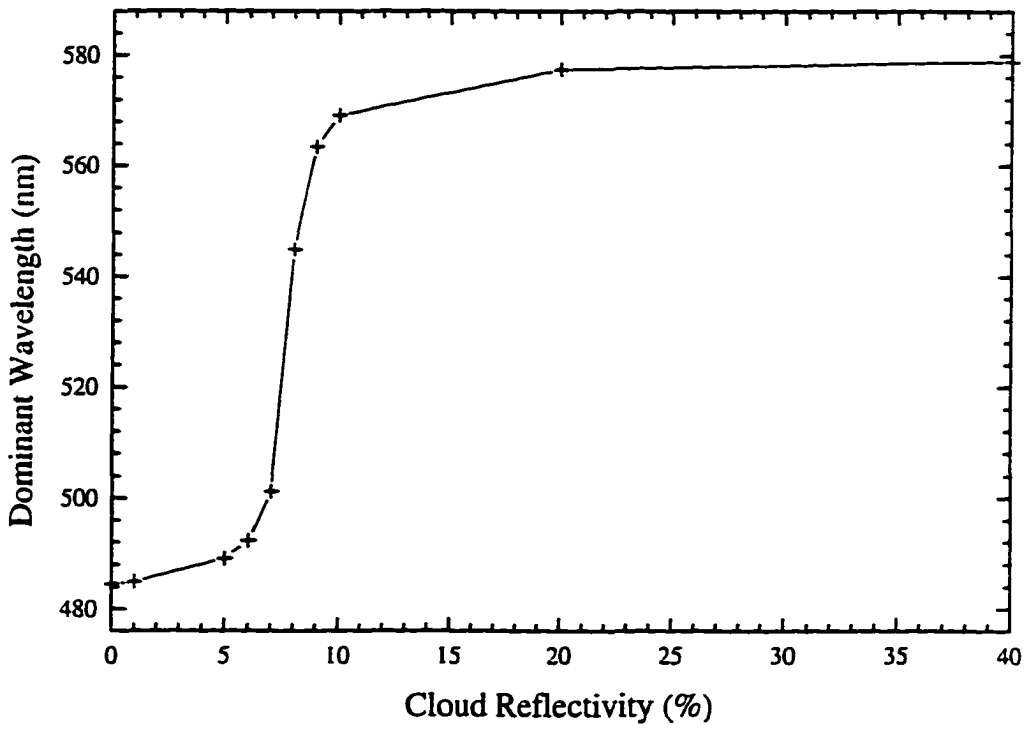

Figure 6-12 - The variation in dominant wavelength with changes in cloud reflectivity using the Fraser theory. The distance to the storm was fixed at 35 km and the solar zenith angle was 70°.

using a distance to the storm of 35 km and a solar zenith angle of 80.5°. As shown in Fig. 6-12, as soon as a reflective cloud is added to the computation the dominant wavelength increases. The dominant wavelength increases slowly for reflectivities below 5 %. But, when the reflectivity increases beyond 6 %, the dominant wavelength changes rapidly. With a cloud reflectivity of 8 %, the reflected light from the cloud overpowers the airlight and the dominant wavelengths approaches that of the solar radiation. For this particular case, there is a small range of cloud reflectivities that allow for the creation of

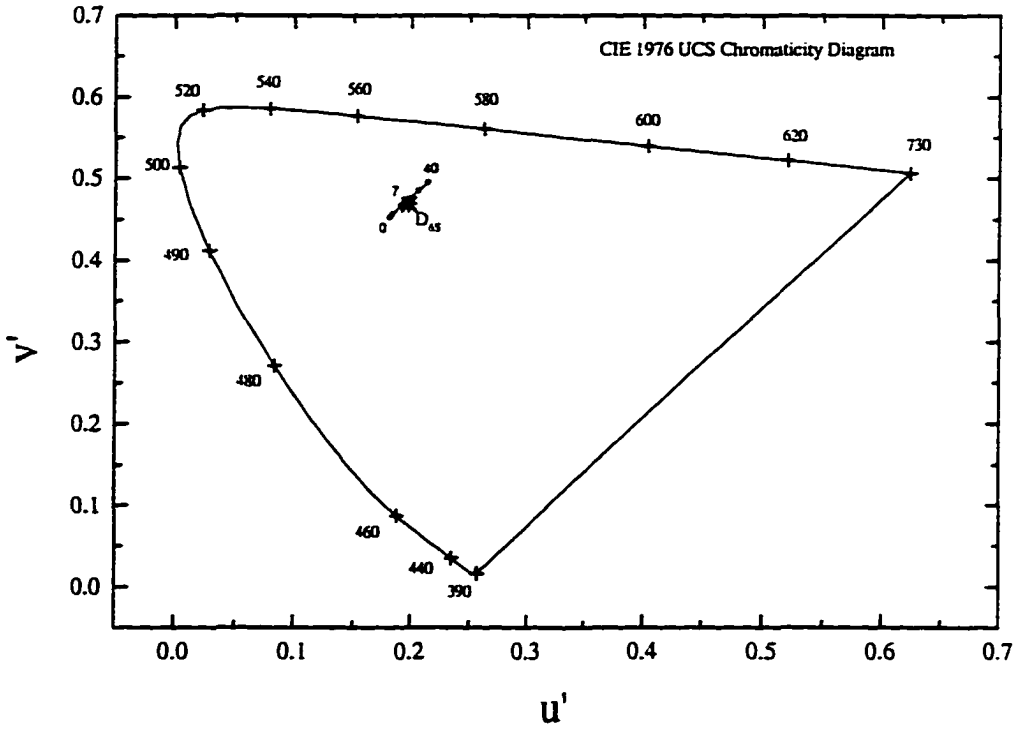

Figure 6-13 - CIE 1976 UCS diagram showing the variation in chromaticity with changes in cloud reflectivity using the Fraser theory. The distance to the storm was 35 km and the solar zenith angle was 70°. The numbers plotted next to the data points represent the cloud reflectivity in percent.

green light. If the reflectivities are changed by no more than 1 % the scattered light is no longer seen and the green color disappears.

Another way to look at the data is shown in Fig. 6-13. The spectral data is plotted on a CIE 1976 UCS chromaticity diagram and the reflectivities, in percent, are shown next to the plotted data. Although most of the data points are very close to the achromatic point, the spectra near 0 % reflectivity would appear a dull blue, and the spectra near 40 % reflectivity would appear a dull red. In between, where the green color is predicted, the chromaticity point of the spectrum is very close to the achromatic point and the observed light would most likely be perceived as white or gray.

The next step is to compare the calculated results of the Fraser theory and the Gray-Cloud approximation to an observation. The spectral data were recorded on 16 April 1995 at 0046 UTC approximately 0.6 km north of Exit 14 on Interstate-44 in southwestern Oklahoma. A strong thunderstorm had moved to the east of the highway and the skies were clearing to the west allowing the setting sun to illuminate the storm to the east. A rainbow was observed to the east and the spectrum of the light from the thunderstorm clouds was recorded in a position somewhat above the center of the arc of the rainbow. This view matched most closely to the Fraser theory configuration although, as indicated by the presence of a rainbow, rain was falling between the observer and the background cloud. The approximate position of the storm was 10 km to the east of the observer and the solar zenith angle was approximately 87.5°. Figure 6-14 shows the three spectra (Fraser theory, Gray-Cloud approximation, and observation) plotted on a CIE 1976 UCS chromaticity diagram.

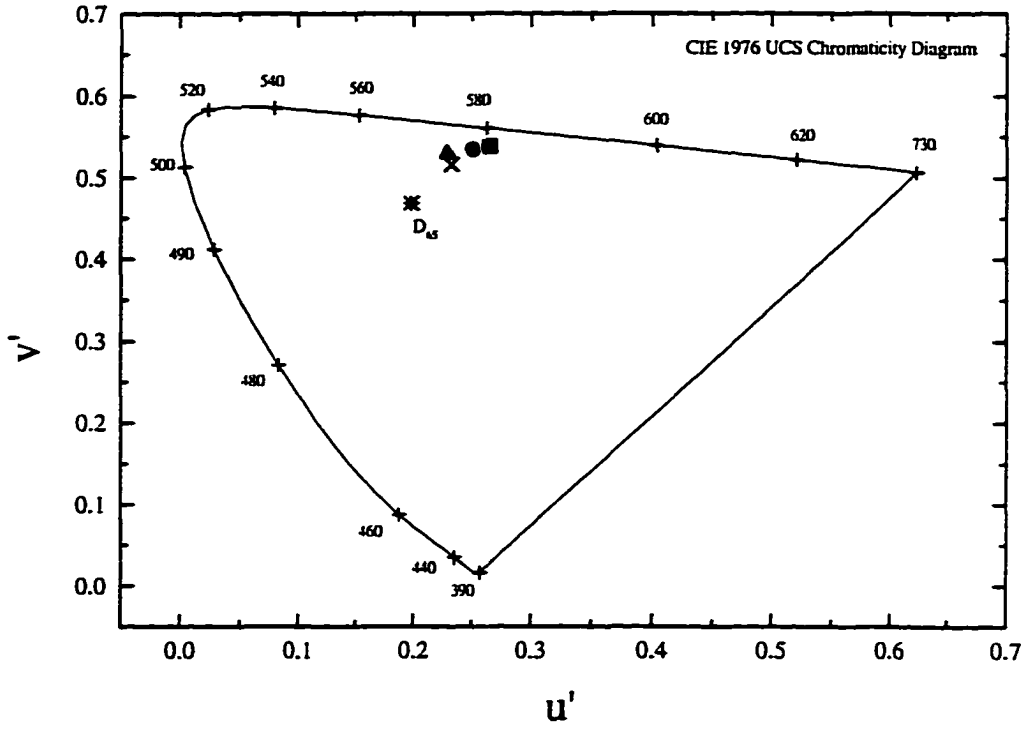

Figure 6-14 - CIE 1976 UCS chromaticity diagram showing an observation (×) compared with three Fraser theory calculations: black cloud (▲), 3 % reflecting cloud (●), and a 10 % reflecting cloud (■).

The Fraser theory for a black cloud predicts a dominant wavelength of 577.3 nm and a purity of 58.4%. The sky color would most likely appear as a highly saturated yellow. The 3 % gray-cloud model shows an increase in the dominant wavelength to 581.1 nm and the purity increased to 68.9%. The color would still be yellow, although slightly more saturated than the zero reflection case. The 10 % gray-cloud model predicts a dominant wavelength of 583.1 nm and a purity of 75.6%. The color of the light would most likely appear to be orange-yellow. The redder color in the latter cases is from the

increased amounts of red light of the setting sun reflecting off the cloud. The observation recorded a dominant wavelength of 580.2 nm and a purity of 46.7%. Observers reported the sky color as bright yellow-white. This description corresponds well with the recorded spectra. In this case, the atmosphere is modeled best by the Fraser theory.

To further illustrate the differences in the theories, the spectra of the observation, Fraser theory, and 3% Gray-Cloud approximation are plotted on the same set of axes (Fig. 6-15). Both the Fraser theory and the Gray-Cloud approximation, reflecting at 3 %,

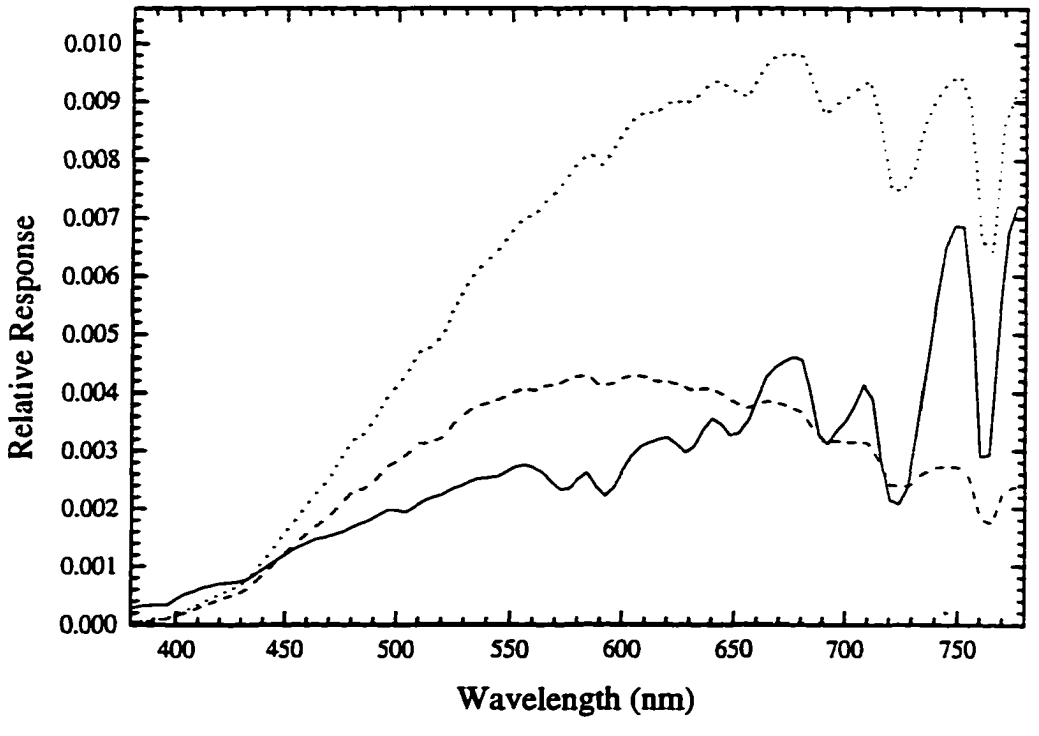

Figure 6-15 - Spectra of an observation and two different Fraser theory calculations. The observation (solid) was recorded on 17 April 1995 at 0046 UTC, 8 km west of Walters, Oklahoma looking east. The black cloud calculation is dashed and the dotted line represents a cloud reflectivity of 3 %.

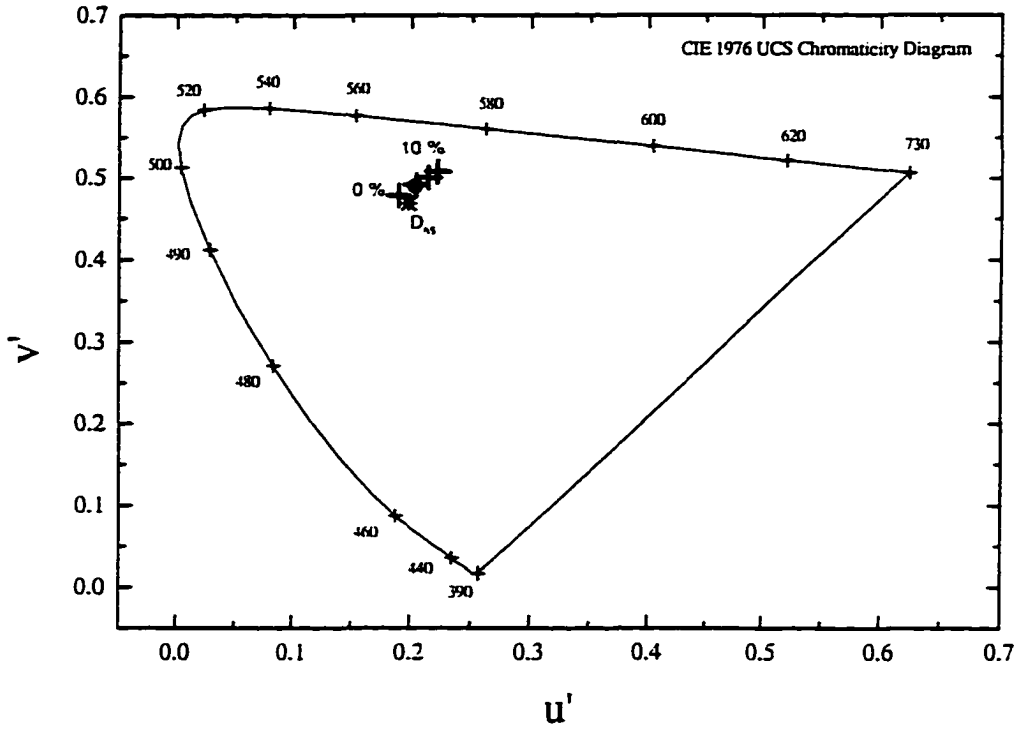

Figure 6-16 - CIE 1976 UCS chromaticity diagram indicating five spectra, one an observation and four of Fraser calculations. The calculations plotted (+) represent a cloud reflectivity of 0, 2, 5, and 10 %. The observation (●) was recorded on 24 July 1995 at 2339 UTC in Ocala, Florida looking to the east-southeast. The distance to the storm was 10 km and the solar zenith angle was 82.5°.

produce far too much radiance in the overall spectrum. This is to be expected as the Fraser theory and Gray-Cloud approximation do not account for scattering by hydrometeors. We should note that the Fraser theory is a limiting case of the Gray-Cloud apporoximation. When the reflectivity of the cloud is zero, we have a black cloud and the Gray-Cloud approximation reverts to the Fraser theory. Here, neither model accurately predicts the sky color of this storm moving off to the east around the time of sunset but

the Fraser theory, assuming a black cloud background, was superior to the Gray-Cloud approximation.

A second example was recorded of a storm that had moved to the ESE of the observer's location at 2239 UTC on 24 July 1995 in Ocala, Florida. The sky appeared dark gray to the observer and there was no observed precipitation between the cloud and the observer. The spectrum, shown in Fig. 6-16, has a dominant wavelength of 568.9 nm and a purity of 10.9 % which one might see as a pale yellow. In this case, where no rain was falling between the observer and the cloud, the Gray-Cloud approximation

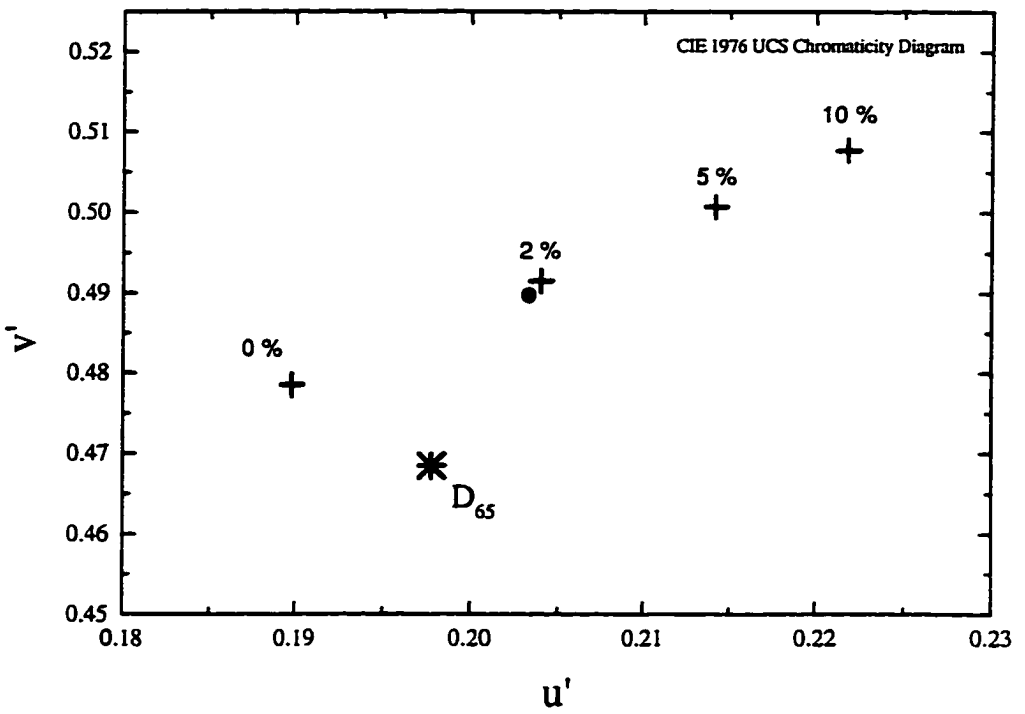

Figure 6-17 - A closeup view of the data shown in Fig. 6-16. The observation (●) and the 2 % Fraser calculation (+) are very close colorimetrically. The D_{65} achromatic point (✳) is shown for reference.

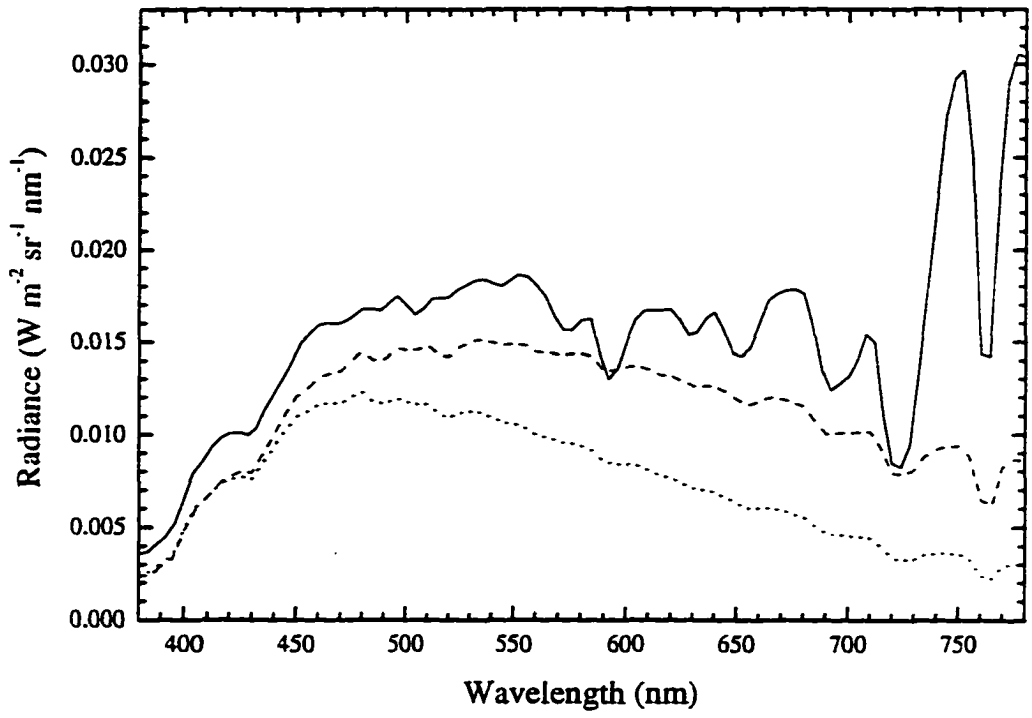

Figure 6-18 - Spectra of the Ocala observation (solid) and the 2% Gray-Cloud approximation computed spectrum (dashed). For reference, a black cloud (Fraser) calculation (dotted) is included. Neither calculation correctly simulates the large radiance variations in the wavelength band beyond 700 nm

colorimetrically matched the observation best. Fig. 6-17 shows a closeup of the CIE diagram where the data are plotted. The D_{65} achromatic point is shown for reference. The observation and the 2 % Gray-Cloud calculation almost overlap. The difference in the chromaticity coordinates between the measurement and the 2 % Gray-Cloud calculation is only slightly larger than the instrumentation error (see Chapter 2). This means that the 2 % Gray-Cloud approximation is, colorimetrically, correctly modeling this particular measured spectrum. Since the colorimetric agreement is good, the next

step is to check to see if the computed spectrum looks anything like the measured one, since it is possible that two very different spectra may have identical colorimetric coordinates.

Figure 6-18 shows the three spectra plotted on the same set of axes. The solid curve represents the average of two closely located spectral measurements. The overall radiance of the measured spectrum is slightly larger than either of the computed spectra at almost all wavelengths. The radiance difference indicates that additional light is being

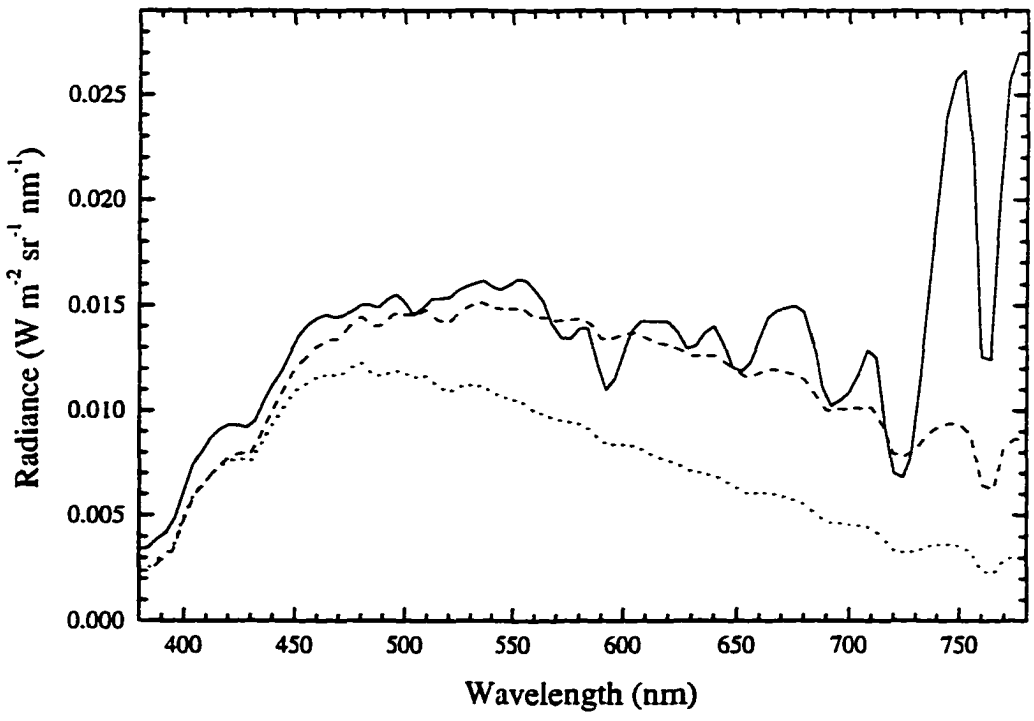

Figure 6-19 - Spectra of the mean Ocala observation (solid) and the 2% Gray-Cloud approximation computed spectrum (dashed). For reference, a black cloud (Fraser) calculation (dotted) is included. Neither calculation correctly simulates the large radiance variations in the wavelength band beyond 700 nm.

scatted by the cloud to the observer than is modeled by the Gray-Cloud approximation. Increasing the cloud reflectivity in the model will increase the radiance but it will also change the shape of the spectrum, as indicated by an increase in dominant wavelength. A 5 % reflecting cloud will have a dominant wavelength of 577.3 nm and a purity of 29.0 %. This would indicate a somewhat saturated yellow color, very different from the dark gray observed in the cloud. Light, other than that directly from the sun, must be illuminating the cloud. This possibility will be discussed in Chapter 8. The dominant wavelengths are nearly the same for the 2 % computed spectrum and the measured spectrum since the shapes of the spectra are similar. The computed spectra do not show such a strong near IR signal as does the measured spectrum. This will be addressed in Chapter 7.

As discussed in Chapter 2, the spectrophotometer measures a region of the sky subtending a 1° field of view. When one looks at a storm, one constantly scans a region of the storm much larger than a 1° field of view. To get an idea of how this might affect the observations, two spectra were recorded of the same region of the storm, but not the same location. These two spectra were recorded within seconds of each other, one about 5° above the horizon, and a second about 20° above the horizon into the same cloud. An average was computed of the two spectra and the result was plotted in the Fig 6-19. The dotted curve is the Fraser (black cloud) theory calculation, and the dashed curve is the 2 % Gray-Cloud approximation. The average curve is in much better agreement with the computed spectrum. Since the Fraser, and the gray-cloud approximation, assume homogeneity of the cloud structure, and the human observer constantly scans over a

region of the cloud much larger than a 1° field of view, an average of multiple spectra would be more representative of what the observer was seeing. An average of multiple 1° spectra recorded of an actual cloud would give better results than any single real-cloud measurement since no real cloud is perfectly homogeneous.

6.5 Another Perspective on the Fraser Theory

Many observers have noted that the sky near the horizon, around the time of sunset or sunrise, can take on a somewhat greenish cast. Often, the color is described as a very pale blue or a light green. Fraser's theory may give some insight into this observation. Meinel and Meinel (1983) state that a "sulfurous green" is seen to the west between the time of sunset and nighttime. The green color appears just above the "golden glow" when looking toward the horizon.

The PR®-650 spectrophotometer is unable to measure such feeble sources of light that Meinel and Meinel suggest is green, but it can measure the greenish coloration before sunset. Minnaert (1954) states that a mechanism similar to the Fraser theory is responsible for "the lovely green seen in the color of the sky at times." To test this rather common optical phenomenon a spectrum (Fig. 6-20) was recorded on 21 June 1995, at 2354 UTC approximately 1 km north of Otis, CO., looking to the east. The very weak greenish-blue color was observed through some breaks in the clouds approximately five degrees above the horizon. The dominant wavelength of the measured spectrum was 493.7 nm with a purity of 3.68 %. This corresponds to what most people would perceive

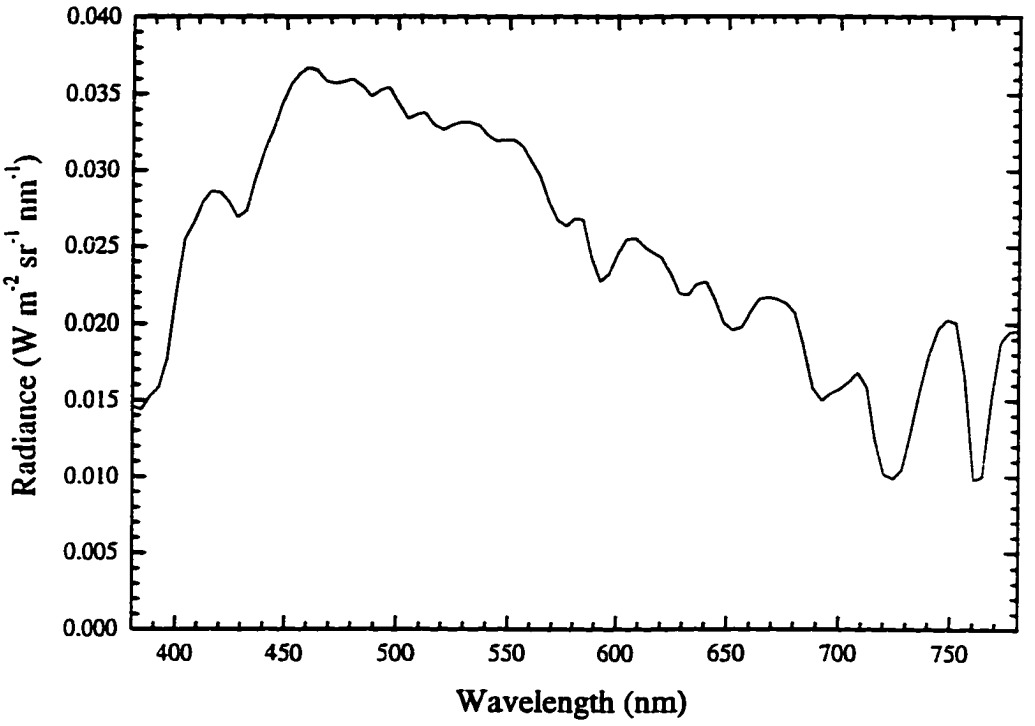

Figure 6-20 - Spectrum of a greenish-blue patch of sky looking to the east on 21 June 1995 at 2354 UTC 1 km north of Otis, Colorado. The dominant wavelength is 493.7 nm and the purity is 3.7%.

as a very pale bluish green. In an earlier part of this chapter is was mentioned that colors with low purities are difficult to differentiate from white (or gray). In those applications, the assumption was made that the entire cloud had the same color so there was no contrast with any other color nearby. Therefore, distinguishing a weak color from gray is difficult to do. In the example of the Otis, Colorado spectrum, the sampled light was juxtaposed with dark gray clouds. Since humans can match colors well and are able to notice small differences in adjacent colors, a high contrast scene will allow for the observer to distinguish colors at lower purity levels than under lower contrast situations.

Even at a purity of less than 4 %, the observer could tell (approximately) the color of the patch of clear sky between the clouds.

To test the applicability of the Fraser theory in this case, a spectrum was computed that would result from sunlight scattered by the atmosphere. The distance over which scattering occurs is such that no storm is required as a background. The computed spectrum was then created by computing the airlight using the equations of the Fraser theory. The measured spectrum (from Otis, CO) and the computed spectrum are shown

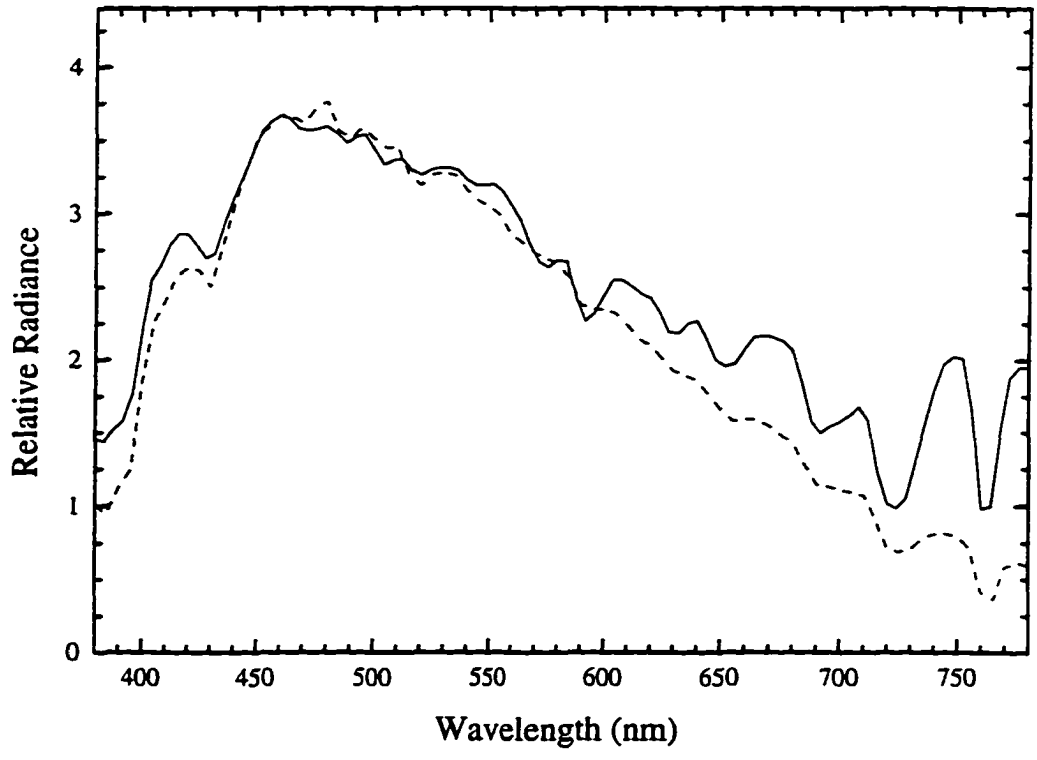

Figure 6-21 - Comparison of an observation (solid) with a calculated spectrum (dotted) using the Fraser theory. The calculated spectrum is scaled in amplitude to match the measurement. The observation was recorded on 21 June 1995 at 2354 UTC in Otis, Colorado, looking to the east. The calculated spectrum was created using a distance to the storm of 100 km and a solar zenith angle of 63°.

on Fig. 6-21. Although the computed spectrum was adjusted in magnitude to make it fit the observed data, the shape of the two curves is remarkably similar. The dominant wavelength of the computed spectrum is 494.3 nm with a purity of 4.5 %. This is in very good agreement with the observed data. This simple example demonstrates that it is possible to create green colors in the atmosphere according to the physical procedure described in the Fraser theory. In almost every case when this mechanism is operating, the purity of the green color is low, indicating a very weak color observed. The Fraser theory can create a weak green color by the combination of the process of sunlight, reddened by the atmosphere, and the process of scattering of the sunlight by the molecules in the atmosphere. The colors are muted or entirely erased by the presence of a background reflector. In nature, this color can sometimes be seen when no thunderstorms are nearby. Often, the green color is masked by stronger background colors and is very difficult to see. This may be the reason that green color, under circumstances required by the Fraser theory mechanism, is rarely seen.

6.6 Summary

The theoretical development presented by Fraser (1978) can produce a spectrum that would be perceived as a very faint green light using the assumption of a perfectly black background thunderstorm. There are two problems with this. The first is that the light produced has so little color that an observer probably could not perceive it. Second is the assumption of a perfectly black background. Severe thunderstorms are certainly not black when observed from a distance of 30-40 km. They may appear very dark but they

are not black. It appears from these simple calculations that the cloud is not necessary in producing the green light of the Fraser theory. The Fraser theory matches fairly well with the two examples shown here, neither of which were green. When the nonblack cloud was added in, the radiances and dominant wavelength increased and only came close to the observations with low cloud reflectivites. The observed cases shown are not green thunderstorm cases but are, rather, situations where the Fraser green thunderstorm theory should have been operating. The addition of a simple nonblack, or gray, cloud as a background increases the radiance calculated and shifts the dominant wavelength toward the red portion of the spectrum.

Chapter 7: Ground Reflection Hypothesis and the IR Spike Phenomenon

Introduction

This chapter is divided into two separate but related parts. The first part treats the possibility that light reflected from foliage on the ground can contribute to, or as some believe, cause the green light from some thunderstorms. In observed spectra, an unusually large fluctuation in the radiance often occurs in the near infrared (λ>700 nm). Although these "IR spikes" can be seen in the solar radiation spectrum of Fig. 6-22, they do not dominate the spectrum. In many of the observed examples, particularly with low light levels, these spikes can have radiances much greater than any other part of the spectrum. These spikes are investigated in the second part of the chapter and are related to the ground reflection phenomenon.

Among those who do not discount observations of green thunderstorms completely, some believe that the green light associated with some severe thunderstorms is directly attributable to reflection from green vegetation. Most people who profess such explanations do not provide any physical reasoning to support their statements. The best arguments seem to involve an area of ground being illuminated by the sun that directly reflects to the bottom of a severe thunderstorm. Bohren and Fraser (1993) refute this hypothesis with some elementary arguments. They consider observations as a weapon

against the ground reflection theory by asking why some thunderstorms appear green when they are observed over non-green terrain. Conversely, they ask why are not all thunderstorms green when they pass over a large region of green vegetation.

7.1 Theoretical Development

For simplicity we shall construct our argument around a nonabsorbing, nonscattering atmosphere that contains an infinitely extending, horizontally homogeneous cloud. The homogeneous ground below the cloud is then uniformly illuminated by the

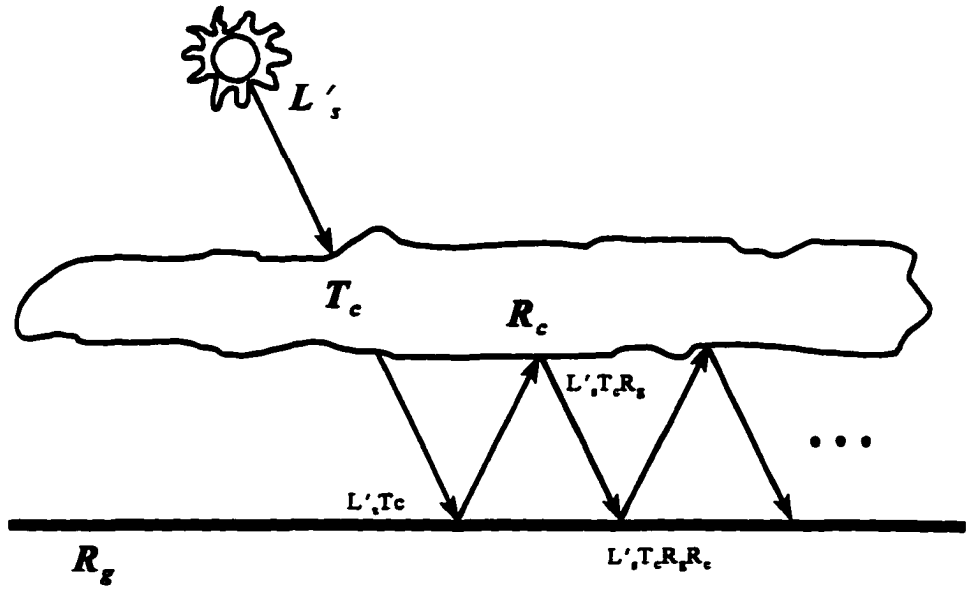

Figure 7-1 - Schematic of the optical path of a beam of light that passes through a cloud, reflects off the ground, then reflects off the cloud, and so on to the observer. Symbols are described in the text.

light transmitted by the cloud. Furthermore, we shall assume that the transmission and reflection functions are spectrally nonselective.

Radiation (L'_s) from the sun is transmitted through the cloud (T_c) and reaches the ground (Fig. 7-1). A portion of that radiation is reflected by the ground (R_g) to the cloud. The cloud then reflects a portion of the radiation (R_c) it receives from the ground back to an observer on the ground and so on. The equation describing this process for the radiance (L'_{obs}) observed at the ground as may be written as:

$$L'_{obs} = L'_s T_c + L'_s T_c R_g R_c + L'_s T_c R_g R_c R_c + \cdots \qquad 7\text{-}1$$

$$L'_{obs} = L'_s T_c (1 + R_g R_c + (R_g R_c)^2 + \cdots) \qquad 7\text{-}2$$

Then,

$$L'_{obs} = \frac{L'_s T_c}{(1 - R_g R_c)} \qquad 7\text{-}3$$

and

$$\frac{L'_{obs}}{L'_s} = \frac{T_c}{(1 - R_c R_g)}. \qquad 7\text{-}4$$

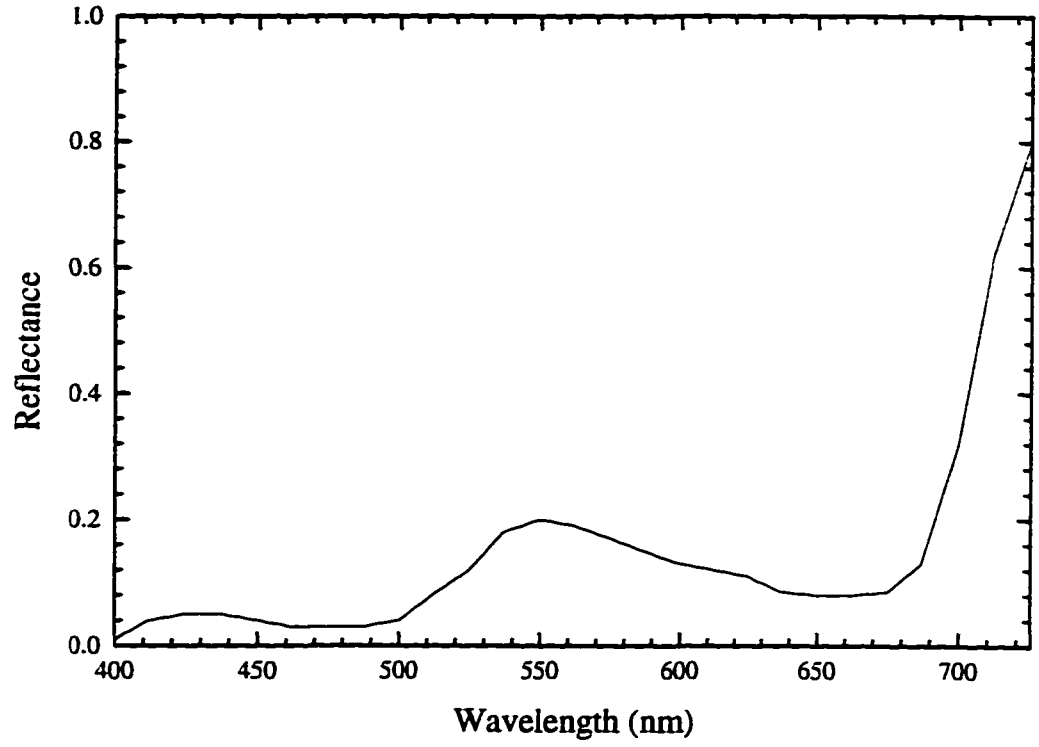

Figure 7-2 - Spectral reflectance curve of green grass (after Wyszecki and Stiles 1982).

For a thick cloud $R_c \approx 1$ then,

$$\frac{L'_{obs}}{L'_s} = \frac{T_c}{1 - R_g} \sim T_c(1 + R_g) \qquad 7\text{-}5$$

for $R_g \ll 1$. To determine the effectiveness of green grass contributing to the light seen by the observer, we need to know the value of R_g. Wyszecki and Stiles (1982) show a figure of spectral reflectance curves (Fig. 7-2), from data published by Krinov, of various

substances including green grass. The peak in the reflectance curve of green grass is 0.2 and this only occurs in a narrow spectral bandwidth centered near 555 nm. As Bohren and Fraser (1993) conclude, the contribution to the total radiation received by an observer is only slightly modified by reflections from the ground. The above example shows that for typical foliage reflectivities, the radiance from the cloud that includes the light reflected from the ground is only slightly higher than the radiance without the reflected light.

7.2 Simple Radiation Model

We shall construct this model assuming an atmosphere that consists only of molecules. Furthermore, we assume that the atmosphere is nonabsorbing. We do this to isolate the property of ground reflection to see if there is any similarity between the calculations and observations. Figure 7-3 shows the geometry of the problem. The cloud is optically thick and is infinite in extent. The observer is on the ground and is looking up at the cloud base. Following the derivation of the Schwarzchild Equation (Eq. 6-6) we recall the equation of radiative transfer:

$$I_\lambda(p,\bar{s}) = I_\lambda(p'',\bar{s})\, e^{-\tau_\lambda'} + \int_0^{\tau_\lambda'} J_\lambda(p',\bar{s})\, e^{-(\tau_\lambda'-\tau_\lambda)}\, d\tau_\lambda \qquad 7\text{-}6$$

where, in this case, $I_\lambda(p,\bar{s})$ is the radiance from the sun attenuated by optical depth τ'_λ plus the sum of all of the light scattered to the observer from the path between the observer and the sun, attenuated by optical depth. In our analysis of the ground reflection

scenario, we needed to consider both the light directly from the sun and the light reflected by the ground, then reflected again by the base of the cloud. As stated previously, the optical depths, are assuming molecular scattering,

$$\tau_{\lambda_s} = \frac{0.001h\lambda^{-4}}{\cos\theta} \qquad 7\text{-}7$$

$$\tau'_{\lambda} = 0.001\lambda^{-4}d = \frac{0.5\lambda^{-4}}{\cos\theta}. \qquad 7\text{-}8$$

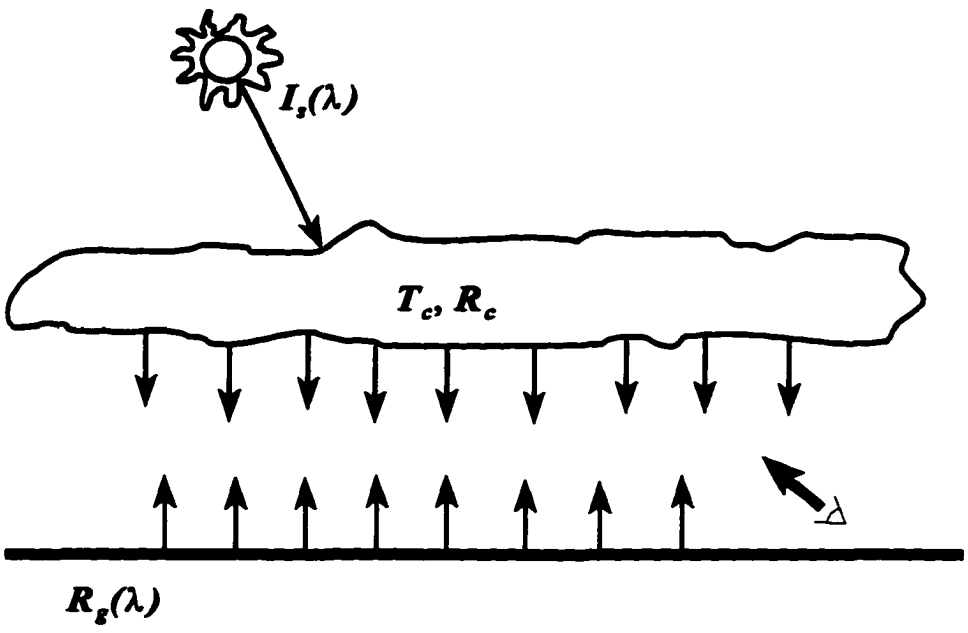

Figure 7-3 - Geometry of the nonabsorbing ground reflection problem. T_c and R_c are the transmissivity and reflectivity of the cloud. R_g is the spectral reflectance of the ground. I_s is the spectral solar radiance.

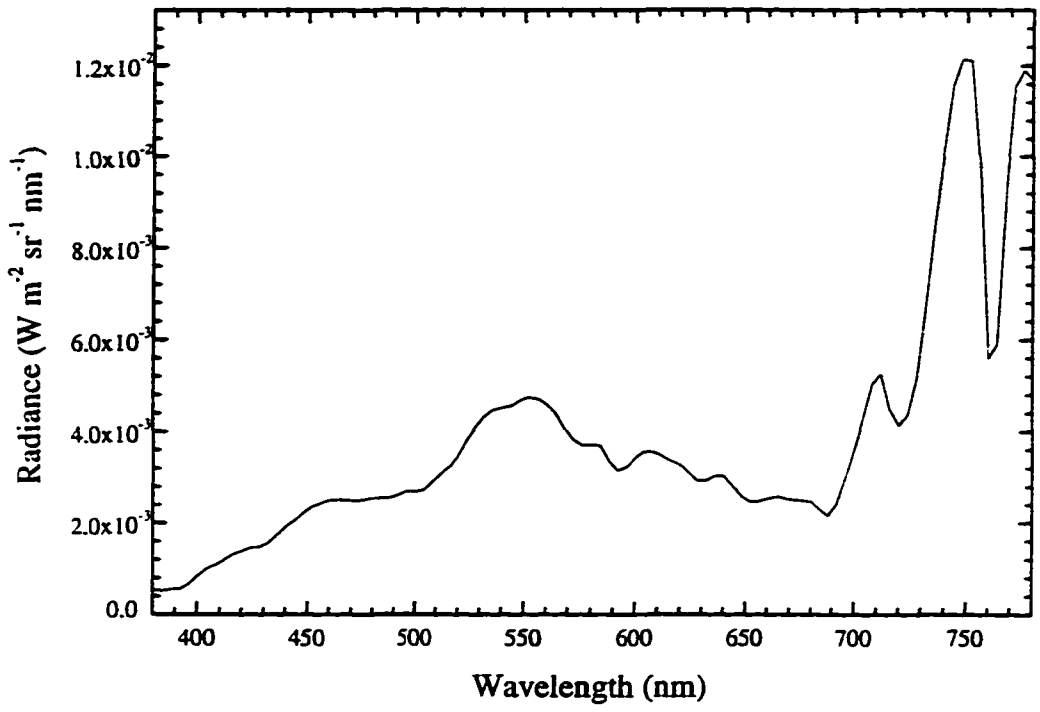

Figure 7-4 - Spectrum of young wheat growing in a field in Mountain Park, Oklahoma. Spectrum was recorded on 7 May 1995 at 2208 UTC looking to the northwest.

h is the scale height of the atmosphere, θ is the solar zenith angle, and d is the distance between the ground and the cloud base. As for the Fraser theory, the $1/\cos\theta$ in $\tau_{\lambda s}$ is replaced by the spherical earth approximation (see Eq. 6-18 or Appendix A). For these calculations, a cloud base of 500 m is assumed so only the light scattered by the atmosphere between the cloud base and the ground is included. The color of the ground is specified by the spectrum recorded of foliage on 7 May 1995 shown in Fig. 7-4. The stipulation that the reflecting surfaces are of an infinite extent means that all of the light reflected from the ground falls on the cloud and is then reflected again to the observer.

The following equation is used for this model

$$I_{obs} = R_c R_{\lambda_g} [T_c I_{\lambda_s} e^{-\tau'_\lambda} + \frac{T_c\ 3\ \delta\omega_s\ (1+\cos^2\theta)}{16\pi} I_{\lambda_s}\ e^{-\tau_{\lambda_s}} (1-e^{-\tau'_\lambda})] +$$

$$[T_c I_{\lambda_s} e^{-\tau'_\lambda} + \frac{T_c\ 3\ \delta\omega_s\ (1+\cos^2\theta)}{16\pi} I_{\lambda_s}\ e^{-\tau_{\lambda_s}} (1-e^{-\tau'_\lambda})] \qquad 7\text{-}9$$

Figure 7-5 shows the computed direct, reflected, and total radiance for a sun located at a solar zenith angle of 45°. Since cumulonimbus clouds are exceedingly thick,

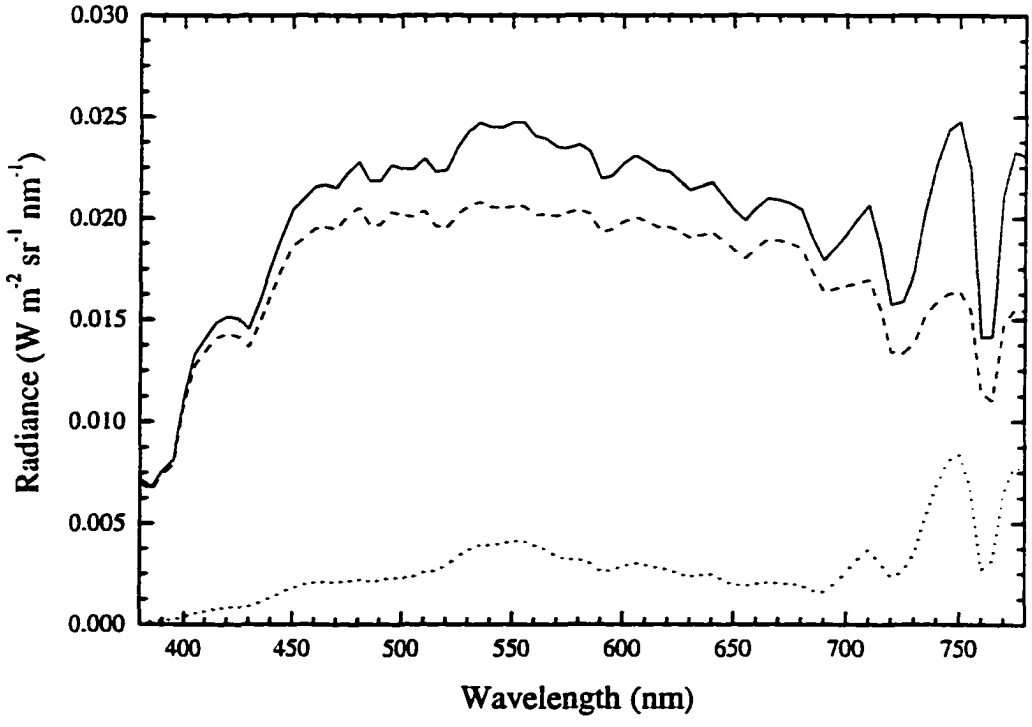

Figure 7-5 - Computed total radiance (solid), transmitted radiance (dashed), and reflected radiance (dotted). The reflection function is given by Fig. 7-4. The input solar radiance is given by Fig. 6-2. The computed radiance was calculated using a cloud reflectance of 1.0 and a cloud transmission of 10^{-6}. The solar zenith angle was 45°.

they reflect most of the radiation incident upon them in the visual spectrum (see the section on IR spikes for a further discussion of this issue) so the cloud reflectance was set to 1.0 and the cloud transmission was set to 1.0×10^{-6}. The figure shows that the direct radiance is still an order of magnitude greater than the reflected radiance at nearly all wavelengths. Although the cloud reflects nearly 100 %, the effects of the reflected light are still small compared to the direct light. The difference between the dominant wavelength of the direct radiance (579.2 nm) and the total radiance (577.1 nm) is about three times smaller than the difference between the reflected radiance (571.4 nm) and the total radiance. The purity of the reflected radiance is much greater than that of either the transmitted or the total. The dominant wavelength of the total radiance is shifted slightly toward that of the reflected radiance, indicating a possible small bias toward the reflected radiance.

Since most green thunderstorms are observed near sunset, a second example, with the solar zenith angle set to 85° is shown in Fig. 7-6. As before, the cloud reflectance was 1.0 and the cloud transmission was 10^{-6}. The reflected radiance adds less than 10% to the total radiance, except for the near IR spectral band. Given that the setting sun is the only light source in the model, the effects of the green surface are almost negligible; the peak in the reflected surface spectrum is small at 550 nm and there is little effect on the colorimetric properties of the spectrum. The dominant wavelengths of all three radiative components (direct=581 nm, reflected=577 nm, and total=581 nm) are closer to each other than in the 45° example. The direct dominant wavelength is closer to the total radiance dominant wavelength than the reflected dominant wavelength. Figure 7-6 show

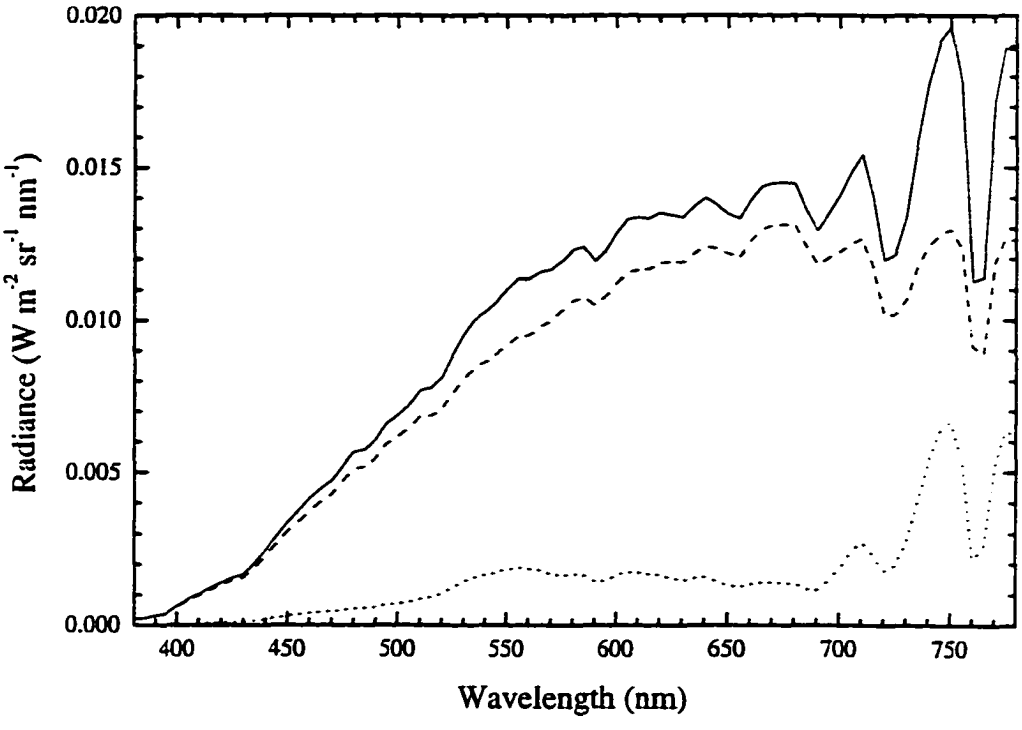

Figure 7-6 - Computed total radiance (solid), transmitted radiance (dashed), and reflected radiance (dotted) with no solid angle dependence, calculated using a cloud reflectance of 1.0 and a cloud transmission of 10^{-6}. The solar zenith angle was 85°.

the three spectra plotted on a CIE chromaticity diagram. The transmitted and total chromaticity points nearly overlap. The reflected chromaticity point is slightly greener and a bit more pure than the other two. As a check to see if any of these simulate a real storm, a green thunderstorm observation is plotted on the same chart. The green thunderstorm observation is very close to the achromatic point and is not representative of either the transmitted light nor the reflected light. The model put severe constraints, such as nonabsorption, on the nature of the transmitted light but the computed reflected light is depicted more realistically. The grass beneath the storm had a dominant wavelength of

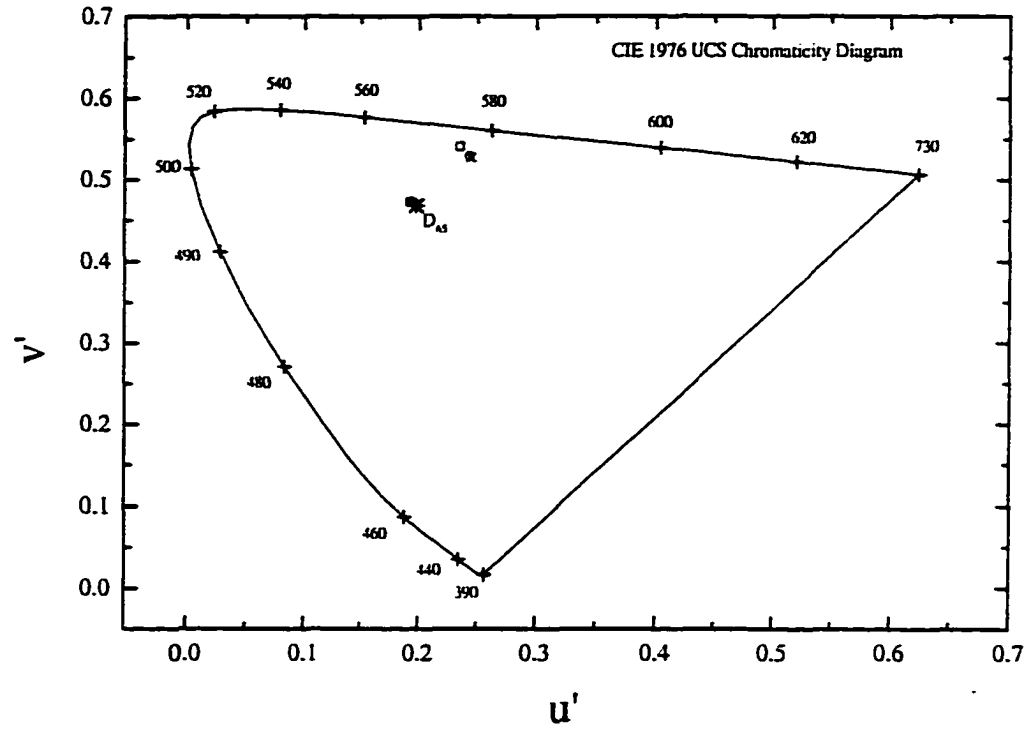

Figure 7-7 - CIE 1976 UCS chromaticity diagram showing the three computed spectra: (○) total light observed, (×) transmitted light, and (□) reflected light. For comparison, a measurement of a green thunderstorm is shown (■). The computed data were for a solar zenith angle of 85°, cloud reflectivity of 1.0, cloud transmissivity of 10^{-6}, and no solar solid angle dependance. The observation was recorded on 7 May 1995 at 2208 UTC at Mountain Park, Oklahoma.

572.6 nm whereas the reflected light had a dominant wavelength of 577.4 nm. The redder dominant wavelength is attributable to the reddened light source of the sun at a solar zenith angle of 85°. This exercise has shown that, even using a realistic light source from the ground and a perfectly reflecting cloud, the contributions of the reflected light are small and have little effect on the appearance of the green light in thunderstorms. To

further build the case against ground reflections, several examples of observational data are offered.

7.3 Observational Data

Since it was a simple matter to make some relevant quantitative observations for comparison, we recorded spectra of ground cover in the vicinities of green and nongreen thunderstorms. All of the measurements we made of the ground were at the ground. Therefore, the data we collected was not representative of the entire surface beneath the storm but, rather, a point measurement at our observation position. This does not

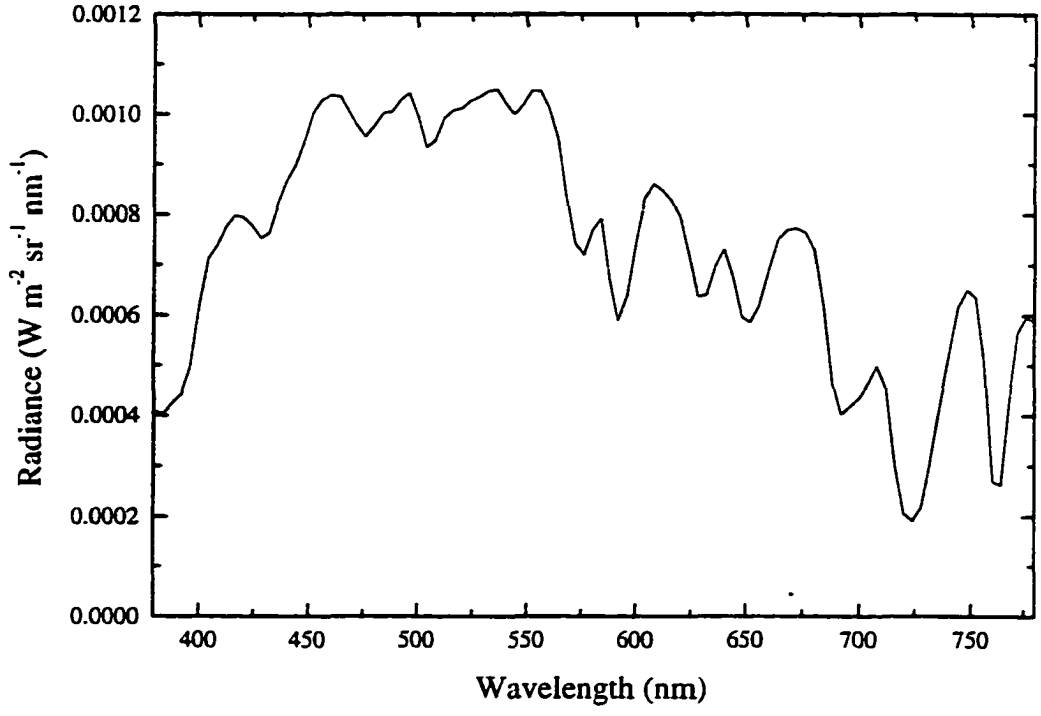

Figure 7-8 - Spectrum of a green thunderstorm recorded on 7 May 1995 at 2231 UTC 16 km east-southeast of Mountain Park, Oklahoma. The view is to the north.

invalidate our argument. For instance, we recorded a spectrum, Figure 7-4 of light reflected by the foliage beneath the approaching storm. This spectrum was chosen as a best case example of a green surface beneath the storm as it consisted of young growing wheat brightly illuminated by sunlight passing through a thin overcast to the southeast. In actuality, the ground beneath the entire storm was more than this; it was a mixture of green fields, plowed fields, and mixed residential and commercial property. Any of the nongreen surface color would certainly not contribute to any green coloration of the clouds if the ground reflection theory were correct. Let us, for a best case example,

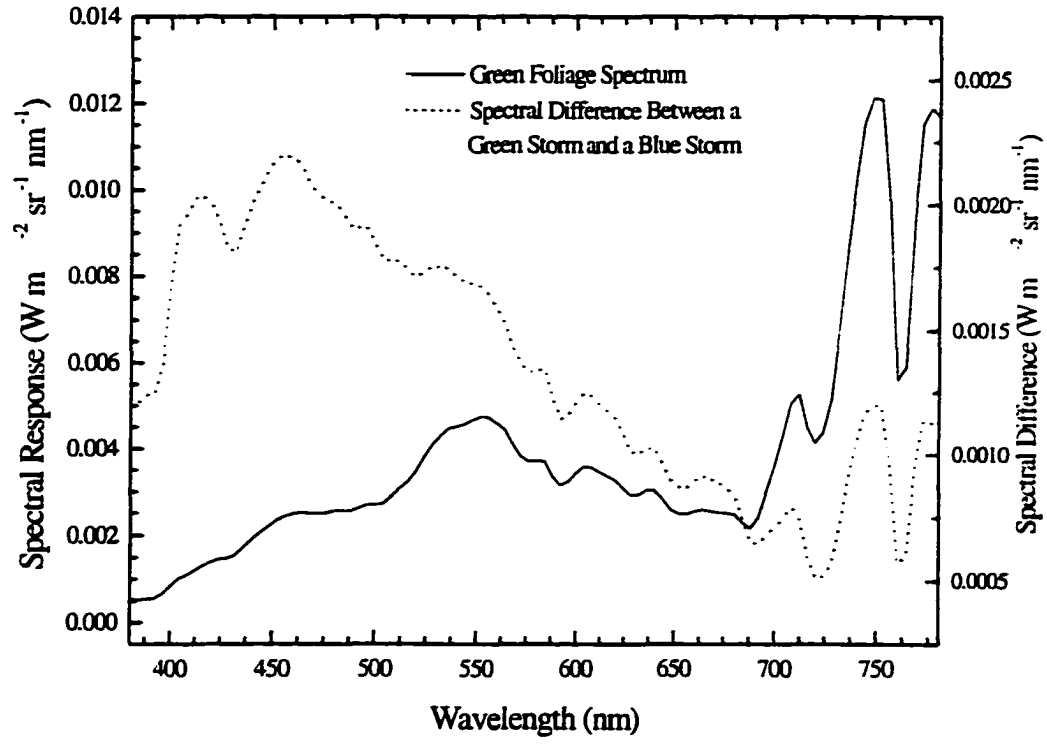

Figure 7-9 - A comparison of the spectrum of foliage underneath a green thunderstorm (solid) to a difference spectrum derived from subtracting a green storm spectrum from a blue thunderstorm spectrum (dotted). The peak in the difference spectrum does not match the peak in the foliage spectrum.

consider the entire surface beneath the storm to be that represented by this green surface spectrum. If the dominant wavelength of the thunderstorm, when it was green, was approximately that of the ground, we could then argue that light from the ground was a possible contributor to the green coloration of some storms. This was not found in our data. The peak in the recorded spectrum of the ground (neglecting the strong near infrared signal) occurred at 552 nm and the dominant wavelength was 572.6 nm. Both agree with the subjective observation of the wheat color, yellow-green. A spectrum of a green thunderstorm (Fig. 7-8) was recorded less than a half hour later from a position approximately 16 km to the southeast of the location where the foliage spectrum was recorded. By the time the green storm spectrum was recorded, the storm had moved into a position near the site of the green foliage spectrum.

A combined plot of the green foliage spectrum with a difference spectrum between a blue-colored storm and a green-colored storm is shown in Fig. 7-9. The spectrum of the blue colored storm was recorded at 2206 UTC in Mountain Park, OK. The green colored storm was recorded at 2232 UTC approximately 16 km to the east-southeast of Mountain Park, OK. The difference spectrum shows a maximum in the spectral response at the shorter wavelengths, not in the wavelengths representative of the green surface. The peak in the difference spectrum is at 456 nm. If ground reflection, in the ideal case of a carpet of green under the cloud, were the cause of the green color in this case we would expect the difference spectrum to be at a maximum near 550 nm, at the maximum of the ground reflection curve.

There is no evidence in the difference spectrum indicating any influence from the ground, green or otherwise. With this one observation we cannot rule out the possibility that, in some cases, reflection of light by vegetation may be important, but it does not seem to be the cause for the shift toward the green in this case. Furthermore, Bohren and Fraser (1993) cite reports of green thunderstorms over ground that was definitely not green. Clearly, reflection by green ground is not necessary for a thunderstorm to appear to be green.

7.4 Ground Reflection Summary

We have attacked the problem of ground reflection from three different perspectives. The first was a simple radiance argument that resulted in a ratio of the observed radiance to the incident radiance. By including a bulk reflectance for the ground ($R_g = 0.2$) and the cloud ($R_c = 1.0$) the resulting ratio of observed radiance to the solar radiance was only slightly larger than the transmittance of the cloud. According to this simple model, the radiance reflected from the ground increased the radiance at the observer by 20% compared to the radiance observed without reflection. This result indicated that cloud reflectance could possibly contribute to green thunderstorms.

A slightly more complex model was created to test the validity of the importance of ground reflections. The model results indicate that the radiance of the reflected light is at least an order of magnitude less than the transmitted light. Also, the most significant contributions of the reflected light occur in the near IR spectral region, a region where the human eye is insensitive to radiation. Finally, the presentation of several measurements

of the light from a green thunderstorm and the light from the ground underneath indicate that the spectral peaks of the two green lights do not coincide (except in the near IR) indicating that, in the portion of the spectrum where human color vision is operating, the effects of ground reflection are minimal in the creation of the green light in green thunderstorms.

7.5 Near Infrared Spikes

In many of the recorded spectra, there are large amplitude variations in the radiance plot beyond 700 nm compared to the rest of the spectrum. The amplitude of these variations was often 50% or more of the maximum of the entire spectrum. In other instances, the variations dominate the spectrum. We must ask ourselves several questions. First, what is the source and nature of these near-infrared (IR) spikes and what is their impact on our spectral analysis of green thunderstorms? Also, are these variations important in our visualization of green thunderstorms? And, finally, can we use these variations to indicate anything about the nature of the light being observed? We shall approach each of these questions carefully in the following sections.

7.6 Observations of Infrared Spikes

The large fluctuations in question occur for wavelengths greater than 700 nm. The term infrared spikes is used (or IR spikes) to refer to this phenomenon. Figure 7-10 shows a spectrum of the Mountain Park, OK green thunderstorm. The spectrum was recorded on 7 May 1995 looking to 320° at a greenish patch of light under the advancing

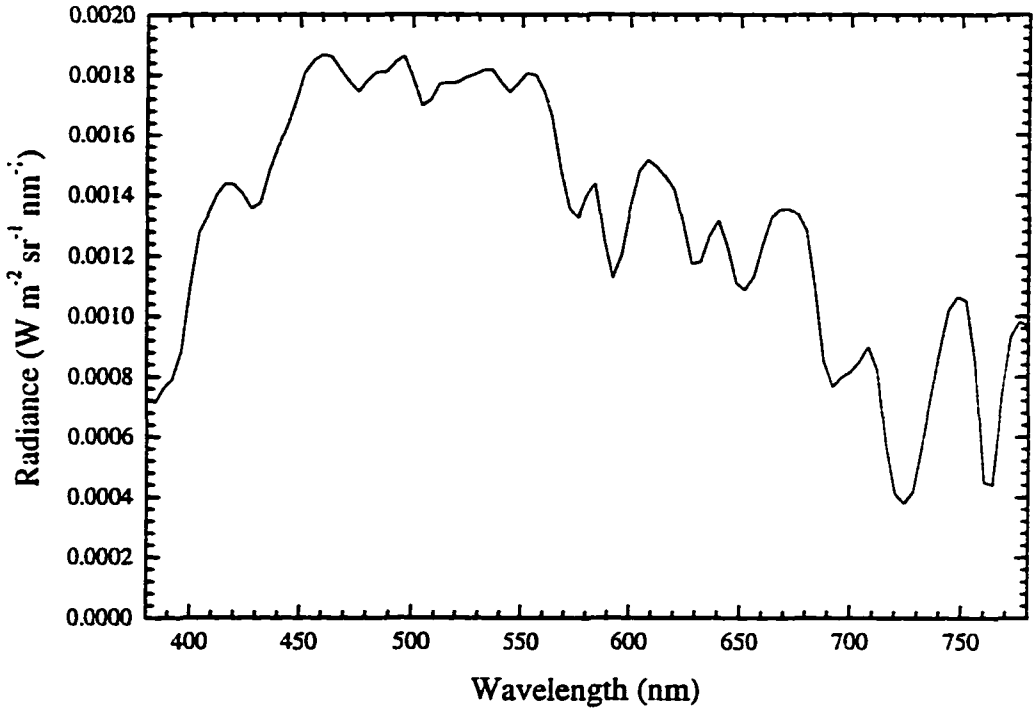

Figure 7-10 - Spectrum of a green thunderstorm. Recorded on 7 May 1995 at 2212 UTC in Mountain Park, Oklahoma. This spectrum was recorded 19 minutes earlier than the spectrum shown in Fig. 7-9.

gust front. The spectrum peaks at 460 nm, has a dominant wavelength of 535.5 nm, and has a purity of 2.2%. The spectral fluctuations for wavelengths greater than 700 nm have an amplitude of over 50% of the peak amplitude of the spectrum. For comparison, a second example is shown in Fig. 7-11. The spectrum was recorded on 25 May 1996, 18 km east of Miami, TX. The spectrum peaks at 556 nm, has a dominant wavelength of 572.3 nm, and has a purity of 22.5%. In this case the IR spikes (776 nm) attain an amplitude of 84.5% of the peak spectrum. A final example shows the IR spikes dominating the spectrum. Fig 7-4 shows a spectrum of young, growing wheat in a field

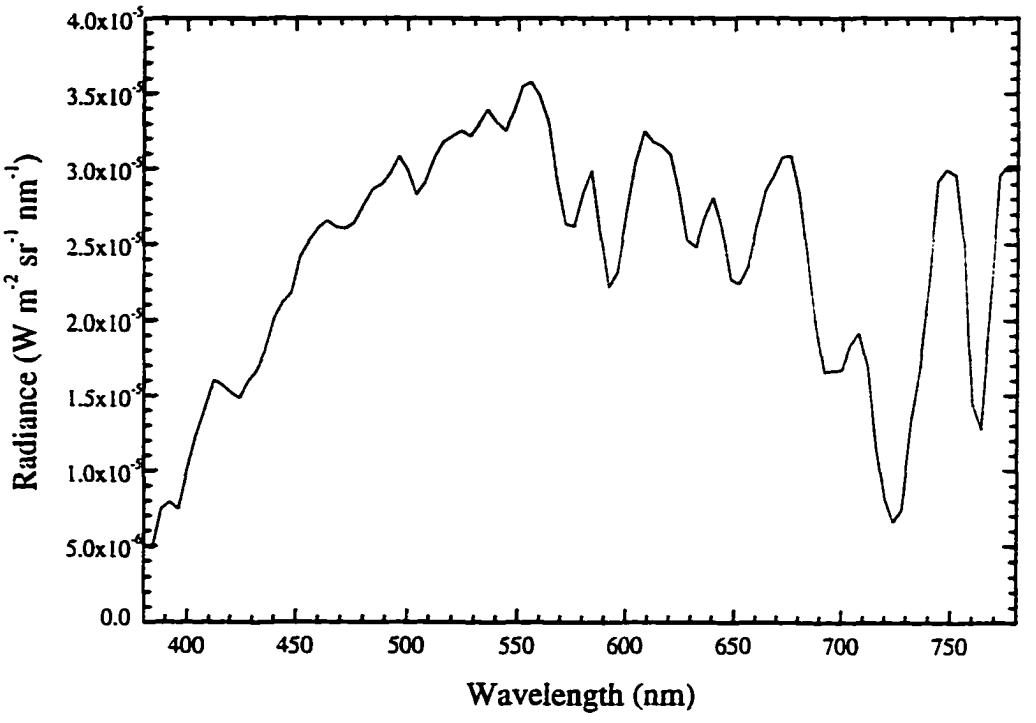

Figure 7-11 - Spectrum of a green thunderstorm. Recorded on 25 May 1996 at 0002 UTC 18 km east of Miami, Texas.

located just north of Mountain Park, OK. The spectrum was recorded on 7 May 1995 looking to the northwest at 2208 UTC. The foliage appeared yellow-green in color and the calculated dominant wavelength of 572 nm supports this. The amplitude of the IR spikes is more than double that of the central peak located at 552 nm. From this spectrum, and many other similar ones, it appears that the primary source of the IR spikes is growing plants.

7.7 Source of IR Spikes

7.7.1 Instrumentation Effects

Before taking measurements to explain the source of the IR spikes in the spectra, we first check to see if the instrument is causing this phenomenon. Any instrument-caused IR spikes would show up in every spectrum recorded by the instrument. Figure 6-2 shows a solar spectrum recorded by the Solar Energy Research Institute (Riordan *et al.* 1990) using an instrument different from the PR®-650. Their results indicate the presence of IR spikes in the solar spectrum. Since all of the thunderstorm spectra have had sunlight as the incident source, we would expect to see these spikes in our data. In order

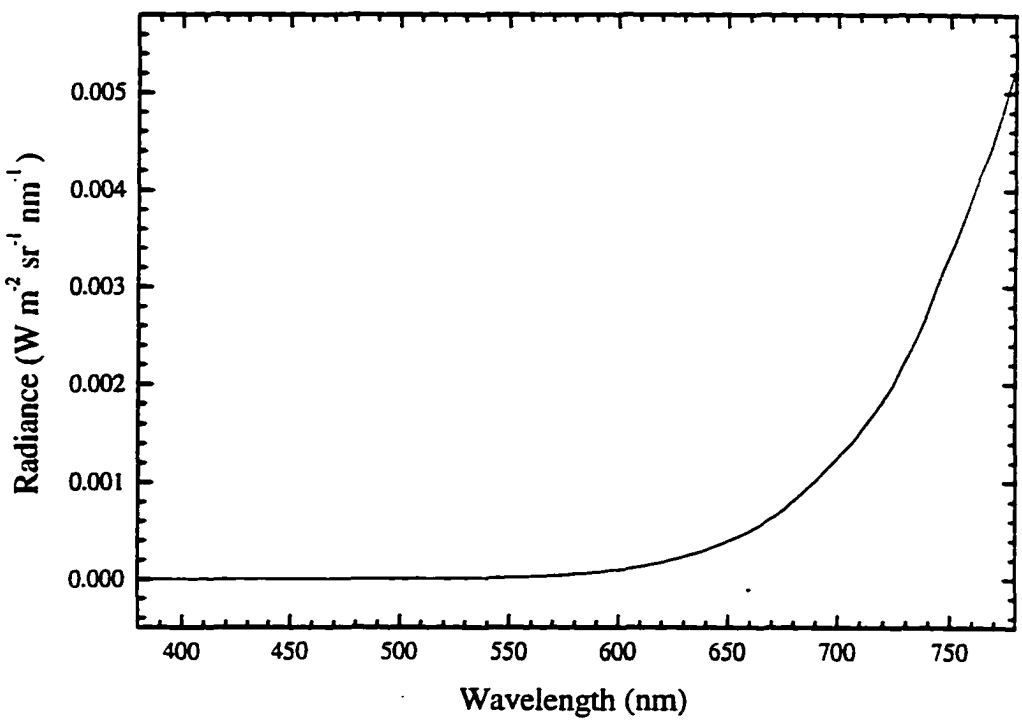

Figure 7-12 - A spectrum of the light from a red-hot stove element set to the highest temperature setting. There are no IR spikes in this spectrum.

to test the PR®-650 on a source that was not influenced by solar radiation, we made several spectral measurements of a source that approximates a blackbody, a red-hot stove element. Figure 7-12 shows the spectrum of a stove element that was set to the highest temperature setting. The curve shows a smooth increase in radiance toward the long wavelength end of the visible spectrum. There are no IR spikes in the data. From this we can conclude that the instrument does not cause or add to the IR spikes that are prevalent in the thunderstorm data. The spikes must be representative of the light being measured by the instrument.

7.7.2 The Bay and the Plains Experiment

To test the hypothesis that the IR spikes are from the foliage, we recorded a series of spectra, the first over the Chesapeake Bay, Maryland, and a second series over a field of growing wheat in Moore, Oklahoma. The spectra were recorded looking at the horizon then increasing in elevation angle until the final spectrum was recorded of the zenith. We then computed the ratio of the radiances at 748 nm to the radiances at 412 nm. The wavelength of 748 nm was selected since it is one of the IR spikes that are observed in many of the storm spectra. The wavelength of 412 nm was selected to represent one of the peaks of a blue sky spectrum. The ratio gives an indication of the relative importance of the near IR spectral component compared to a blue component. Figure 7-13 shows a plot of the radiance ratios for both the Chesapeake Bay spectra and the Moore, Oklahoma spectra. The ratios over wheat are larger than those over the water for all elevation viewing angles although the largest difference between the curves is below 30 degrees in

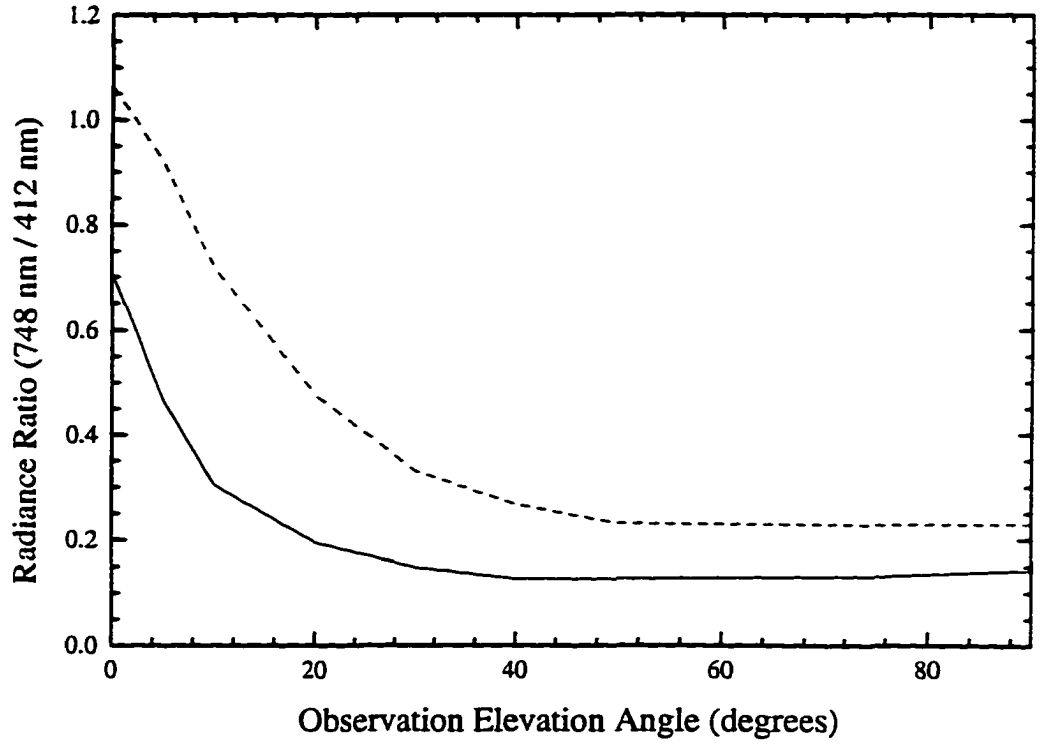

Figure 7-13 - A comparison of the ratio of 748 nm to 412 nm wavelengths at various observation angles over water and over a field of growing wheat. The spectra over the water (solid) were recorded on 17 March 1997 looking east over the Chesapeake Bay. The spectra over wheat (dashed) were recorded on 17 April 1997 in Moore, Oklahoma.

elevation viewing angle. This indicates, particularly at lower observation angles where there is a greater chance of multiple scatter, that the IR signal from the foliage is being scattered back to the observer by the sky. Although the effect is weak, it may enhance the appearance of the spikes in the green thunderstorm spectra. The next step is to check to see if this effect is enhanced by the setting of the sun.

7.8 Effect of Skylight and Solar Zenith Angle

7.8.1 Analytical Computations

Many of the spectra show an increasing presence of the IR spikes as the sun becomes lower in the sky. To check to see if there is any effect of skylight and solar zenith angle, The ratio of attenuation (due to molecular scattering) of blue to red light was computed. We used 470 nm as blue light and 700 nm as red light. The 470 nm was chosen since it was near a radiance maximum in the spectrum of sunlight and the 700 nm was chosen as it was a maximum between several near-IR minima. The equation used for the ratio was:

$$ratio = e^{-\frac{0.001\,h}{\cos\theta}(\lambda_r^{-4}-\lambda_b^{-4})} \qquad 7\text{-}10$$

where h is the scale height (~8 km), θ is the solar zenith angle, λ_r=700 nm, and λ_b=470 nm. Figure 7-14 shows that the attenuation ratio is nearly constant until the solar zenith angle is greater than about 60°. Still the effect is small until the solar zenith angle is greater than 80°.

7.8.2 Setting Sun Experiment

Some measurements were made of the MacBeth Color Checker chart "white" square at fifteen minute intervals (except near sunset) beginning at 1615 CDT. Exceptions to this timing occur near sunset. The chart was oriented such that the normal to the chart was approximately parallel to the "rays of the sun." Figure 7-15 shows some

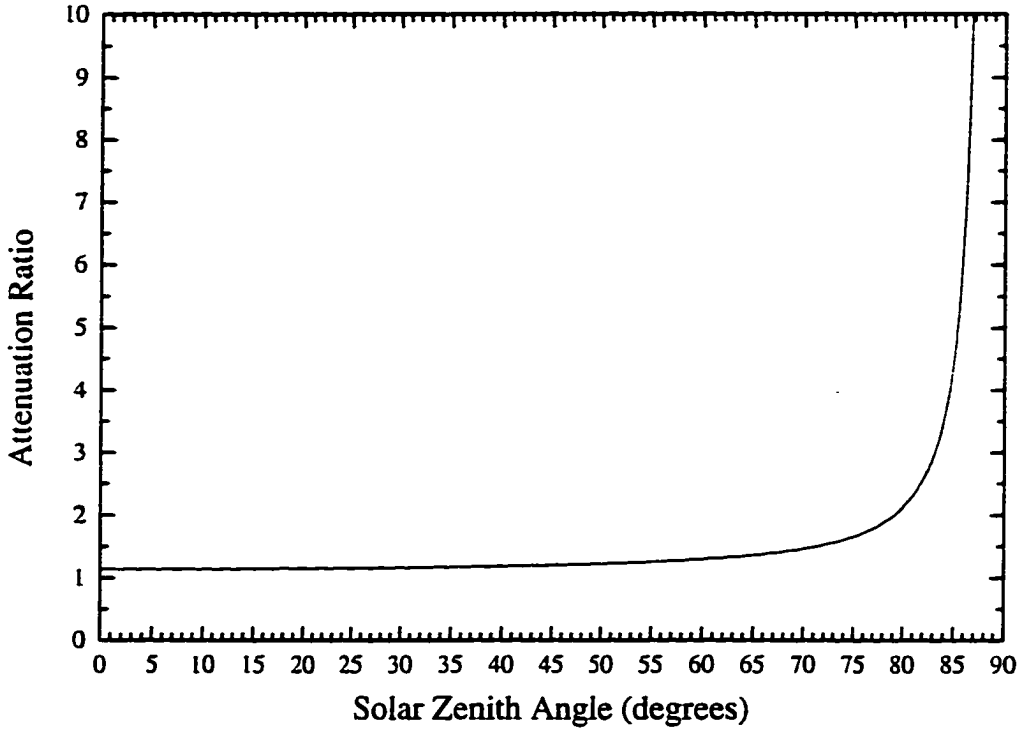

Figure 7-14 - Computed attenuation ratio of blue (470 nm) light to red (700 nm) light in a molecular atmosphere.

selected spectra. The solar zenith angle was determined by using the time of day and Oklahoma City location in the SkyGlobe astronomy computer program.

As expected, the overall radiance decreases as the solar zenith angle increases. Furthermore, the reduction in the blue part of the spectrum is greater, with increasing solar zenith angle, than the reduction in the red part of the spectrum. The result is an increase in the relative amplitude of the IR spikes seen in many low light spectra. The minima in the near-IR spectra are the result of atmospheric absorption, primarily by molecular oxygen and water vapor.

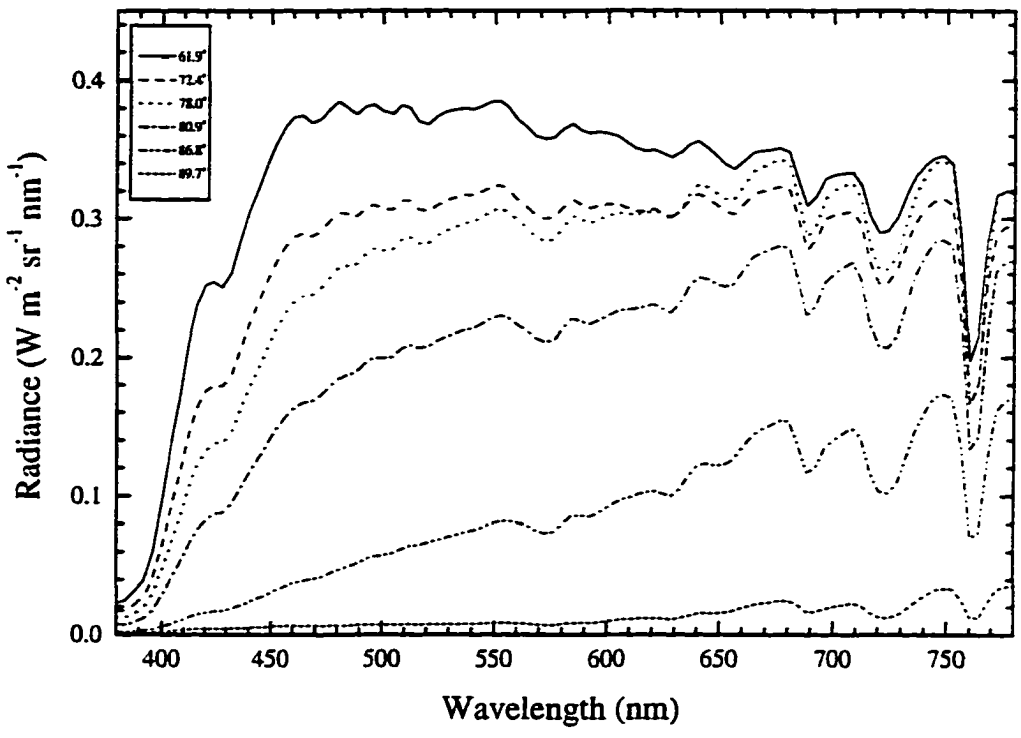

Figure 7-15 - The spectra of solar radiation reflected off the MacBeth "White" square on the MacBeth Color Checker Chart at various solar zenith angels. The spectra were recorded on 18 October 1996 in Moore, Oklahoma. There were no clouds in the sky during the time the spectra were recorded. Solar zenith angles are indicated in the legend.

Figure 7-16 shows a difference spectrum between the 1615 CDT measurement and the 1830 CDT measurement. The largest difference in radiance is in the blue portion of the spectrum, as expected. The small spike near 750 nm is probably the result of a slight shift in the spectral position of one of the IR spikes. There is also a slight shift in the minimum near 755 nm toward the IR with increasing solar zenith angle. The ratio of the attenuation (blue to red) between the 1615 CDT and 1830 CDT curves is approximately 1.72, a value lower than predicted by the simple model. The reduction in

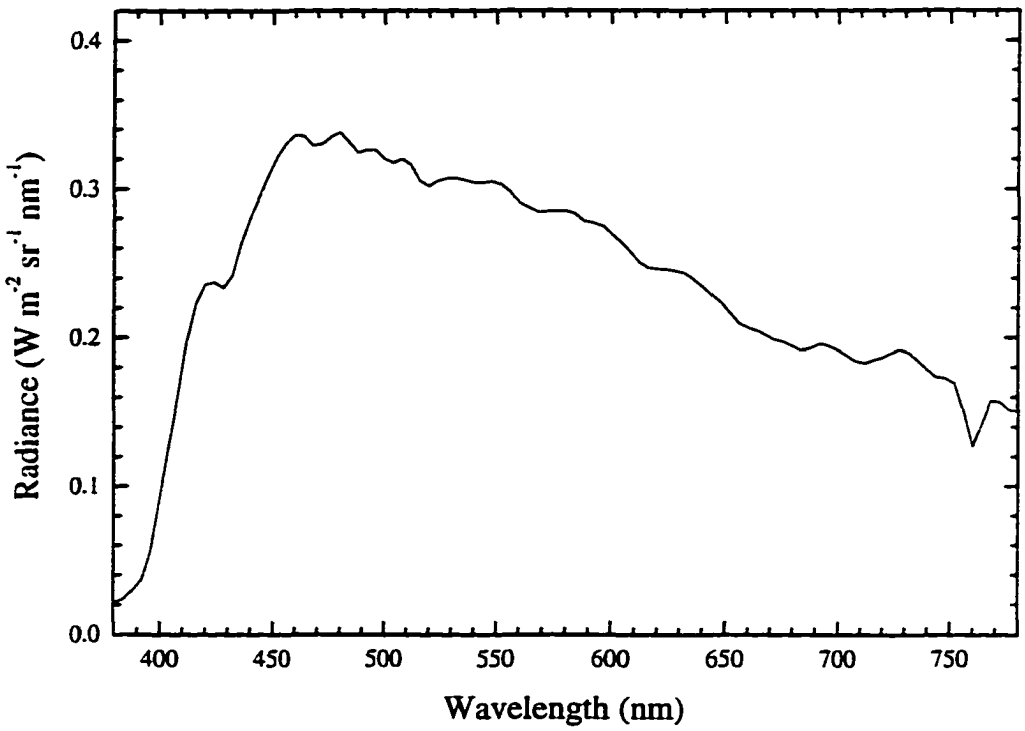

Figure 7-16 - Difference spectrum between spectra recorded at solar zenith angles of 61.9° and 86.8°. The spectra were recorded on 18 October 1996 in Moore, Oklahoma. There were no clouds in the sky during the time the spectra were recorded.

the blue portion of the spectrum leaves the IR spikes as the predominant feature in many of the measurements.

7.8.3 Ground Reflection Indicator

We have seen that the presence of foliage greatly enhances the likelihood that the IR spikes will be large or even dominate the spectrum particularly as the sun sets. Ground reflection has been put forth as a possible mechanism for the creation of the green light in some thunderstorms. In some cases where the clouds are exceedingly close to the

ground, the clouds may reflect some light from the ground.

To explain why this is important we must first discuss the reflection of light by clouds. Clouds essentially reflect light of all wavelengths equally because of multiple scattering. In a single-scattering environment, with large droplets, the droplets will scatter all wavelengths approximately equally. However, water weakly absorbs red light, so we would expect the reflected light to be slightly blue in color. By looking at puffy cumulus clouds we see that this is not the case; we see white. To explain this we invoke the principle of multiple scattering. When light enters an optically thick cloud it gets scattered by the droplets inside the cloud. The majority of the radiation is scattered from droplet to droplet and eventually reemerges from the cloud. Essentially equal quantities of the various wavelengths of white light reemerge from the cloud, hence we see white. As the sun sets, the color of clouds can change from white to a reddish color as the light illuminating the clouds becomes redder. Similarly, one often observes an orange glow from city lights reflecting off low clouds as they pass over a city at night. The color of the city lights is not changed appreciably on reflection by the clouds for the same reason that we see clouds as white. In each of these cases, the source of light was extremely bright compared to the surrounding illumination allowing the cloud to take on the color of that illumination. In the case of ground reflection, the light from the ground is much weaker compared to the dominating illumination. The increase in the IR signal from the clouds may be a better indicator of light being reflected by the clouds from the ground.

7.8.4 Ground Reflection Examples

Figure 7-17 shows a spectrum of a brownish looking cloud where brown is defined as a color name for the perception of dark yellow or dark orange (OSA 1953). The cloud was at the leading edge of a gust front and was the lowest cloud element in the nearby storm environment. The surrounding terrain was a mixture of plowed and planted fields and residential/light industrial land use. The brownish appearance of the clouds is not unexpected if the light was indeed reflected from the ground. The spectrum shows a rather flat curve from about 450 nm to 700 nm indicating no strong preference in color.

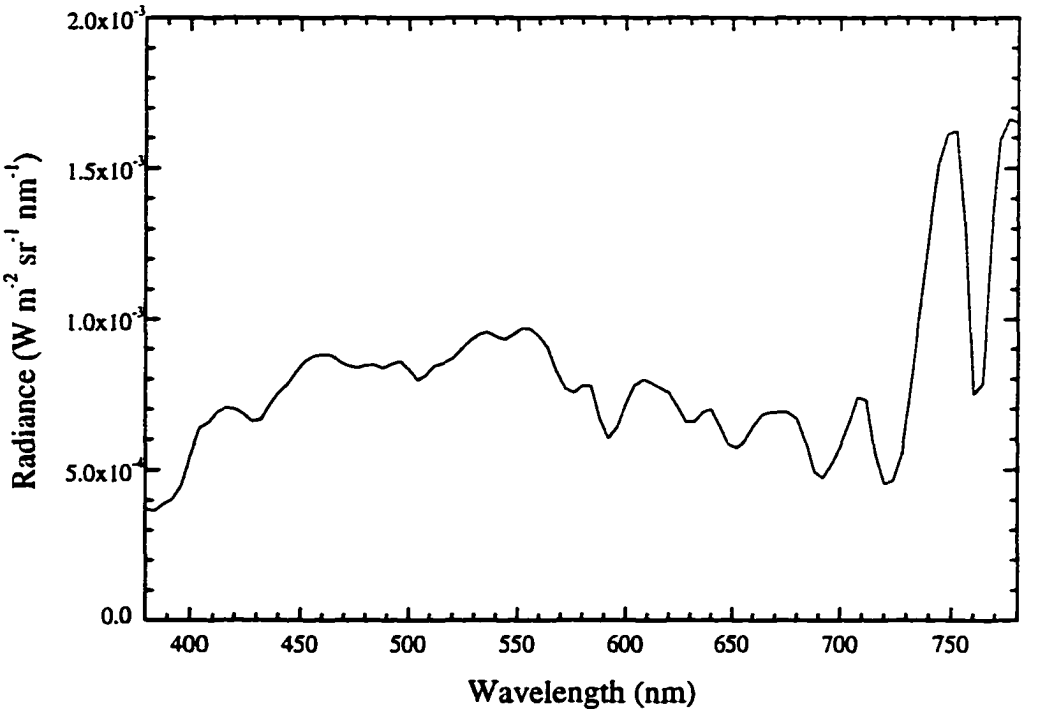

Figure 7-17 - Spectrum of a "brownish" looking cloud. Spectrum recorded on 7 May 1995 at 2232 UTC 16 km east southeast of Mountain Park, Oklahoma. The dominant wavelength is 568.2 nm and the purity is 7.6%.

The peak in the visible is near 556 nm which may give the cloud a brownish-yellow color. The dominant feature in the spectrum is the strong IR spikes that occur after 700 nm. Comparing this spectrum to Fig. 7-4, a spectrum of the surrounding foliage, we see that IR spikes occur at the same wavelengths. This suggests that the source of the IR spikes in the low gust front cloud is from the surrounding foliage.

Another example of this phenomenon is shown in Fig. 7-18. This spectrum was recorded near Rose, OK on 17 May 1995 looking to the east-northeast. This spectrum also shows a flat curve from 450 to 700 nm followed by a large IR spike. The peaks of

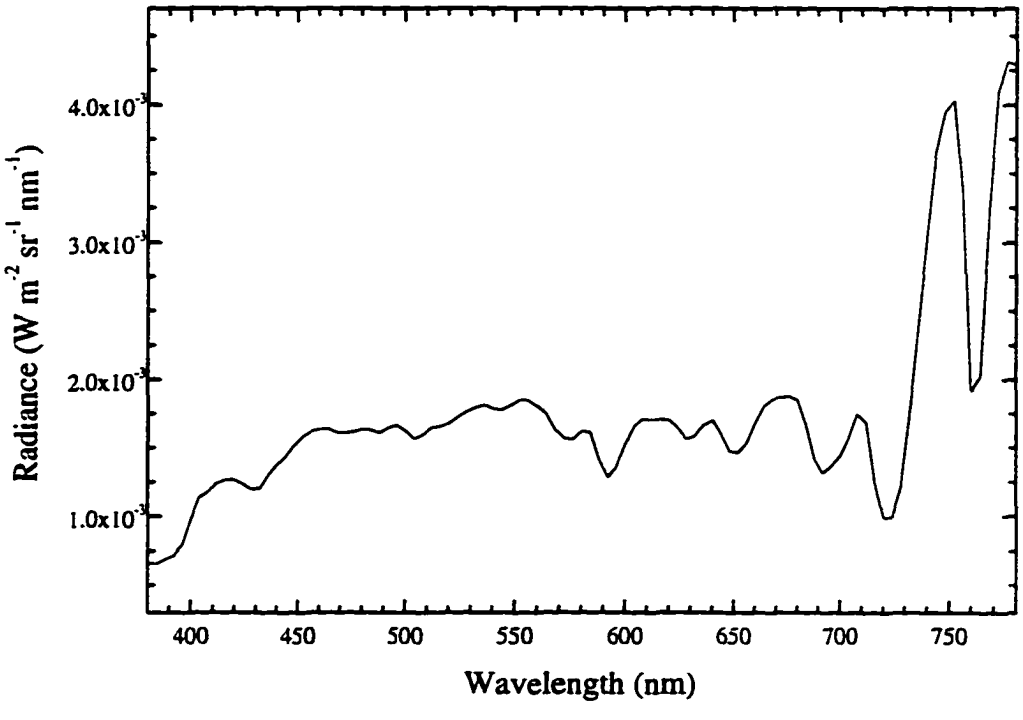

Figure 7-18 - Spectrum of a "brownish" looking cloud. Spectrum recorded on 18 May 1995 at 0011 UTC in Rose, Oklahoma. The dominant wavelength is 578 nm and the purity is 13.4%.

the IR spikes again match spikes from spectra recorded of foliage. Again, we can attribute the IR spikes to the surrounding foliage reflecting off the base of very low clouds. This is an indicator of ground reflection mechanism working; if the IR spikes dominate the spectrum of a cloud, then ground reflection is indicated.

7.8.5 Visual Effects of IR Spikes

To test whether the IR spikes influence how we see clouds, we selected three spectra that contained significant IR spikes. We computed the dominant wavelength and purity of each spectrum, a rather good method of determining quantitatively the color a normal human would perceive (see Chapter 3), and then changed the spectrum to remove the IR spikes. The first spectrum tested was of a green thunderstorm (Fig. 7-19). The spectrum shows a maximum in the wavelength band of 450-550 nm. The IR spikes are present but only amount to approximately half the amplitude of the overall peak in the spectrum. The dominant wavelength was computed to be 535.5 nm with an excitation purity of 2.2%. The spectrum was then adjusted (dotted line in Fig. 7-19) to have a constant value of the radiance at 700 nm. The recomputed dominant wavelength and purity did not change. By looking at the two spectra, we can see that the adjusted spectrum actually increased the overall radiance in the band 700-780 nm but there was no change in the colorimetric quantities.

A second example is shown in Fig. 7-20. This is another spectrum of a green thunderstorm, this one located in the Texas panhandle. The amplitude of the IR spikes is nearly 85% the amplitude of the rest of the spectrum. Any modification of this spectrum

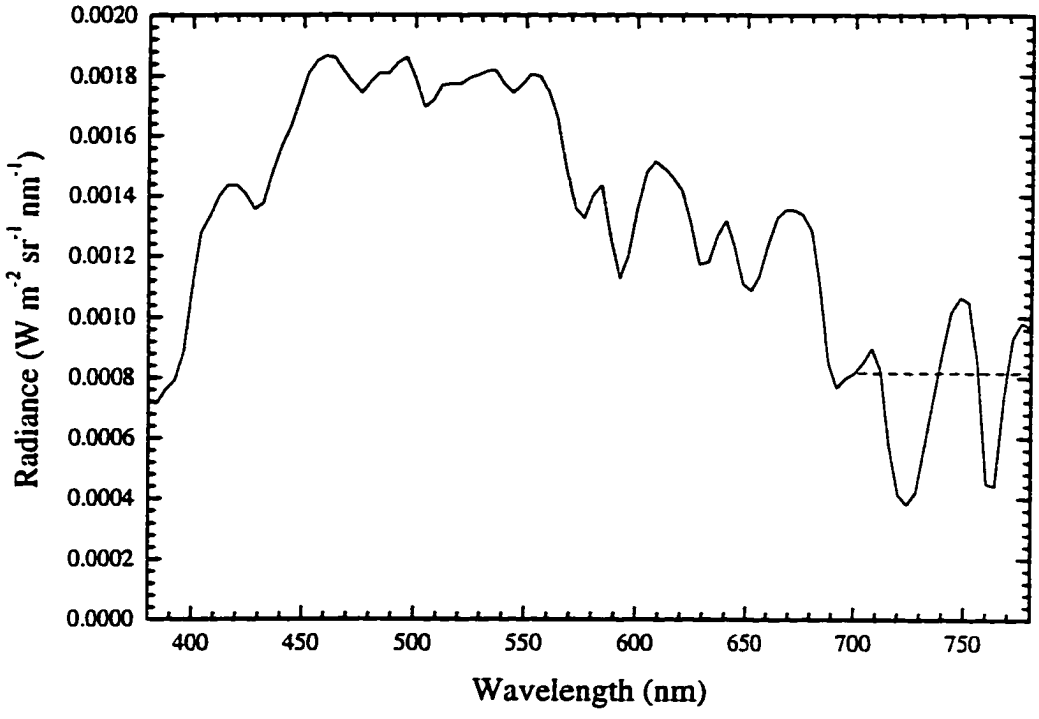

Figure 7-19 - Actual and "corrected" spectra of a green thunderstorm. Spectrum recorded on 7 May 1995 at 2212 UTC in Mountain Park, Oklahoma. The solid line is the actual spectrum, the dashed line is the corrected spectrum.

should result in greater changes than the previous example. As shown in Fig. 7-20, the adjusted spectrum is shown as being flat from 700 nm and greater. The dominant wavelength of the original spectrum was 572.3 nm with a purity of 22.5%. As in the above example, the dominant wavelength and purity of the adjusted spectrum were identical.

Neither of the above examples is convincing that removing the IR spikes does or does not cause a change in the colors a normal human would see. To definitively check the effects of removing, or at least severely reducing, the effects of the IR spikes, we look

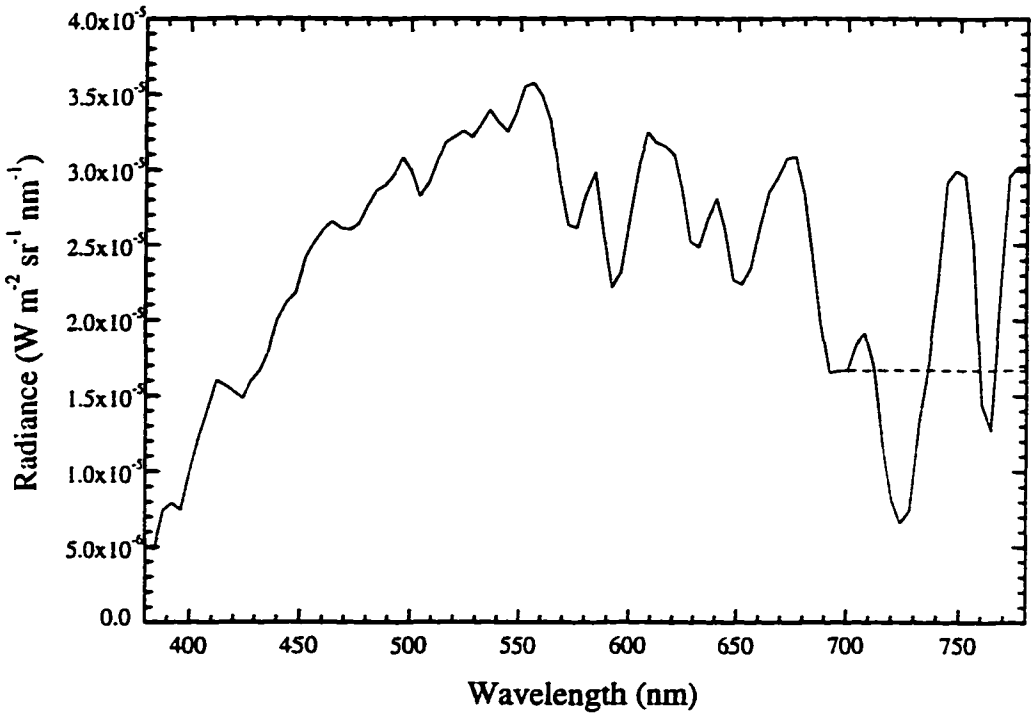

Figure 7-20 - Actual and "corrected" spectra of a green thunderstorm. Spectrum recorded on 25 May 1996 at 0002 UTC 18 km east of Miami, Texas. The solid line is the actual spectrum, the dashed line is the corrected spectrum.

at the spectrum of the young, growing foliage found under the green thunderstorm on 7 May 1995 near Mountain Park, OK. Fig. 7-21 shows the original ground spectrum and the adjusted spectrum. The adjusted spectrum was altered, as above, with the 700 nm radiance value constant for the 700-780 nm wavelength band. In this case, the IR spike, which was nearly three times the amplitude of the foliage signal, has been reduced to approximately two-thirds of the foliage signal. The dominant wavelength of the original spectrum is 572.6 nm with a purity of 35.36%. The dominant wavelength of the modified spectrum is 572.6 nm with a purity of 35.35%. The change in the purity is essentially

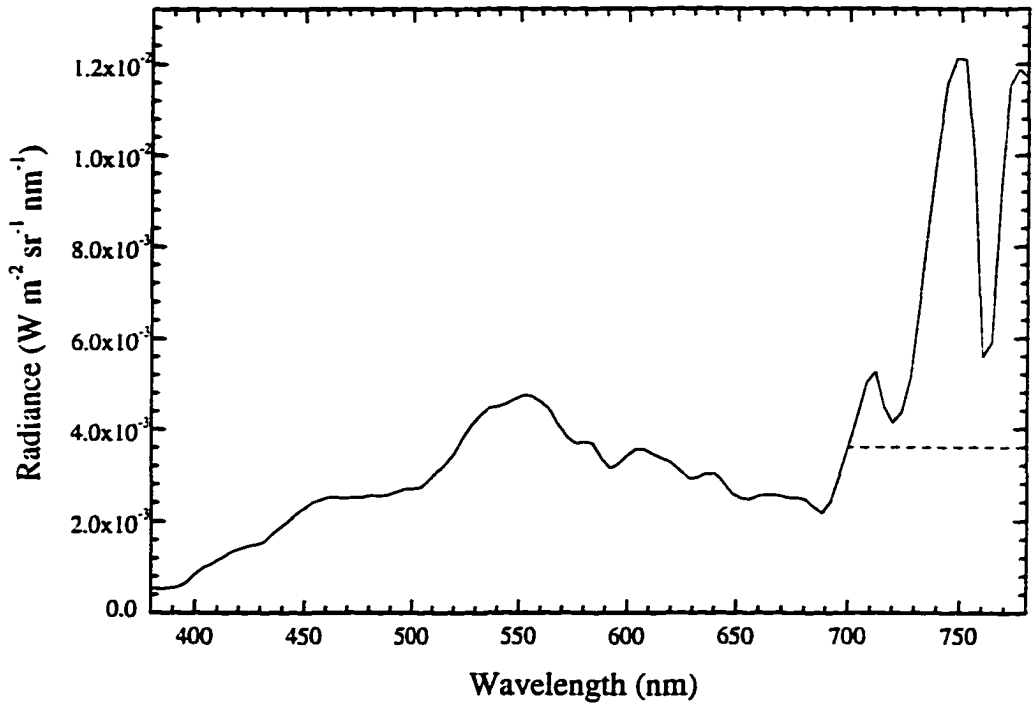

Figure 7-21 - Actual and "corrected" spectra of green foliage beneath a green thunderstorm. Spectrum recorded on 7 May 1995 at 2208 UTC in Mountain Park, Oklahoma. The solid line is the actual spectrum, the dashed line is the corrected spectrum.

imperceptible to a human and the two spectra would appear the same color. As shown above, the absence or presence of this strong IR signal does little to change the color of the clouds to an observer. Any reflection that can be seen is usually a very faint brown superimposed on the typical gray/blue color of the cloud. We have shown that, in the visible part of the spectrum, that light from the ground, green or otherwise, plays a small role in the color of the clouds.

Chapter 8: The Bohren Theory and Why Thunderstorms are Green

Introduction

In the development of the optical model used to verify the Bohren green thunderstorm theory, we start from first principles. We take the cloud, melt any ice, and squeeze all of the water into an infinite plane-parallel slab of adjustable thickness. Water has a spectral absorption curve (see Fig. 8-2) where the absorption is the strongest in the red portion of the visible spectrum. Bohren (Bohren and Fraser 1993) speculates that the predominately red light from a setting sun passes through water, acting as a filter, to produce green light. This only works if the incident light has some blue or green component in it. We assume that the scattering of light in the atmosphere is by molecules only. The molecules scatter blue light more than red light but not all of the blue (or green) light is removed from the incident solar radiation.

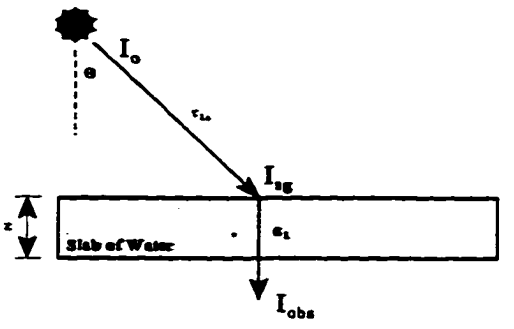

Figure 8-1 - Schematic of the path of light simulated by the slab model. The symbols are described in the text.

8.1 Theoretical Development

Figure 8-1 shows the path of the radiation for this model. Light from the

sun, at solar zenith angle θ, is perfectly transmitted into the water at an angle normal to the smooth surface of the water. Another way to visualize this process is that the slab remains positioned such that its normal is always oriented at the solar zenith angle and there is no reflection at the interface The slab has a thickness of z with an absorption coefficient of α_λ. For simplicity, the light is not scattered by the water. As in the analysis of the Fraser model we assume an atmosphere that consists of molecules only. So we use the same optical depth τ_λ (from Chapter 6) that varies with wavelength

$$\tau_{\lambda_s} = \frac{s_\lambda \, h}{\cos\theta} \qquad 8\text{-}1$$

where s_λ is the extinction coefficient of the atmosphere and h is the scale height of the atmosphere (~ 8 km). Again, following Kodratyev (1969) and Fraser (1978) we shall use the result

$$\tau_{\lambda_s} = \frac{0.001 \; h \; \lambda^{-4}}{\cos\theta}. \qquad 8\text{-}2$$

The radiation received at the top of the slab of water is

$$I_{sg} = I_o \, e^{-\tau_{\lambda s}}. \qquad 8\text{-}3$$

The radiance is exponentially attenuated as the wave traverses the water slab (Bohren and Huffman 1983) so the radiance received by the observer is

$$I_{obs} = I_{sg} \, e^{-\alpha_\lambda z} = I_o \, e^{-\tau_{\lambda s}} \, e^{-\alpha_\lambda z} \qquad 8\text{-}4$$

where α_λ, with units m^{-1}, is the absorption coefficient of pure water, and z is the thickness (in meters) of the slab. The inverse of the absorption coefficient represents the thickness of the material that the light must traverse in order to be attenuated by a factor of 1/e. As

shown in the figure, we do not need to divide I_{obs} by the cosine of the solar zenith angle since we are interested in the effects of the depth of the water independent of the solar zenith angle effects. The radiance measurements are always assumed to be along the normal pointing at the illuminating source.

8.1.1 Water is Blue

We first discuss briefly why water is a blue substance. Water owes its intrinsic blueness to selective absorption in the red part of the visible spectrum. Figure 8-2 shows a curve of the absorption of pure liquid water. The absorbed photons promote transitions to

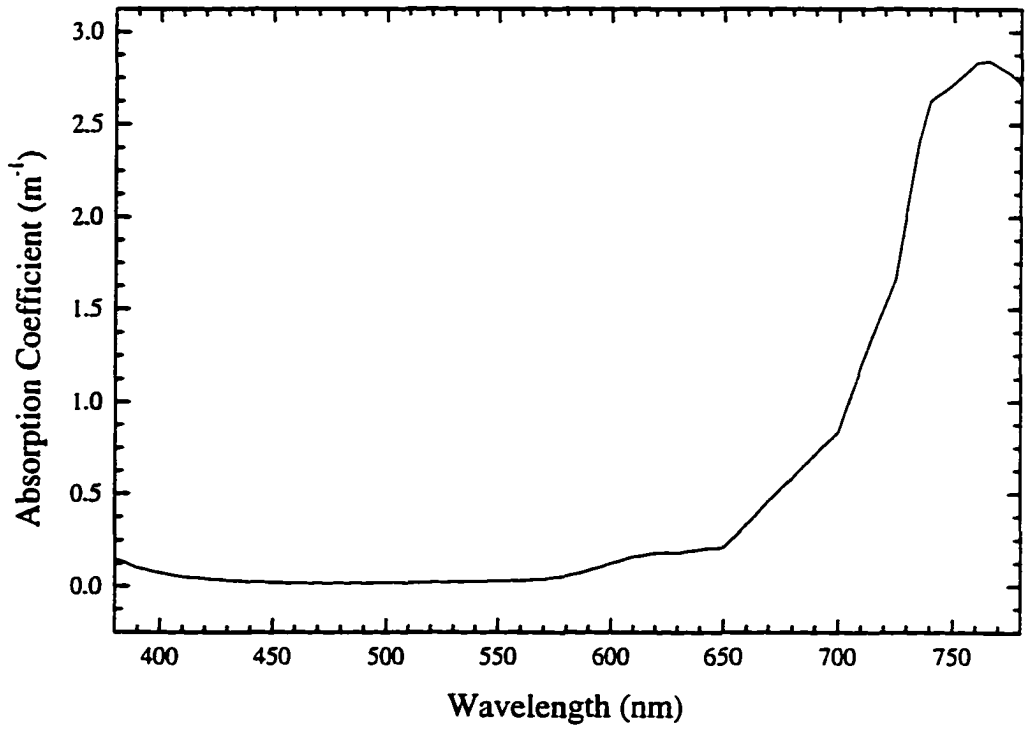

Figure 8-2 - Absorption of radiation by pure liquid water (Smithsonian Institution 1949).

high overtone and combination states of the nuclear motions of the molecule (highly excited vibrations). According to Braun and Smirnov (1993), the intrinsic blueness of water is the only known example from nature in which color results from vibrational transitions.

A molecule may absorb energy by the molecule undergoing an energy transition from one quantum state to another. Absorption may occur through rotational, vibrational, or electronic transitions. Of interest to us are the vibrational transitions in a water molecule. A free water molecule has three basic vibration modes, designated ν_1, ν_2, and ν_3. In water vapor, these occur at 0.45, 0.20, and 0.47 eV respectively. Vibrations usually can have overtones, that is harmonics such as $2\nu_1$, and also combinations, such as $\nu_2+\nu_3$ or $2\nu_1+\nu_3$.

The absorption for wavelengths shorter than 700 nm contributes to the color of water. For the measured absorption at 660 nm, the transmission through 3 m of water is 44 %, a loss of red intensity that should be perceptible by humans (see Section 8.1.2). Water is unique among the molecules of nature as it has a high concentration of OH bonds. Most important, the OH symmetric (ν_1) and antisymmetric (ν_3) vibrational stretching fundamentals are at high enough energy so that a four quantum overtone transition ($\nu_1+3\nu_3$) occurs at 698 nm (14 318.77 cm^{-1}), just at the red edge of the visible spectrum (Braun and Smirnov 1993).

8.1.2 Numerical Simulations

Simulations were run, using the previous mathematical framework, to test the effects of the absorptive properties of water with sunlight at various solar zenith angles. A realistic irradiance, measured at the surface at Cape Canaveral, Florida on 4 June 1987 at 1531 UTC (Fig. 6-2) is used for the incident radiation.

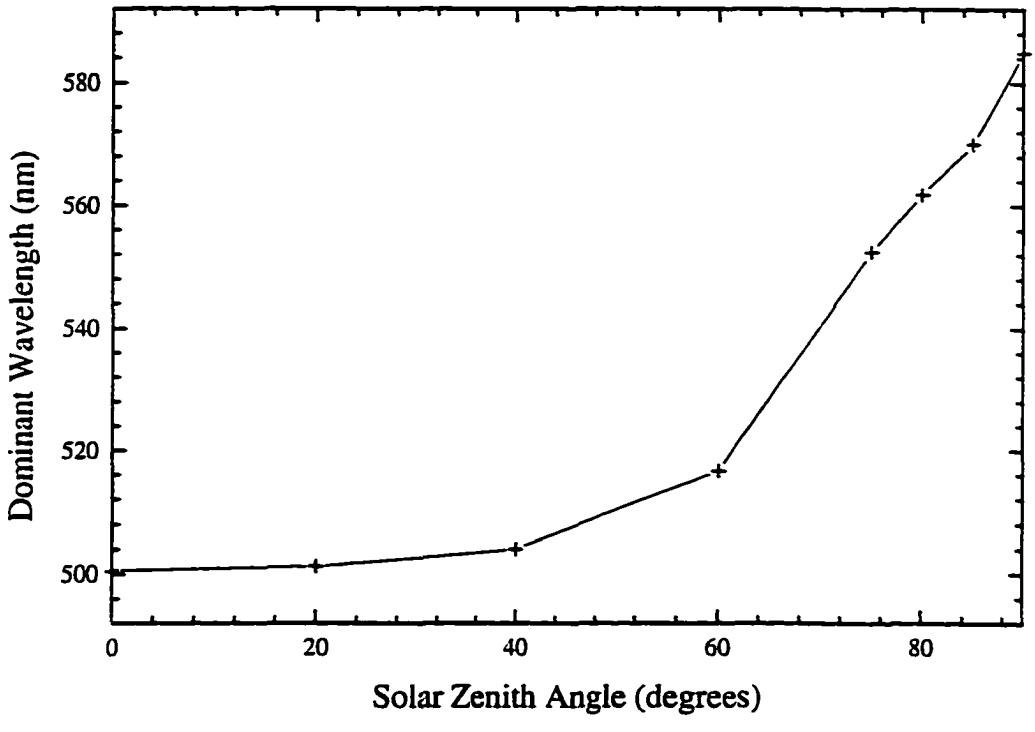

Figure 8-3 - Relationship between the solar zenith angle of the incident radiation and the dominant wavelength of the resultant illumination. The slab depth is 5 m.

The first calculation was designed to test to see how the dominant wavelength varied as the solar zenith angle and the total depth of the slab of water were changed. Figure 8-3 shows the relationship between the dominant wavelength and solar zenith

angle for a slab depth of 5 m. The figure shows that the dominant wavelength increases with increasing solar zenith angle. This is expected since, as the sun sets, more blue light is scattered from the incident beam, leaving a redder light source. Although water absorbs primarily in the longer wavelengths, there is still some absorption in the short and medium wavelengths. Figure 8-4 shows a similar result with the water thickness of 10 m. The dominant wavelengths are lower at each measurement point than for the 5 m thickness since more red light is absorbed through the increased thickness of water. As with the 5 m curve, the dominant wavelength increases with solar zenith angle. At large

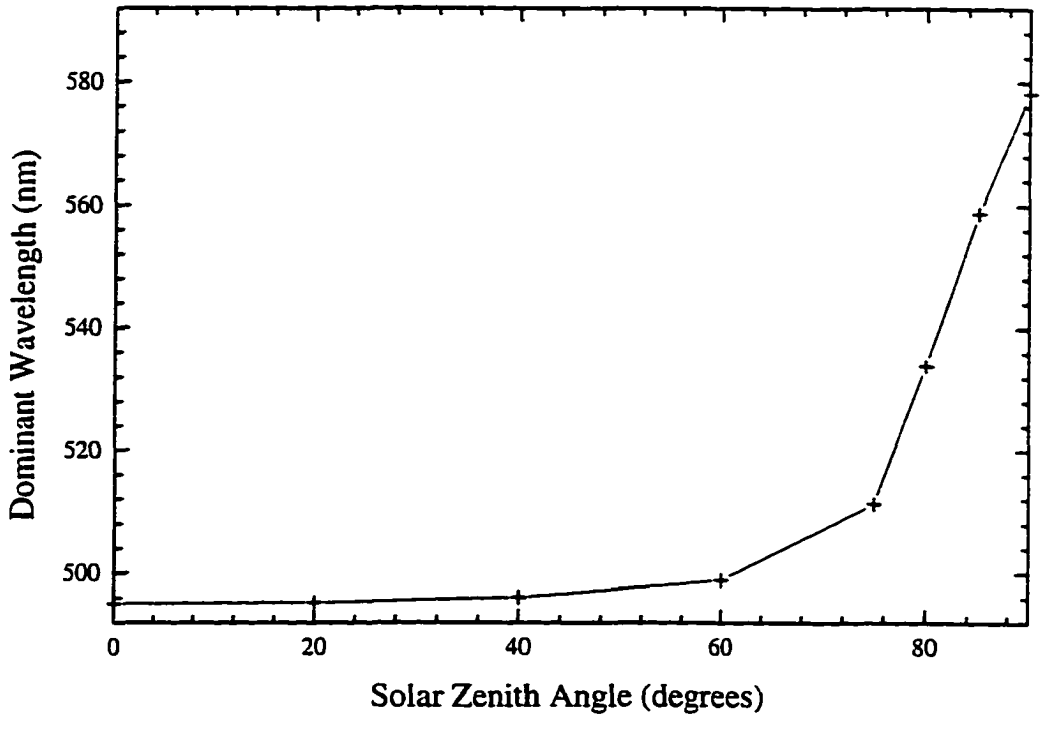

Figure 8-4 - Relationship between the solar zenith angle of the incident radiation and the dominant wavelength of the resultant illumination. The slab depth is 10 m.

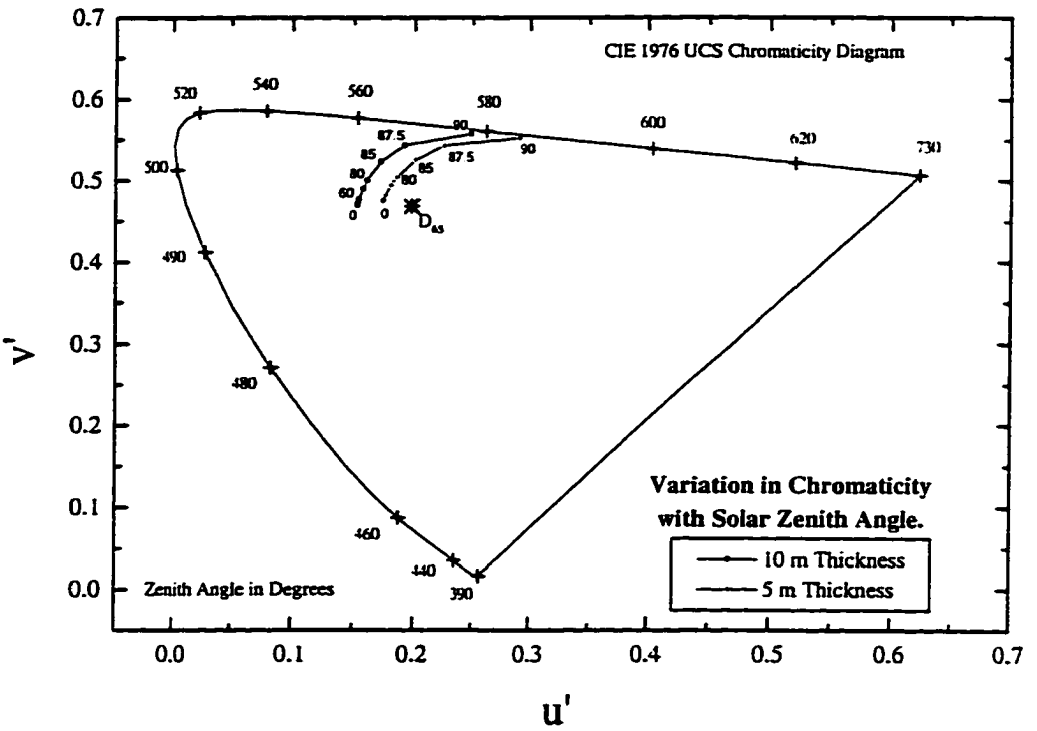

Figure 8-5 - CIE 1976 UCS chromaticity diagram showing the variation in chromaticity with a change in solar zenith angle. Solid circles are for a slab of 10 m in depth. Plus signs are for a slab of 5 m in depth. The zenith angle is in degrees.

solar zenith angles, more of the blue light is scattered out of the incident beam. Hence, the dominant wavelength increases.

Another way to visualize the trend in the color of the perceived light is by the use of the CIE chromaticity diagram. Since dominant wavelengths are dependent on the selection of a particular achromatic point, the plotting of individual chromaticity coordinates can clearly show the trend in the color of the light without resorting to a numerical value. Figure 8-5 shows the variation in chromaticity with solar zenith angle for slab thicknesses of five and ten meters. Two characteristics of the set of curves are

easily identified. The first is the trend toward redder and purer colors as the solar zenith angle is increased. Both curves show a smooth arc starting near the achromatic point (D_{65}) and approaching the spectrum locus near 580 nm. Although a setting sun is usually regarded as red, these curves indicate that the absorption in the red by the liquid water slab has changed the appearance of the sunlight to a yellow color. The second characteristic is that the 5 m curve is closer to the achromatic point than the 10 m curve although both curves eventually get extremely close to the spectrum locus of pure colors. Since the absorption is stronger through 10 m of water than 5 m and the absorption of

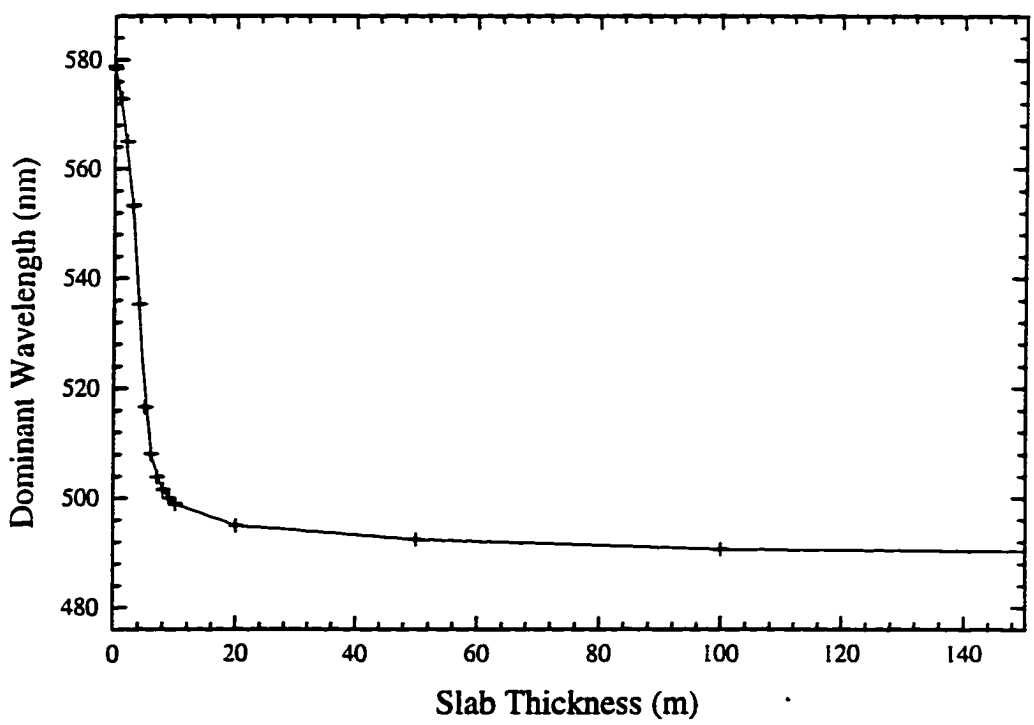

Figure 8-6 - The variation in dominant wavelength of the simulated light from the bottom of a slab of water of various thickness. The solar zenith angle of the incident radiation is 60°.

light by water is not achromatic, the shape of the resulting spectral curve will become less flat, or less white, resulting in a perception of more vivid colors.

The next set of calculations was to determine the relationship between the dominant wavelength and slab thickness for a given solar zenith angle. Figure 8-6 shows a curve of the variation in the dominant wavelength of the resulting light after passing through a slab of variable thickness. The dominant wavelength rapidly shifts from a yellow (near 580 nm) to a bluish green (near 490 nm) with increasing depth of the slab. Beyond a depth of 20 m, the dominant wavelength change is small, but the purity

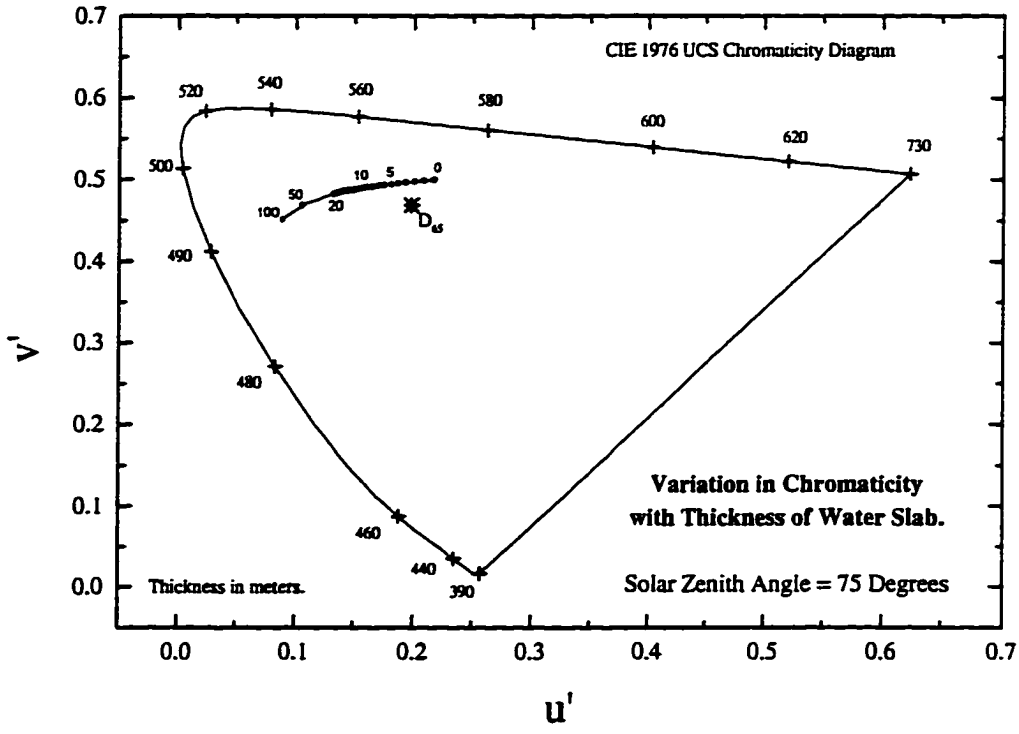

Figure 8-7 - CIE 1976 UCS chromaticity diagram indicating the variation in chromaticity of the light passing through the slab with a change in the thickness of the slab. The solar zenith angle is 75° and the thicknesses indicated are in meters.

increases. As before, the relationship between the thickness of the water slab and the color of the emitted light can be shown on a CIE chromaticity diagram. Figure 8-7 shows a the variation in chromaticity of light passing through a slab of varying thickness for a solar zenith angle of 75°. At zero thickness, the light is that of the sun at 75° solar zenith angle, a yellow-white color. As the slab increases in thickness, more of the red color is absorbed from the incident light and the curve moves toward the blue part of the spectrum ending in a color that is normally associated with blue green. Because of the absorption by water, photographers have to be careful about the selection of film and artificial lighting when shooting under water. Photographs taken without artificial lighting will have a predominant blue-green cast at depths greater than five meters.

Figure 8-8 shows a series of (computed) spectra that are representative of the light passing through slabs of various thicknesses. The red light, particularly at wavelengths greater than 600 nm, gets absorbed more than light in other parts of the visible spectrum, although all wavelengths are attenuated to some degree. As more and more light is absorbed, dominant wavelength shifts toward the blue end of the spectrum. Furthermore, as the slab depth increases, the spectrum becomes less flat, and the purity increases. With a slab depth of 50 m, the incident light is depleted of short (violet) and long (red) wavelength radiation.

But what does all of this have to do with green thunderstorms? As stated above, Bohren suggests that the absorption of a reddish light by water can create green. As shown above, for very large depths of water, green light can be created. To check this, Figure 8-9 shows a plot of the relationship between slab thickness and solar zenith angle

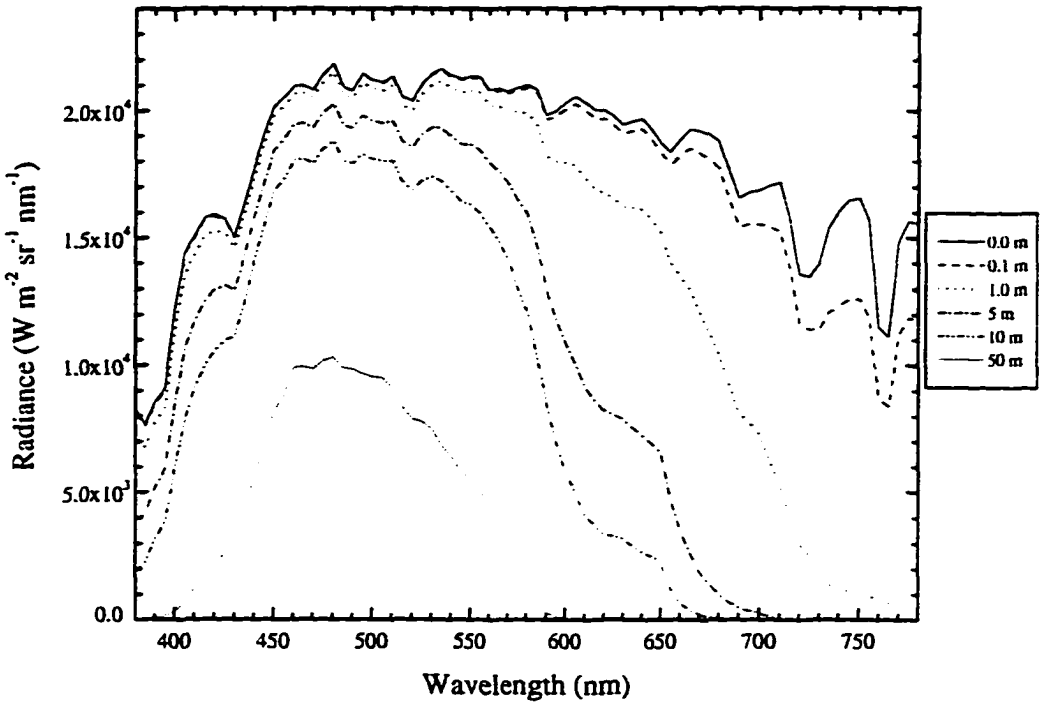

Figure 8-8 - Spectra of light from the slab model for a solar zenith angle of 75° and various slab depths. Attenuation is stronger in the red portion of the spectrum.

for a green light, assumed to be near 510 nm, exiting the slab of water. The scale of the figure is somewhat misleading in order to include very deep water. For solar zenith angles less than 75°, slab depths of 10 m or less can create green light.

We finally make a direct comparison between an observation of a green thunderstorm (7 May 1996, 2231UTC) and a calculated spectrum. Figure 8-10 shows a plot of the two spectra. The radiance of the slab spectrum is approximately eight orders of magnitude larger than the observation. This is primarily due to the use of direct solar radiation through the slab whereas the observation consists of diffuse radiation. Nevertheless, the peaks in both spectra occur near the same wavelength. The modeled

spectrum is from a calculation with a slab thickness of 10.5 m and a solar zenith angle of 75 degrees. The dominant wavelength is 509.7 m and the purity is 12.8 %. This would most likely appear as a green color to a normal observer. Two differences are apparent in the computed spectrum compared to the observation. The first is the lack of model radiance for wavelengths longer than 700 nm. The second is that the model simulation does not predict well the radiance in the blue region ($\lambda < 450$ nm). The good news is that the simulation does not produce a pronounced spike in the spectrum. The top of the computed spectrum is relatively flat in the wavelength region between 480 nm and 550

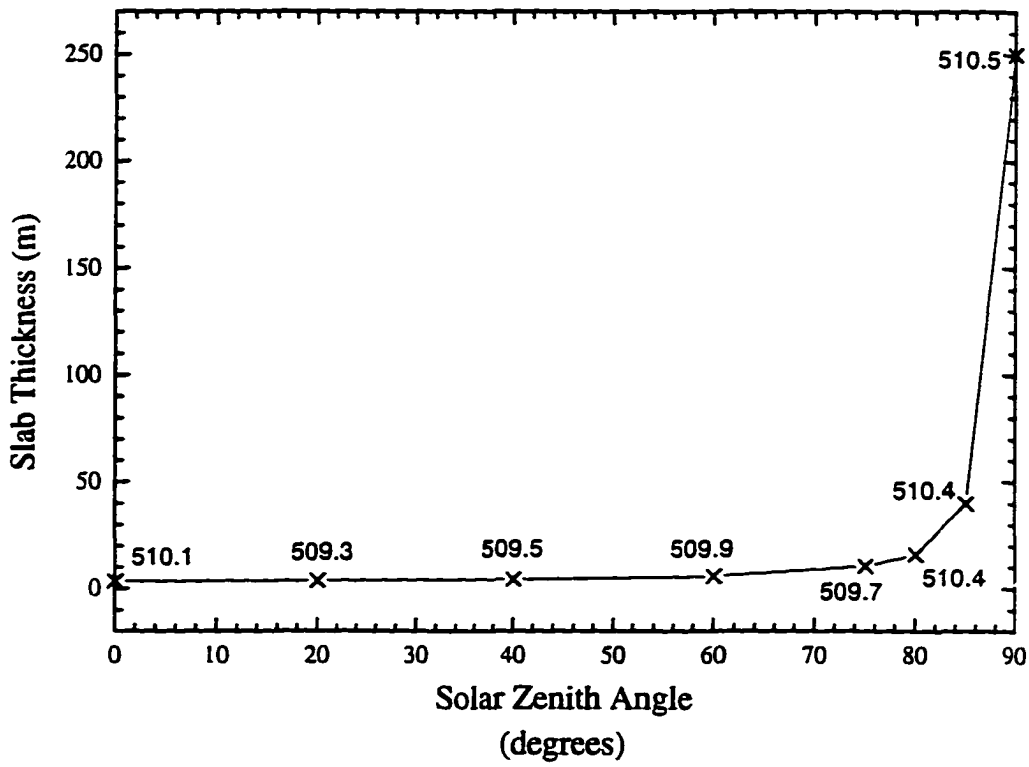

Figure 8-9 - Slab thickness for green light for different solar zenith angles. A wavelength of 510 nm was chosen to represent "green" light. The actual value of the dominant wavelength is shown on the graph.

nm. This is in agreement with observations. It is clear that the mechanism of creating green light by the absorption of sunlight by liquid water is at least plausible. It should be noted that 10 m of water is a significant depth of water. How does this compare with the typical amount of water observed in thunderstorms? Consider the following observations.

A green storm was seen by storm chasers, not the author, along the Red River on 20 September 1996. The storm was enveloping green with the observer estimating dominant wavelength of 515 nm and a purity of 15% by referring to a colored CIE

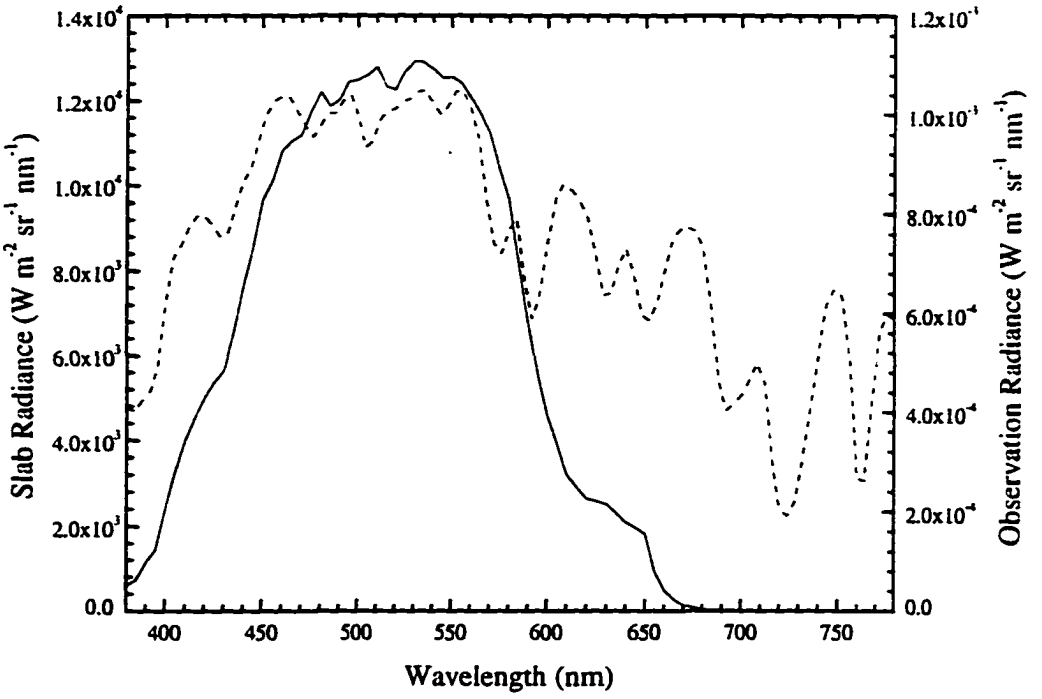

Figure 8-10 - Comparison of a computed spectrum (solid) to an observation (dashed). The computed spectrum is for a pure water slab of 10.5 m thick and a solar zenith angle of 75°. The observation of a green thunderstorm was recorded on 7 May 1995 at 2231 UTC 16 km east-southeast of Mountain Park, Oklahoma looking to the north.

chromaticity diagram. No spectral measurements were made of the storm since this was a casual observation by a colleague, not part of the planned observations. WSR-88D Doppler radar indicated a vertically integrated liquid water content (VIL) of 80 kg m^{-2} while the sky was green. This may be approximated by a homogeneous slab of water of 8 cm thick. Calculations for an 0.08 m slab and a solar zenith angle of 64.8° (computed from the ephemeris) gave a dominant wavelength of 578.5 nm and a purity of 19.8%. This is not very different from that of the sun without any water at all. It is not obvious how this amount of liquid water content could account for the observed green color using the Bohren theory. Again, we see that there is more to the story than just absorption by liquid water.

8.2 Bohren Theory of Green Thunderstorms

8.2.1 Introduction

Bohren (Bohren and Fraser 1993) states that green light does emanate from the thunderstorm itself. Since absorption of light by water, either in a solid or liquid state, is at a minimum in the wavelengths of light that correspond to a blue color and rises steadily with increasing wavelength (Fig. 8-2), any sunlight that passes through a significant distance in cloud hydrometeors will take on a bluish cast. Late in the day, sunlight is enriched in the longer wavelength (redder) light because a large portion of the shorter wavelength (bluer) light is scattered out. When this reddened light illuminates an object with an absorption minimum in the blue, the result can be perceptually green transmitted light. The primary requirement is that the path through the water (or ice) is long enough

to allow sufficient absorption of the light at the long-wavelength (red) end of the spectrum.

8.2.2 Theoretical Analysis

8.2.2.1 Optical Thickness

Since the primary requirement is that the path of radiation through the hydrometeors is sufficiently long to allow for selective absorption to occur, we must look at the equations that describe this effect. Optical thickness (or optical depth) is such a quantity that represents the efficiency of the extinction per unit depth of material. It is defined by an integral of the extinction coefficient

$$\tau_\lambda = \int_p^{p'} s_\lambda \, ds' \qquad 8\text{-}5$$

where s_λ is the extinction coefficient (m^{-1}) and ds is the path length (m). The optical depth is dimensionless and positive definite.

When radiation passes through a material such as droplets of water, two things can happen to the radiation: it can get absorbed or it can get scattered. These two effects are described by absorption (κ) and scattering (β) coefficients respectively. The sum of these coefficients create the extinction coefficient used in the above definition (Eq. 8-5) of optical depth. For a thick cloud of depth h the integral is evaluated and the optical thickness results in the product of the extinction coefficient and the path length:

$$\tau = \int_0^h s_\lambda \, ds' = (\beta + \kappa) \, h \qquad 8\text{-}6$$

where we have dropped the lambda subscript for simplicity.

8.2.2.2 Scattering in a Cloud

The albedo of single scatter (ω_o) is defined as the ratio of the scattering coefficient to the extinction coefficient,

$$\omega_o = \frac{\beta}{\beta + \kappa} \qquad 8\text{-}7$$

Figure 8-11 shows the basic geometry of the scattering problem. Incident light I_o interacts with a particle and radiation (I) is scattered in the θ direction. This can mathematically be written as (van de Hulst 1957):

$$I = \frac{I_o\, F(\theta,\ \phi)}{k^2\ r^2} \qquad 8\text{-}8$$

where $k=2\pi/\lambda$ is the wavenumber of the incident radiation and $F(\theta,\phi)$ is a nondimensional function of direction but not a function of r. The scattering cross section is analogous to geometric area and represents the amount of energy removed from the original beam by the particles (Liou 1980). The units of this term are area (usually cm^2) and is represented by

$$C_{sca} = \int F(\theta,\phi)\ d\omega \qquad 8\text{-}9$$

where $d\omega=\sin\theta d\theta d\phi$ is an element of solid angle. When $F(\theta,\phi)$ is divided by k^2C_{sca}, where C_{sca} is the scattering cross section described below, the phase function is obtained.

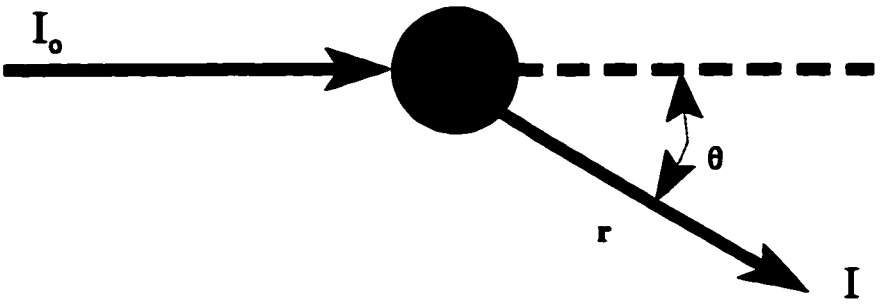

Figure 8-11 - Basic scattering geometry for an incident ray of light (I_o) being scattered by a particle in the **r** direction. Scattered radiation is represented by I.

The phase function, which represents the angular distribution of scattered energy as a function of direction (Liou 1992), may then be written as (van de Hulst 1957)

$$P(\theta,\phi) = \frac{F(\theta,\phi)}{k^2\, C_{sca}} \qquad 8\text{-}10$$

If a cloud contains many scattering particles and is optically thin such that the incident intensity (I_o) for each particle is the same (van de Hulst 1957), then for each particle i:

$$I_i = \frac{F_i(\theta,\phi)}{k^2\, r^2}\, I_o \qquad 8\text{-}11$$

For the entire cloud we simply sum the result:

$$F(\theta,\phi) = \sum_i F_i(\theta,\phi). \qquad 8\text{-}12$$

This addition also holds for cross sections. We now consider a volume element V that contains N identical particles per unit volume each characterized by $F(\theta,\phi)$. The cloud size spectrum may be described by

$$\frac{dn(a)}{da} \qquad (cm^{-3}\ \mu m^{-1}) \qquad 8\text{-}13$$

where a is the drop radius. The total number of cloud particles is computed by intgrating the size spectrum over a given size range (e.g. a_1 to a_2)

$$N = \int_{a_1}^{a_2} \frac{dn(a)}{da} da \qquad 8\text{-}14$$

The number of particles in the volume is then NV and the intensity at r is given by:

$$I = \frac{NV}{k^2\ r^2} F(\theta,\phi)\ I_o \qquad 8\text{-}15$$

We now assume that all of the particles are sufficiently far apart from each other that the distance between them is much greater than the incident wavelength. This allows us to add the radiances scattered by various particles without regard to the phase of the scattered wave. This is called independent or incoherent scattering (Liou 1980).

8.2.2.3 Absorption and Cross Sections

If the scattering cross section is C_{sca} then the extinction and scattering coefficients may be written as

$$\beta_e = \int_{a_1}^{a_2} C_{ext}(a) \frac{dn(a)}{da} da,$$
$$\beta_s = \int_{a_1}^{a_2} C_{sca}(a) \frac{dn(a)}{da} da. \qquad 8\text{-}16$$

We now allow for all radii and write in the form of equations 5 and 6 of Bohren and Fraser (1993)

$$\beta = \int_0^{\infty} C_{sca}(a)\ N(a)da,$$
$$\kappa = \int_0^{\infty} C_{abs}(a)\ N(a)da. \qquad 8\text{-}17$$

If the particle is large compared with the wavelength of light, then, for a>>λ

$$C_{sca} + C_{abs} \approx 2\pi a^2. \qquad 8\text{-}18$$

A weakly absorbing water sphere is given by

$$C_{abs} = \frac{4}{3}\pi\ a^3\ \alpha\ f(n) \qquad 8\text{-}19$$

where α is the absorption coefficient of pure water and f(n) is a function of the real part of the index of refraction.

Let us take a slight detour to see if there is any significant difference between the absorption cross section for ice and the absorption cross section for liquid water using Equation 8-21. From Halliday and Resnick (1978) the index of refraction for pure water at standard temperature and pressure is 1.33. Hobbs (1974) gives the index of refraction for ice at a temperature of -3°C and a wavelength of 546.09 nm (18312 cm^{-1}) in a vacuum of 1.3104. We shall compute n^*, the ratio of the functionals f(n) in Equations 8-21 and 8-22 where

$$f(n) = \frac{n^3 - (n^2-1)^{3/2}}{n} \qquad 8\text{-}20$$

So we can write the ratio

$$n^* = \frac{f_l(n)}{f_i(n)} = \frac{n_i}{n_l} * \frac{[n_l^3-(n_l^2-1)^{3/2}]}{[n_i^3-(n_i^2-1)^{3/2}]} \qquad 8\text{-}21$$

where n_l is the real part of the index of refraction for liquid water and n_i is the real part of the index of refraction for ice. Substituting the values given above for n_l and n_i, then $n^*=1.0066$. Since the ratio is so close to 1.0, only the value of the index of refraction for liquid water will be used in further analysis and use the equation for a weakly absorbing sphere (Eq. 8-19) in the rest of the analysis.

8.2.3 Bohren's Derivation

We begin the derivation presented by Bohren (Bohren and Fraser 1993) by evaluating the single scattering coefficient. Using Eq. 8-7 we can rewrite the single scatter equation

$$1-\omega_o = \frac{\beta+\kappa}{\beta+\kappa} - \frac{\beta}{\beta+\kappa} \qquad 8\text{-}22$$

By using the definitions in Eq. 8-17, Eq. 8-22 can be written as

$$1-\omega_o = \frac{\int C_{abs}(a)N(a)da}{\int C_{sca}(a)N(a)da + \int C_{abs}(a)N(a)da} \qquad 8\text{-}23$$

Simplifying,

$$1-\omega_o = \frac{\int C_{abs}(a)\ N(a)\ da}{\int (C_{sca}(a)+C_{abs})\ N(a)\ da} \qquad 8\text{-}24$$

Using equations 8-18 and 8-19 we can now substitute in for the scattering and absorption coefficients

$$1-\omega_o = \int \frac{\frac{4}{3}\ \pi\ a^3\ \alpha\ f(n)}{2\ \pi\ a^2} N(a)\ da \qquad 8\text{-}25$$

This can be simplified to

$$1-\omega_o = \frac{2}{3}\,\alpha\, f(n) \int \frac{a^3\, N(a)\, da}{a^2\, N(a)\, da} \qquad 8\text{-}26$$

We now define moments over the size distribution

$$\begin{aligned} \langle a^3 \rangle &= \int a^3\, N(a)\, da \\ \langle a^2 \rangle &= \int a^2\, N(a)\, da \end{aligned} \qquad 8\text{-}27$$

then

$$1-\omega_o = \frac{2}{3}\,\alpha\, f(n)\, \frac{\langle a^3 \rangle}{\langle a^2 \rangle} \qquad 8\text{-}28$$

From Flatau *et al.* (1989), the effective radius is defined as

$$D_{eff} = \frac{\int_{D_{min}}^{D_{max}} n(D)\, D^3\, dD}{\int_{D_{min}}^{D_{max}} n(D)\, D^2\, dD} = \frac{\langle D^3 \rangle}{\langle D^2 \rangle} \qquad 8\text{-}29$$

so we can write the effective diameter as twice the effective radius:

$$d = 2\, \frac{\langle a^3 \rangle}{\langle a^2 \rangle} \qquad 8\text{-}30$$

then Eq. 8-28 becomes

$$1-\omega_o = \frac{d\, \alpha\, f(n)}{3} \qquad 8\text{-}31$$

Recall that the optical thickness is defined as the product of the sum of the absorption and scattering coefficients and the path length (Eq. 8-6). Then the optical path can be written as

$$\tau = \left(\int_0^\infty C_{sca}(a)\ N(a)\ da + \int_0^\infty C_{abs}(a)\ N(a)\ da\right) h$$

$$\tau = h \int_0^\infty 2\ \pi\ a^2\ N(a)\ da \qquad 8\text{-}32$$

The eventual goal is to find a relationship for τ that contains parameters that we can measure in a cloud. Consider the mass of a cloud water drop. The mass of a drop is simply the product of the density and the volume and can be written as

$$m(D) = \rho_w \frac{4\pi}{3} \left[\frac{D}{2}\right]^3 = \frac{\pi}{6} D^3 \rho_w \qquad 8\text{-}33$$

where D is the diameter of the drop and n(D) is the number concentration of the drops. Now consider the mass per unit area. This can be written as

$$\frac{mass}{area} = \frac{\rho_w \int_0^\infty \frac{\pi}{6} D^3\ n(D)\ dD}{\int_0^\infty \frac{\pi}{2} D^2\ n(D)\ dD} = \frac{d\ \rho_w}{3} \qquad 8\text{-}34$$

where D is the diameter of the drop and n(D) is the number concentration of the drops. From Flatau *et al.* (1989), the liquid water content of a cloud is given by

$$\ell = \int_0^\infty m(D)\ n(D)\ dD \qquad 8\text{-}35$$

where m(D) is defined in Eq. 8-33 and n(D) is the number density. Equate Eq. 8-34 to the quantity $\ell h/\tau$,where τ is defined by Eq. 8-32, and ℓ is found by substituting Eq. 8-33 into Eq. 8-35. Solving for τ we get

$$\tau = \frac{3\,h\,\ell}{d\,\rho_w} \qquad 8\text{-}36$$

where h is the thickness of the cloud, ℓ is the liquid water content (LWC), d is the mean drop diameter, and ρ_w is the density of water. These are the only parameters necessary to study the optical depth of a thunderstorm. As a final note, we can determine the makeup of Bohren's "H" which he states is the integrated cloud water. Unfortunately, the integrated cloud water is not a commonly reported quantity in the literature. Nevertheless, we can see that

$$H = \frac{\ell\,h}{\rho_w} \qquad 8\text{-}37$$

8.2.4 Eddington's Approximation

To test Bohren's theory we shall use the Eddington approximation for radiative transfer. In this method, we write the phase function in terms of an expansion in Legendre Polynomials, and the intensity may be written in the form of two radiation streams I_0 and I_1 according to

$$I(\tau,\mu) = I_0(\tau,\mu) + \mu I_1(\tau,\mu) \qquad 8\text{-}38$$

After much mathematical manipulation following Shettle and Weinman (1970), shown in detail in Appendix B, the equation for the downwelling diffuse flux at a level τ in the atmosphere may be represented by

$$F^{\downarrow}(\tau) = F^{\downarrow}(0)\frac{4Ke^{-K\tau}}{3(1-g)(1-e^{-2K\tau})} \qquad 8\text{-}39$$

where $F^{\downarrow}(0)$ is the flux of radiation at the top of the atmosphere, τ is the optical depth, g is the asymmetry parameter, and K is a parameter that includes the effects of absorption and is written as

$$K = \sqrt{3(1-g)(1-\omega_o)} \qquad 8\text{-}40$$

where ω_o is the albedo of single scatter. Equations 8-39 and 8-40 form the basis for the optical model of a thunderstorm.

8.3 Description of a Simple Numerical Model

The decision to create a simple model was based on the need to first understand the results of Bohren and Fraser (1993), to verify their results, and to extend their calculations by including a more realistic illumination source and by including a larger range of solar zenith angles, mean drop diameters, and liquid water contents. The transmitted light is computed by using equations 8-42 and 8-43 based on the Eddington approximation, which assumes a cloud of infinite horizontal extent, given previously.

Three variables, the solar zenith angle, the effective drop radius, and the cloud liquid water content may be varied to determine their effects on the transmitted light.

The solar input to the model is a realistic spectrum of the solar radiation in the wavelength band of 380 to 780 nm obtained by computing the radiance at 5 nm intervals from irradiance data given by Riordan *et al.* (1990). The effect of the setting sun is accomplished through the variation of the optical path of a ray sunlight through the atmosphere that accounts for a spherical earth.

Skylight was incorporated into the incident radiance by using the measurement of

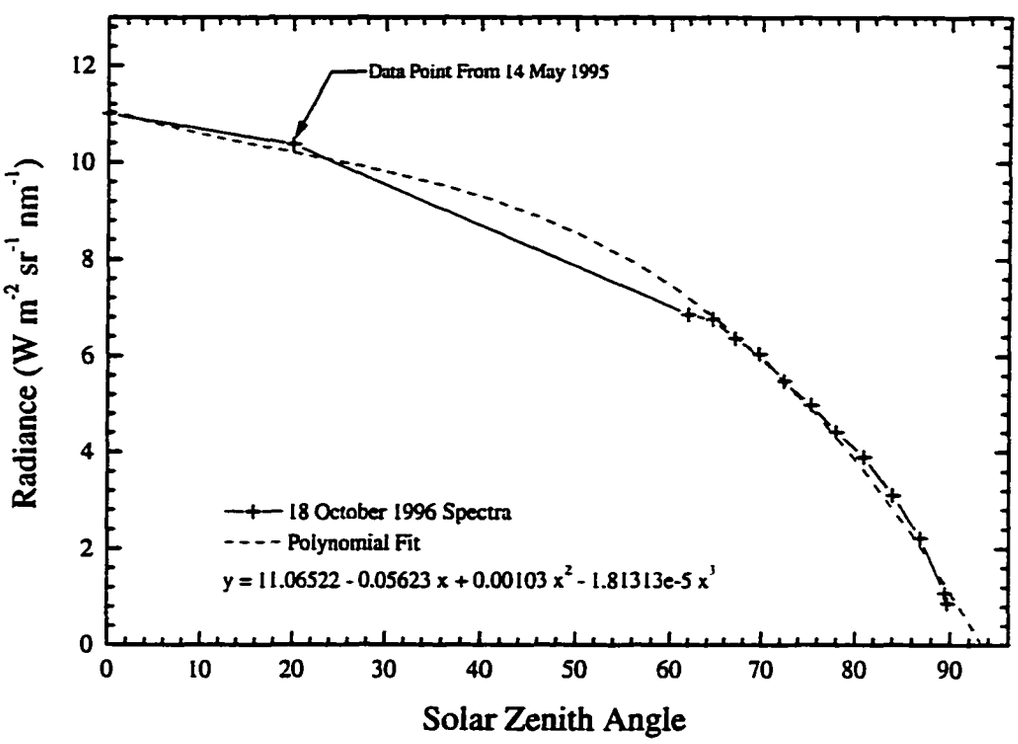

Figure 8-12 - The dashed curve shows the third order approximation used in the Green Thunderstorm Optical Model. The crosses represent the data taken of blue sky on two different days, 18 October 1996 and 14 May 1995, both in Moore, Oklahoma.

blue sky radiance (Figs. 3-4 and 3-5) to simulate the skylight in the calculations. The intensity of the simulated skylight decreases as the solar zenith angle increases as shown in Fig. 8-12. This is an approximate curve that was derived from measurements that showed that the radiance of the sky at sunset is nearly 10% that of the skylight at midday on cloudless days. All but one of the measurements was recorded on 18 October 1996 on a cloudless afternoon in Moore, Oklahoma. The remaining data point was recorded on 14 May 1995, also from Moore, Oklahoma. Although different days were used for this analysis, the May data point does not appear to be an outlier so the approximation is accepted. This curve was normalized against the y-intercept then used to reduce the radiance of the blue sky spectrum with solar zenith angle.

8.4 Model Parameters

8.4.1 Cloud Thickness

To effectively use the model to simulate the color of the perceived light coming from the bottom of severe thunderstorms, realistic values of the variable parameters must be determined. As shown by Eq. 8-39, the optical thickness of the cloud is directly proportional to the thickness of the cloud. For this study, storm cloud thicknesses are defined as the distance from the base to the top of the visible cloud. These thicknesses will in general differ from those determined by radar data. Thicknesses can range from 1.5 km for garden variety cumulus clouds (Rogers and Yau 1989) to over 15 km for cumulonimbus clouds (Chisholm and Renick 1972, Browning and Foote 1976, Fankhauser *et al.* 1983, Musil *et al.* 1986, Brandes *et al.* 1995). Given that most of the

green storms observed in this study were supercellular, a type of thunderstorm that has specific characteristics (e.g., Browning and Ludlam 1962, Browning and Donaldson 1963, Browning 1965, Chisholm 1970, Marwitz 1972, Renick, Chisholm, and Summers 1972, Nelson and Braham 1975, and Browning and Foote 1976), a thickness of 15 km was chosen for the bulk of the study. A few examples are given for a thickness of 2 km to show the effects of changing thickness of the cloud.

8.4.2 Drop Size Distributions

There is much uncertainty in the estimation of the size and type of hydrometeors contained in a supercell. The best data has been obtained from research flights of aircraft, particularly the armored T-28 flown by the South Dakota School of Mines and Technology (Sand and Schleusener 1974). The T-28 aircraft has been used to obtain detailed information about the makeup of convective clouds (e.g., Johnson and Smith 1980, Knight and Squires 1982, Detwiler 1990, Musil and Smith 1989, Detwiler *et al.* 1993, Brandes *et al.* 1995, Ramachandran *et al.* 1996). Of particular interest here are the liquid water content of clouds and the hydrometeor size distribution. Knight and Squires (1982) found that the most frequent mean droplet diameter varies from 13 μm in downdrafts to 17 μm in updrafts in hailstorms studied in Wyoming. Musil and Smith (1989) report a particle size of 12 μm observed in an updraft of a thunderstorm studied during COHMEX (Dodge *et al.* 1986) although a few particles as large as 45 μm were reported in their data set. They also show that, in the region of maximum precipitation, the maximum hydrometeor diameter was between 8 and 10 mm although the number

density was fewer than 1000 m^{-3} compared to approximately 100 cm^{-3} for the cloud droplets. Since the optical model requires a single drop size, the maximum cloud droplet size of 17 μm was selected to simulate a vigorous supercell cloud. To consider the effects of precipitation, the model was run with a drop size of 3 mm. Finally, the effects of both cloud and precipitation water were considered by taking a mass-weighted average of two drop size distributions. The two distributions were:

Cloud — 17 μm diameter at a concentration of 1500 cm^{-3}

Precipitation — 5 mm diameter at a concentration of 75 m^{-3}.

A mass weighted average results in a drop size of 22 μm. This was used for most of the model simulations.

8.4.3 Liquid Water Content

In addition to measuring the hydrometeor size and distribution, instruments on the aircraft measured the liquid water content of the clouds. In a flight from the 22 July 1976 case study, Knight and Squires (1982) report measured peak liquid water content values of 2.5 g m^{-3}. In this particular storm the liquid water content values never exceeded 2.7 g m^{-3}. Three days later, in a separate case study, they report the measurement of liquid water content values peaked near 4 g m^{-3}. Musil *et al.* (1986) show data from a storm in Montana with a very strong updraft (~50 m s^{-1}) that contained measurements of liquid water contents near 6 g m^{-3}. If cloud water and precipitation is included, values of total

mass concentration have been reported as high as 14 g m^{-3} (Straka and Anderson 1993). In running the simulations, the liquid water content variable was iterated, in 0.5 g m^{-3} increments, from 0.5 g m^{-3} up to 15 g m^{-3} to account for cloud water drops only, then a mixture of cloud droplets and precipitation particles.

8.5 Model Calculations

8.5.1 Small Drops

The first calculation was to show how the chromaticity of simulated spectra vary with changes in liquid water content for a fixed cloud thickness, mean drop diameter, and solar zenith angle. The assumption was made that the simulated storm would be a mature cumulonimbus of 15 km in height but all the hydrometeors (liquid or ice spheres) had a diameter of 5 μm. The solar zenith angle was set at 85° to simulate a late afternoon sun and the solar radiation was incident only upon the top of the cloud. Figure 8-13 shows a CIE 1976 UCS diagram of the results of the model simulation. The cloud with a small liquid water content (0.2 g m^{-3}) has a dominant wavelength of 576 nm, a wavelength normally associated with yellow, but the dominant wavelength decreases with increasing liquid water content (LWC). For a LWC of 1.0 g m^{-3} the dominant wavelength has shifted to 498 nm, a wavelength normally associated with blue-green. Further increasing LWC results in a storm that appears bluer. At a LWC of 5 g m^{-3} the dominant wavelength is 490 nm, a wavelength that is normally associated with the color greenish-blue. The computed purity (66%) is much too high compared to observations and is probably due to the unrealistic geometry of the model. Nevertheless, the computed dominant wavelength

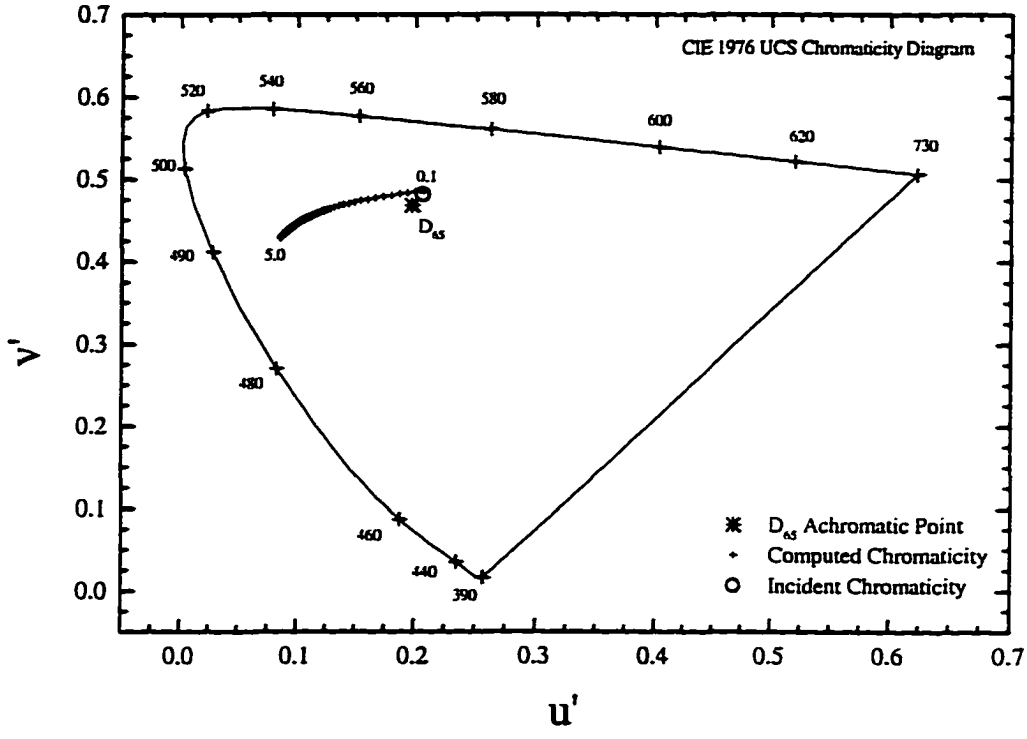

Figure 8-13 - CIE 1976 UCS chromaticity diagram showing the variation in chromaticity of a simulated cumulonimbus cloud with changes in cloud liquid water content. Liquid water content (g m^{-3}) is shown next to the chromaticity points. The cloud thickness is 15 km, the mean drop diameter is 5 μm, and the solar zenith angle is 85°. The open circle represents the chromaticity for the input radiance. D_{65} is the CIE 6500 K achromatic reference.

matches well with typical observations of "gray" clouds that has a dominant wavelength near 485 nm. One would expect a very thick cumulonimbus cloud consisting of small drops and a high LWC to appear bluish-gray in color and this is the color typically seen when observing a severe thunderstorm. As shown previously, a green color is a possible result for LWC's between 0.6 and 1.0 g m^{-3} but, for mature thunderstorms, the mean drop

size is much larger than the 5 μm used in this calculation (Schemenauer *et al.* 1980). A larger drop size would be more representative of precipitating cumulonimbus clouds.

8.5.2 Realistic Drop Sizes

Now that an example of a small drop size has been given, it is time to investigate a more realistic mean drop diameter. Knight and Squires (1982) report that during a T-28 probe of thunderstorms during the 1975 to 1976 observing period found that the most

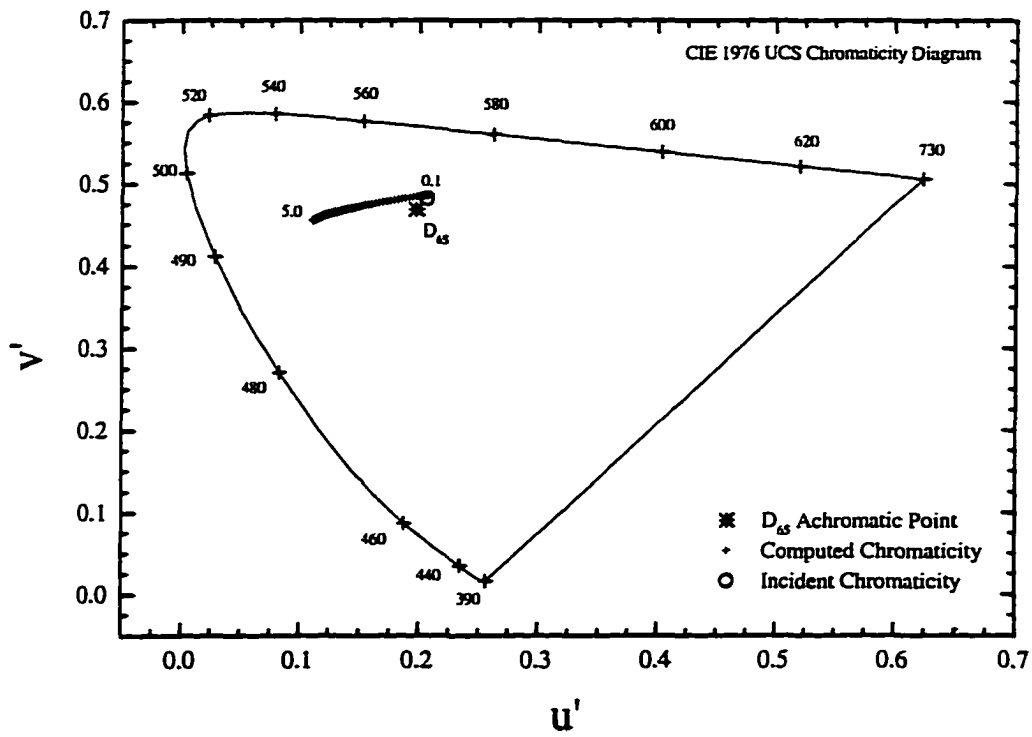

Figure 8-14 - CIE 1976 UCS chromaticity diagram showing the variation in chromaticity of a simulated cumulonimbus cloud with changes in cloud liquid water content. Liquid water content (g m^{-3}) is shown next to the chromaticity points. The cloud thickness is 15 km, the mean drop diameter is 22 μm, and the solar zenith angle is 85°. D_{65} is the CIE 6500 K achromatic reference.

common droplet concentration was 900 cm^{-3} but there were a significant fraction, about 2% of all drops, with concentrations above 1500 cm^{-3}. Furthermore, they found that the mean droplet diameter for droplets of concentrations greater than 100 cm^{-3} was 17 μm. Given this, a drop size of 17 μm with a best case concentration of 1500 cm^{-3} was chosen as parameters in the simulation. Musil and Smith (1989) report that number concentrations for particles as large as 5 mm was 75 m^{-3}. This value was used for large hydrometeors in the model to calculate the effect on chromaticity. However, the model only accepts a single drop size so a mass weighted average was taken of the two drop size/concentration pairs. The resulting drop size was found to be 22 μm.

Figure 8-14 shows the variation in chromaticity with changes in liquid water content for a cloud thickness of 15 km, a mean drop diameter of 22 μm, and a solar zenith angle of 85°. The dominant wavelength using a LWC of 0.5 g m^{-3} is 574.6 nm, a wavelength not too far from that of the incident solar radiation. As the LWC is increased, the dominant wavelength progressively decreases. Between LWC values of 1.3 and 2.0, the dominant wavelength is in the band associated with greenish colors, with yellow-green for the low LWC end, and blue-green at the high end. Since the observed dominant wavelength of green thunderstorms is bimodal (see Chapter 4), this simulation suggests that there are two potentially favored values of LWC in severe thunderstorms. The peak in the observed data near 570 nm is represented by a LWC of 0.6 g m^{-3}. Musil and Smith (1989) show that on several flights by the T-28, values of LWC were found near this level, with measured LWC never exceeding a value of 3 g m^{-3}. This suggests that the larger drops are partially responsible for producing the yellowish-green type of green

thunderstorms but are not needed for the blue-green type. Figure 8-14 shows that, for a 22 μm mean drop size, the LWC values measured by Musil and Smith (1989) produces the yellow-green type of green thunderstorm. Higher liquid water contents, associated with the updraft or core regions of the storm can produce the blue-gray color seen in most thunderstorms and is responsible for the wavelength peak observed near 485 nm in the bimodal distribution..

8.6 Comparisons With Measurements

The optical model used in this study is not designed to recreate the spectrum of the light from a thunderstorm. We are not necessarily interested in obtaining an exact spectrum, but rather a satisfactory colorimetric representation of the light being observed. Given this, we consider three different storm thicknesses. The first thickness, 15 km, is used to simulate the sunlight that is incident only on the top of the thunderstorm. The other thickness, 5 km, is used to test the effects of sunlight incident on the side of the thunderstorm. Figure 8-15 shows a schematic of two examples. The solar radiation passes through more of the atmosphere to reach the 5 km cloud than the 15 km cloud. The radiation incident on the 5 km thick cloud has been scattered by more of the atmosphere and is therefore redder than the radiation incident on the 15 km cloud. The solar zenith angle of the incident radiation in the model was fixed at 55°, the mean solar zenith angle between the yellow-green observation (57°) and the blue-green observation (53°).

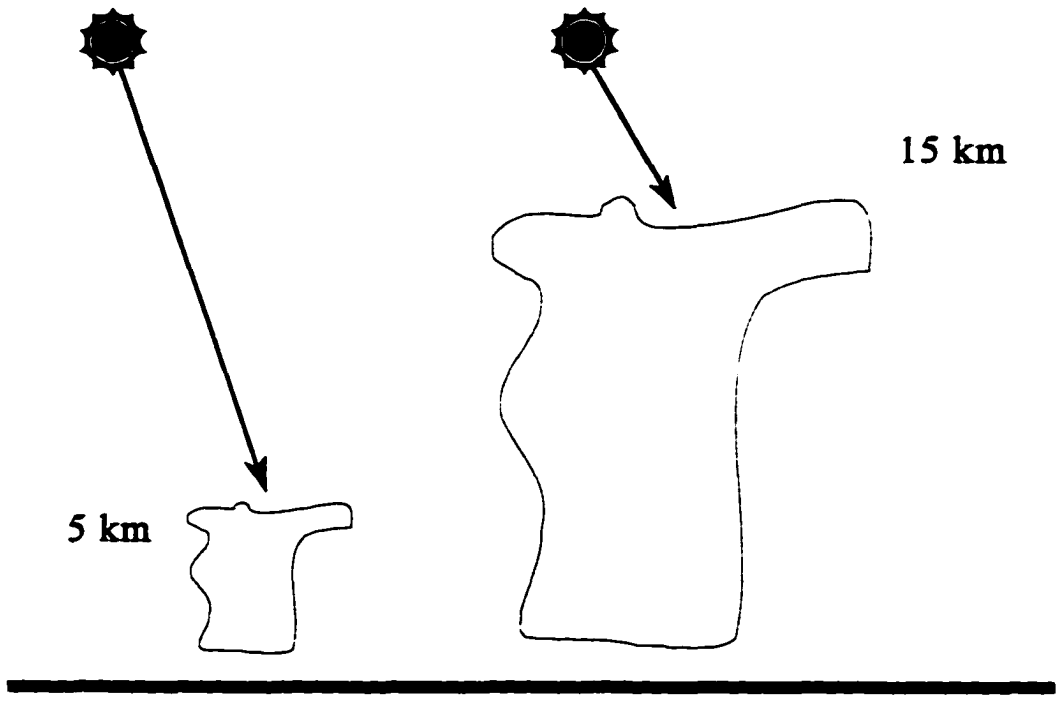

Figure 8-15 - The path of solar radiation through the atmosphere is much longer for a cloud 5 km thick compared to a 15 km thick cloud.

8.6.1 15 km Thickness

Figure 8-16 shows a CIE 1976 UCS diagram of the variation in chromaticity with liquid water content for a 15 km thick cloud with a mean drop diameter of 5 μm. Because the cloud top is so high in the atmosphere, little reddening of the incident solar radiation occurs. The absorption of light by cloud water changes the dominant wavelength of the transmitted light to a blue color even with low liquid water contents. Increasing the liquid water content, the transmitted light becomes bluer. As a result, the blue-green thunderstorm type (31 May 1995) of light is created with a liquid water

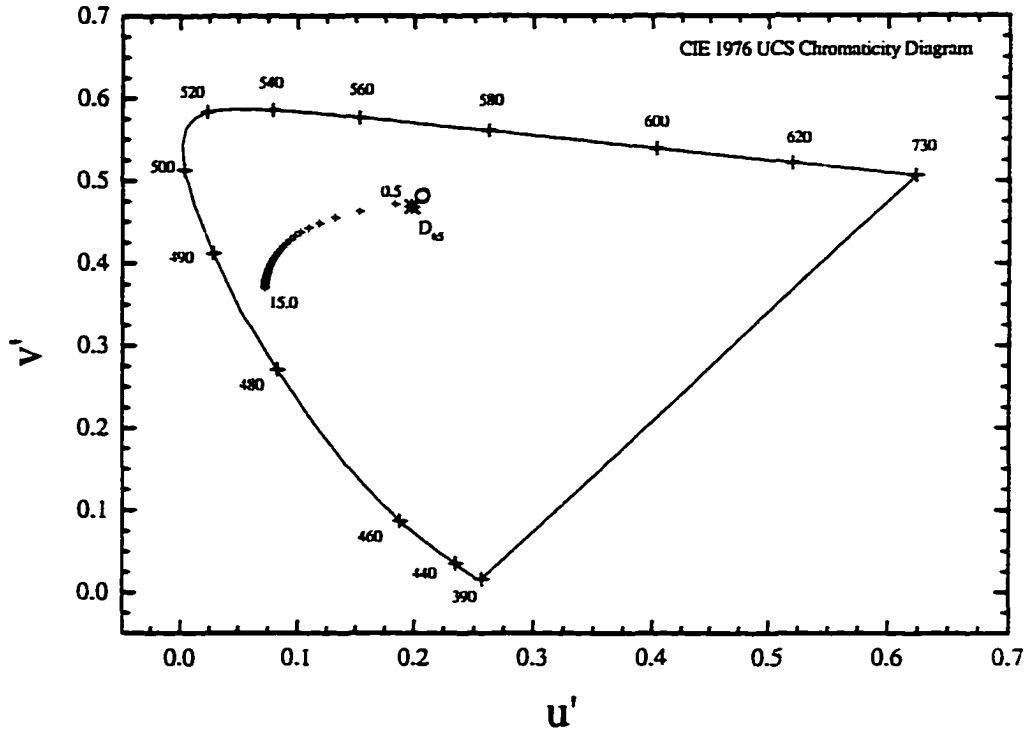

Figure 8-16 - CIE 1976 UCS chromaticity diagram showing the variation in chromaticity of a simulated cumulonimbus cloud with changes in cloud liquid water content. Liquid water content (g m^{-3}) is shown next to the chromaticity points. The cloud thickness is 15 km, the mean drop diameter is 5 μm, and the solar zenith angle is 55°. The circle represents the chromaticity of the incident radiance. D_{65} is the CIE 6500 K achromatic reference.

content of only 1 g m^{-3} and the yellow-green type thunderstorm (7 May 1995) is not created at all. The calculated spectrum, for a liquid water content of 1 g m^{-3}, is shown in Fig. 8-17 compared to the blue-green thunderstorm observed on 31 May 1995 near Sweetwater, TX. The shape of the two curves is remarkably similar for wavelengths between 450 nm and 600 nm. The calculated spectrum does not account for much of the radiance measured at wavelengths longer than 600 nm. This is likely due to the model

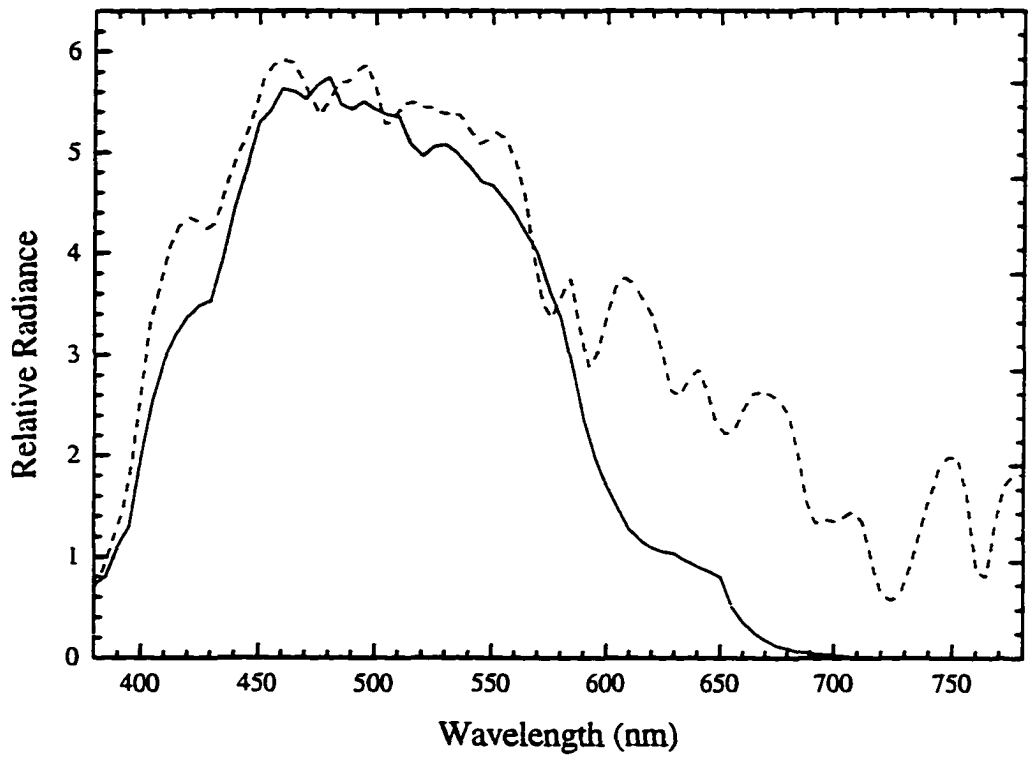

Figure 8-17 - Calculated spectrum (solid) for a 15 km thick cloud with a 5 μm mean drop diameter and liquid water content of 1 g m^{-3} compared to an observation (dashed) of a blue-green thunderstorm. The observation was recorded on 31 May 1995 at 2232 UTC near Sweetwater, TX.

infinite cloud structure that does not allow any other light sources such as light reflected by nearby clouds.

As the drop size is increased to 22 μm somewhat less absorption occurs and the slightly reddened sunlight allows for the yellow-green color to appear with a liquid water content of 0.8 g m^{-3}. More absorption occurs with the addition of more liquid water in the cloud for the same mean drop diameter. The model indicates a blue-green dominant wavlength, similar to the one measured on 31 May 1995, using a liquid water content of

2.2 g m^{-3}. Further increasing the drop size to 3000 μm reduces the absorption to the extent that the blue-green light observed on 31 May 1995 is no longer indicated by the model with liquid water contents less than 15 g m^{-3}.

Although the model requires a single drop size and liquid water content to represent the entire cloud, the colors of observed green thunderstorms can be simulated even with a cloud as thick as 15 km and sunlight incident only on the top of the cloud. A

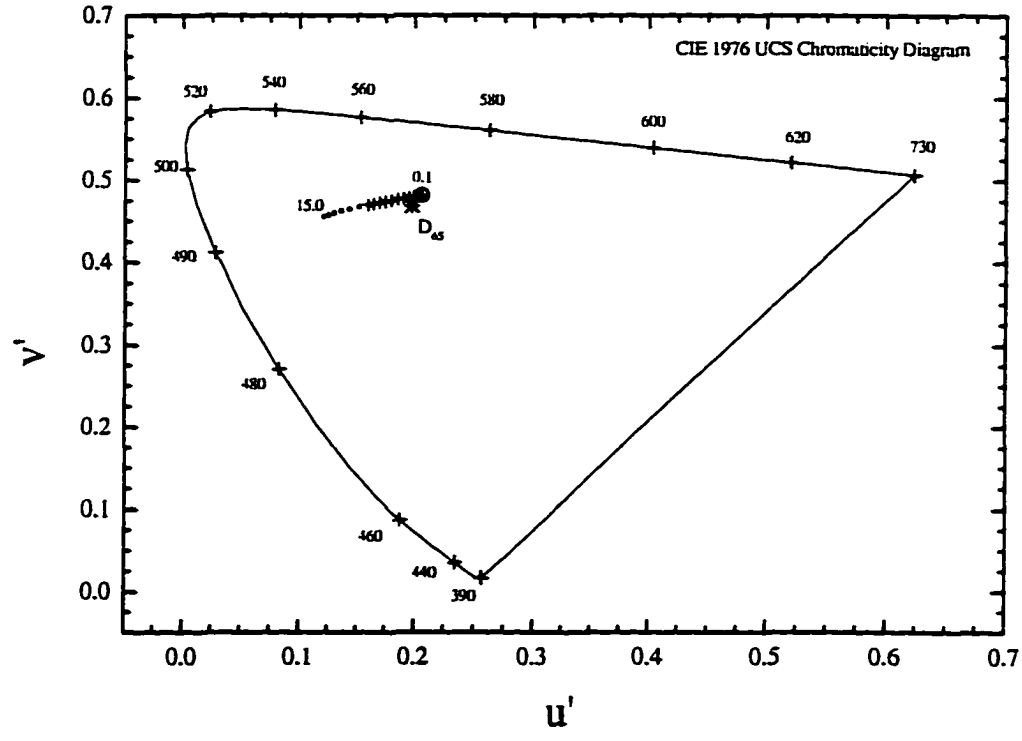

Figure 8-18 - CIE 1976 UCS chromaticity diagram showing the variation in chromaticity of a simulated cumulonimbus cloud with changes in cloud liquid water content. Liquid water content (g m^{-3}) is shown next to the chromaticity points. The cloud thickness is 5 km, the mean drop diameters are 5 μm drops (•) and 22 μm drops (+), and the solar zenith angle is 55°. The circle represents the chromaticity of the incident radiance. D_{65} is the CIE 6500 K achromatic reference.

better representation of the storm would be to allow for sunlight to be incident on the sides of the cloud rather than just the top. We approximate this by reducing the thickness of the cloud to a point where the light need only travel through one-third the thickness of a 15 km cloud.

8.6.2 5 km Thickness

The reduction in the thickness of the cloud allowed the light from the sun to pass through a much greater distance in the atmosphere before being incident on the cloud. The additional scattering reddens the light source such that the green colors of light are produced with lower amounts of cloud liquid water content. Furthermore, the calculated spectrum is more realistic in that there is more transmitted radiance in the longer wavelength portion of the spectrum. Figure 8-18 shows a CIE 1976 UCS diagram of the variation in chromaticity with changes in liquid water contents for a cloud that consists of 5 μm drops (•) and 22 μm drops (+). At very low liquid water content the dominant wavelengths for both drop sizes are near that of the incident radiation. As the liquid water content increases, the absorption increases and the dominant wavelengths shift toward the short wavelength portion of the spectrum. With a liquid water content of 15 g m^{-3}, both drop sizes have dominant wavelengths near 490 nm, but the smaller drop size creates a much more pure color.

Figure 8-19 shows a plot of the simulated spectrum using a mean drop diameter of 22 μm and a liquid water content of 2.9 g m^{-3} compared to an observed yellow-green spectrum. In this example, the computed spectrum matches the observation very well in

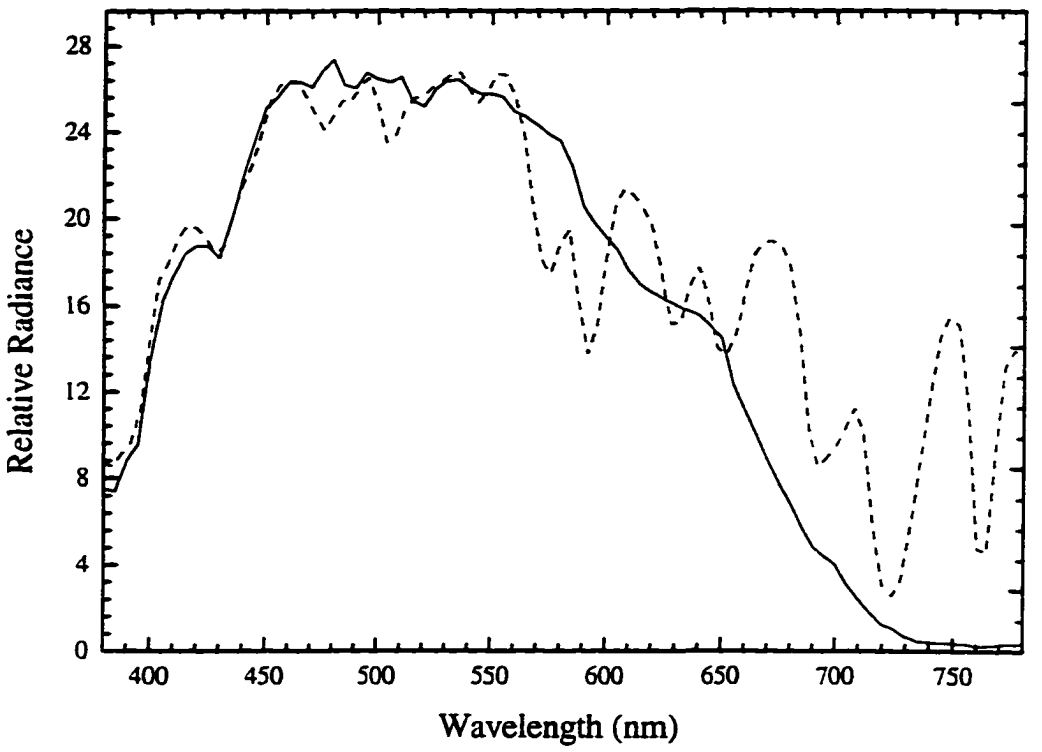

Figure 8-19 - Calculated spectrum (solid) for a 5 km thick cloud with a 22 μm mean drop diameter and liquid water content of 2.9 g m^{-3} compared to an observation (dashed) of a blue-green thunderstorm. The observation was recorded on 7 May 1995 at 2231 UTC in Mountain Park, OK.

the wavelength band of 380 nm to 650 nm, essentially the entire bandwidth of human vision. This simulated spectrum, using a thinner cloud, is in much better agreement with the observation than was the computed spectrum of Fig. 8-17.

8.7 Hail as the Cause of the Green Light — Part 2

To examine the effects of larger hydrometeors, such as graupel or small hail, the drop size was increased to 3 mm. Figure 8-20 shows the variation in chromaticity of the

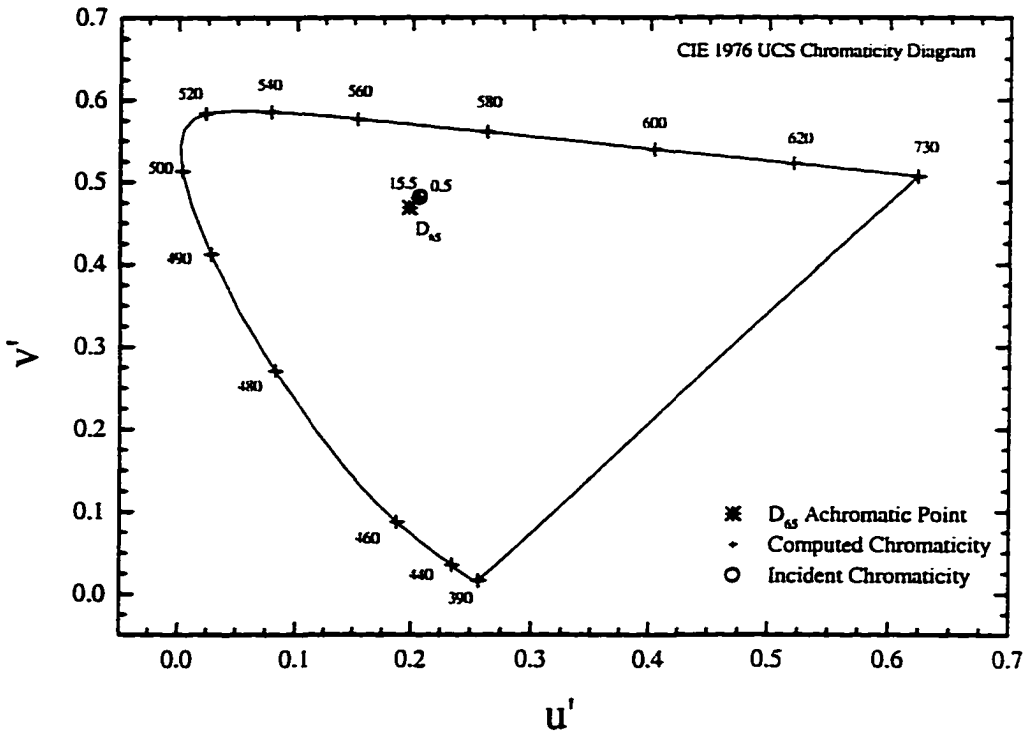

Figure 8-20 - CIE 1976 UCS chromaticity diagram showing the variation in chromaticity of a simulated cumulonimbus cloud with changes in cloud liquid water content. Liquid water content (g m^{-3}) is shown next to the chromaticity points. The cloud thickness is 5 km, the mean drop diameter is 3000 µm, and the solar zenith angle is 55°. The circle represents the chromaticity of the incident radiance. D_{65} is the CIE 6500 K achromatic reference.

simulated spectrum with drop diameter of 3 mm with variations in cloud liquid water content. With the hydrometeor size so large, the optical depth never gets large enough to allow for the water absorption mechanism to work sufficiently to absorb a large portion of the red light. Although the reddened sunlight incident on the sides of the storm, assuming a zenith angle of 55°, still has significant blue and green components, there is insufficient absorption by the large hydrometeors, at all realistic liquid water contents, to

create any kind of green light. From this, very large water drops or hail alone cannot account for the creation of blue or green light in a thunderstorm. The dominant wavelengths range from 580 nm for a LWC of 0.5 g m^{-3} to 575 nm for a LWC of 15 g m^{-3}. As shown in the figure, the calculated chromaticity does not differ significantly from the incident chromaticity at any realistic liquid water content. The light seen from a "cloud" made up of such large hydrometeors would look similar in color to the sun, nearly white (or light gray depending on the radiance). This numerical data, in addition to field observations (See Chapter 9), finally answers whether hail can cause the green light; it cannot.

8.8 The Slab Model — Reprise

Throughout this chapter it has been shown that it is possible to create green light from sunlight passing through a certain amount of water. Two concepts have been examined, bulk absorption by liquid water, and distributed absorption by cloud water. The natural question that follows is: Is it possible to relate the meaning of the two results? The answer is, of course, yes. In doing so, only very rough approximations will be considered as we are only concerned about an approximate correlation between the thickness of the slab of water and any of the parameters that make up the cloud water.

Earlier in the chapter we found that a green light can be created by passing sunlight, at a zenith angle of 75°, through 10.5 m of pure liquid water. We want to find out how much liquid water content, and later the liquid water path referred to in Bohren

and Fraser (1993), is required for the same result. To do this, in a very approximate manner, we equate the exponents of equations 8-4 and 8-40 to yield

$$\sqrt{3\ (1-g)\ (1-\omega_o)}\ \frac{3\ h\ \ell}{d\ \rho_w} \approx \alpha_\lambda z. \qquad 8\text{-}41$$

Using the following parameters

$g = 0.85$	$1-\omega_0 = 6.7 \times 10^{-4}$
$\alpha_\lambda = 0.5\ m^{-1}$	$z = 10.5\ m$
$d = 10 \times 10^{-6}\ m$	$h = 15 \times 10^3\ m$

results in a liquid water content (ℓ) of 1.74 g m^{-3}, a realistic value. Furthermore, Bohren's liquid water path (H) is found to be 2.6 cm, also a realistic value. Light passing through a cloud, enduring many multiple scatters, can pass through an amount of liquid water that equals the path through a slab of liquid water over 10 m thick. In both instances, green light is produced in the process.

8.9 Conclusion

These two show that the Bohren transmission model, successfully simulates the observed spectrum of green thunderstorms. We have shown that green light can be produced using the Bohren theory for clouds that are as thick as 15 km with sunlight incident only on the top of the storm. A blue-green colored storm is predicted for small

drop sizes, and a yellow-green storm is predicted for larger drop sizes. Both types can be produced with intermediate sized drops. To simulate the effects of sunlight incident on the sides of the clouds better, the cloud thickness was reduced to 5 km. In this example, both types of green thunderstorms can be produced with small drop sizes, no green storms can be produced with large drops (or hail), and only the yellow-green type can be produced with intermediate drop sizes. The green light produced by yellow-green storms comes from a cloud of much lower optical thickness. This can occur, and has been observed, in the green light from significant precipitation or from near the rear flank downdraft of severe thunderstorms.

Chapter 9: A Mechanism for the Green Light - 7 May 1995

We shall now revisit a storm that was first covered in Chapter 4. This example is from a storm VORTEX (Rasmussen *et al.* 1994) teams intercepted in southwestern

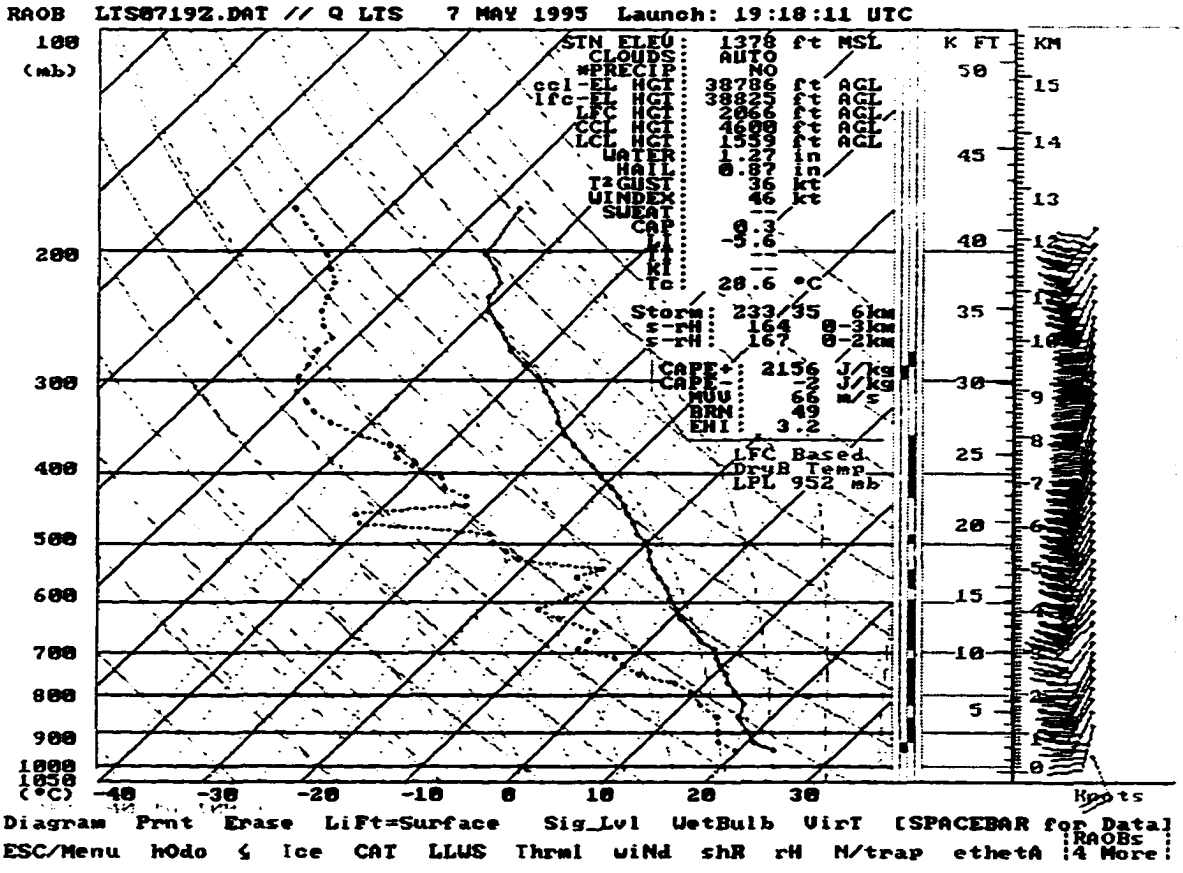

Figure 9-1 - Sounding from Altus, Oklahoma on 7 May 1995. Launch time is 1918 UTC.

Oklahoma during the afternoon of 7 May 1995. Storms during this day produced 10 tornadoes (NOAA 1995), with a particularly damaging one that began in Montague, Texas and ended just north of Ardmore, Oklahoma (Weaver *et al.* 1996). The storms of concern here formed later in the day along the dryline that had developed in western Texas and the Texas Panhandle. The sounding from Altus, Oklahoma at 2000 UTC (Fig. 9-1) indicates fairly deep surface moisture and steep lapse rates that are favorable conditions for deep convection to occur later in the day. A large amount of convective available potential energy (CAPE) and the vertical wind shear are also favorable for

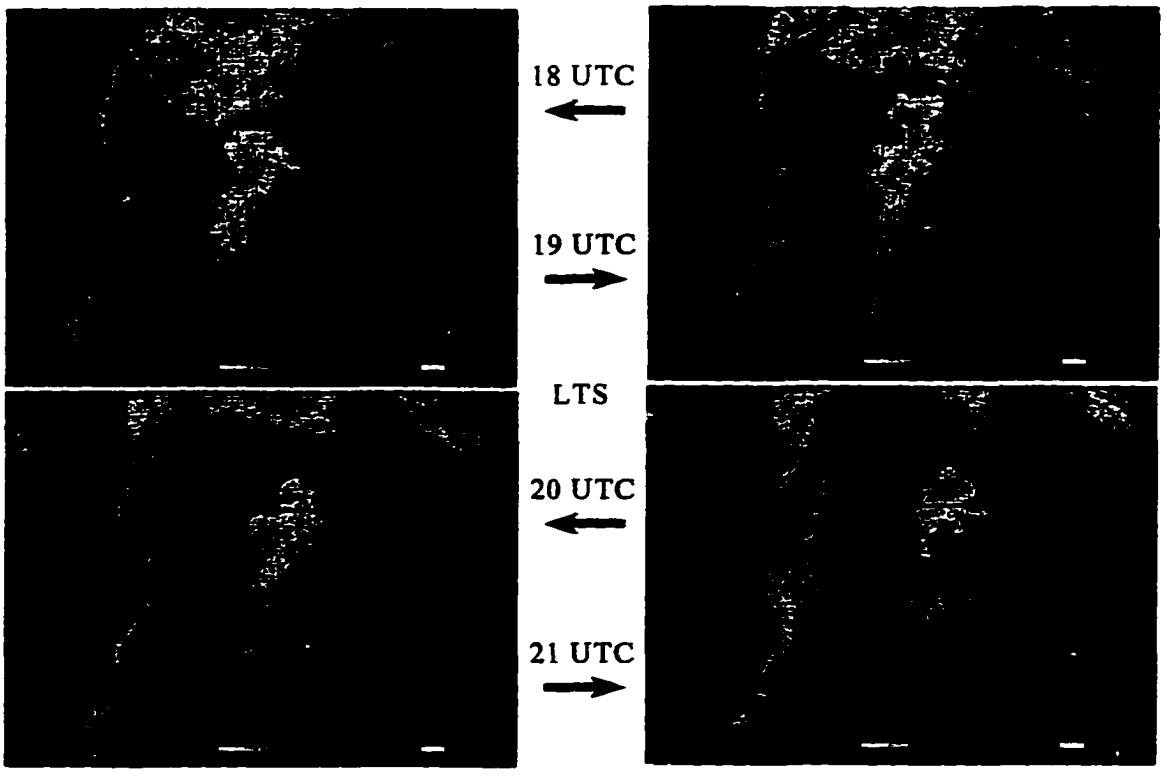

Figure 9-2 - Composite radar summary for 7 May 1995 between 1800 UTC and 2100 UTC in Oklahoma and north Texas.

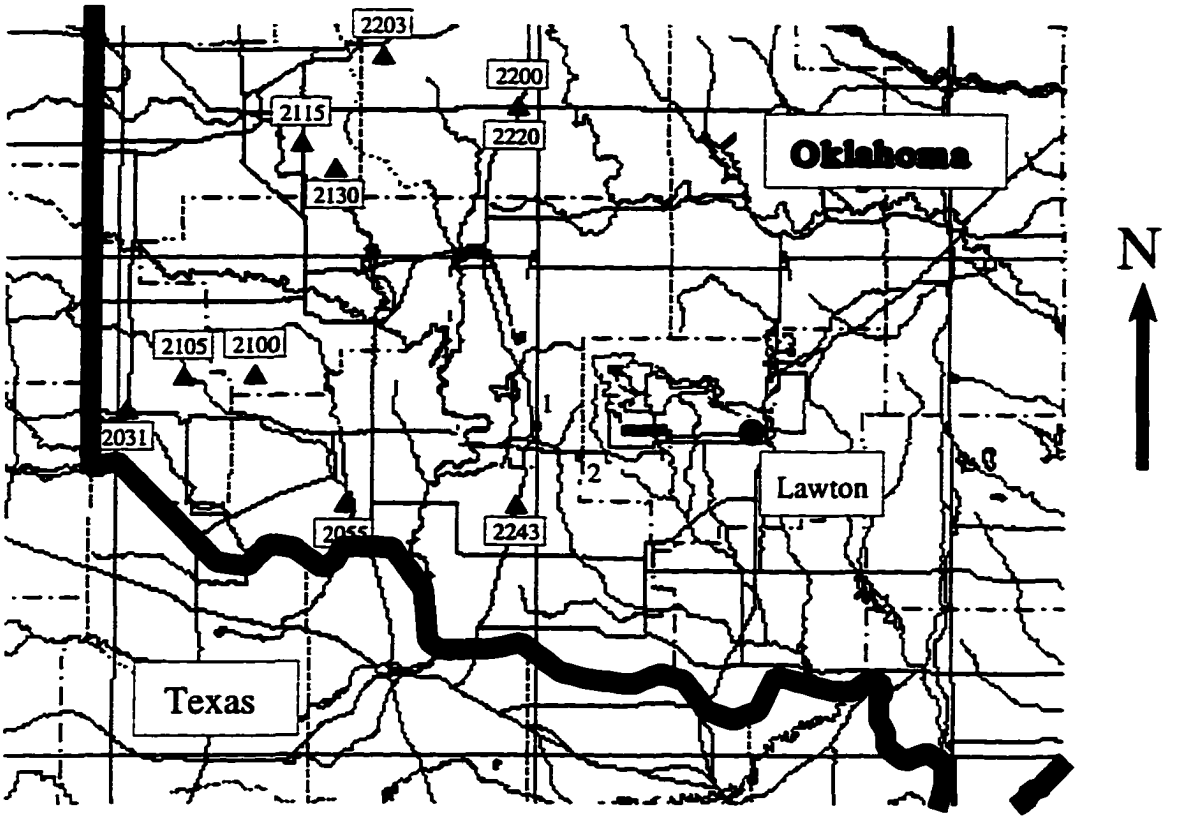

Figure 9-3 - A map of significant hail fall reports in southwestern Oklahoma on 7 May 1995. Time of the hail report is given near the triangle marker and is in UTC. The small squares indicate the sites where spectra were recorded. The first site, identified by the number "1" next to the marker, is in Mountain Park, Oklahoma. The second site, identified by the number "2" next to the marker, is 16 km to the east southeast of Mountain Park.

severe thunderstorms. A broken squall line developed in the Texas Panhandle at 1800 UTC and progressed eastward into Oklahoma by 2000 UTC (Fig. 9-2). The storms produced heavy rain and hail as they entered Oklahoma. Hail reports, in Oklahoma, began with 2.24 cm hail in Hollis, Oklahoma at 2031 UTC and are indicated by small triangles on the map of southwestern Oklahoma (Fig. 9-3). The storms continued to progress eastward and were just to the west of Mountain Park, Oklahoma at 2200 UTC

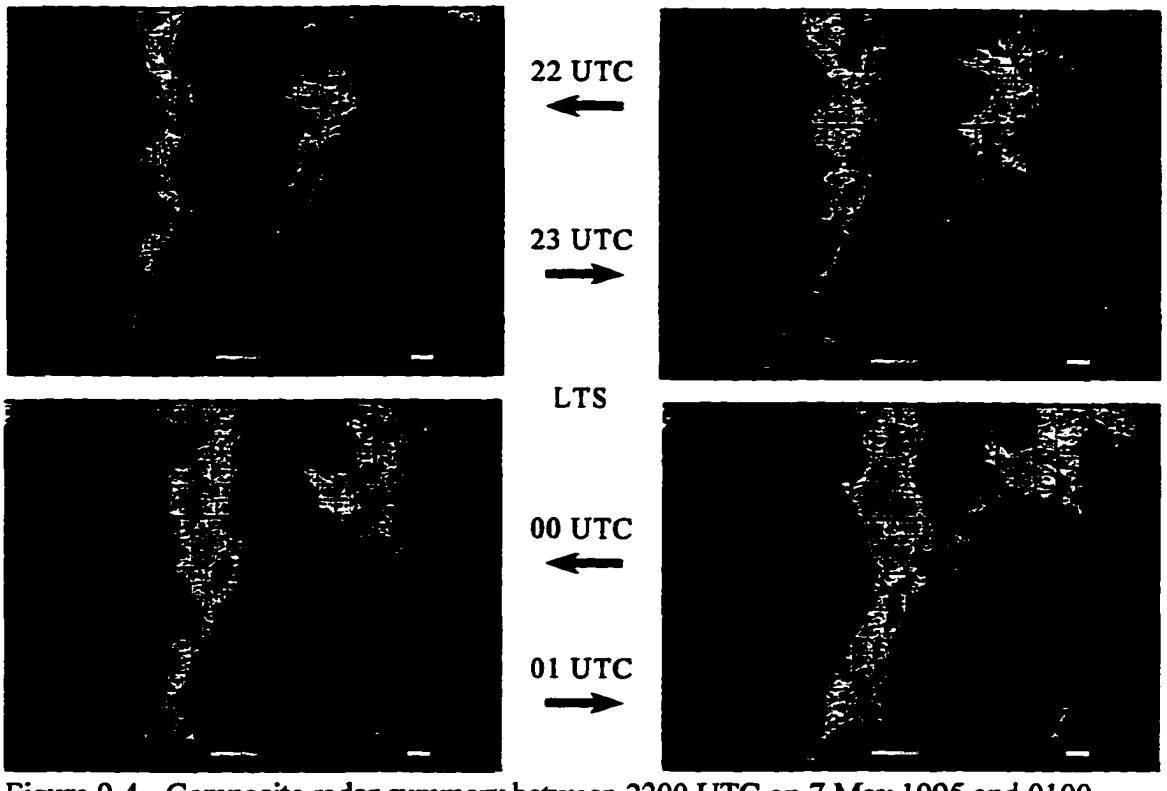

Figure 9-4 - Composite radar summary between 2200 UTC on 7 May 1995 and 0100 UTC on 8 May 1995 in Oklahoma and north Texas.

(Fig. 9-4). The first spectra (Fig. 9-5a) of the storm were recorded in Mountain Park, Oklahoma (site "1" in Fig. 9-3) at 2206 UTC looking to the northwest. A closer look at Twin Lakes WSR-88D radar data (Fig. 9-6) indicates that the recorded spectrum was viewing a region of the storm with some of the highest radar reflectivities. A gust front surged out ahead of the precipitation core but had yet to reach the observation site in Mountain Park. The spectrum was recorded of the darkest area beneath the gust front looking into the precipitation core of the storm. The spectrum was taken viewing a deeply shadowed region of the thunderstorm but the observer was illuminated by skylight and reflected sunlight (Fig. 9-7). Since the spectrophotometer gathered data from light beneath the central part of the storm, the primary path of the radiation to the observer is

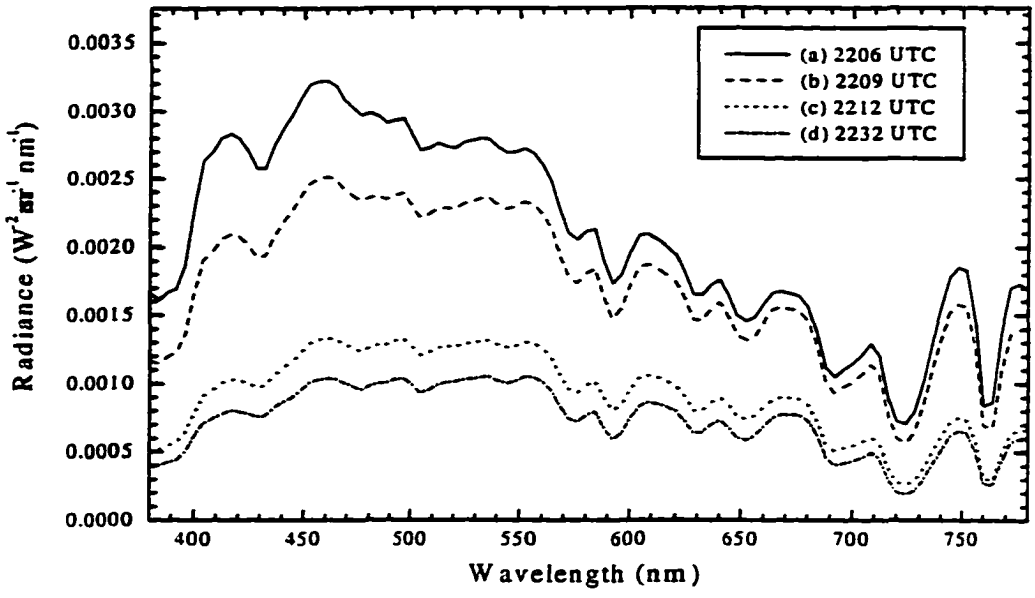

Figure 9-5 - Spectra of a severe thunderstorm observed near Mountain Park, Oklahoma on 7 May 1995 looking to the northwest. (a) 2206 UTC: The storm appeared to be dark blue in color. The peak spectral radiance occurs at 456 nm. The dominant wavelength is 486.1 nm and the excitation purity is calculated to be 8.00%. (b) 2209 UTC: The sky coloration had changed little from that of 2206 UTC. The peak spectral radiance occurs at 460 nm. The dominant wavelength is 494.7 nm and the excitation purity is calculated to be 3.23%. (c) 2212 UTC: Visual observers noted a greenish cast to the clouds. Spectrum was recorded looking to the north. The peak spectral radiance occurs at 460 nm. The dominant wavelength is 522.9 nm and the excitation purity is calculated to be 2.12%. (d) 2232 UTC: Spectrum of a green thunderstorm. Spectrum was recorded 16 km east-southeast of Mountain Park, Oklahoma looking to the north. The peak spectral radiance occurs at 536 nm. The dominant wavelength is 536.8 nm and the excitation purity is calculated to be 2.86%.

that light transmitted through the cloud. There were no reports of hail in the vicinity of the storm when the first spectrum was recorded (Fig. 9-3). The vertically integrated liquid (VIL) estimates from the TLX radar do not have enough spatial resolution to give a good measure of the water content over the observation point and the FDR radar was not recording during this part of the day. As a result, an assumed

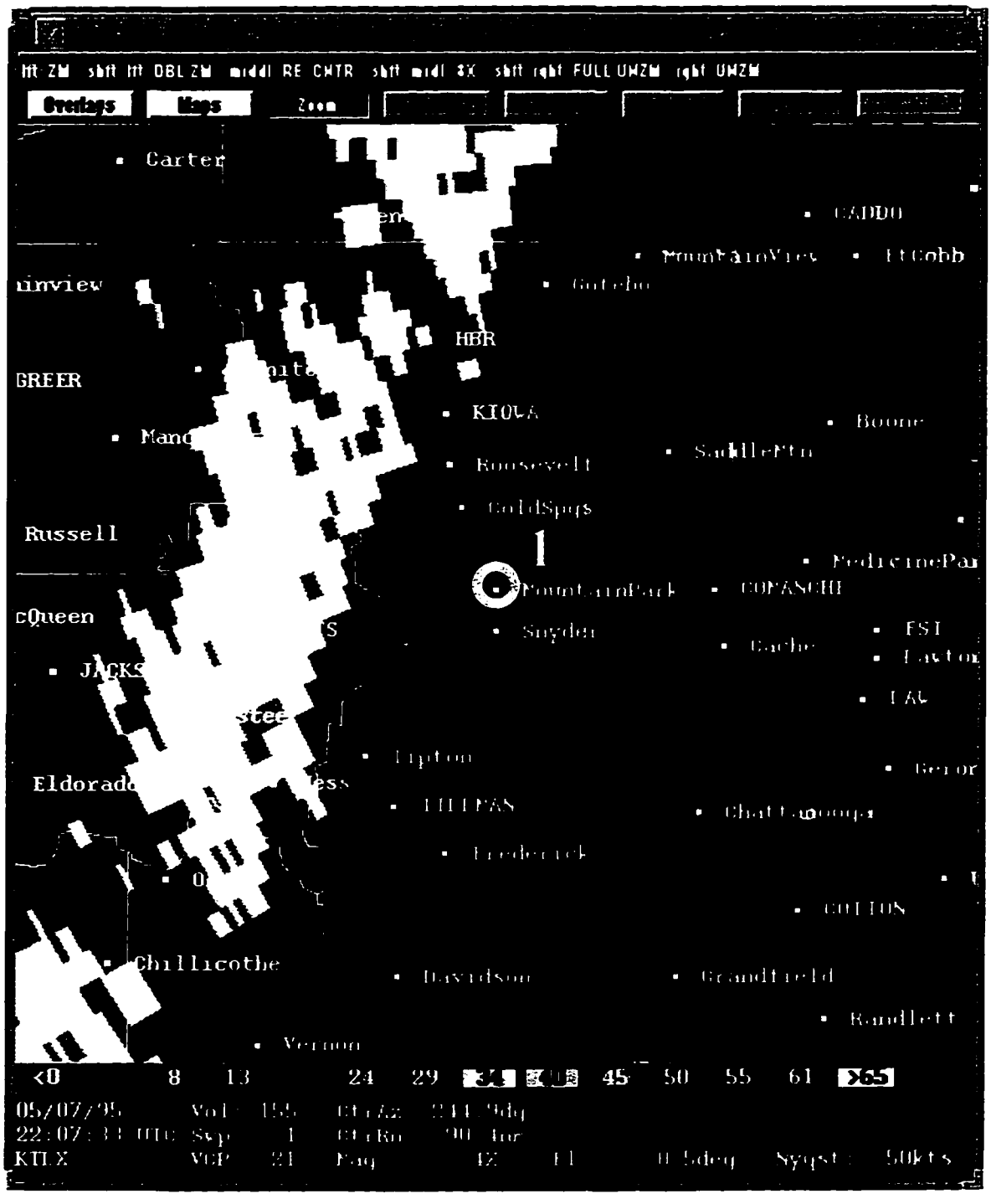

Figure 9-6 - WSR 88D reflectivity from the Twin Lakes (TLX) radar. The circle indicates the location of the first spectrum recorded of this storm (Fig 9-5a) at 2206 UTC looking toward the northwest.

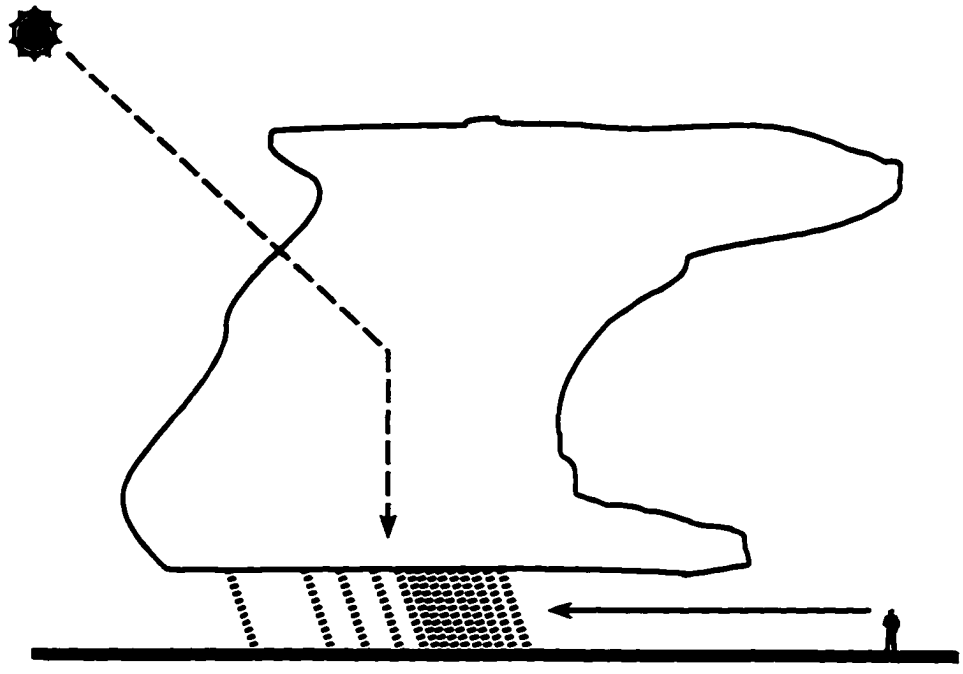

Figure 9-7 - Schematic of the path of light through the thunderstorm and the relative position of the observer when the first spectrum was recorded at 2206 UTC in Mountain Park, Oklahoma on 7 May 1995.

drop size distribution and liquid water content were necessary to compute the downwelling diffuse radiance beneath the cloud using the Eddington approximation. Composite radar data from the National Meteorological Center (NMC) indicated echo tops of 49 000 feet or 14.9 km. The solar zenith angle was calculated to be 52° at the time the first spectrum was recorded. Using a mean drop size of 22 μm, and the above parameters, the Eddington approximation model for transmitted light alone predicted a dominant wavelength of less than 493 nm for liquid water contents greater than 4.0 g m^{-3}, a realistic value for the precipitation core in severe thunderstorms. The dominant

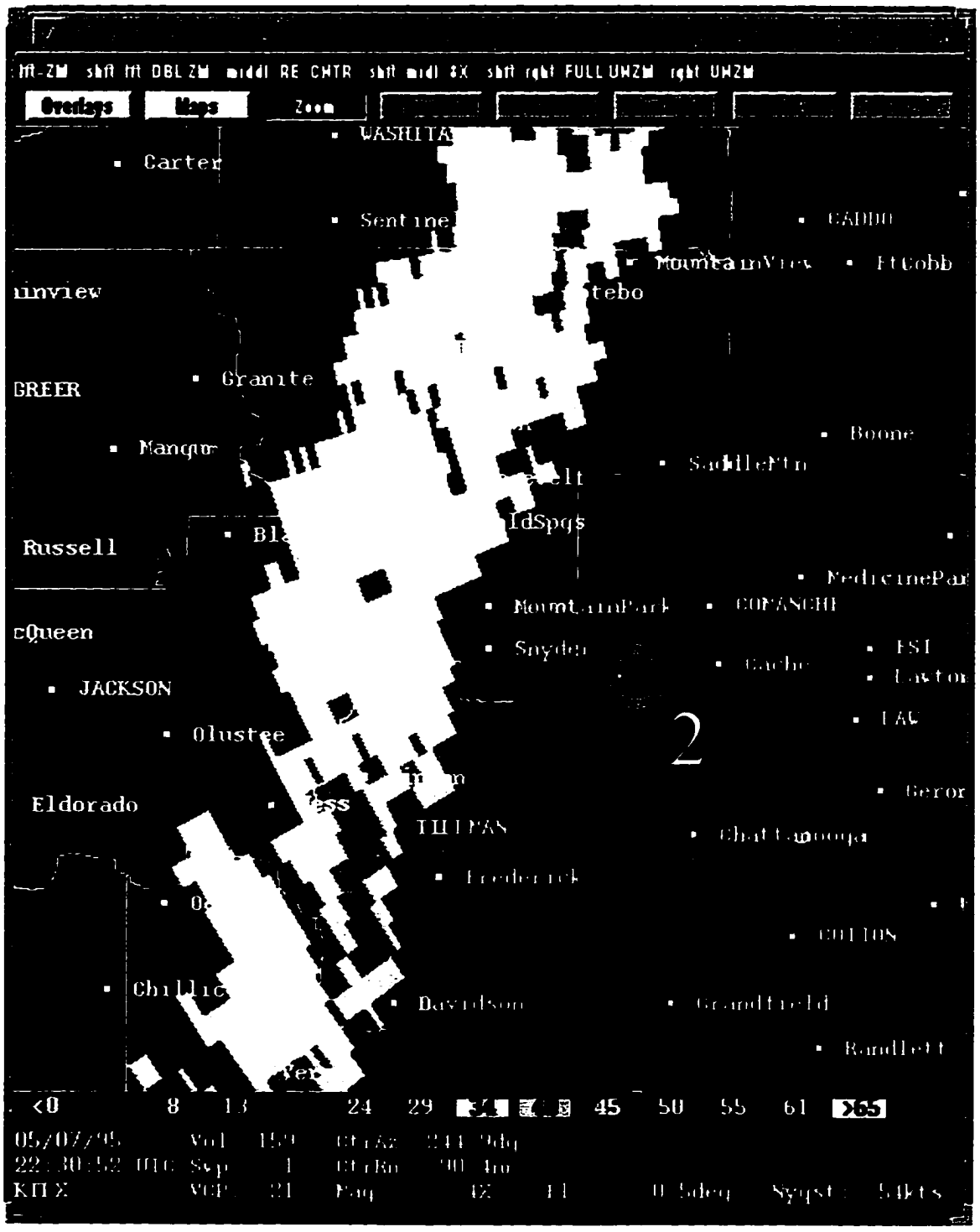

Figure 9-8 - WSR 88D reflectivity from the Twin Lakes (TLX) radar. The circle indicates the location of the last spectrum recorded of this storm (Fig 9-5d) at 2232 UTC looking toward the north.

wavelength of the measured spectrum was 486.1 nm and the purity of 8 %. This agrees with the observer seeing a "blue-gray" colored

The observers watched the storm advance for several moments and recorded spectra at three minute-intervals (Fig 9-5b,c). The approaching storm required the observers to move to a safer area located to the east. By the time the observers had moved to a location 16 km east southeast of Mountain Park (Position 2 on Fig 9-1 and position 2 on Fig. 9-8), the color of the clouds had turned to a spectacular aqua-green color. Heavy precipitation was falling in Mountain Park (Fig. 9-8) and the gust front had moved overhead. The leading edge of the clouds was now located to the east of the observers. The perceived green color came from the clouds to the north and northwest under the gust front. The spectrum recorded at 2232 UTC (Fig. 9-5d) was looking to the north of these green clouds. Figure 9-9 shows a possible scenario for the light that reached the observer. To check this, the Eddington model was run using a drop size of 7 μm (to simulate a cloud-only environment), a thickness of 2 km (the approximate thickness of the overhead clouds), and a solar zenith angle of 57°. Skylight was included in the calculations. The model run shows that for a liquid water content of 5 g m^{-3}, a spectrum that is colorimetrically similar to the one recorded on 7 May 1995 is produced. There were no hail reports from the region where the spectrum was recorded (Fig. 9-3).

The radar images (Figs. 9-6 and 9-8) indicate that little had changed in the structure of the squall line between the time that the first (blue) spectrum was recorded and the time the last (green) spectrum was recorded. Also, there were no reports of significant hail in the vicinity of either measurement site during the observation period.

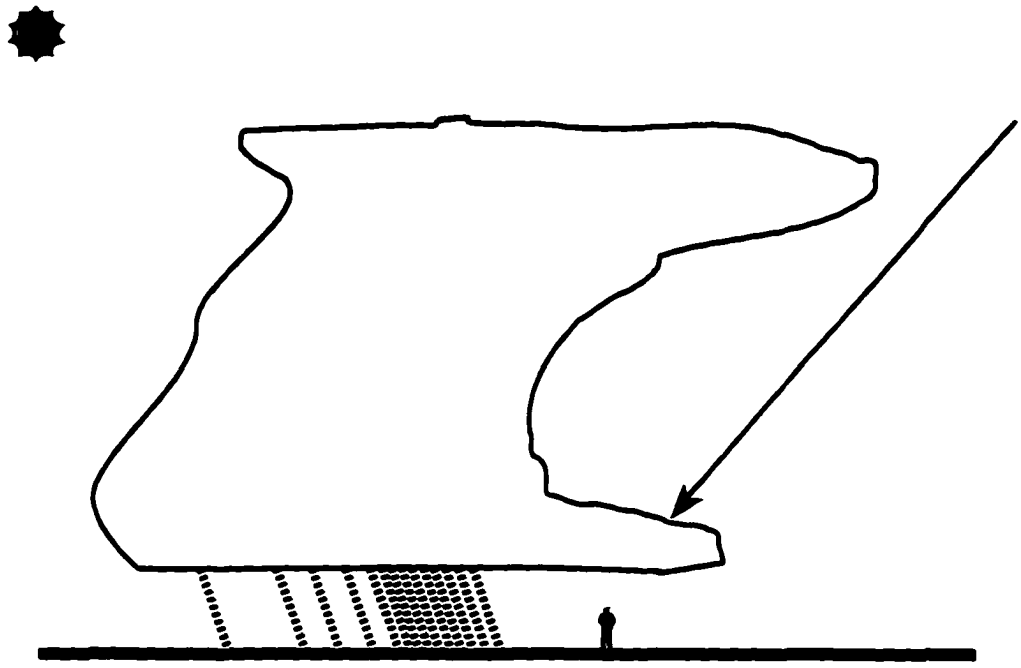

Figure 9-9 - Schematic of the path of light through the thunderstorm and the relative position of the observer when the last spectrum was recorded at 2232 UTC 16 km to the east southeast of Mountain Park, Oklahoma on 7 May 1995.

The only significant change was the location of the observer with respect to the oncoming storm and the region of the storm being measured. In the first case, the storm was farther away and the spectrum was recorded of the light beneath the core of the storm. That light was produced by sunlight diffusely transmitted through a very thick cloud. Most of the longer wavelength light had been absorbed by the water in the cloud yielding a bluish-gray light at the bottom.

At the second observation site, the leading edge of the gust front (arcus) cloud had moved to the east of the observers and the green color of the clouds was observed to be emanating from the underside of the arcus. The spectrum was recorded of light that was

transmitted through a comparatively thin layer of clouds. As measured by the spectrophotometer, the color of the light was yellow-green.

As stated previously there were no hail reports associated with this storm in the Mountain Park area. Also, there was no hail, or even precipitation, reported at both observing sites when the observations were being made. Since the green spectrum (Fig. 9-5d) was recorded looking to the north, along the gust front and not into the core region, there is little likelihood that hail was in any great quantity aloft. The TLX WSR-88D radar shows a reflectivity of less than 34 dBZ in the region where the instrument was pointing. This is not a reflectivity level that suggests a significant amount of hail was present. From this evidence, and the theoretical arguments made earlier, one can conclude that hail is not a necessary requirement for the creation of the perceived green color in some thunderstorms. What is necessary is the correct geometry to place the observer in the right place at the right time.

Chapter 10: Summary and Conclusions

During the spring and summer of 1995, a portable spectrophotometer was used to record the spectrum of visible light transmitted and reflected by thunderstorms in Oklahoma, Colorado, Texas, Kansas, and Florida under a variety of conditions. There were several objectives to be accomplished in this study. The first was to determine whether the green color in some severe thunderstorms is real or a figment of a fertile imagination that have been passed on from one generation to the next. It is clear, from the measurements presented here, that green thunderstorms exist and the green light can be safely and accurately measured using a handheld spectrophotometer. Spectra of thunderstorms that appear green to the human observer from both ground level as well as from the air have now been well documented. Furthermore, it has been demonstrated that, to the surface-based observer, the optical properties of thunderstorms do undergo transformations, often with a change in color toward the green during the storms' lifetimes. The change in color is gradual but may appear dramatic to an observer between observation intervals as short as one-half hour. The location and viewing perspective of the observer is critical in seeing these optical effects. It has been shown that, although the luminance of the clouds is decreasing as the color of the clouds shifts toward the green, observers often perceive the green clouds to be brighter. This may be attributable to the

fact that green is an unusual color overhead, and therefore may be more striking to the observer. Finally, observations have shown that the green color may last for an extended time, although an observer on the ground would note the color only as the storm passed by.

The second objective was to test the validity of prevailing hypotheses including those of of Bohren and Fraser (1993) pertaining to the occurrence of thunderstorms that appear to the human observer to be green. It has been shown that the type of green thunderstorm discussed by Fraser is not the type typically associated with Great Plains severe thunderstorms. His theory, although theoretically pleasing, is not suited too terribly well to the real world. His assumption that a thunderstorm is black is quite unrealistic. Reflected light from the non-black background storm dominates any airlight effect that has been shown to cause "Fraser" green thunderstorms. Observations and calculations indicate that the color of the light perceived is usually reduced to that of the setting sun.

Bohren's theory matches the observations better than any of the other hypotheses. It has been shown theoretically that light from the sun, not necessarily the setting sun, and an appropriate specification of cloud hydrometeors, can create almost any shade of colored light from blue-green to yellow-green. The only catch is that the purity of the color is so low that the observer, unless looking very hard, may not perceive it. However, the Bohren transmitted light hypothesis tells only part of the story. Light gets underneath the thunderstorm from all directions. Although light reflected by the ground plays only a minimal role in the color seen in the clouds (unless the cloud is *very* low and the ground

is *brightly* illuminated), the skylight is important in reproducing the shape of the spectrum, yet the color seen by the clouds is changed minimally from the color of light that was exclusively transmitted.

The results of this study suggest that the most important factor in whether the green light is seen by the observer is the observers storm relative position. From the limited quantitative data taken on green thunderstorms to date it would be reckless to offer a set of rules or guidelines to be followed by those in pursuit of the green light and none shall be given here. It was demonstrated in Chapter 9 that a storm with little structural variation over time may appear colorimetrically entirely different depending on the position of the observer.

Conventional wisdom and general folklore, at least in the Midwest and Great Plains, often attribute the green appearance of thunderstorms to the presence of hail. Until now, there has been no objective documentation of the occurrence of green storms in conjunction with thunderstorms or deep convection. Much of the folklore regarding green thunderstorms involves the notions that hail or ground reflections cause the coloration of the clouds. It has been shown that ground reflections alone cannot account entirely for the green coloration. Furthermore, an example has been presented in which a cloud appeared both green and non-green, in the same storm, where hail was not reported at the observation site and no significant hail was reported in the vicinity of the observations. It is possible that the storms observed to be green in this study satisfy the requirement of Bohren's hypothesis (which does not require hail) but were also so large that hail was produced by them as a byproduct. The optical depth is one of the main

parameters which determine the amount of absorption by of water clouds. Certainly the presence of hail changes the hydrometeor size distribution and reduces the optical depth, but hail alone cannot create the green light.

During all these observational periods, there was not a single observation that fit the anecdotal description of an eerie, sickening yellow-green light that is often reported in coincidence with exceptionally severe storms. Indeed, the color slides taken with the spectral measurements do not show the spectacular coloration of the storms reported by observers in the field, though the spectral measurements clearly confirmed the subjective impression of the color of the storm. We have only scratched the surface in our attempt to solve this mystery. Many more observations, in conjunction with better studies of hydrometeor size and habit, by both *in situ* and multi-parameter radar observations are the next logical step in the attempt to understand this elusive phenomenon.

References

Bedford, R.E., and G.W. Wyszecki, 1958: Luminosity function for various field sizes and levels of retinal illuminance. *J. Opt. Soc. Amer.*, **48,** 406-411.

Birch, J., and W.D. Wright, 1961: Color discrimination. *Physics in Med. and Biol.*, **6,** 3.

Bohren, C.F., 1991: *What Light Through Yonder Window Breaks?* John Wiley & Sons, New York, 190 p.

Bohren, C.F., and A.B. Fraser, 1993: Green thunderstorms. *Bul. Amer. Meteor. Soc.*, **74,** 2185-2193.

Bohren, C.F., and D.R. Huffman, 1983: *Absorption and Scattering of Light by Small Particles.* John Wiley & Sons, New York, 530 p.

Bouman, M.A., and P.L. Walraven, 1972: Color discrimination data, in: *Handbook of Sensory Physiology,* Vol. VII/4: *Visual Psychophysics* (D. Jameson and L.M. Hurvich, Eds.), Chapter 19, pp. 484-516, Springer-Verlag, New York.

Brandes, E.A., J. Vivekanandan, J.D. Tuttle, and C.J. Kessinger, 1995: A study of thunderstorm microphysics with multiparameter radar and aircraft observations. *Mon. Wea. Rev.*, **123,** 3129-3143.

Braun, C. L., and S. N. Smirnov, 1993: Why is water blue? *J. Chem. Educ.*, **70,** 612-614.

Browning, K.A., 1965: A family outbreak of severe local storms — A comprehensive study of the storms in Oklahoma on 26 May 1963: Part I. *AFCRL-65-695(1), Spec. Rept. 32,* Clearinghouse for Federal Scientific and Technical Information, Springfield, VA, 346 pp.

Browning, K.A., and R.J. Donaldson, Jr., 1963: Airflow and structure of a tornadic storm. *J. Atmos. Sci.*, **20,** 533-545.

Browning, K.A., and G.B. Foote, 1976: Airflow and hail growth in supercell storms and some implications for hail suppression. *Q. J. R. Meteorol. Soc.*, **102,** 499-533.

Browning, K.A., and F.H. Ludlam, 1962: Airflow in convective storms. *Q. J. R. Meteor. Soc.*, **88**, 117-135.

Burke, J., 1978: *Connections.* Little Brown & Co., Boston.

Chisholm, A.J., 1970: Alberta hailstorms: a radar study and model. Ph.D. thesis, McGill University, Montreal, Ontario, 287 pp.

Chisholm, A.J., and H. Renick, 1972: The kinematics of multicell and supercell Alberta hailstorms. Alberta Hail Studies, 1972, Research Council of Alberta, Edmonton, Alberta, Hail Studies Report No. 72-2, 24-31.

Cornsweet, T.N., 1970: *Visual Perception.* Academic Press, New York, 475 p.

Daniel, M., 1996: *Photometry and Colorimetry.* Photo Research Inc., Chatsworth, California.

Detwiler, A., 1990: Analysis of cloud imagery using box counting. *Int. J. Rem. Sensing,* **11(5)**, 887-898.

Detwiler, A.G., R.F. Kelly, and P.L. Smith, 1993: *Summary Report of T-28 Deployment to Colorado (June 1992).* Institute of Atmospheric Sciences, South Dakota School of Mines and Technology, Rep. IAS/R-92/09, 33 pp. plus appendixes.

Dodge, J., J. Arnold, G. Wilson, J. Evans, and T.T. Fujita, 1986: The cooperative Huntsville Meteorological Experiment (COHMEX). *Bull. Amer. Meteorol. Soc.*, **67**, 417-419.

Donaldson, R.J., A.A. Spatola, and K.A. Browning, 1965: A family outbreak of severe local storms — A comprehensive study of the storms in Oklahoma on 26 May 1963: Part I. *AFCRL-65-695(1), Spec. Rept. 32,* Clearinghouse for Federal Scientific and Technical Information, Springfield, VA, pp. 73-97.

Doswell, C.A., III, and D.W. Burgess, 1993: Tornadoes and Tornadic Storms: A Review of Conceptual Models, in *The Tornado: Its Structure, Dynamics, Prediction, and Hazards,* edited by C. Church, D. Burgess, C. Doswell, and R. Davies-Jones, pp 161-172, American Geophysical Union, Washington, D.C.

Edwards, L., 1995: Storm troopers. *Details,* November 1995, 131-135, 180.

Fankhauser, J.C., G.M. Barnes, L.J. Miller, P.M., and Roskowski, 1983: Photographic documentation of some distinctive cloud forms observed beneath a large cumulonimbus. *Bull. Amer. Meteorol. Soc.*, **64**, 450-462.

Flatau, P. J., g. J. Tripoli, J. Verlinde, and W. R. Cotton, 1989: *The CSU-RAMS Microphysics Module: General Theory and Code Documentation.* Department of Atmospheric Science, Colorado State University, Fort Collins, Colorado, 88 pp.

Foukal, P., 1990: *Solar Astrophysics.*, J. Wiley & Sons.

Fraser, A.B., 1978: Why green thunderstorms are severe. *Topical Meeting on Meteorological Optics,* Keystone , CO, Optical Society of America.

Fuller J.G., 1987: *Tornado Watch #211.* William Morrow and Company, New York, p. 66.

Gallagher, F.W., III, W.H. Beasley, and C.F. Bohren, 1996: Green thunderstorms observed. *Bull. Amer. Meteorol. Soc.,* **77,** 2889-2897.

Goody, R. M., and Y. L. Yung, 1989: *Atmospheric Radiation Theoretical Basis, 2nd Ed.,* Oxford University Press, New York, 519 pp.

Halliday, D., and R. Resnick, 1978: *Physics,* 3rd Ed., John Wiley and Sons, New York, 1131 pp.

Hobbs, P. V., 1974: *Ice Physics.* Oxford University Press, London, 835 pp.

Johnson, G.N. and P.L. Smith, Jr., 1980: Meteorological instrumentation system on the T-28 thunderstorm research aircraft. *Bull. Amer. Meteorol. Soc.,* **61,** 972-979.

Kaiser, P.K., J.P. Comerford, and D.M. Bodinger, 1976: Saturation of spectral lights. *J. Opt. Soc. Amer.,* **66,** 818-826.

Knight, C.A., and P. Squires, 1982: *Hailstorms of the Central High Plains, I. The National Hail Research Experiment.* Colorado Associated University Press, Boulder, CO, 282 pp.

Kondratyev, K. YA., 1969: *Radiation in the Atmosphere.* Academic Press, New York, 912 pp.

Liou, K. N., 1980: *An Introduction to Atmospheric Radiation.* Academic Press, San Diego, 392pp.

Liou, K.N., 1992: *Radiation and Cloud Processes in the Atmosphere: Theory, Observation, and Modeling.* Oxford University Press, Oxford, 487pp.

Lynch, D.K., and W.C. Livingston, 1995: *Color and Light in Nature.* Cambridge University Press, Cambridge, 254 p.

Marwitz, J.D., 1972: The structure and motion of severe hailstorms: Part I. Supercell storms. *J. Appl. Meteorol.,* **11,** 166-179.

Meinel, A., and M. Meinel, 1983: *Sunsets, twilights, and evening skies.* Cambridge University Press, Cambridge.163 pp.

Minnaert, M., 1954: *The Nature of Light & Color in the Open Air.* Dover Publications, New York, 362pp.

Mish, F.C., 1989: *Webster's Ninth New Collegiate Dictionary.* Merriam-Webster Inc., Springfield, MA.

Musil, D.J., and P.L. Smith, 1989: Interior characteristics at mid-levels of thunderstorms in the southeastern United States. *Atmos. Res.,* **24,** 149-167.

Musil, D.J., A.J. Heymsfield, and P.L. Smith, 1986: Microphysical characteristics of a well-developed weak echo region in a High Plains supercell thunderstorm. *J. Climate Appl. Meteorol.,* **25,** 1037-1051.

Nelson, S.P., and R.R. Braham, Jr., 1975: Detailed observational study of a weak echo region. *Pure Appl. Geophys.,* **113,** 735-746.

NOAA, 1995: *Storm data, Volume 37, Number 5.* U.S. Department of Commerce, Washington D.C.

Optical Society of America, Committee on Colorimetry, 1953: *The Science of Color.* Thomas Y. Crowell Co., New York.

Pick W.H., 1930: The significance of the green sky. *Q. J. R. Meteorol. Soc.,* **56,** 350-352.

QJRMS, 1930: Editorial note. *Q. J. R. Meteorol. Soc.,* **56,** 364.

Ramachandran, R., A. Detwiler, J. Helsdon, Jr., and P.L. Smith, 1996: Precipitation development and electrification in Florida thunderstorm cells during Convection and Precipitation/Electrification Project. *J. Geophys. Res.,* **101(D1),** 1599-1619.

Rasmussen, E.N., J.M. Straka, R. Davies-Jones, C.A. Doswell III, F.H. Carr, M.D. Eilts, and D.R. MacGorman, 1994: Verification of the origins of rotation in tornadoes experiment: VORTEX. *Bull. Amer. Meteor. Soc.,* **75,** 995-1006.

Renick, J.H., A.J. Chisholm, and P.W. Summers, 1972: The seedability of multi-cell and supercell storms using dropable pyrotechnic flares. *Preprints 3rd Conf. On Weather Modification,* Rapid City, SD, June 26-29, 1972. Amer. Meteorol. Soc., Boston, 272-278.

Riordan, C.J., D.R. Myers, and R.L. Hulstrom, 1990: *Solar Spectral Radiation Data Base Documentation, Vol. I.* Solar Energy Research Institute, Golden, CO.

Robertson, A.R., 1992: Color perception. *Phys. Today,* **Dec. 1992,** 24-29.

Rogers, R.R., and M.K. Yau, 1989: *A Short Course in Cloud Physics.* 3rd Ed., Pergamon Press, Oxford, 290 pp.

Sand, W.R., and R.A. Schleusener, 1974: Develpment of an armored T-28 aircraft for probing hailstorms. *Bull. Amer. Meteorol. Soc.,* **55,** 1115-1122.

Schemenauer R.S., J.I. MacPherson, G.A. Isaac, and J.W. Strapp, 1980: Canadian participation in HIPLEX 1979. Report APRB 110 P 34, Atmospheric Environment Service, Environment Canads, 206 pp.

Shettle, E. P., and J. A. Weinman, 1970: The transfer of solar irradiance through inhomogeneous turbid atmospheres evaluated by Eddington's approximation. *J. Atmos. Sci.,* **27,** 1048-1055.

Smithsonian Institution, 1949: *Smithsonian Meteorological Tables,* R. J. List, Ed., Smithsonian Institution Press, Washington D. C.

Straka, J.M., and J.R. Anderson, 1993: Numerical simulations of microburst-producing storms: Some results from storms observed during COHMEX. *J. Atmos. Sci.,* **50,** 1329-1348.

Tricker, R.A.R., 1970: *Introduction to Meteorological Optics.* American Elsevier Publishing Co. Inc., New York, 285 pp.

van de Hulst, H. C., 1957: *Light Scattering by Small Particles.* Dover Publications, New York, 470 pp.

Wallace, and Hobbs, 1977: *Atmospheric Science, an Introductory Survey.*, Academic Press

Weaver, J.F., J.F.W. Purdom, and C.A. Doswell, III, 1996: A preliminary look at the Ardmore, OK tornado of 7 May 1995. *Preprints, 18th Conf. on Severe Local Storms,* American Meteorological Society, Boston, 137-140.

Wyszecki, G., and W. S. Stiles, 1982: *Color Science. Concepts and Methods, Quantitative Data and Formulae, 2nd Ed.*, John Wiley and Sons, New York, 950 p.

Zuev, V.E., 1970: *Atmospheric Transparancy in the Visible and Infrared.* U.S. Department of Commerce, Springfield, VA, 215 p.

Appendix A

Derivation of the Spherical Earth Approximation

Consider the problem of the increase in optical path for increasing solar zenith angles on a sphere. A spherical shell represents an atmosphere of uniform depth *h* with a uniform number density of molecules equal to the sea level value. Given these constraints, the optical depth is finite. Consider the following geometry:

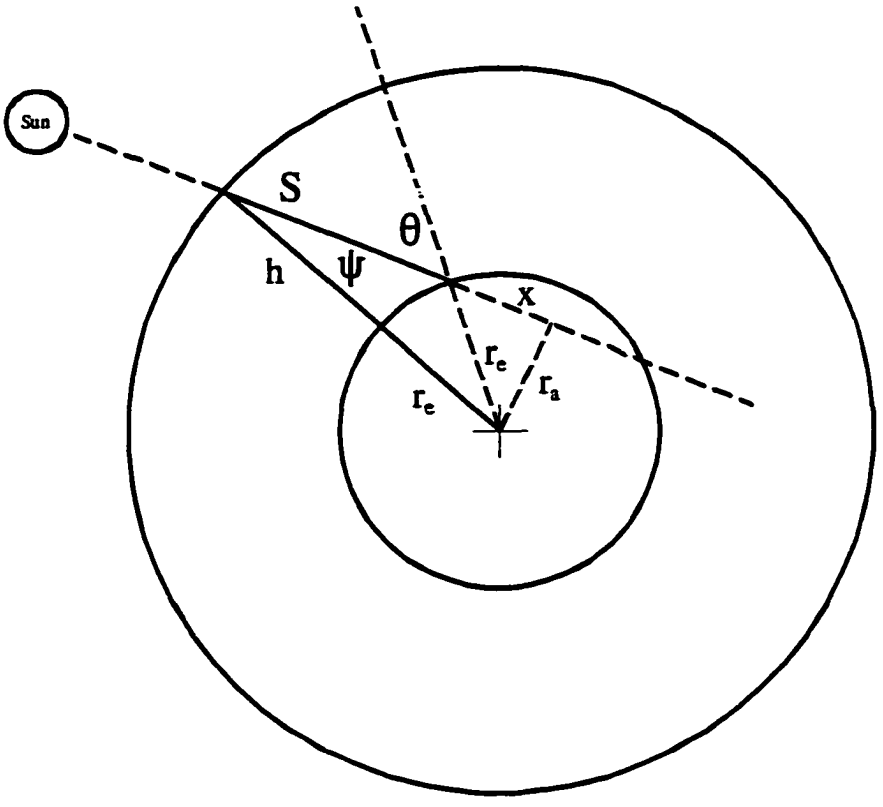

Figure A-1 - Geometry used for the spherical earth approximation derivation.

where r_e is the radius of the earth and θ is the solar zenith angle. To begin, the known variables are r_e, h, and θ. The objective is to determine the ratio of the slant height (S) in the atmosphere to the vertical height, h. First consider the triangle bounded by r_e, r_a, and x. Solving for x,

$$x = r_e \cos\theta \qquad \text{A-1}$$

Using the Pythagorean theorem,

$$r_e^2 \cos^2\theta + r_a^2 = r_e^2$$

$$r_a = r_e \sqrt{1-\cos^2\theta} \qquad \text{A-2}$$

$$r_a = r_e \sin\theta$$

Next consider the triangle bounded by (r_e+h), (x+S), and r_a. Using the definition of the sine function for ψ,

$$\sin\psi = \frac{r_a}{r_e + h} = \frac{r_e \sin\theta}{r_e + h}$$

$$\psi = \sin^{-1}\left[\frac{r_e \sin\theta}{r_e + h}\right] \qquad \text{A-3}$$

Since

$$\cos\psi = \frac{S+x}{r_e+h} \qquad \text{A-4}$$

then

$$(r_e + h)\cos\psi - x = S \qquad \text{A-5}$$

giving the final result of

$$\frac{S}{h} = \frac{(r_e + h)\cos[\sin^{-1}(\frac{r_e \sin\theta}{r_e + h})] - r_e \cos\theta}{h} \qquad \text{A-6}$$

Check Solution — $\theta = 0$

As a check on the validity of this derivation, Eq. A-6 is verified at the limits of the solar zenith angle. First the limit at solar noon, where $\theta=0°$, is checked. Using Eq. A-6,

$$\frac{S}{h} = \frac{(r_e + h) - r_e}{h} = 1 \qquad \text{A-7}$$

so, at solar noon, the slant path length equals the vertical path length.

Check Solution — $\theta = \pi/2$

The second limit is at sunset where $\theta=\pi/2$. Again using Eq. A-6,

$$\frac{S}{h} = \frac{(r_e + h)\cos[\sin^{-1}(\frac{r_e \sin(\frac{\pi}{2})}{r_e + h})]}{h} \qquad \text{A-8}$$

$$\frac{S}{h} = 39.92$$

To check to see if this is reasonable, consider the sunset geometry

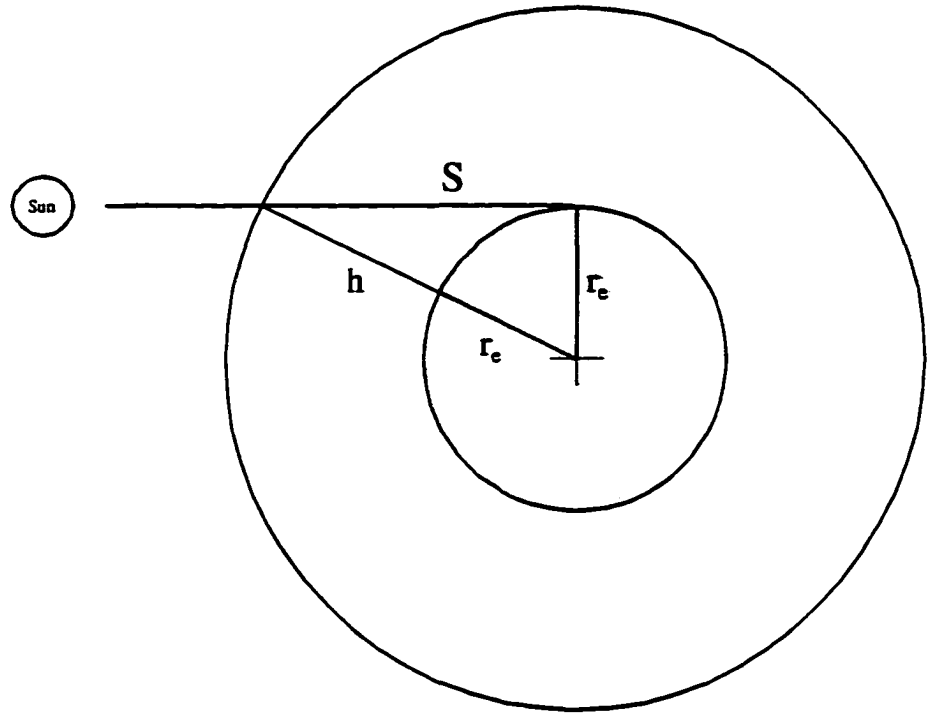

Figure A-2 - Sunset geometry.

By using the Pythagorean theorem,

$$S^2 + r_e^2 = (r_e + h)^2$$

$$S = h\sqrt{\frac{2r_e}{h} + 1} \qquad \text{A-9}$$

Then the ratio S/h is

$$\frac{S}{h} = \sqrt{\frac{2r_e}{h} + 1} = 39.92 \qquad \text{A-10}$$

and the solution checks.

Appendix B: Derivation of the Eddington Approximation

Radiative Transfer Equation

The derivation begins with a simple introduction to the radiative transfer equation. The radiative transfer equation states that a change in radiative intensity (radiance) can be attributed to two factors. The first is a reduction in the intensity after passing through a portion of the atmosphere. If the path traversed by the radiation is assumed to be ds then the change in intensity can be written as:

$$dI_\lambda = -k_\lambda \rho I_\lambda ds \qquad \text{B-1}$$

where I_λ is the monochromatic radiant intensity (W m^{-2} sr^{-1} nm^{-1}), ρ is the density of the air (kg m^{-3}), and k_λ is the mass extinction coefficient (m^2 kg^{-1}). The extinction coefficient includes the effects of both absorption and scattering. The negative sign indicates that the intensity is reduced by the interaction of the radiation with the atmosphere.

The intensity may be increased by emission by the material and radiation being scattered into the viewing solid angle. This can be represented by:

$$dI_\lambda = j_\lambda \rho ds \qquad \text{B-2}$$

where j_λ is the source function coefficient (m^2 kg^{-1}). A source function can be defined that incorporates both the extinction and source function coefficients. This is called the source function and is written as:

$$J_\lambda = \frac{j_\lambda}{k_\lambda}. \qquad \text{B-3}$$

The combination of equations B-1, B-2, and B-3 forms the basic radiative transfer equation (RTE):

$$\frac{dI_\lambda}{k_\lambda \rho \, ds} = -I_\lambda + J_\lambda. \qquad \text{B-4}$$

To better focus the problem to an atmosphere, a simple plane-parallel atmosphere is used.

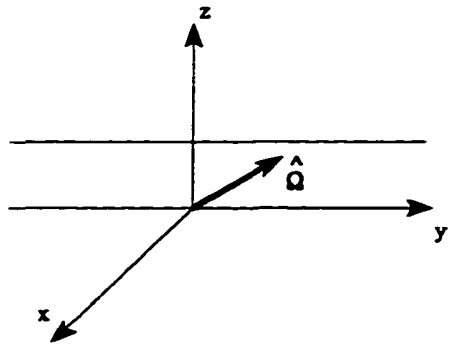

Figure B-1 - Plane parallel geometry.

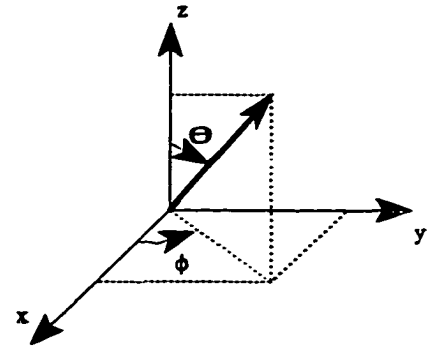

Figure B-2 - Spherical coordinates.

A plane-parallel atmosphere is one for which the absorption coefficient and temperature are functions of the vertical coordinate alone (Goody and Yung 1989). If z is the vertical coordinate then the geometry shown in Figures B-1 and B-2 is used for the plane-parallel assumption.

The simulated atmosphere is illuminated by a flux of radiation from the sun (**I**) and any diffuse intensity is exclusively from below. The geometry shown above will be used for this preliminary analysis. In this case, the three Cartesian axes are represented by x, y, and z. The two parallel lines (left figure) indicate the plane-parallel nature of the

simplified atmosphere. The darker line indicates the directional element of solid angle that represents the pencil of radiation, denoted by Ω which is a function of both the solar zenith angle (μ) and the azimuthal angle (ϕ). So, in future equations Ω can be written as $\Omega = \Omega(\mu,\phi)$.

The radiative transfer equation representing both the direct radiation from the sun and the diffuse radiation from the atmosphere is then written in Ω notation as follows:

$$\mu \frac{dI(\tau,\Omega)}{d\tau} + I(\tau,\Omega) = \omega_o \int P(\Omega',\Omega) I(\tau,\Omega') d\Omega' \qquad \text{B-5}$$

where I is the radiance (or intensity), τ is the optical depth, ω_o is the single scatter albedo, and P is the scattering phase function. The optical depth is a measure of the amount of material that the radiation must traverse. It is defined as an integral quantity, measured from the top of the atmosphere downward, which includes the effects of extinction coefficient, density, and path length. Mathematically it is defined as:

$$\tau = \int_z^\infty k_\lambda \, \rho \, dz'. \qquad \text{B-6}$$

The radiative transfer equation can now be written in terms of optical depth and the cosine of the zenith angle where $\mu = \cos\theta$:

$$\mu \frac{dI_\lambda(\tau;\mu,\phi)}{d\tau} = I_\lambda(\tau;\mu;\phi) - J_\lambda(\tau;\mu,\phi). \qquad \text{B-7}$$

The plane-parallel atmosphere is allowed to be illuminated by a flux of radiation emitted by the sun (πF_o). As before, the only diffuse intensity is from below the observation point. As a result, the reduction of the differential diffuse intensity is caused by events of single scattering and absorption (Liou 1980).

As before, the basic equation of radiative transfer can be written as:

$$dI_\lambda = -k_\lambda \rho \, ds \, I_\lambda + k_\lambda \rho \, ds \, J_\lambda. \qquad \text{B-8}$$

where the change in radiance is a function of two processes: the decrease in radiance due to extinction, and the increase in radiance due to emission and scattering. Using the geometry above, the first component as can be rewritten as:

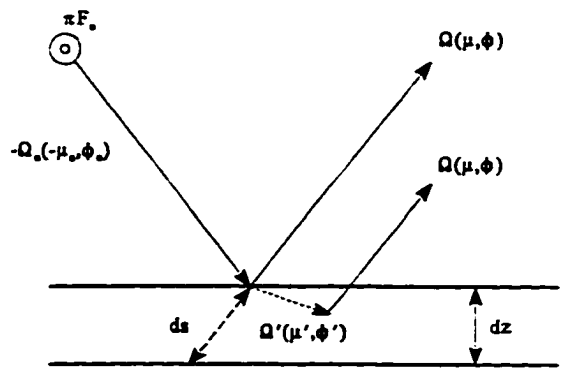

Figure B-3 - Scattering geometry of incident solar radiation.

$$dI_\lambda(z,\Omega) = \frac{-\sigma_e \, N \, I_\lambda(z,\Omega) \, dz}{\cos\theta} \qquad \text{B-9}$$

where $ds = dz/\cos\theta$ is the differential thickness. In (B-9), N represents the number of particles per unit volume, and σ_e represents the mean extinction cross section. There is an increase in intensity due to multiple scattering into Ω from Ω'. This is shown in (B-10) where σ_s is the mean scattering coefficient. $P(\Omega,\Omega')$ is the nondimensional phase function which indicates the probability of radiation from Ω' being scattered into Ω. The integral

$$dI_\lambda(z,\Omega) = \frac{\sigma_s \, N \, dz}{\cos\theta} \int_{4\pi} I_\lambda(z,\Omega') \frac{P(\Omega,\Omega')}{4\pi} \, d\Omega') \qquad \text{B-10}$$

is over the entire solid angle and gives all possible contributions of scattered light. The

RTE is rewritten ignoring the λ notation while remembering that these are monochromatic equations

$$\mu \frac{dI(\tau,\Omega)}{d\tau} = -I(\tau,\Omega) + \frac{\omega_o}{4\pi}\int_{4\pi} I(\tau,\Omega')\ P(\Omega,\Omega')\ d\Omega' \qquad \text{B-11}$$

where ω_o is the albedo of single scatter and indicates the relative importance of scattering compared to total extinction.

The incident intensity can be separated into two components: a direct component from the sun, and a diffuse component from the light scattered by the atmosphere. The direct component is simply the intensity outside the atmosphere, at the mean earth-sun distance (I_o), attenuated by the optical depth of the atmosphere (where μ_o is the solar zenith angle) and is written as

$$I_{dir} = I_o\ e^{-\frac{\tau}{\mu_o}}. \qquad \text{B-12}$$

The direct component is represented by delta functions over solar zenith angle and the azimuthal angle (ϕ). This is necessary since the incident radiation is restricted to a small pencil of light. The direct solar radiation is written as:

$$I_o = \overline{I_o}\ \delta(\mu-\mu_o)\ \delta(\phi-\phi_o) \qquad \text{B-13}$$

where $\overline{I_o}$ is the solar intensity at the top of the atmosphere at the mean earth-sun distance, μ represents the zenith angle of Ω, μ_o represents the solar zenith angle, ϕ represents the azimuthal angle of Ω, and ϕ_o represents the solar azimuthal angle. The flux of the solar radiation is defined as the normal component of I integrated over the entire spherical solid

angle. Therefore $\bar{I}_o$ represents the solar flux. To verify this, the integral of the intensity is taken over all solar zenith angles and azimuthal angles:

$$F = \int_{\Omega} I \cos\theta \, d\Omega. \qquad \text{B-14}$$

or

$$F = \int_0^{2\pi} \int_0^{\frac{\pi}{2}} I(\theta,\phi) \cos\theta \sin\theta \, d\theta \, d\phi. \qquad \text{B-15}$$

If only downwelling irradiance is considered at the top of the atmosphere we get

$$\begin{aligned} F^{\downarrow}(0) &= -\int_0^{2\pi} \int_1^0 I_o(\mu,\phi) \, \mu \, d\mu \, d\phi \\ F^{\downarrow}(0) &= \int_0^{2\pi} \int_0^1 I_o(\mu,\phi) \, \mu \, d\mu \, d\phi \end{aligned} \qquad \text{B-16}$$

noting that I_o is nonzero only at $\mu=\mu_o$ and $\phi=\phi_o$. The integration is carried out to yield

$$\int_0^{2\pi} \int_0^1 I_o(\mu,\phi) \, \mu \, d\mu \, d\phi) = \mu_o \bar{I}_o \qquad \text{B-17}$$

where

$$I_o(\mu,\phi) = \begin{cases} I_o & \mu=\mu_o, \ \phi=\phi_o \\ 0 & \textit{Elsewhere} \end{cases} \qquad \text{B-18}$$

where $\bar{I}_o$ is the flux of radiation so $\bar{I}_o \rightarrow F$ can be reassigned. Hence the direct intensity can be written (by combining [B-12] and [B-13]) as

$$I_{dir} = F \, \delta(\mu-\mu_o) \, \delta(\phi-\phi_o) \, e^{-\frac{\tau}{\mu_o}}. \qquad \text{B-19}$$

From this the RTE is written as,

$$\mu\frac{dI_{dir}}{d\tau} + I_{dir} + \mu\frac{dI_{diff}}{d\tau} + I_{diff} = \omega_o\int I_{diff}P(\Omega,\Omega')d\Omega' + \omega_o\int I_{dir}P(\Omega,\Omega')d\Omega' \qquad \text{B-20}$$

We now turn our attention to the direct scattering intensity term. The direct scattered intensity is the radiation that is scattered into Ω from the direct beam of the sun (which is attenuated by optical depth). This can be written as

$$\int I_{dir}\ P(\Omega,\Omega')\ d\Omega' = \iint F\ \delta(\mu'-\mu_o)\ \delta(\phi'-\phi_o)\ e^{-\frac{\tau}{\mu_o}}\ P(\mu,\phi;\mu',\phi')\ d\mu\ d\phi \qquad \text{B-21}$$

where $P(\mu,\phi;\mu'',\phi) = P(\Omega,\Omega')$. Since the delta functions are only nonzero at $\mu=\mu_o$ and $\phi=\phi_o$, the equation can be simplified

$$\int I_{dir}\ P(\Omega,\Omega')\ d\Omega' = F\ e^{-\frac{\tau}{\mu_o}}\ P(\mu_o,\phi_o;\mu,\phi) \qquad \text{B-22}$$

Now, the RTE becomes

$$\mu\frac{dI_{dir}}{d\tau} + I_{dir} + \mu\frac{dI_{diff}}{d\tau} + I_{diff} = \omega_o\int I_{diff}P(\Omega,\Omega')d\Omega' + \omega_o\ F\ e^{-\frac{\tau}{\mu_o}}\ P(\mu_o,\phi_o;\mu,\phi) \qquad \text{B-23}$$

given that

$$I_{dir} = \begin{cases} I_{dir} & \mu=\mu_o,\ \phi=\phi_o \\ 0 & \textit{Elsewhere} \end{cases} \qquad \text{B-24}$$

The present goal is to obtain an equation that defines the diffuse green thunderstorm radiance. Underneath a large cumulonimbus cloud there is a negligible chance that any direct radiation will reach the surface. So, only the cases $\mu\neq\mu_o$ and $\phi\neq\phi_o$ are important. This simplifies the RTE equation to

$$\mu \frac{dI_{diff}}{d\tau} + I_{diff} = \omega_o \int I_{diff}\, P(\Omega,\Omega')\, d\Omega' + \omega_o\, F\, e^{-\frac{\tau}{\mu_o}}\, P(\mu_o,\phi_o;\mu,\phi) \qquad \text{B-25}$$

The last term on the right hand side of (B-25) describes that the scattered direct sunlight is a source of diffuse radiation. The phase function, $P(\mu_o,\phi_o;\mu,\phi)$, represents the probability that light from (μ_o,ϕ_o) is scattered into (μ,ϕ). Since diffuse radiation is exclusively being considered, the "diff" notation can be dropped from the equations. The RTE is now

$$\mu \frac{dI}{d\tau} + I = \omega_o \int I\, P(\Omega,\Omega')\, d\Omega' + \omega_o\, F\, e^{-\frac{\tau}{\mu_o}}\, P(\mu_o,\phi_o;\mu,\phi) \qquad \text{B-26}$$

In a stratified atmosphere, the variations in optical depth in the horizontal are negligible and only variations in the vertical are allowed. In the Eddington approximation the goal is to obtain a set of coupled ordinary differential equations in two functions of intensity. Then, an analytical solution for the homogeneous layer can be found. Eventually, the goal is to find an analytic solution to the downwelling diffuse flux that emanates beneath deeply convective cloud.

Eddington Approximation

In the Eddington Approximation, the diffuse intensity is separated into terms of two new functions called I_0 and I_1. Since only stratified atmosphere is being considered, the new functions are themselves only functions of optical depth, any dependence on zenith angle is nil. The diffuse intensity can be written as

$$I_{diff}(\tau,\mu) = I_0(\tau) + \mu I_1(\tau) \qquad \text{B-27}$$

The phase function is represented by

$$P(\Omega,\Omega') = P(\mu,\phi;\mu',\phi') \qquad \text{B-28}$$

and signifies the probability of light from direction (μ',ϕ') is scattered into direction (μ,ϕ). The phase function can be written as $P(\cos\Theta)$ where Θ is the scattering angle as shown in the figure. To solve for Θ one simply takes the dot product of the two direction vectors in spherical coordinates. The two vectors are represented by

$$\begin{aligned} \Omega &= \cos\phi\sin\theta\ \boldsymbol{i} + \sin\phi\sin\theta\ \boldsymbol{j} + \cos\theta\ \boldsymbol{k} \\ \Omega' &= \cos\phi'\sin\theta'\ \boldsymbol{i} + \sin\phi'\sin\theta'\ \boldsymbol{j} + \cos\theta'\ \boldsymbol{k} \end{aligned} \qquad \text{B-29}$$

The dot product is defined by (B-30).

$$\Omega \bullet \Omega' = |\Omega|\ |\Omega'|\ \cos\Theta \qquad \text{B-30}$$

Knowing that the vectors Ω and Ω' are unit vectors, carrying out the dot product results in

$$\begin{aligned} \Omega \bullet \Omega' &= \cos\phi\cos\phi'\sin\theta\sin\theta' + \sin\phi\sin\phi'\sin\theta\sin\theta' + \cos\theta\cos\theta' \\ &= (\cos\phi\cos\phi' + \sin\phi\sin\phi')\sin\theta\sin\theta' + \cos\theta\cos\theta' \\ &= \cos(\phi-\phi')\sin\theta\sin\theta' + \cos\theta\cos\theta' \\ &= \cos(\phi-\phi')[1-\cos^2\theta]^{1/2}[1-\cos^2\theta']^{1/2} + \cos\theta\cos\theta' \end{aligned} \qquad \text{B-31}$$

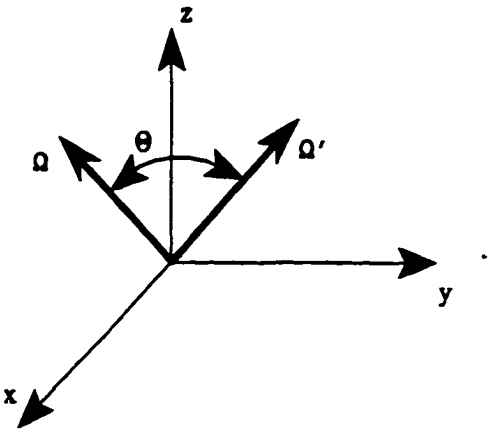

Figure B-4 - Scattering angle geometry.

Redefining variables

$$\begin{aligned} \mu &= \cos\theta \\ \mu' &= \cos\theta' \end{aligned} \qquad \text{B-32}$$

the solution for the scattering angle is

$$\Omega \bullet \Omega' = \cos(\phi-\phi')(1-\mu^2)^{1/2}(1-\mu'^2)^{1/2} + \mu\mu' = \cos\Theta \qquad \text{B-33}$$

The asymmetry factor is defined as

$$g = \int_0^1 P(\cos\Theta)\ \cos\Theta\ d\cos\Theta \qquad \text{B-34}$$

and is the first moment of the phase function and describes the nature of the scattering. For isotropic scattering the asymmetry factor is zero and increases as the diffraction peak of the phase function becomes increasingly sharpened in the forward direction. The asymmetry factor is then positive or negative according as the particle scatters more energy into the forward or backward direction respectively.

As stated earlier, the plane-parallel atmosphere has azimuthal symmetry. The relation for the Eddington approximation (B-27) is substituted into the equation of radiative transfer (B-26):

$$\begin{aligned} \mu\frac{d}{d\tau}(I_o + \mu I_1) + (I_o + \mu I_1) &= \omega_o\int(I_o + \mu I_1)\ P(\Omega,\Omega')\ d\Omega' \\ &+ \omega_o\ F\ e^{-\tau/\mu_o}\ P(\mu_o,\phi_o;\mu,\phi) \end{aligned} \qquad \text{B-35}$$

then

$$\begin{aligned} \mu\frac{dI_o}{d\tau} + \mu\frac{d(\mu\ I_1)}{d\tau} + I_o + \mu I_1 &= \omega_o\int I_o\ P(\Omega,\Omega')\ d\Omega' \\ + \ \omega_o\int\mu I_1\ P(\Omega,\Omega')\ d\Omega' &+ \omega_o\ F\ e^{-\tau/\mu_o}\ P(\mu_o,\phi_o;\mu,\phi) \end{aligned} \qquad \text{B-36}$$

The phase function is normalized and is defined by

$$\int_0^{2\pi}\int_0^{\pi}\frac{P(\cos\theta)}{4\pi}\sin\theta\ d\theta\ d\phi = 1 \qquad \text{B-37}$$

This phase function may be expanded in a series of Legendre polynomials with a finite number of terms

$$P(\cos\theta) = \sum_{l=0}^{N} \beta_l\ P_l(\cos\Theta) \qquad \text{B-38}$$

where β_l are a set of N+1 constants and β_0=1. So, using μ and ϕ, the expansion in a series of Legendre polynomials becomes

$$P(\mu,\phi;\mu',\phi') = \sum_{m=0}^{N}\sum_{l=m}^{N} \beta_l^m\ P_l^m(\mu)\ P_l^m(\mu')\ \cos[m(\phi'-\phi)] \qquad \text{B-39}$$

where

$$\beta_l^m = (2 - \delta_{0,m})\ \frac{(l-m)!}{(l+m)!} \qquad \text{B-40}$$

and

$$\delta_{0,m} = \begin{cases} 1 & m=0 \\ 0 & \textit{Elsewhere} \end{cases} \qquad \text{B-41}$$

The β_n constants must now be solved for. The expansion (B-38)

$$P(\cos\theta) = \sum_{l=0}^{N} \beta_l\ P_l(\cos\theta) \qquad \text{B-42}$$

is then substituted into the definition of the phase function (B-37) resulting in

$$\int_0^{2\pi}\int_0^{\pi} \frac{P(\cos\theta)}{4\pi} \sin\theta \; d\theta \; d\phi = 1$$

$$= \sum_{l=0}^{N} \beta_l \int_0^{2\pi}\int_0^{\pi} P_l(\cos\theta) \sin\theta \; d\theta \; d\phi \qquad \text{B-43}$$

$$= 2\pi\sum_{l=0}^{N} \beta_l \int_0^{\pi} P_l(\cos\theta) \sin\theta \; d\theta$$

Again, notation is changed $\mu=\cos\theta$ and $d\mu=-\sin\theta \; d\theta$ and (43) becomes

$$1 = 2\pi\sum_{l=0}^{N} \beta_l \int_1^{-1} -P_l(\mu) \; d\mu \qquad \text{B-44}$$

To solve for β_0 the β_0 term is separated out from the rest of the sum

$$1 = 2\pi\beta_0 \int_{-1}^{1} P_0(\mu) d\mu + 2\pi\sum_{l=1}^{N} \int_{-1}^{1} \beta_l \; P_l(\mu) \; d\mu \qquad \text{B-45}$$

Legendre polynomials have a nice orthogonality property that will be used frequently in this derivation

$$\int_{-1}^{1} P_m(x) \; P_n(x) = 0 \qquad for \quad m \neq n$$

$$\int_{-1}^{1} P_n^2(x) \; dx = \frac{2}{(2n+1)} \qquad \text{B-46}$$

Now, the second term on the right hand side of (B-45) can be written as:

$$2\pi\sum_{l=1}^{N} \int_{-1}^{1} \beta_n \; P_n(\mu) \; d\mu = 2\pi\sum_{l=1}^{N} \beta_n \int_{-1}^{1} (1) \; P_n(\mu) \; d\mu \qquad \text{B-47}$$

where $P_0(x) = 1$, then

$$2\pi\sum_{l=1}^{N} \int_{-1}^{1} \beta_n \; P_n(\mu) \; d\mu = 2\pi\sum_{l=1}^{N} \beta_n \int_{-1}^{1} P_0(\mu) \; P_n(\mu) \; d\mu$$

$$2\pi\sum_{l=1}^{N} \beta_n \int_{-1}^{1} P_0(\mu) \; P_n(\mu) \; d\mu = 0 \qquad \text{B-48}$$

by the orthogonal properties of the Legendre polynomials. The first term on the right hand side of B-45 is now considered:

$$
\begin{aligned}
1 &= 2\pi\beta_0\int_{-1}^{1} P_0(\mu)d\mu \\
&= 2\pi\beta_0\int_{-1}^{1} 1d\mu \\
&= 2\pi\beta_0\mu\,|_{-1}^{1} = 4\pi\beta_0
\end{aligned}
\qquad \text{B-49}
$$

Solving for β_0

$$
\beta_0 = \frac{1}{4\pi} \qquad \text{B-50}
$$

To solve for β_1, the asymmetry factor is used. The Legendre polynomial expansion in the asymmetry factor is then used, with the orthogonality properties of the Legendre polynomials, to solve for β_1. To start, the definition of the asymmetry factor (B-34) is repeated

$$
\begin{aligned}
g &= \int_0^1 P(\cos\Theta)\ \cos\Theta\ d\cos\Theta \\
&= \int_0^{2\pi}\int_{-1}^{1} P(\mu)\ \mu\ d\mu\ d\phi \\
&= 2\pi\int_{-1}^{1} P(\mu)\ \mu\ d\mu
\end{aligned}
\qquad \text{B-51}
$$

The Legendre polynomial expansion is substituted in (B-51) and the β_0 and β_1 components are separated out. The orthogonality properties of Legendre polynomials are used to solve for β_1.

$$
\begin{aligned}
g &= 2\pi\int_{-1}^{1}\sum_{l=0}^{N} P_l(\mu)\ \mu\ d\mu \\
&= 2\pi\int_{-1}^{1}\beta_0\ P_0(\mu)\ \mu\ d\mu\ +\ 2\pi\int_{-1}^{1}\beta_1\ P_1(\mu)\ \mu\ d\mu \\
&\quad +\ 2\pi\int_{-1}^{1}\sum_{l=2}^{N}\beta_l\ P_l(\mu)\ \mu\ d\mu
\end{aligned}
\qquad \text{B-52}
$$

Recalling that $P_0(\mu)=1$, the first term on the right hand side of (B-52) is now integrated

$$
2\pi\int_{-1}^{1}\beta_0\ \mu\ d\mu = 2\pi\beta_0\frac{\mu^2}{2}\Big|_{-1}^{1} = 0 \qquad \text{B-53}
$$

Similarly, recalling that $P_1(\mu)=\mu$, the third term on the right hand side of (B-52) is integrated

$$2\pi\int_{-1}^{1}\sum_{l=2}^{N}\mu\ P_l(\mu)\ d\mu\ =\ 2\pi\int_{-1}^{1}\sum_{l=2}^{N}P_1(\mu)\ P_l(\mu)\ d\mu\ =\ 0 \qquad \text{B-54}$$

Finally the second term on the right hand side of (B-52), recalling that $P_1(\mu)=\mu$, is integrated

$$\begin{aligned} g\ &=\ 2\pi\int_{-1}^{1}\beta_1\ P_1(\mu)\ \mu\ d\mu\ =\ 2\pi\int_{-1}^{1}\beta_1\ \mu^2\ d\mu \\ g\ &=\ 2\pi\beta_1\frac{\mu^3}{3}\Big|_{-1}^{1}\ =\ \frac{4\ \pi\ \beta_1}{3} \\ \beta_1\ &=\ \frac{3g}{4\pi} \end{aligned} \qquad \text{B-55}$$

The results of (B-50) and (B-55) are substituted into the definition of the phase function (B-38) to yield

$$\begin{aligned} P(\cos\theta)\ &=\ \frac{1}{4\pi}\ +\ \frac{3g}{4\pi}\ +\ \sum_{n=2}^{\infty}\beta_n\ P_n(\cos\theta) \\ P(\cos\theta)\ &=\ \frac{1}{4\pi}(1\ +\ 3g\mu)\ +\ \sum_{n=2}^{\infty}\beta_n\ P_n(\cos\theta) \end{aligned} \qquad \text{B-56}$$

Integral over the Phase Function

The phase function contains information regarding how scattering occurs in the atmosphere. To determine the effects of scattering, the phase function must be integrated over μ and ϕ. By looking at the expanded RTE (B-36) there are two integrals to solve, both of which involve an integral over the phase function.

$$\mu\frac{dI_o}{d\tau} + \mu\frac{d(\mu\ I_1)}{d\tau} + I_o + \mu I_1 = \omega_o\int I_o\ P(\Omega,\Omega')\ d\Omega'$$
$$+ \omega_o\int \mu I_1\ P(\Omega,\Omega')\ d\Omega' + \omega_o\ F\ e^{-\tau/\mu_o}\ P(\mu_o,\phi_o;\mu,\phi) \qquad \text{B-57}$$

Both I_0 and I_1 are not functions of μ or ϕ and are thereby not functions of Ω and can therefore be pulled out of the equation. That leaves only an integral over the phase function. Recall the expression for the definition of the phase function (B-38)

$$P(\cos\theta) = \sum_{n=0}^{\infty}\ \beta_n\ P_n(\cos\Theta) \qquad \text{B-58}$$

Using (B-39), (B-40), and (B-41) the expansion of the phase function in Legendre polynomials can be written as

$$P_l(\cos\theta) = \sum_{m=0}^{n}\sum_{l=m}^{n}(2-\delta_{0,m})\frac{(l-m)!}{(l+m)!}P_l^m(\mu)P_l^m(\mu')\cos[m(\phi-\phi')]$$
$$P_l(\cos\theta) = P_l(\mu,\phi;\mu',\phi') \qquad \text{B-59}$$

where $P_l^m(\mu)$ are the associated Legendre polynomials. The equation can be split into two parts, one for m=0 and the other for the remaining m. For m=0

$$P_l(\cos\theta) = (2-\delta_{0,0})\frac{(0-0)!}{(0+0)!}P_l^0(\mu)P_l^0(\mu')\cos[0(\phi-\phi')]$$
$$P_l(\cos\theta) = P_l(\mu)P_l(\mu) \qquad \text{B-60}$$

and for m≠0

$$P_l(\cos\theta) = 2\sum_{m=1}^{n}\frac{(l-m)!}{(l+m)!}P_l^m(\mu)P_l^m(\mu')\cos[m(\phi-\phi')] \qquad \text{B-61}$$

Summing the two the result is

$$P_l(\cos\theta) = P_l(\mu)P_l(\mu') + 2\sum_{m=1}^{n} \frac{(l-m)!}{(l+m)!} P_l^m(\mu)P_l^m(\mu')\cos[m(\phi-\phi')] \qquad \text{B-62}$$

Integral over the I_o phase function term

The first integral to look at more carefully is the integral over the phase function for the I_0 term in (B-57)

$$\int P(\cos\theta)d\Omega' = \int \sum_{l=0}^{N} \beta_l \, P_l(\cos\Theta) \, d\Omega' \qquad \text{B-63}$$

using (B-59) in (B-63)

$$\int P_l(\cos\theta) \, d\Omega = \int \beta_0 \, d\Omega$$
$$+ \int \sum_{n=1}^{\infty} \beta_n \left\{ P_l(\mu)P_l(\mu') + 2\sum_{m=1}^{n} \frac{(l-m)!}{(l+m)!} P_l^m(\mu)P_l^m(\mu')\cos[m(\phi-\phi')] \right\} d\Omega \qquad \text{B-64}$$

or

$$\int_0^{2\pi}\int_{-1}^{1} P_l(\cos\theta) \, d\mu' \, d\phi' = \int_0^{2\pi}\int_{-1}^{1} \beta_0 \, d\mu' \, d\phi'$$
$$+ \int_0^{2\pi}\int_{-1}^{1} \sum_{n=1}^{\infty} \beta_n \left\{ P_l(\mu)P_l(\mu') \right.$$
$$\left. + 2\sum_{m=1}^{n} \frac{(l-m)!}{(l+m)!} P_l^m(\mu)P_l^m(\mu')\cos[m(\phi-\phi')] \right\} d\mu' \, d\phi' \qquad \text{B-65}$$

In (B-65) there are two integrals on the right hand side that must be evaluated. The first integral is rather simple. Using (B-50) yields

$$\beta_0 \int_0^{2\pi} \int_{-1}^{1} d\mu' \, d\phi' = 4\pi\beta_o = 1 \qquad \text{B-66}$$

Next, by utilizing orthogonality properties (B-46) of Legendre polynomials and the identity that $P_0(\mu')=1$ the next integral is solved

$$\int_0^{2\pi}\int_{-1}^{1} \sum_{n=1}^{\infty} \beta_n P_l(\mu)P_l(\mu')\, d\mu'\, d\phi' = \sum_{n=1}^{\infty} \beta_n\, 2\pi\, P_n(\mu)\int_{-1}^{1} P_n(\mu')d\mu'$$

$$= \sum_{n=1}^{\infty} \beta_n\, 2\pi\, P_n(\mu)\int_{-1}^{1} P_0(\mu')\, P_n(\mu')d\mu' \qquad \text{B-67}$$

$$= 0 \qquad \textit{By orthogonality}$$

The third integral is also solved by orthogonality

$$\int_0^{2\pi}\int_{-1}^{1} 2\beta_n \sum_{n=1}^{\infty} \sum_{m=1}^{n} \frac{(l-m)!}{(l+m)!} P_l^{\,m}(\mu)P_l^{\,m}(\mu')\cos[m(\phi-\phi')]\, d\mu'\, d\phi'$$

$$= 2\sum_{n=1}^{\infty} \sum_{m=1}^{n} \frac{(l-m)!}{(l+m)!} P_l^{\,m}(\mu)\int_{-1}^{1} P_n^{\,m}(\mu')\, d\mu' \int_{-1}^{1}\cos[m(\phi-\phi']d\phi'$$

$$= 2\sum_{n=1}^{\infty} \sum_{m=1}^{n} \frac{(l-m)!}{(l+m)!} P_l^{\,m}(\mu)\int_{-1}^{1} P_0^{\,m}(\mu')\, P_n^{\,m}(\mu')\, d\mu' \int_{-1}^{1}\cos[m(\phi-\phi']d\phi' \qquad \text{B-68}$$

$$= 0 \qquad \textit{By orthogonality}$$

Combining (B-66), (B-67), and (B-68) results in

$$\int_0^{2\pi}\int_{-1}^{1} P_l(\cos\theta)\, d\mu'\, d\phi' = 1 \qquad \text{B-69}$$

Integral over the I_l phase function term

The second integral is over the phase function for the I_l term in (B-57)

$$\int_0^{2\pi}\int_{-1}^{1} P_l(\cos\theta)\ \mu'\ d\mu'\ d\phi' = \int_0^{2\pi}\int_{-1}^{1} \beta_0\ \mu'\ d\mu'\ d\phi'$$
$$+ \int_0^{2\pi}\int_{-1}^{1} \sum_{n=1}^{\infty} \beta_n \Big\{ P_l(\mu)P_l(\mu')\ \mu'$$
$$+ 2\sum_{m=1}^{n} \frac{(l-m)!}{(l+m)!} P_l^{\,m}(\mu)P_l^{\,m}(\mu')\ \mu'\ \cos[m(\phi-\phi')]\Big\}\ d\mu'\ d\phi' \qquad \text{B-70}$$

As before, each of the integrals are solved individually. The first integral is rather simple

$$\beta_0 \int_0^{2\pi} \int_{-1}^{1} \mu'\ d\mu'\ d\phi' = 2\pi\beta_o \frac{\mu'^2}{2}\Big|_{-1}^{1} = 0 \qquad \text{B-71}$$

By using the orthogonality properties (B-46) of Legendre polynomials and the identity that $P_0(\mu')=1$, the second integral is solved

$$\int_0^{2\pi}\int_{-1}^{1} \sum_{n=1}^{\infty} \beta_n P_l(\mu)P_l(\mu')\ \mu'\ d\mu'\ d\phi' = \sum_{n=1}^{\infty} \beta_n\ 2\pi\ P_n(\mu)\int_{-1}^{1} P_n(\mu')\ \mu'\ d\mu'$$
$$= \sum_{n=1}^{\infty} \beta_n\ 2\pi\ P_n(\mu)\int_{-1}^{1} P_1(\mu')\ P_n(\mu')d\mu' \qquad \text{B-72}$$
$$= 0 \qquad \textit{By orthogonality} \quad -- \quad \textit{for } n\neq 1$$

For n=1 the result is

$$\int_0^{2\pi}\int_{-1}^{1} \beta_1 P_1(\mu)P_1(\mu')\ \mu'\ d\mu'\ d\phi' = \beta_1\ 2\pi\ P_1(\mu)\int_{-1}^{1} P_n(\mu')\ \mu'\ d\mu'$$
$$= \beta_1\ 2\pi\ P_1(\mu)\int_{-1}^{1} (\mu')^2 d\mu' \qquad \text{B-73}$$
$$= \beta_1\ 2\pi\ P_1(\mu)\frac{\mu'^2}{3}\Big|_{-1}^{1} = \frac{4\pi}{3}\beta_1\mu$$

(B-55) is used to simplify (B-73)

$$\frac{4\pi}{3}\beta_1\mu = g\mu \qquad \text{B-74}$$

The third integral is also solved by integrating the cosine term over ϕ'

$$\int_0^{2\pi}\int_{-1}^{1} 2\beta_n \sum_{n=1}^{\infty} \sum_{m=1}^{n} \frac{(l-m)!}{(l+m)!} P_l^{\,m}(\mu) P_l^{\,m}(\mu')\ \mu'\ \cos[m(\phi-\phi')]\ d\mu'\ d\phi'$$

$$\int_0^{2\pi}\cos[m(\phi-\phi')]\ d\phi' = -\frac{1}{m}\int_0^{2\pi}\cos(x)\ dx = -\frac{1}{m}\sin(mx)\Big|_0^{2\pi} = 0 \qquad \text{B-75}$$

All of the solutions can now be substituted into the RTE

$$\mu\frac{d}{d\tau}(I_o + \mu I_1) + (I_o + \mu I_1) = \omega_o I_0 + \omega_o g\mu I_1 + \omega_o F e^{-\tau/\mu_o} P(\mu_o,\phi_o;\mu,\phi) \qquad \text{B-76}$$

The term that remains untouched in the analysis is the remaining phase function term. The plane-parallel atmosphere has azimuthal symmetry such that the intensity terms are independent of μ. Recall the expansion of the phase function, this time allowing only for the direct solar radiation

$$P_l(\mu_o,\phi_o;\mu,\phi) = \beta_0$$
$$+ \sum_{n=1}^{\infty} \beta_n\left\{P_l(\mu_o)P_l(\mu) + 2\sum_{m=1}^{n} \frac{(l-m)!}{(l+m)!} P_l^{\,m}(\mu_o)P_l^{\,m}(\mu)\cos[m(\phi-\phi_o)]\right\} \qquad \text{B-77}$$

As before, this term needs to be integrated over Ω.

$$\int_0^{2\pi} P(\mu_o,\phi_o;\mu,\phi)\ d\phi = 2\pi\beta_o + 2\pi\sum_{n=1}^{\infty} \beta_n\ P_n(\mu_o)\ P_n(\mu) \qquad \text{B-78}$$

where the cosine term integrates to zero. Equation (B-78) is normalized by dividing by 2π then inserting the result into (B-76) to yield

$$\mu\frac{dI_o}{d\tau} + \mu^2\frac{dI_1}{d\tau} + I_o + \mu I_1 = \omega_o I_0 + \omega_o g\mu I_1$$
$$+ \omega_o F e^{-\tau/\mu_o}[\beta_o + \sum_{n=1}^{\infty} \beta_n P_n(\mu_o) P_n(\mu)] \qquad \text{B-79}$$

In order to obtain a pair of equations for I_0 and I_1, (B-79) is integrated over μ and by (B-79) times μ, all over μ. The first equation is generated by

$$\int_{-1}^{1}\mu\frac{dI_o}{d\tau}\,d\mu + \int_{-1}^{1}\mu^2\frac{dI_1}{d\tau}\,d\mu + \int_{-1}^{1}I_o\,d\mu + \int_{-1}^{1}\mu I_1\,d\mu$$
$$= \int_{-1}^{1}\omega_o I_0\,d\mu + \int_{-1}^{1}\omega_o g\mu I_1\,d\mu \qquad \text{B-80}$$
$$+ \int_{-1}^{1}\omega_o F e^{-\tau/\mu_o}[\beta_o + \sum_{n=1}^{\infty} \beta_n P_n(\mu_o) P_n(\mu)]\,d\mu$$

$$0 + \frac{2}{3}\frac{dI_1}{d\tau} + 2I_o + 0 = 2\omega_o I_0 + 0$$
$$+ 2\omega_o F e^{-\tau/\mu_o}\beta_o + \int_{-1}^{1}\omega_o F e^{-\tau/\mu_o}[\beta_o + \sum_{n=1}^{\infty} \beta_n P_n(\mu_o) P_n(\mu)]\,d\mu \qquad \text{B-81}$$

The final integral is solved by using the orthogonal properties of Legendre polynomials

$$\int_{-1}^{1}\omega_o F e^{-\tau/\mu_o}\sum_{n=1}^{\infty} \beta_n P_n(\mu_o) P_n(\mu)\,d\mu$$
$$= \omega_o F e^{-\tau/\mu_o}\sum_{n=1}^{\infty} \beta_n P_n(\mu_o)\int_{-1}^{1}P_n(\mu)\,d\mu \qquad \text{B-82}$$
$$= \omega_o F e^{-\tau/\mu_o}\sum_{n=1}^{\infty} \beta_n P_n(\mu_o)\int_{-1}^{1}P_0(\mu) P_n(\mu)\,d\mu = 0$$

then

$$\frac{2}{3}\frac{dI_1}{d\tau} + 2I_o = 2\omega_o I_0 + 2\omega_o F e^{-\tau/\mu_o}\beta_o \qquad \text{B-83}$$

Using (B-50) in (B-83) the final differential equation is found

$$\frac{dI_1}{d\tau} = -3\, I_o\, (1-\omega_o) + \frac{3\omega_o F e^{-\tau/\mu_o}}{4\pi} \qquad \text{B-84}$$

The second equation is found by multiplying (B-79) by μ and then integrating over μ.

$$\int_{-1}^{1}\mu^2\frac{dI_o}{d\tau}\,d\mu + \int_{-1}^{1}\mu^3\frac{dI_1}{d\tau}\,d\mu + \int_{-1}^{1}\mu I_o\,d\mu + \int_{-1}^{1}\mu^2 I_1\,d\mu$$

$$= \int_{-1}^{1}\omega_o\mu I_0\,d\mu + \int_{-1}^{1}\omega_o g\mu^2 I_1\,d\mu \qquad \text{B-85}$$

$$+ \int_{-1}^{1}\omega_o\mu F e^{-\tau/\mu_o}[\beta_o + \textstyle\sum_{n=1}^{\infty}\beta_n\, P_n(\mu_o)\, P_n(\mu)]\,d\mu$$

Carrying out the integration yields

$$\frac{2}{3}\frac{dI_o}{d\tau} + 0 + 0 + \frac{2}{3}I_1 = 0 + \frac{2}{3}\omega_o g I_1 + 0 + 0 \qquad \text{B-86}$$

$$for\ n \neq 1$$

For n=1 the last integral must be reevaluated

$$\int_{-1}^{1}\omega_o\mu F e^{-\tau/\mu_o}\beta_1\, P_1(\mu_o)\, P_1(\mu)\,d\mu$$

$$= \int_{-1}^{1}\omega_o\mu F e^{-\tau/\mu_o}\beta_1\, P_1(\mu_o)\,\mu^2\,d\mu \qquad \text{B-87}$$

$$= \frac{2}{3}\omega_o F e^{-\tau/\mu_o}\beta_1 P_1(\mu_o)$$

Using (B-55) in (B-87) yields

$$\int_{-1}^{1}\omega_o\mu F e^{-\tau/\mu_o}\beta_1\, P_1(\mu_o)\, P_1(\mu)\,d\mu = \frac{2}{3}\omega_o F e^{-\tau/\mu_o}\frac{3g\mu_o}{4\pi} \qquad \text{B-88}$$

Using the results from (B-85) and (B-88) we get our final result for the change in the I_o intensity

$$\frac{dI_o}{d\tau} = -I_1(1-\omega_o g) + \frac{3\omega_o e^{-\tau/\mu_o} F\mu_o g}{4\pi} \qquad \text{B-89}$$

Irradiance Boundary Conditions

The downward directed diffuse irradiance (or flux) at the top of the atmosphere is assumed to be zero. Only direct irradiance from the sun is allowed to enter the atmosphere from the top. This irradiance is computed from the Eddington approximation intensities by

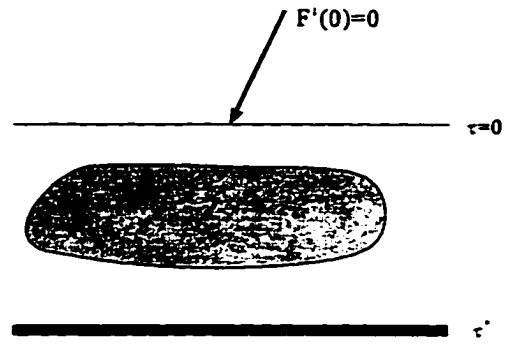

Figure B-5 - Geometry for irradiance boundary conditions.

$$F^{\downarrow}_{diff}(0) = \int_0^{2\pi}\int_0^1 I\ \mu\ d\mu\ d\phi \qquad \mu \geq 0$$

$$= 2\pi\int_0^1 (I_0 + \mu I_1)\ \mu\ d\mu = 0 \qquad \text{B-90}$$

so

$$\pi[I_0(0) + \frac{2}{3}I_1(0)] = 0 \qquad \text{B-91}$$

We now consider the flux at the top from below. The integration is carried out as before but changing the limits of μ to -1 to 1:

$$F^{\downarrow}(0) = \int_0^{2\pi}\int_{-1}^{0} I\ \mu\ d\mu\ d\phi \qquad \mu \le 0$$

$$= 2\pi\int_{-1}^{0}(I_0 + \mu I_1)\ \mu\ d\mu \qquad \text{B-92}$$

then

$$F^{\downarrow}(0) = \pi(I_0 - \frac{2}{3}I_1) \qquad \text{B-93}$$

so the relation for the diffuse flux at optical depth τ is

$$F^{\downarrow}(\tau) = \pi[I_0(\tau) \pm \frac{2}{3}I_1(\tau)] \qquad \text{B-94}$$

where $F^{\downarrow}$ is represented by the sum and $F^{\uparrow}$ is represented by the difference. Consider now the upward directed irradiance at the bottom of the atmosphere. This upward irradiance is equal to the product of the downward directed irradiances and the albedo of the ground where the ground diffusely reflects all of the incident radiation. This is written as

$$F^{\uparrow}(\tau^*) = [F^{\downarrow}_{diff} + F^{\downarrow}_{dir}] * albedo$$

$$F^{\uparrow}(\tau^*) = \pi[I_0(\tau^*) - \frac{2}{3}I_1(\tau^*)] \qquad \text{B-95}$$

Using (B-12), (B-13), and (B-14) the downward irradiance at the surface (τ^*) is

$$F^{\downarrow}_{dir}(\tau^*) = \mu_o F_o e^{-\tau^*/\mu_o} \qquad \text{B-96}$$

so

$$F^{\uparrow}(\tau^{*}) = \pi[I_0(\tau^{*}) - \frac{2}{3}I_1(\tau^{*})]$$

$$F^{\downarrow}(\tau^{*}) = \left\{\pi[I_0(\tau^{*}) + \frac{2}{3}I_1(\tau^{*})] + \mu_{oFe}^{-\tau^{*}/\mu_o}\right\} a \qquad \text{B-97}$$

where a is the albedo of the surface.

Solution to Coupled Differential Equations

We now have a set (B-84), (B-89) of differential equations. According to Shettle and Weinman (1970) it is not possible to find an analytical solution to this set of differential equations. However, they state that these equations can be solved in the special cases of an atmosphere composed of homogeneous layers. This can be described by

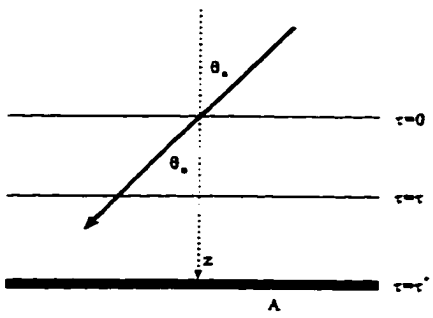

Figure B-6 - Layered, plane-parallel atmosphere geometry.

$$\frac{\partial \omega_{oi}}{\partial \tau} = \frac{\partial g_i}{\partial \tau} = 0 \qquad \text{B-98}$$

where ω_{oi} is the albedo for single scattering and g_i is the asymmetry factor for each ith layer. For our solution (following Shettle and Weinman (1970)) we will consider an atmosphere which is represented by layers, each of which is homogeneous, and we will assume that each layer is characterized by different values of ω_{oi} and g_i. Recall the set of differential equations

$$\frac{dI_1}{d\tau} = -3\ I_o\ (1-\omega_o) + \frac{3\omega_o F e^{-\tau/\mu_o}}{4\pi} \qquad \text{B-99}$$

$$\frac{dI_o}{d\tau} = -I_1(1-\omega_o g) + \frac{3\omega_o e^{-\tau/\mu_o} F \mu_o g}{4\pi} \qquad \text{B-100}$$

For simplicity let

$$\overline{F} = \frac{3\omega_o F}{4\pi} \qquad \text{B-101}$$

then the differential equations can be written in matrix form

$$\frac{d}{d\tau}\begin{bmatrix} I_1 \\ I_0 \end{bmatrix} = \begin{bmatrix} 0 & -3(1-\omega_o) \\ -(1-\omega_o g) & 0 \end{bmatrix}\begin{bmatrix} I_1 \\ I_0 \end{bmatrix} + \overline{F}\begin{bmatrix} 1 \\ g\mu_o \end{bmatrix} e^{-\tau/\mu_o} \qquad \text{B-102}$$

To simplify the equations further, (B-102) is divided by $\overline{F}$ resulting in

$$\overline{I_1} = \frac{I_1}{\overline{F}} \quad , \quad \overline{I_0} = \frac{I_0}{\overline{F}} \qquad \text{B-103}$$

$$\frac{d}{d\tau}\begin{bmatrix} \overline{I_1} \\ \overline{I_0} \end{bmatrix} = \begin{bmatrix} 0 & -3(1-\omega_o) \\ -(1-\omega_o g) & 0 \end{bmatrix}\begin{bmatrix} \overline{I_1} \\ \overline{I_0} \end{bmatrix} + \begin{bmatrix} 1 \\ g\mu_o \end{bmatrix} e^{-\tau/\mu_o} \qquad \text{B-104}$$

To form a single differential matrix equation let

$$\xi = \begin{bmatrix} \overline{I_1} \\ \overline{I_0} \end{bmatrix}, \quad M = \begin{bmatrix} 0 & -3(1-\omega_o) \\ -(1-\omega_o g) & 0 \end{bmatrix}, \quad \overline{b} = \begin{bmatrix} 1 \\ g\mu_o \end{bmatrix} \qquad \text{B-105}$$

then

$$\frac{d\xi}{d\tau} = M\xi + \overline{b}e^{-\tau/\mu_o} \qquad \text{B-106}$$

The homogeneous and particular solutions are solved for separately.

Homogeneous Solution

To solve the homogeneous solution, the second term on the right hand side of (B-106) is set to zero.

$$\frac{d\xi}{d\tau} - M\xi = 0 \qquad \text{B-107}$$

To solve this equation, an exponential solution is assumed

$$\xi = \bar{a}e^{\alpha\tau} \qquad \text{B-108}$$

where $\bar{a}$ is a constant and α is the eigenvalue. Substituting the solution (B-108) into the differential equation (B-107) results in

$$\begin{aligned} \alpha\bar{a}e^{\alpha\tau} &= M\bar{a}e^{\alpha\tau} \\ \alpha\bar{a} &= M\bar{a} \end{aligned} \qquad \text{B-109}$$

This can be rewritten using the identity matrix **I**

$$\begin{aligned} M\bar{a} &= \alpha I\bar{a} \\ M\bar{a} - \alpha I\bar{a} &= 0 \\ \bar{a}(M - \alpha I) &= 0 \end{aligned} \qquad \text{B-110}$$

Since a nontrivial solution is sought

$$|M - \alpha I| = 0 \qquad \text{B-111}$$

then substituting values for **M** and **I** in matrix form

$$\left| \begin{bmatrix} 0 & -3(1-\omega_o) \\ -(1-\omega_o g) & 0 \end{bmatrix} - \alpha \begin{bmatrix} 1 & 0 \\ 0 & 1 \end{bmatrix} \right| = 0 \qquad \text{B-112}$$

or

$$\begin{vmatrix} -\alpha & -3(1-\omega_o) \\ -(1-\omega_o g) & -\alpha \end{vmatrix} = 0 \qquad \text{B-113}$$

then

$$\begin{aligned} \alpha^2 - [-(1-\omega_o g) \bullet -3(1-\omega_o)] &= 0 \\ \alpha^2 - [3(1-\omega_o g)(1-\omega_o)] &= 0 \\ \alpha^2 &= [3(1-\omega_o g)(1-\omega_o)] \end{aligned} \qquad \text{B-114}$$

Referring back to the assumed solution (B-108), $\alpha^2 \rightarrow K^2$ where K represents the inverse scattering path for diffuse radiation (Goody and Yung 1989). So $\alpha = \pm K$ and

$$K = [3(1-\omega_o)(1-\omega_o g)]^{1/2} \qquad \text{B-115}$$

Because there are two solutions for α, there are two solutions for $\bar{\xi}$, each of which have two different coefficients ($\bar{a}_+$ and $\bar{a}_-$). The homogeneous solutions are

$$\xi_h^+ = \bar{a}_+ e^{K\tau}, \qquad \xi_h^- = \bar{a}_- e^{K\tau} \qquad \text{B-116}$$

where the coefficient matrices are

$$\bar{a}_+ = \begin{bmatrix} a_+ \\ b_+ \end{bmatrix}, \qquad \bar{a}_- = \begin{bmatrix} a_- \\ b_- \end{bmatrix} \qquad \text{B-117}$$

These two solutions, when added to the particular solution, will form the set of solutions to the Eddington approximation. Each part of the homogeneous solution is now solved for. As before, the assumed solution (with coefficients, [B-108]) is substituted into the original differential equation (B-107).

For a_+

$$\overline{a_+}Ke^{K\tau} = M\overline{a_+}e^{K\tau}$$

$$\overline{a_+}K = M\overline{a_+}$$

$$I\overline{a_+}K = M\overline{a_+} \qquad \text{B-118}$$

$$(M - KI)\overline{a_+} = 0$$

Substituting for **M** and **I** using (B-105)

$$\left\{\begin{bmatrix} 0 & -3(1-\omega_o) \\ -(1-\omega_o g) & 0 \end{bmatrix} - K\begin{bmatrix} 1 & 0 \\ 0 & 1 \end{bmatrix}\right\}\overline{a_+} = 0 \qquad \text{B-119}$$

or

$$\begin{bmatrix} -K & -3(1-\omega_o) \\ -(1-\omega_o g) & -K \end{bmatrix}\begin{bmatrix} a_+ \\ b_+ \end{bmatrix} = \begin{bmatrix} 0 \\ 0 \end{bmatrix} \qquad \text{B-120}$$

This results in a set of simultaneous equations with variables K, a_+, and b_+. Only two of these variables can be solved for at any one time. Fortunately K is known (B-115) and is easily verified. In order to let a_+ appear in the solution by itself, b_+ is solved

$$b_+ = \frac{Ka_+}{3(1-\omega_o)} \qquad \text{B-121}$$

This result is substituted back into the original assumed solution (B-116) giving

$$\xi_h^+ = \overline{a_+}e^{K\tau} = \begin{bmatrix} a_+ \\ -\dfrac{Ka_+}{3(1-\omega_o)} \end{bmatrix} e^{K\tau} \qquad \text{B-122}$$

Factoring out the a_+ and substituting for K (B-115) results in

$$\xi_h^+ = a_+ \begin{bmatrix} \sqrt{3(1-\omega_o)} \\ -\sqrt{(1-\omega_o g)} \end{bmatrix} e^{K\tau} \qquad \text{B-123}$$

For a_

The procedure follows the treatment above.

$$\begin{aligned} \overline{a_-}(-K)e^{-K\tau} &= M\overline{a_-}e^{-K\tau} \\ \overline{a_-}(-K) &= M\overline{a_-} \\ I\overline{a_-}(-K) &= M\overline{a_-} \\ (M - KI)\overline{a_-} &= 0 \end{aligned} \qquad \text{B-124}$$

Substituting for **M** and **I** using (B-105)

$$\left\{ \begin{bmatrix} 0 & -3(1-\omega_o) \\ -(1-\omega_o g) & 0 \end{bmatrix} + K \begin{bmatrix} 1 & 0 \\ 0 & 1 \end{bmatrix} \right\} \overline{a_-} = 0 \qquad \text{B-125}$$

or

$$\begin{bmatrix} K & -3(1-\omega_o) \\ -(1-\omega_o g) & K \end{bmatrix} \begin{bmatrix} a_- \\ b_- \end{bmatrix} = \begin{bmatrix} 0 \\ 0 \end{bmatrix} \qquad \text{B-126}$$

This results in a set of simultaneous equations with variables K, a_-, and b_-. Only two of the three can be solved for at any one time. Fortunately, K is known (B-115) and is easily checked. In order to let a_- appear in the solution by itself, solve for b_-.

$$b_- = \frac{Ka_-}{3(1-\omega_o)} = a_-\sqrt{\frac{(1-\omega_o g)}{3(1-\omega_o)}} \qquad \text{B-127}$$

This result is substituted back into the original assumed solution (B-116) giving

$$\xi_h^- = \overline{a}_- e^{-K\tau} = \left[\frac{1}{\sqrt{\frac{1-\omega_o g}{3(1-\omega_o)}}}\right] e^{K\tau} \qquad \text{B-128}$$

Factoring out a_- yields

$$\xi_h^- = a_-\left[\frac{\sqrt{3(1-\omega_o)}}{\sqrt{(1-\omega_o g)}}\right] e^{-K\tau} \qquad \text{B-129}$$

We now have solved for our two solutions to the homogeneous problem. If the notation is changed slightly [$a_+ \to A$, $a_- \to B$] using the solutions (B-123) and (B-129) then

$$\xi_h = A\ e^{K\tau}\left[\frac{\sqrt{3(1-\omega_o)}}{\sqrt{-(1-\omega_o g)}}\right] + B\ e^{-K\tau}\left[\frac{\sqrt{3(1-\omega_o)}}{\sqrt{(1-\omega_o g)}}\right] \qquad \text{B-130}$$

Particular Solution

The direct beam of sunlight is now included such that the the particular solution must be solved. Recall the "complete" differential equation for this process (B-106)

$$\frac{d\xi}{d\tau} = M\xi + \bar{b}e^{-\tau/\mu_o} \qquad \text{B-131}$$

The particular solution can be written as

$$\xi_p = \bar{c}e^{-\tau/\mu_o} \qquad \text{B-132}$$

As before, the assumed solution (B-132) is substituted into the differential equation (B-131) then the coefficients are solved

$$-\frac{\bar{c}}{\mu_o}e^{-\tau/\mu_o} = M\bar{c}e^{-\tau/\mu_o} + \bar{b}e^{-\tau/\mu_o}$$

$$-\frac{\bar{c}}{\mu_o} = M\bar{c} + \bar{b} \qquad \text{B-133}$$

$$\frac{\bar{c}}{\mu_o} + M\bar{c} = -\bar{b}$$

The coefficients are represented by the matrix

$$C = \begin{bmatrix} c_1 \\ c_2 \end{bmatrix} \qquad \text{B-134}$$

and we can rewrite our differential equation as

$$(M + \frac{I}{\mu_o})\, C = -\bar{b} \qquad \text{B-135}$$

Substituting for **M** and **I** (as before) using (B-105)

$$\left\{ \begin{bmatrix} 0 & -3(1-\omega_o) \\ -(1-\omega_o g) & 0 \end{bmatrix} + \frac{1}{\mu_o} \begin{bmatrix} 1 & 0 \\ 0 & 1 \end{bmatrix} \right\} \begin{bmatrix} c_1 \\ c_2 \end{bmatrix} = \begin{bmatrix} -1 \\ -g\mu_o \end{bmatrix}$$

$$\begin{bmatrix} 1 & -3\mu_o(1-\omega_o) \\ -\mu_o(1-\omega_o g) & 1 \end{bmatrix} \begin{bmatrix} c_1 \\ c_0 \end{bmatrix} = - \begin{bmatrix} 1 \\ g\mu_o \end{bmatrix} \qquad \text{B-136}$$

This results in a set of simultaneous equations with variables c_1, and c_2. Using the old fashioned algebraic manipulation routine, we find

$$c_1 = \frac{\mu_o[1 + 3\mu_o^2(1-\omega_o)g]}{\mu_o^2 K^2 - 1}$$

$$c_2 = \frac{\mu_o^2[1 - \omega_o g + g]}{\mu_o^2 K^2 - 1} \qquad \text{B-137}$$

The coefficients (B-137) are then substituted back into the assumed solution (B-132) using (B-134) to get

$$\xi_p = \frac{\mu_o e^{-\tau/\mu_o}}{\mu_o^2 K^2 - 1} \begin{bmatrix} 1 + 3\mu_o^2(1-\omega_o)g \\ \mu_o[1 + (1-\omega_o)g] \end{bmatrix} \qquad \text{B-138}$$

This leads to the total solution from the sum of the homogeneous solutions and the particular solution

$$\xi = A\, e^{K\tau} \begin{bmatrix} \sqrt{3(1-\omega_o)} \\ -\sqrt{(1-\omega_o g)} \end{bmatrix} + B\, e^{-K\tau} \begin{bmatrix} \sqrt{3(1-\omega_o)} \\ \sqrt{(1-\omega_o g)} \end{bmatrix}$$

$$+ \frac{\mu_o e^{-\tau/\mu_o}}{\mu_o^2 K^2 - 1} \begin{bmatrix} 1 + 3\mu_o^2(1-\omega_o)g \\ \mu_o[1 + (1-\omega_o)g] \end{bmatrix} \qquad \text{B-139}$$

Using (B-103) and (B-105), this result can be split into the two intensity components

$$I_1 = \overline{F}Ae^{K\tau}\sqrt{3(1-\omega_o)} + \overline{F}Be^{-K\tau}\sqrt{3(1-\omega_o)}$$

$$+ \frac{\overline{F}\mu_o e^{-\tau/\mu_o}}{\mu_o^2 K^2 - 1}[1 + 3\mu_o^2(1-\omega_o)g] \qquad \text{B-140}$$

$$I_0 = -\overline{F}Ae^{K\tau}\sqrt{1-\omega_o g} + \overline{F}Be^{-K\tau}\sqrt{1-\omega_o g}$$

$$+ \frac{\overline{F}\mu_o^2 e^{-\tau/\mu_o}}{\mu_o^2 K^2 - 1}[1 + (1-\omega_o)g] \qquad \text{B-141}$$

We now redefine some constants

$$A = \frac{\overline{F}A}{\sqrt{3(1-\omega_o)}}, \quad B = \frac{\overline{F}B}{\sqrt{3(1-\omega_o)}}, \quad \beta = \sqrt{\frac{1-\omega_o g}{3(1-\omega_o)}} \qquad \text{B-142}$$

$$D_1 = \frac{\overline{F}\mu_o}{\mu_o^2 K^2 - 1}[1 + 3\mu_o^2(1 - \omega_o)g]$$

$$D_0 = \frac{\overline{F}\mu_o}{\mu_o^2 K^2 - 1}[1 + (1 - \omega_o)g] \qquad \text{B-143}$$

Using these substitutions, the following equations for I_0 and I_1 result.

$$I_1 = Ae^{K\tau} + Be^{-K\tau} + D_1 e^{-\tau/\mu_o}$$
$$I_0 = -A\beta e^{K\tau} + B\beta e^{-K\tau} + D_0 e^{-\tau/\mu_o} \qquad \text{B-144}$$

Boundary Conditions

We must now consider our boundary conditions in the solution. Recall the equation for the flux at a given level of the atmosphere (B-94)

$$F^{\uparrow}(\tau) = \pi[I_0(\tau) \pm \frac{2}{3}I_1(\tau)] \qquad \text{B-145}$$

At the top of the atmosphere, the boundary condition is defined as that there is no downwelling diffuse component such that

$$F^{\downarrow}(0) = \pi[I_0(0) + \frac{2}{3}I_1(0)] = 0 \qquad \text{B-146}$$

Then for τ=0 (B-144) becomes

$$I_1(0) = A + B + D_1$$
$$I_0(0) = -A\beta + B\beta + D_0 \qquad \text{B-147}$$

or

$$-A\beta + B\beta + D_0 + \frac{2}{3}(A + B + D_1) = 0$$
$$-[D_0 + \frac{2}{3}D_1] = A(\frac{2}{3} - \beta) + B(\frac{2}{3} + \beta) \qquad \text{B-148}$$

From the definition of the D's (B-143) it can be shown that

$$D_0 + \frac{2}{3}D_1 = \frac{\overline{F}\mu_o}{\mu_o^2 K^2 - 1}\left[\frac{2}{3} + 2\mu_o^2(1-\omega_o)g + \mu_o(1 + (1-\omega_o)g)\right] \qquad \text{B-149}$$

Consider the lower boundary condition for the diffuse radiance at the bottom of the atmosphere where $\tau=\tau^*$. At the bottom, the upward diffuse irradiance is equal to the product of the downward direct irradiance and the albedo (a) of the ground. Recall the upward diffuse irradiance (B-97)

$$F^{\uparrow}(\tau^*) = \pi[I_0(\tau^*) - \frac{2}{3}I_1(\tau^*)]$$

$$F^{\uparrow}(\tau^*) = \left\{\pi[I_0(\tau^*) + \frac{2}{3}I_1(\tau^*)] + \mu_{oFe}^{-\tau^*/\mu_o}\right\} a \qquad \text{B-150}$$

then

$$I_0(\tau^*) - \frac{2}{3}I_1(\tau^*) = a[I_0(\tau^*) + \frac{2}{3}I_1(\tau^*) + \frac{\mu_o F_o}{\pi}e^{-\tau^*/\mu_o}] \qquad \text{B-151}$$

(B-144) is then substituted into (B-151) to get

$$Ae^{K\tau^*}[a(\beta-\frac{2}{3})-(\beta+\frac{2}{3})] + Be^{K\tau^*}[(\beta-\frac{2}{3})-a(\beta+\frac{2}{3})]$$

$$= e^{-\tau^*/\mu_o}[D_0(a-1) + \frac{2}{3}D_1(a+1) + \frac{a\mu_o F_o}{\pi}] \qquad \text{B-152}$$

where a is the albedo at the surface.

Downward Irradiance Below a Cloud

We finally get a peek at the green thunderstorm problem. Consider the following geometry. The downwelling irradiance is that only from the sun at the top of the

atmosphere. Recall that the downwelling irradiance at any level τ is the sum of the diffuse and direct downwelling irradiances. Using the equations for the diffuse (B-94) and direct (B-96) downwelling irradiances the result is

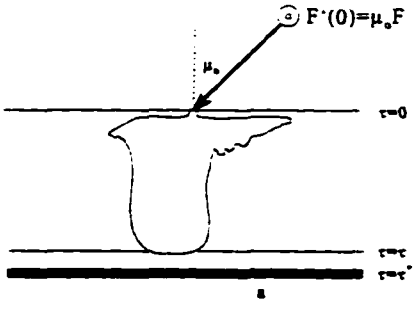

Figure B-7 - Geometry for the downwelling irradiance below a thunderstorm.

$$F^{\downarrow}(\tau) = \pi[I_0(\tau) + \frac{2}{3}I_1(\tau)] + \mu_o F e^{-\tau/\mu_o} \qquad \text{B-153}$$

where $F = \pi F_o$ and represents the solar irradiance perpendicular to the direction of incidence. Recall the irradiance equations (B-144)

$$\begin{aligned} I_1 &= Ae^{K\tau} + Be^{-K\tau} + D_1 e^{-\tau/\mu_o} \\ I_0 &= -A\beta e^{K\tau} + B\beta e^{-K\tau} + D_0 e^{-\tau/\mu_o} \end{aligned} \qquad \text{B-154}$$

Substitute these relations into (B-153) and use the definitions for the constants [(B-115), (B-142), (B-143), and (B-144)] the following results

$$\begin{aligned} F^{\downarrow}(\tau) &= \pi[Ae^{K\tau}(\frac{2}{3} - \beta) + Be^{-K\tau}(\frac{2}{3} + \beta)] \\ &+ \pi e^{-\tau/\mu_o}[D_0 + \frac{2}{3}D_1 + \mu_o F_o] \end{aligned} \qquad \text{B-155}$$

where $D_o + \frac{2}{3}D_1$ is defined by (B-149)

$$\begin{aligned} F^{\downarrow}(\tau) &= \pi[Ae^{K\tau}(\frac{2}{3} - \beta) + Be^{-K\tau}(\frac{2}{3} + \beta)] \\ &+ \frac{\pi e^{-\tau/\mu_o}\overline{F}\mu_o}{\mu_o^2 K^2 - 1}[\frac{2}{3} + 2\mu_o^2(1-\omega_o)g + \mu_o(1 + (1-\omega_o)g)] + \mu_o F_o] \end{aligned} \qquad \text{B-156}$$

Scale Analysis and Approximations

Green thunderstorms are usually encountered in the late afternoon when the sun angle is rather low (high solar zenith angle) thereby μ_o tends toward zero. Furthermore, a cloud is a weak absorber of solar radiation so the albedo of single scatter approaches unity. The following approximation can be made

$$\mu_o^2 K^2 = \mu_o^2[3(1-\omega_o)(1-\omega_o g)] \qquad \text{B-157}$$

given that μ_o is small. Also, as ω_o approaches 1, $(1-\omega_0)$ becomes very small. So the entire relation $\mu_o^2K^2$ is negligible compared to unity, so the denominator in (B-156) goes to -1. In (B-149) the D_0 and D_1 terms contain μ_o and ω_o. After some simple analysis,

$$D_0 + \frac{2}{3}D_1 = -\frac{F_o\mu_o}{2\pi} \qquad \text{B-158}$$

But is this a reasonable approximation? This is checked by first assuming a storm late in the afternoon when the sun is only 10° above the horizon giving a solar zenith angle of 80° or a μ_o of 0.17. The albedo of single scattering is described by

$$\omega_o = \frac{\beta_s}{\beta_s + k_a} \qquad \text{B-159}$$

where ω_o is the albedo for single scatter, β_s is the scattering coefficient, and k_a is the absorption coefficient. So the albedo of single scatter is the ratio of the scattering coefficient to the total extinction coefficient. $(1-\omega_o)$ is simply the ratio of the absorption coefficient to the extinction coefficient

$$1-\omega_o = \frac{k_a}{\beta_s + k_a} \qquad \text{B-160}$$

The scattering and absorption coefficients are defined by an integral of the scattering and absorption cross sections , multiplied by the number density, over the radius.

$$\beta_s = \int_0^\infty C_{sca}(a)\ N(a)\ da$$
$$k_a = \int_0^\infty C_{abs}(a)\ N(a)\ da \qquad \text{B-161}$$

For diameters that are much larger than the wavelength of light, which is a certainty in the case of the thunderstorm environment, the sum of the cross sections is approximately twice the geometric area

$$C_{sca} + C_{abs} \approx 2\pi a^2 \qquad a \gg \lambda \qquad \text{B-162}$$

Bohren (1983) gives a relationship for the absorption coefficient of a weakly absorbing sphere

$$C_{abs} = \frac{4}{3}\pi a^3 (\frac{k_i}{n})[n^3 - (n^2 - 1)^{3/2}] \qquad \text{B-163}$$

where n is the real part of the index of refraction, k_i is the absorption coefficient, and a is the radius of the sphere. (B-160) can be approximated using (B-162) and (B-163)

$$1-\omega_o = \frac{\frac{4}{3}\pi a^3 (\frac{k_i}{n})[n^3 - (n^2 - 1)^{3/2}]}{2\pi a^2} \qquad \text{B-164}$$

Consider the right hand side of (B-164) inserting typical values for the variables and a rather large raindrop of 8 mm in diameter. Also a relatively high value for the absorption

coefficient of 0.5 m^{-1} is chosen. Using an index of refraction of 1.33, the values of $(1-\omega_o)$ and $(K^2\mu_o^2)$ can be computed. Doing the calculations results in

$$1-\omega_o = 1.69 \times 10^{-6}$$

$$K^2\mu_o^2 = 1.29 \times 10^{-7}$$

so the approximation of $(K^2\mu_o^2-1)\rightarrow -1$ is valid. Now consider the second term on the right hand side of (B-149)

$$[\frac{2}{3} + 2\mu_o^2(1-\omega_o)g + \mu_o(1 + (1-\omega_o)g)] \qquad \text{B-165}$$

If the computations are carried out, assuming g=0.85 representing a strong forward scatterer, the result is

$$\frac{2}{3} + 8.3\times10^{-8} + 0.17 + 2.4\times10^{-7}$$
$$\Rightarrow \mu_o + \frac{2}{3} \qquad \text{B-166}$$

so the simplified equation can be written as

$$D_o + \frac{2}{3}D_1 = -\frac{F_o\mu_o}{2\pi} \bullet [\mu_o + \frac{2}{3}] \qquad \text{B-167}$$

However, with $\mu_o \approx 0.17$, μ_o is not small compared to ⅔ but we can approximated by

$$\mu_o + \frac{2}{3} \approx 1 \qquad \text{B-168}$$

There will be no error in wavelength dependence, which is what we are much more interested in, but there will be some error in magnitude of the computed irradiance. So the original approximation (B-158) is valid. Rewriting our approximation

$$D_0 + \frac{2}{3}D_1 = -\frac{F_o\mu_o}{2\pi} \qquad \text{B-169}$$

The equation for the downwelling flux can be written

$$F^{\downarrow}(\tau) = \pi[Ae^{K\tau}(\frac{2}{3} - \beta) + Be^{-K\tau}(\frac{2}{3} + \beta) + e^{-\tau/\mu_o}\frac{\mu_o F_o}{2\pi}] \qquad \text{B-170}$$

Now consider the β term in (B-170)

$$\beta = \frac{1-\omega_o g}{K} \qquad \text{B-171}$$

but the approximations for β are

$$\frac{2}{3} - \beta = -\beta$$
$$\frac{2}{3} + \beta = \beta \qquad \text{B-172}$$

We now turn our attention to the optical depth of the green thunderstorm. Following the development of Bohren and Fraser (1993) the optical depth (τ) is given as

$$\tau = 3\frac{H}{d} \qquad \text{B-173}$$

where H is the integrated liquid water depth and d is the mean droplet diameter. If a cumulonimbus cloud with a single drop size of 40μm and a liquid water depth of 1.5 cm

is assumed then the resulting optical depth is 1125. An optical depth of this size reduces the exponential term to near zero so the downwelling flux equation reduces to

$$F^{\downarrow}(\tau) = \pi[-A\beta e^{K\tau} + B\beta e^{-K\tau}] \qquad \text{B-174}$$

The coefficients A and B must now be solved for. To do this, boundary conditions are once again brought to use. Recall the result (B-148) for the downwelling irradiance at the top of the atmosphere

$$-[D_0 + \frac{2}{3}D_1] = A(\frac{2}{3} - \beta) + B(\frac{2}{3} + \beta) \qquad \text{B-175}$$

Also, recall the result of the upwelling irradiance at the surface (B-152)

$$\begin{aligned} &Ae^{K\tau^*}[a(\beta-\frac{2}{3})-(\beta+\frac{2}{3})] + Be^{K\tau^*}[(\beta-\frac{2}{3})-a(\beta+\frac{2}{3})] \\ &= e^{-\tau^*/\mu_o}[D_0(a-1) + \frac{2}{3}D_1(a+1) + \frac{a\mu_o F_o}{\pi}] \end{aligned} \qquad \text{B-176}$$

but, in this case, the surface albedo is assumed to be zero. Furthermore, given the optical depth of 1125, the exponential term is zero. The result is

$$-Ae^{K\tau^*}(\beta+\frac{2}{3}) + Be^{K\tau^*}(\beta-\frac{2}{3}) = 0 \qquad \text{B-177}$$

Puting (B-175) and (B-177) in matrix for, and using (B-169) gives

$$\begin{bmatrix} \frac{2}{3}-\beta & \frac{2}{3}+\beta \\ -e^{K\tau}(\beta+\frac{2}{3}) & -e^{K\tau}(\beta-\frac{2}{3}) \end{bmatrix} \begin{bmatrix} A \\ B \end{bmatrix} = \begin{bmatrix} \frac{F_o\mu_o}{2\pi} \\ 0 \end{bmatrix} \qquad \text{B-178}$$

Solving for A

$$A = \frac{-\frac{F_o\mu_o}{2\pi}e^{-K\tau}(\frac{2}{3}-\beta)}{e^{K\tau}(\frac{2}{3}+\beta)^2 - e^{-K\tau}(\frac{2}{3}-\beta)^2} \qquad \text{B-179}$$

and solving for B results in

$$B = \frac{\frac{F_o\mu_o}{2\pi}e^{-K\tau}(\frac{2}{3}+\beta)}{e^{K\tau}(\frac{2}{3}+\beta)^2 - e^{-K\tau}(\frac{2}{3}-\beta)^2} \qquad \text{B-180}$$

These are then substituted into the equation for the downwelling flux (B-155) recalling again that the thick optical depth reduces the last term on the right hand side to zero

$$F^{\downarrow}(\tau) = \pi[Ae^{K\tau}(\frac{2}{3}-\beta) + Be^{-K\tau}(\frac{2}{3}+\beta)] \qquad \text{B-181}$$

Continuing to make the substitutions and recalling that

$$|\beta| \gg \pm\frac{2}{3}, \qquad \beta = \frac{1-\omega_o g}{K} \sim \frac{1-g}{K} \qquad \text{B-182}$$

then we get our final result of

$$\boxed{\begin{aligned} F^{\downarrow}(\tau) &\approx \frac{4F^{\downarrow}(0)}{3(1-g)}\,\frac{Ke^{-K\tau}}{1-e^{-2K\tau}} \\ K &= \sqrt{3(1-\omega_o)(1-g)} \end{aligned}} \qquad \text{B-183}$$